Analysis of Metal-oxide Protected Photoelectrochemical Systems for Water Splitting

Thesis by

Michael Yang Lichterman

In Partial Fulfillment of the Requirements for the degree of

Ph.D. in Chemistry

CALIFORNIA INSTITUTE OF TECHNOLOGY

Pasadena, California

2018

(Defended April 16, 2018)

Michael Lichterman
ORCID: 0000-0002-0710-7068

Acknowledgements

I have been incredibly lucky to have great mentors and colleagues in my time here at Caltech. I must thank Nate Lewis and Harry Gray for providing and open and relaxed environment in which I could ask questions and work on a diverse set of projects, while providing advice whenever it was necessary. I must also thank Bruce Brunschwig and Achim Lewerenz for their assistance with instrumentation and project design, as well as, among others, Shu Hu and Matthias Richter in particular, without whom the later AP-XPS experiments would not have been possible. Generally this research was supported by the US Department of Energy, for which I am very grateful.

In Caltech, Azhar Carim, Jonathan Thompson, and Fadl Saadi have provided a great deal of support and suggestions or ideas in my time here, in addition to making my time here a great deal more fun. I must thank Dan Torielli and Adam Nielander for captaining the Lewis group softball team to a number of victories. In my other primary sporting adventure, a large cast of supporting characters have contributed to a great many exciting games and tournaments of ultimate frisbee in which I have participated: Aaron Krupp, Magnus Haw, Liz Jensen, Daryl Yee, and Seth Gillum, among others. Naturally with this list I must also add the physical therapists who have occasionally had to put me back together, in particular Jenny Norris.

In other walks of life, I must thank my lovely wife, Yue Yang, for her understanding and support and I look forward to many years together. I also thank my parents, without whose help my achievements would not have been possible.

Abstract

The photoelectrochemical splitting of water into oxygen and hydrogen gas is one pathway toward the renewable and economic generation of a fuel which is sufficiently scalable to power a large fraction, or even a majority, of the power requirements of modern society. In order to make such a device economically promising, it must be sufficiently cheap, have sufficiently high efficiency, or some combination thereof. In this work, two primary routes toward such a device are discussed; the first is the use of a cheaply prepared photoanode material, $BiVO_4$, the interactions of this material with cobalt oxide based catalysts, and the use of such structures in more extreme pH ranges than have previous been reported. The second route details the application of a protective layer, TiO_2, on otherwise unstable materials such as GaP and CdTe when operated as photoanodes in alkaline media. The further work herein applies *operando* ambient-pressure x-ray photoelectron spectroscopy (AP-XPS) to understand the nature of the energetics which allow conduction in the aforementioned TiO_2, as well as other energetics in the electrochemical double layer in the adjacent electrolyte. Further experiments using Raman spectroscopy on associated III-V photoanode devices are also described.

Summary Introduction

Chapter I examines primarily the photoanodic material $BiVO_4$ and is devoted to different catalysts and the stability of their interactions with this material and with the electrolyte. Chapter II describes my work with TiO_2 applied to GaP and CdTe semiconductors, which is a different way to make a photoanode but one which, like the $BiVO_4$ mentioned previously, could account for one half of a photoelectrochemical cell, or in the case of a photoanode with a very high built-in voltage, the entire photoelectrochemical cell. Chapter III includes *operando* AP-XPS experiments undertaken to better understand the basis of conductivity in the TiO_2 used in Chapter II, as well as demonstrating a means by which any photoelectrochemical material may be interrogated by XPS. Chapter IV is also an AP-XPS chapter but instead analyzes the electronics in the electrolyte layer adjacent to the electrode instead of within the electrode itself; both are important in an overall photoelectrochemical cell. Chapter V details more recent, and as of yet unpublished, work to investigate the band bending characteristics of different n-GaAs based solar cells built from different overlayer approaches, but also including the TiO_2 mentioned previously. All of these works generally contribute to a better understanding in the field of the construction of superior photoelectrochemical systems.

Published Content and Contributions

Chapter I:

1. Lichterman, M. F.; Shaner, M. R.; Handler, S. G.; Brunschwig, B. S.; Gray, H. B.; Lewis, N. S.; Spurgeon, J. M., Enhanced Stability and Activity for Water Oxidation in Alkaline Media with Bismuth Vanadate Photoelectrodes Modified with a Cobalt Oxide Catalytic Layer Produced by Atomic Layer Deposition. *J. Phys. Chem. Lett.* **2013,** *4* (23), 4188-4191. doi: 10.1021/jz4022415

MFL designed the study, conducted the experiments, and wrote the manuscript.

Chapter II:

2. Lichterman, M. F.; Carim, A. I.; McDowell, M. T.; Hu, S.; Gray, H. B.; Brunschwig, B. S.; Lewis, N. S., Stabilization of n-cadmium telluride photoanodes for water oxidation to O2(g) in aqueous alkaline electrolytes using amorphous TiO2 films formed by atomic-layer deposition. *Energy Environ. Sci.* **2014,** *7* (10), 3334-3337. doi: 10.1039/c4ee01914h

MFL designed the study, conducted the experiments, and wrote the manuscript.

Chapter III:

3. Lichterman, M. F.*; Hu, S.*; Richter, M. H.*; Crumlin, E. J.*; Axnanda, S.; Favaro, M.; Drisdell, W.; Hussain, Z.; Mayer, T.; Brunschwig, B. S.; Lewis, N. S.; Liu, Z.; Lewerenz, H.-J., Direct observation of the energetics at a semiconductor/liquid

junction by operando X-ray photoelectron spectroscopy. *Energy Environ. Sci.* **2015,** *8* (8), 2409-2416. doi: 10.1039/c5ee01014d

MFL, along with the listed coauthors, designed the study and ran the experiments; MFL and MHR analyzed the findings, and MFL wrote the manuscript.

4. Lichterman, M. F.*; Richter, M. H.*; Hu, S.*; Crumlin, E. J.*; Axnanda, S.; Favaro, M.; Drisdell, W.; Hussain, Z.; Brunschwig, B. S.; Lewis, N. S.; Liu, Z.; Lewerenz, H.-J., An Electrochemical, Microtopographical and Ambient Pressure X-Ray Photoelectron Spectroscopic Investigation of Si/TiO2/Ni/Electrolyte Interfaces. *J. Electrochem. Soc.* **2016,** *163* (2), H139-H146. doi: 10.1149/2.0861602jes

MFL, along with the listed coauthors, designed the study and ran the experiments; MFL and MHR analyzed the findings, and MFL wrote the manuscript.

Chapter IV:

5. Lichterman, M. F.*; Richter, M. H.*; Brunschwig, B. S.; Lewis, N. S.; Lewerenz, H.-J., Operando X-ray photoelectron spectroscopic investigations of the electrochemical double layer at Ir/KOH(aq) interfaces. *Journal of Electron Spectroscopy and Related Phenomena* **2017,** *221* (Supplement C), 99-105. Doi: 10.1016/j.elspec.2017.03.011

MFL designed the study, MHR and MFL ran the experiments and analyzed the findings, and MFL wrote the paper.

For as-yet unpublished manuscript 6, chapter V, MFL was responsible for experimental design, undertaking, analysis, and writeup.

Table of Contents

I. Cobalt Oxides and their use with $BiVO_4$, a wide-bandgap metal oxide semiconductor

Introduction.

Cobalt oxide has gained much interest as a water oxidation catalyst, particularly as one which may function in neutral conditions with appropriate choice of electrolyte. However, cobalt oxide, like many metal oxides, may also function as an oxygen evolution reaction (OER) catalyst at elevated pH conditions as well. The means by which cobalt oxide is deposited on an electrode or photoelectrode, as well as the pH (and, if relevant, buffer) in which it is ran, play a key role in the catalytic activity that results from the electrode. Furthermore, while generally, a thicker catalyst will be more active on a geometric basis, this can incur a significant penalty if light absorption by a semiconductor beneath the catalyst will drive photoinduced water oxidation. In such a case, the requirements for an active catalyst must be balanced by the requirement that the underlying semiconductor absorbs a significant fraction of incident sunlight such that photocurrent is delivered to the catalyst at the surface.

$BiVO_4$ is a metal oxide semiconductor which has attracted much attention in recent times due to its relatively small bandgap (~2.45eV) when compared to other metal oxides such as TiO_2 (~3.2eV). This smaller bandgap originates from Bi; where most metal oxides have a valence band formed from O 2p orbitals and a conduction band from metal d orbitals (3d, 4d, etc), $BiVO_4$ has a valence band that originates from a mixing of the O 2p and Bi 6s orbitals, which results in an elevated (more negative; closer to

vacuum) valence band. However, while 2.45eV is small compared to other semiconductors, it is still a large bandgap compared to the ideal bandgap size (1.1-1.4eV) for a light absorber of the AM 1.5G solar spectrum. While a maximum photocurrent of 7.5mA cm^{-2} is possible for a light absorber with this bandgap, in practice, $BiVO_4$ photoelectrodes have generally produced a much lower photocurrents due to deleterious effects such as recombination. Any light with energy >2.45eV absorbed by the catalyst is thus very deleterious with respect to overall system performance; while on a small-bandgap absorber, the loss of a few mA cm-2 may only decrease the overall photocurrent from 30mA cm^{-2} to 27 mA cm^{-2}, in this case, the decrease could be from 4 mA cm^{-2} to 1 mA cm^{-2}. Therefore, the emplacement of a catalyst with a minimal absorption profile is crucial for the construction of a device with a significant current density.

I.1. Pyrophosphate solutions as a new way to deposit cobalt oxide

The efficient conversion of solar energy to fuels for a sustainable source of energy remains a great challenge for current research. An integrated device in which a photocathode and photoanode separate electrons and holes to split water by producing hydrogen and oxygen, respectively, requires either a different semiconductor for either side, or multiple buried junctions in the same semiconductor, to achieve respectable efficiencies. However, while silicon based devices using buried p/n junctions with attached proton reduction catalysts such as platinum or NiMo can capture sunlight efficiently and store it as hydrogen, silicon is prone to oxidation when used as a photoanode. In addition, it has certain drawbacks in terms of expense and the energetics required to create solar-grade silicon devices. As a result, one avenue of research is to use silicon as a photocathode and a separate semiconductor as the photoanode. If one wishes to make a tandem structure using silicon for the photocathode and the different semiconductor for the photoanode, however, the identity of the photoanode remains problematic.[1]

Using cheap, stable, and abundant semiconductors to split water has thus become an active area of research[2]. Bismuth vanadate is a cheap semiconductor which may be prepared by a variety of methods and can achieve an impressive fraction of its theoretical maximum energy output without a highly expensive synthesis in terms of economic or energetic costs as it creates charge separation via a semiconductor-liquid junction instead of a buried p/n junction. It has appropriate band alignment for such a junction to oxidize

water to oxygen, enabling it to function as the photoanode in a PEC type water splitting device.[3] Herein, we discuss the use of this semiconductor with a focus on two avenues of research: first, the deposition of a thin film for both photoactivity in terms of oxygen production and photostability of the semiconductor; and second, improvements to the J-V performance of this system when optical transparency and reflection are considered.

Initial work was devoted to developing a new method, not necessarily atomic-layer deposition based, by which to deposit a thin, optically transparent, cobalt oxide catalyst on a surface (semiconductor surface or fluorine-doped tin oxide (FTO)). This work was originally designed around the interlinking of a surface (such as TiO_2) to a catalyst above it, but was redirected upon the realization that such work was effectively pointless given the numerous tools at our disposal. Thus, varying the conditions of the electrodeposition bath was chosen as a means by which an ideal film of cobalt oxide might be deposited onto a catalyst surface.

Nocera and coworkers have shown that the use of a phosphate buffer deposits a catalyst that was termed "Co-P_i", as it was surmised that the inclusion of inorganic phosphate ("P_i") into the structure was crucial for the functioning of the electrocatalyst.[4] However, as was shown by Jeon and coworkers[1], when a thick film of this catalyst was deposited onto $BiVO_4$ using these conditions, the resulting black film effectively destroyed the photoactivity of the photoelectrodes due to the very highly absorbing "Co-P_i" (cobalt oxide) film. By using essentially identical conditions but using a pyrophosphate buffer ("P_iP_i") instead of a phosphate buffer, we deposited a cobalt oxide

under anodic conditions with a different structure at the atomic scale which appears to be less absorbing.

Catalyst was electrodeposited following standard 3-electrode electrochemical means. A SCE electrode was used to contact an electrodeposition solution containing 5mM Co(NO3)2 and either .1M KP_i, pH 6.8, or .1 M $K_2P_iP_i$, pH 6.8. A carbon rod was used as the counter electrode. The volume of solution used for these depositions was 50mL ddH2O. Depositions were run by setting the working electrode to 1050, 1125, or 1200 mV vs SCE for 10 minutes followed by an open circuit period for 1 minute, and this was repeated for whatever length of time was desired. The above voltages were generally found to perform similarly.

The as-prepared $BiVO_4$ films were found to pass oxidizing cur-rent even in the absence of a catalyst at 400mV positive of RHE and higher in neutral pH .1M KPi buffer; however, this was shown be highly unstable as shown in repeated CV sweeps in Figure 1, below.

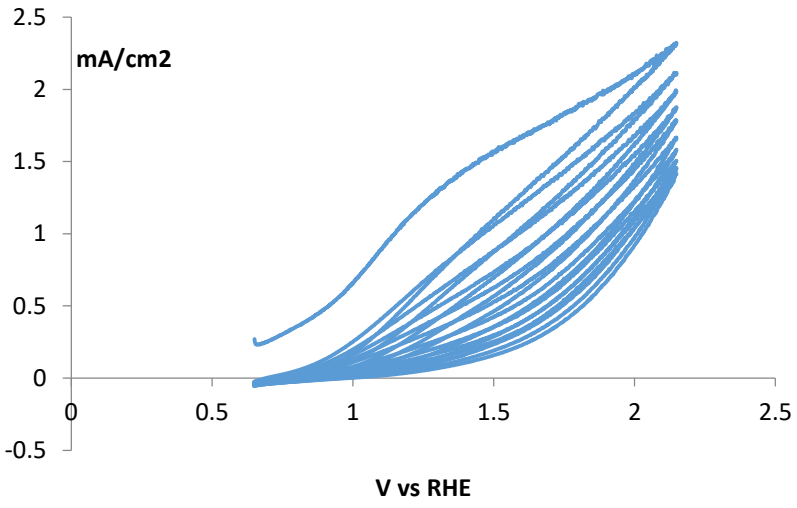

Figure 1. Repeated CV sweeps of $BiVO_4$ (bare) in pH 7 electrolyte with AM 1.5G illumination.

We hoped to maintain or improve this current density while stabilizing the BiVO4 films with a catalyst layer that would allow for O2 production using front illumination. Deposition of CoPi following published procedure was found in previous papers to give a black film that absorbs light; however, we found that using disodium pyrophosphate at similarly neutral pH solutions gave a much thinner, much more transparent film. As a result, we turned to this catalyst formation procedure and varied deposition times, initially between 10 and 40 minutes. In this time window, CoPi depositions at 1125 mV vs SCE leads to decreasing current densi-ties by front illumination; however, no corresponding decrease was observed for the CoPiPi system. Moreover, the system appeared remarkably stable over the course of the CV sweeps used to quickly determine photoactivity. Thus, we decided to increase the deposition time to give an optimal amount of catalyst, and it was found that depositions for 2 hours gave excellent photoresponse and stability. Figure 2 shows the front and back illumination JV curves for such an electrode.

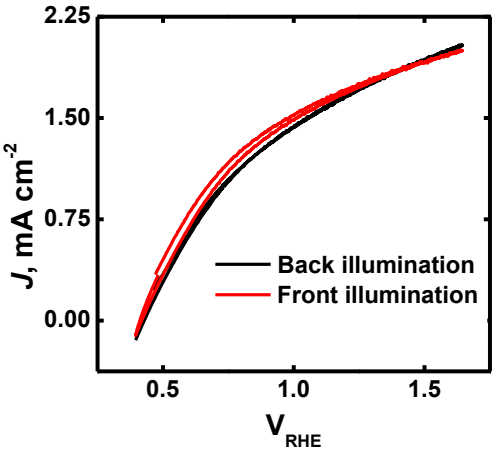

Figure 2. Repeated (4) Front and Back CV sweeps of a CoP_iP_i coated $BiVO_4$/FTO electrode at AM1.5G, 1 sun illumination.

Following the collection of the CV data shown in Figure 2, oxygen detection experiments were carried out to verify that the current delivered is oxidizing water to oxygen. A fluorescence experiment was carried out as described in the experimental section in Section 2. As shown in Figure 3a and 3b, both front and back illumination give effectively stoichiometric oxygen production (any non-stoichiometric current flow is within the margin of error for this type of experiment due to bubble formation).

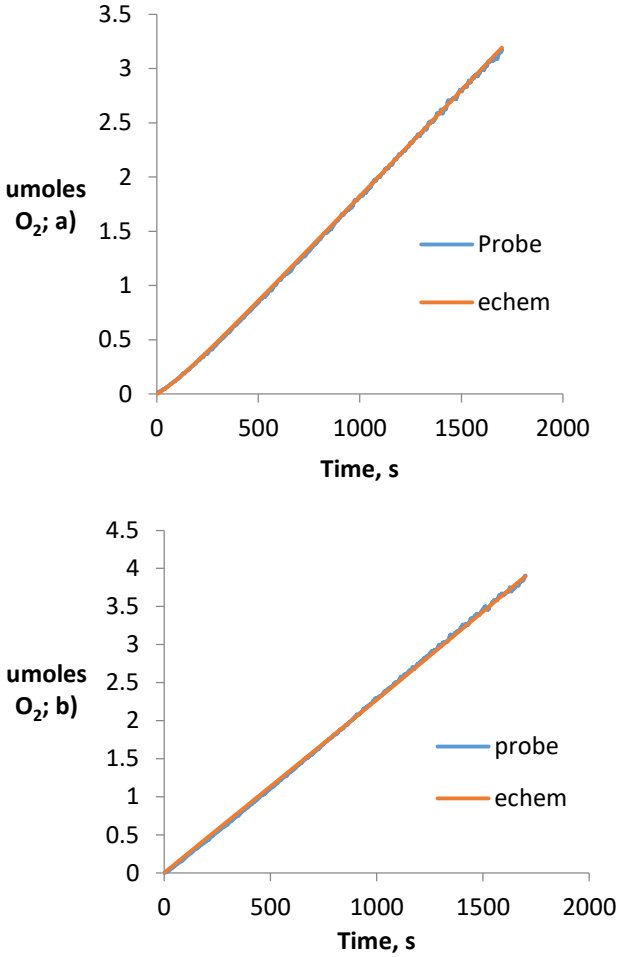

Figure 3. a) O_2 produced by front illumination at a constant voltage and illumination as calculated by coulombs of charge passed and O_2 detected by florescence probe; b) the same, for back illumination.

These samples were shown to be remarkably stable with respect to back illumination; a constant current could be observed for approximately 12 hours, as shown below. However, with front illumination, the catalyst film was seen to be stable for a much shorter amount of time. Over the course of approximately 5 hours, it would turn

black and obscure light. XANES[5] and EXAFS[6] was employed to analyze the changes that may have occurred here, and it was found that the organization of the catalytic layer had changed remarkably as the color change took place.

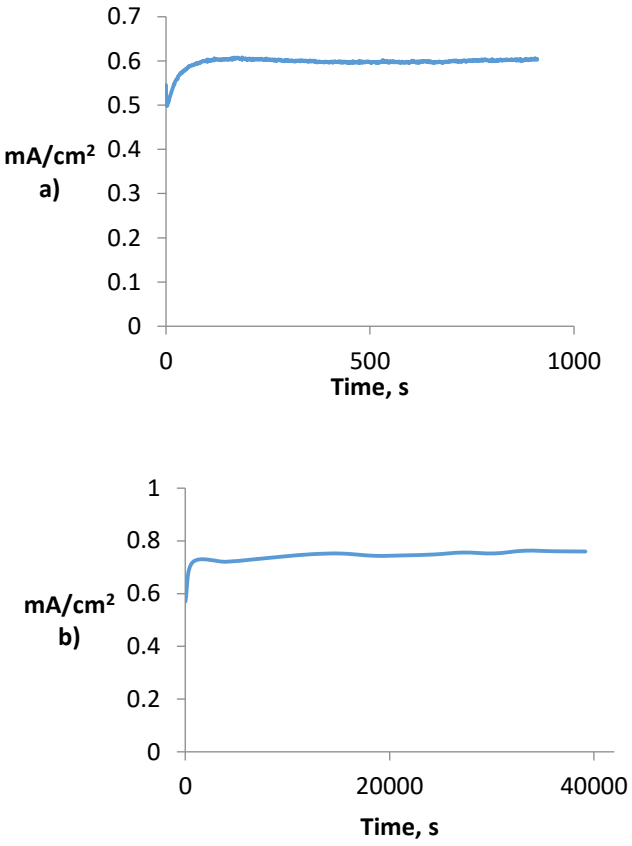

Figure 4. a) Current vs Time for front illumination for 15 minutes -.1 vs SCE, 1 sun, b) back illumination for 12 hours, -.1 vs Ag/AgCl, 1 sun.

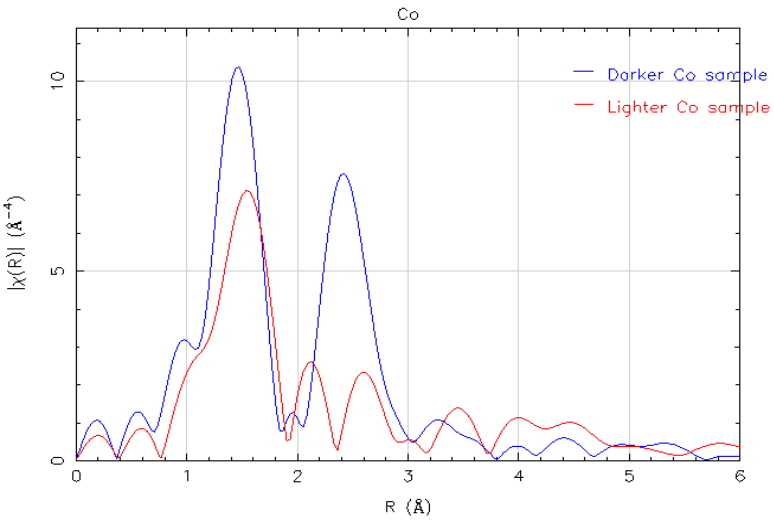

Figure 5. Fourier Transformed EXAFS data for Cobalt Oxide layer, lighter film and darker film. The darker film had been run with front illumination for hours before being analyzed by EXAFS.

As figure 5 shows, the lighter, as-deposited film contains a much lower amount of order beyond 2 angstroms. This suggests a more disordered structure when it is deposited which then, when used in phosphate buffer, slowly turns to a dark black CoP_i layer, which has more long range order and absorbs a higher amount of light. Unfortunately, when a PiPi pH 6.8 buffer was used for PEC experiments, the buffer resulted in the dissolution of the $BiVO_4$ electrode. Thus, while the catalyst may have been stable in these conditions, the semiconductor was not.

Acknowledgements: I would like to thank Joshua Spurgeon and Dr. Eitan Anzenberg for their assistance in collecting the above data.

References

1. (a) Walter, M. G.; Warren, E. L.; McKone, J. R.; Boettcher, S. W.; Mi, Q.; Santori, E. A.; Lewis, N. S., Solar Water Splitting Cells. *Chem. Rev.* **2010,** *110* (11), 6446-6473; (b) Ding, C.; Shi, J.; Wang, D.; Wang, Z.; Wang, N.; Liu, G.; Xiong, F.; Li, C., Visible light driven overall water splitting using cocatalyst/BiVO4 photoanode with minimized bias. *Phys. Chem. Chem. Phys.* **2013,** *15* (13), 4589-4595.
2. (a) Abdi, F. F.; Han, L.; Smets, A. H. M.; Zeman, M.; Dam, B.; van de Krol, R., Efficient solar water splitting by enhanced charge separation in a bismuth vanadate-silicon tandem photoelectrode. *Nat. Commun.* **2013,** *4*; (b) Abdi, F. F.; Firet, N.; van de Krol, R., Efficient BiVO4 Thin Film Photoanodes Modified with Cobalt Phosphate Catalyst and W-doping. *ChemCatChem* **2013,** *5* (2), 490-496.
3. (a) Gawande, S.; Thakare, S., Graphene wrapped BiVO4 photocatalyst and its enhanced performance under visible light irradiation. *Int Nano Lett* **2012,** *2* (1), 1-7; (b) Pilli, S. K.; Deutsch, T. G.; Furtak, T. E.; Brown, L. D.; Turner, J. A.; Herring, A. M., BiVO4/CuWO4 heterojunction photoanodes for efficient solar driven water oxidation. *Phys. Chem. Chem. Phys.* **2013,** *15* (9), 3273-3278.
4. Kanan, M. W.; Nocera, D. G., In Situ Formation of an Oxygen-Evolving Catalyst in Neutral Water Containing Phosphate and Co2+. *Science* **2008,** *321* (5892), 1072.
5. Mierwaldt, D.; Mildner, S.; Arrigo, R.; Knop-Gericke, A.; Franke, E.; Blumenstein, A.; Hoffmann, J.; Jooss, C., In Situ XANES/XPS Investigation of Doped Manganese Perovskite Catalysts. *Catalysts* **2014,** *4* (2), 129-145.
6. Yano, J.; Pushkar, Y.; Glatzel, P.; Lewis, A.; Sauer, K.; Messinger, J.; Bergmann, U.; Yachandra, V., High-Resolution Mn EXAFS of the Oxygen-Evolving Complex in Photosystem II: Structural Implications for the Mn(4)Ca Cluster. *J. Am. Chem. Soc.* **2005,** *127* (43), 14974-14975.

I.2. ALD as a way to deposit cobalt oxide catalyst and its use at pH 13

Originally published as "Enhanced Stability and Activity for Water Oxidation in Alkaline Media with Bismuth Vanadate Photoelectrodes Modified with a Cobalt Oxide Catalytic Layer Produced by Atomic Layer Deposition" in the Journal of Physical Chemistry Letters[1].

An integrated solar fuels system in which electrons and holes are separated and used to split water requires either a single wide band-gap absorber or multiple absorbers that in aggregate produce the required driving force of 1.23 V plus overpotentials and resistance losses.[2] A tandem device that uses a small band-gap absorber such as Si therefore requires that the second absorber have a larger band gap and provide a large photovoltage. Silicon, the most widely studied photoabsorber, is generally unstable toward oxidation when used as a photoanode. Thus one approach to the development of a tandem device is to utilize a larger band-gap semiconductor as the photoanode in combination with material having a band gap of ~ 1.1 – 1.2 eV as the photocathode. Bismuth vanadate, $BiVO_4$, and related oxides are promising candidate materials for this photoanode.

$BiVO_4$, a 2.4-eV band-gap semiconductor that is composed of earth-abundant elements, can be prepared by a variety of methods.[3,4,5] The valence band of $BiVO_4$ is sufficiently positive of the water-oxidation potential to allow n-$BiVO_4$ to function as a photoanode for the oxygen-evolution reaction (OER). Furthermore, the conduction-band

edge of $BiVO_4$ is relatively negative in potential for a metal oxide, and its position overlaps the potential of the Si valence band.[6,7]

Although the behavior of n-$BiVO_4$ in neutral[8,9] and near-neutral media[4a, 10] has been extensively investigated, little work has been reported for water oxidation using n-$BiVO_4$ photoanodes at elevated pH values. Elevated pH (13 and above) has the benefits of high electrolyte conductivity without the need for extra buffering species or electrolytes; little or no pH gradient near the working electrodes under operating conditions; and the existence of gas-separating, hydroxide-conducting membranes capable of functioning in a complete, intrinsically safe, solar-driven water-splitting system.[11] We investigated the potential use of $BiVO_4$ at high pH to facilitate the design of a fully operational water-splitting device in alkaline media, due to the relative abundance of active catalysts for the hydrogen-evolution reaction (HER) and for the OER in this pH range,[1] in addition to the other benefits high pH would provide such as the lack of a buffer which may electrodialyze over time.[12] However, $BiVO_4$ is kinetically sluggish for water oxidation, which leads to poor photoelectrical performance and photocorrosion in alkaline media. At alkaline pH, water oxidation can be readily achieved using non-noble metal oxide catalysts such as nickel oxide, nickel-iron oxide[13], and cobalt oxide.[14] Herein we report the use of atomic-layer deposition (ALD) to form a thin layer of cobalt oxide on the surface of a bismuth vanadate photoanode, with the resulting material showing improved stability and acting as a catalytic protecting layer that enables the sustained oxidation of water by n-$BiVO_4$ in pH = 13 aqueous media.

n-$BiVO_4$ electrodes were synthesized by a solution-cast method following a published procedure[15] (see ESI for details). Cobalt oxide was deposited via ALD from a cobaltocene precursor, using a modification of a published procedure[16] in a Cambridge Nanotechnology (Savannah) ALD system. The cobaltocene was heated to 80 °C and the substrate maintained at 150 °C. An ALD cycle consisted of a 5 s pulse of the cobaltocene precursor; a 15 s purge with N_2(g) at 20 cm^3 min^{-1} (at STP); a 2 s ozone pulse; and another 15 s N_2(g) purge.

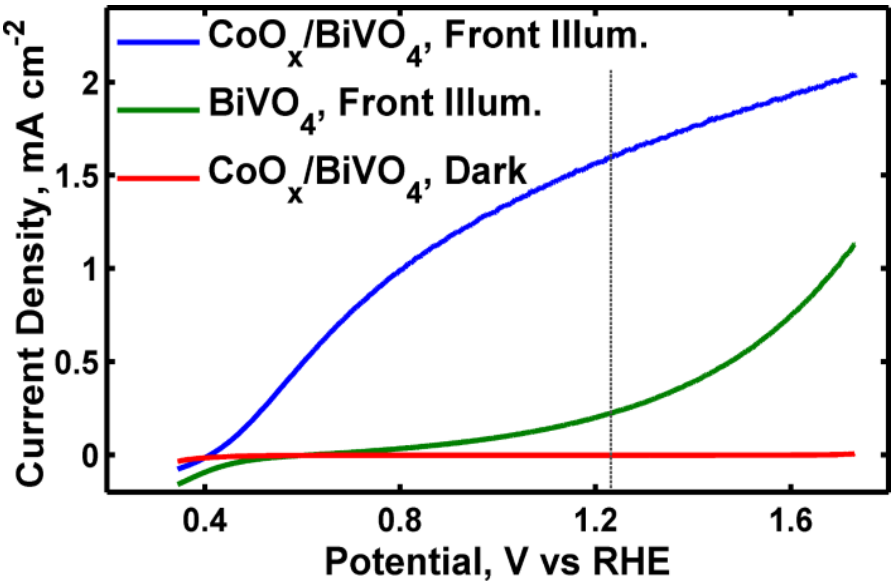

Figure 1. Linear Sweep Voltammogram (LSV) *J-E* scans in pH 13 KOH(aq) under 100 $mWcm^{-2}$ (Simulated 1 Sun) AM 1.5G. illumination: (blue) ALD-CoO_x/$BiVO_4$ front illumination, (green) $BiVO_4$ front illumination, (red) ALD-CoO_x/$BiVO_4$ dark sweep. Dotted line indicates 1.23 V vs RHE.

Use of > 25 ALD cycles for the CoO_x deposition resulted in poor photoelectrochemical behavior in the resulting n-$BiVO_4$ photoanodes (Fig. S2), suggesting a different interface with the catalyst when thick CoO_x layers were used. This conclusion was further

supported by experiments conducted with a sacrificial hole accepter (sulfite) indicating that the junction resulting from the deposition of thicker ALD CoO_x layers did not exhibit rectifying behavior (Fig. S3)." In contrast, 15-20 ALD cycles of CoO_x deposition yielded much improved current density (*J*) vs. potential (*E*) behavior (Fig. 1) as well as improved current density vs. time performance relative to the behavior of an uncoated n-$BiVO_4$ photoelectrode (Fig. 2). Under 100 mW cm^{-2} of simulated Air Mass 1.5 global (AM 1.5G) illumination in pH 13 (KOH) solution, the CoO_x/$BiVO_4$ photoanodes yielded photocurrent densities, *J*, of 1.49 (± .2) mA cm^{-2} at the potential for water oxidation, 1.23 V vs. the reversible hydrogen electrode, RHE[1], and open-circuit photopotentials of 0.404 (± 0.049) V vs. RHE, representing a photovoltage of 0.826 V for water oxidation under these conditions. This improved performance, in addition to the decrease in performance with slightly thicker layers, indicates that the thin CoO_x layer acts primarily as a catalyst that allows for facile hole collection relative to recombination, as opposed to producing a change in the energetics of the semiconductor/liquid junction. CoO_x was also electrodeposited on $BiVO_4$ electrodes, but thick CoO_x films were required to yield stable photocurrents and these thick films adhered poorly to the electrode, blocked incident light, and produced low photocurrent densities upon front illumination of the electrode. In addition, $BiVO_4$ films were prepared using 0 to 2% and 0 to 1% molybdenum doping at a concentration gradient, which has been shown, with optimization of light management parameters, to yield photocurrent densities as high as 3 mA cm^{-2} under 100 mW cm^{-2} of simulated AM1.5 G illumination. In our electrode configuration, ALD deposition of CoO_x on such doped $BiVO_4$ films produced electrodes that exhibited

[1] $E_{RHE} = E_{NHE} + 0.059 \quad pH = E_{Ag/AgCl} + 0.197 + 0.059 \quad pH$

similar *J-E* performance to the ALD CoO_x deposited on the undoped $BiVO_4$ films described herein.

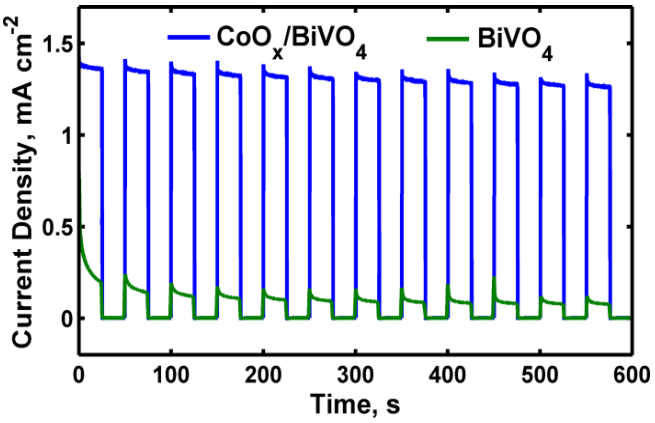

Figure 2. Current density vs. time behavior in pH 13 KOH (aq) at 1.23 V vs. RHE, under 100 mW cm^{-2} of simulated 1 Sun AM 1.5G front illumination.

Figure 2 shows the current density vs. time behavior, under potentiostatic conditions at an electrode potential, E = 1.23 V vs. RHE, with 100 mW cm^{-2} of simulated AM1.5 front-side illumination of the n-$BiVO_4$. Under these operating conditions, the stability of the photocurrent was significantly improved by the presence of the CoO_x overlayer.

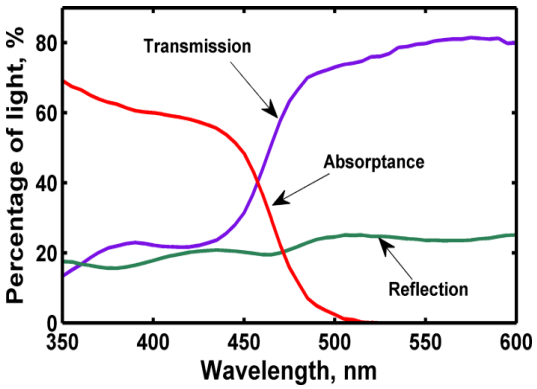

Figure 3. Transmission, reflection, and absorptance of $BiVO_4$ electrode before and after deposition of 15 ALD cycles of CoO_x. The curves were the same within experimental error before and after deposition of catalyst.

As the larger band-gap material in a tandem water-splitting device, front illumination is likely required for $BiVO_4$ photoanodes, making the optical transmission of the catalytic layer an important system design consideration. Figure 3 shows the transmission (T), reflection (R), and absorptance (A) (where 1.0=T+R+A) data for a representative n-$BiVO_4$ sample before and after deposition of the CoO_x film using ALD.

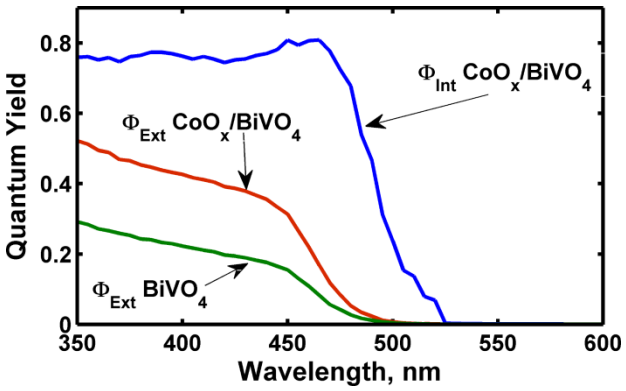

Figure 4. Quantum yields of $CoO_x/BiVO_4$ and $BiVO_4$ in pH 13 KOH(aq).

At 15-20 ALD cycles, the CoO_x film had little effect on the optical properties of the n-$BiVO_4$ photoelectrodes. The high degree of transmission above 500 nm would allow a substantial amount of light in this range to be captured by a silicon or GaAs cell in a tandem device structure. A recent analysis has concluded that the optimal thickness of a spatially uniform overlayer of CoO_x to balance light absorption with catalytic

performance is ~ 2.9 nm,[17] in accord with the properties described herein exhibited by the ultrathin, high coverage catalyst layers produced by ALD. The observed behavior contrasts with the significant optical losses produced by deposition of thick catalytic films.[15]

Figure 4 displays the external quantum yield, Φ_{Ext}, (i.e., the incident photon-to-current efficiency) and the internal quantum yield, Φ_{Int}, (the absorbed photon-to-current efficiency) of $BiVO_4$ and $CoO_x/BiVO_4$ photoelectrodes from 350 to 600 nm. These data were obtained by analysis of the spectral response and UV-visible absorption data on the electrodes of interest. Figure 4 displays the quantum yield data at E = 1.23 V vs. RHE, whereas data obtained at other voltages are plotted in Figure S4. From 350 to 400 nm, the catalyst-semiconductor system exhibited Φ_{Ext} ~ 0.45 and Φ_{Int} ~ 0.8. The lower performance of the bare n-$BiVO_4$ semiconductor (Fig. 4) indicated that the catalyst increased favorably the ratio of carrier collection to interfacial carrier recombination. This behavior is in accord with the behavior of $BiVO_4$ described previously at a less alkaline pH of 9 in a borate buffer.[4a]

The Co oxidation states and catalyst layer thickness data were evaluated using X-ray photoelectron spectroscopy (XPS). Figure S5 displays the XPS data of the $CoO_x/BiVO_4$ electrodes. Although the signal-to-noise ratio in the thin layer of cobalt oxide on these samples did not allow for definitive determination of the cobalt oxidation state, further samples were prepared using 200 ALD cycles of CoO_x on fluorine-doped tin oxide (FTO) coated glass (Fig. S6). The as-deposited samples contained a Co(II) species such as $Co(OH)_2$ or CoO, in addition to either the mixed spinel, Co_3O_4, or CoOOH. After

10 *J-E* scans, and after 30 min of potentiostatic operation under illumination at a potential E = 0.97 V vs. RHE for the $CoO_x/BiVO_4$ samples, peaks consistent with a more highly oxidized cobalt species were observed. Analysis of the thicker CoO_x/FTO films following a similar procedure indicated that this species was predominantly CoOOH. Following procedures described previously,[18] the thickness of the cobalt oxide layer was calculated to be 0.9 nm from XPS data for a sample produced using 20 ALD cycles (see ESI for details). Atomic-force microscopy images (Fig. S7) indicated similar surface morphology for the n-$BiVO_4$ with and without a number of layers of CoO_x.

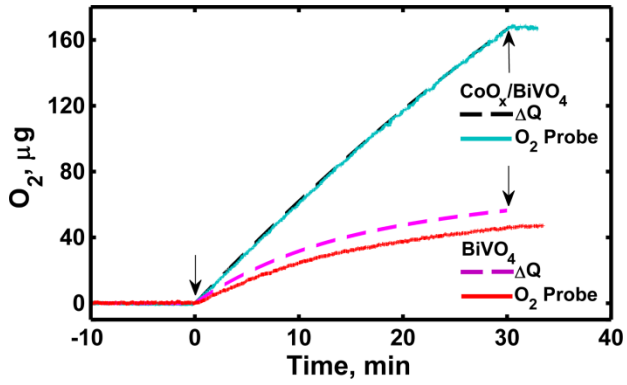

Figure 5. Oxygen production as detected by probe and coulometry at 0.97 V vs. RHE in pH 13 KOH(aq), AM 1.5G illumination. Arrows mark the beginning and end of current flow from the potentiostat.

Introduction of a co-catalyst to the photoanode can improve the system by kinetically directing a greater percentage of the photogenerated holes into the desired chemical reaction rather than photocorrosion of the semiconductor itself. Figure 5 displays the faradaic efficiency for production of O_2(g) by n-$BiVO_4$, as determined by an oxygen sensor in conjunction with coulometry. An air-tight cell was purged with Ar(g)

before a 10 min period during which the electrode was held at open circuit to quantify the oxygen leak rate. The electrode was then biased potentiostatically at $E = 0.00$ V vs. Ag/AgCl(sat) (0.97 V vs. RHE) for 30 min under front illumination. This system exhibited essentially 100% faradaic efficiency for O_2 evolution (Fig. 5), because conversion of the number of coulombs passed into the mass of O_2 expected, assuming 100% faradic efficiency ('ΔQ'), yielded a value of the amount of expected O_2 that was in excellent agreement with the observed mass of O_2 as detected by the O_2 probe ('Probe').

The pure n-$BiVO_4$ electrode exhibited a rapid decrease in current with time, with a decline of over 50% within 2 min of operation (Fig. 2), as well as a modest faradaic O_2 yield of ~ 70%. Hence passivation of the semiconductor occurred due to a low branching ratio for the holes created at the semiconductor/liquid junction. A significant decrease in the photocurrent on the CoO_x/n-$BiVO_4$ system also occurred, leading to ~50% of the initial photocurrent remaining after 1 h of anodic operation under illumination. This behavior is in accord with expectations based on the loss of the cobalt oxide film from the surface as well as the formation of a vanadium-poor, bismuth rich contacting layer. However, compared to bare n-$BiVO_4$, the decline in current was strongly inhibited by the presence of the CoO_x layer. This behavior, in conjunction with the data shown in Figure 5, suggests that the CoO_x allowed photogenerated holes produced by the n-$BiVO_4$ to oxidize water efficiently and quickly, better stabilizing the semiconductor against corrosion. Thus, the ALD catalyst coating promoted OER current over photopassivation of the n-$BiVO_4$ for this system, and hence similar catalyst attachment methods may find utility as a useful protection strategy for other photoanode systems.[19]

In conclusion, we have demonstrated the improved performance, stability, and faradaic water oxidation efficiency for n-$BiVO_4$ films at pH 13 which had been modified with CoO_x by an ALD process. The ALD process can be easily generalized to other metal oxide electrodes, suggesting that the protection of unstable electrodes at high pH is possible. Further work is under way to explore stabilization at higher pH conditions, where full, intrinsically safe, and efficient water-splitting systems can be readily built with established system designs.[11a]

Supporting Information.

Further experimental details, electrochemical, AFM, and XPS characterization. This material is available free of charge via the Internet at http://pubs.acs.org.

The authors declare no competing financial interest.

Acknowledgments

This work was supported through the Office of Science of the U.S. Department of Energy under award DE-SC0004993 to the Joint Center for Artificial Photosynthesis, a DOE Energy Innovation Hub. XPS and AFM data were collected at the Molecular Materials Research Center of the Beckman Institute of the California Institute of Technology. We thank Dr. Ragip Pala for helpful discussions.

Corresponding Authors

*Email:

Harry B. Gray: hbgray@caltech.edu

Nathan S. Lewis: nslewis@caltech.edu

Joshua M. Spurgeon: spurgeon@caltech.edu

Supporting Information: Experimental

Preparation of Electrodes

n-$BiVO_4$ electrodes were produced using a slight modification of published spin-coating procedures[15]. A stoichiometric solution of $Bi(NO_3)_3$•$5H_2O$ (Sigma Aldrich, 99.99%) and $VO(acac)_2$ (Sigma Aldrich, 98%) was prepared by making a solution of 398 mg of $VO(acac)_2$ in 50 mL 2,4-pentanedione (Acros, >99%) and a solution of 728 mg of $Bi(NO_3)_3$•$5H_2O$ in 7.5 mL 2,4-pentanedione. These solutions were then combined and mixed thoroughly. The resulting solution was spin-cast onto a slide of TEC-15 FTO glass (Hartford Glass) by masking the top 0.5 cm of glass using Scotch tape, coating the exposed area, and spinning twice at 1000 rpm for 6 s each time, per coating cycle, on a Laurell Technologies spin-coater with the acceleration set to 150. After each coating cycle, the tape was removed, and the glass was placed on a quartz holder and heated in an oven at 500 °C for 10 min. Nine deposition cycles were used to make $BiVO_4$ photoanodes; after the last coating cycle, the slide was sintered at 500 °C for 2 h. Figure S1 shows four FTO slides on a quartz plate after sintering, with a penny for size comparison. The slides were scored and broken into 1- × 2.5-cm pieces.

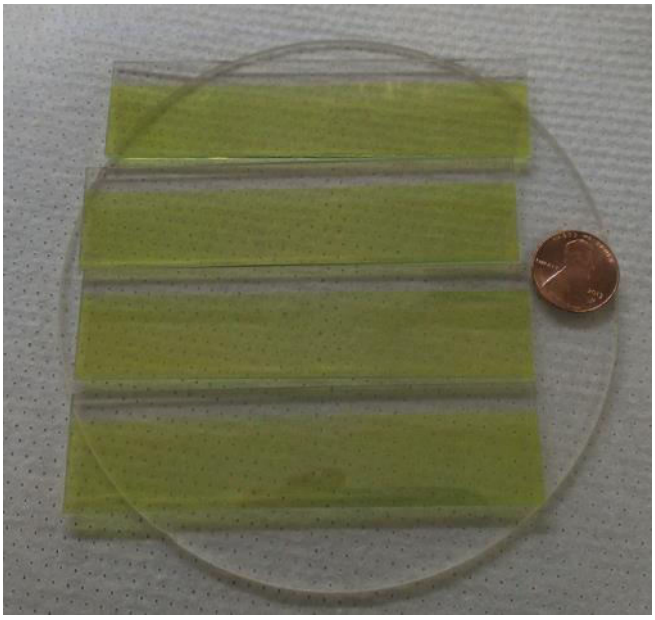

Figure S1: Multiple FTO slides being prepared with n-$BiVO_4$ simultaneously.

Cobalt oxide was deposited on n-$BiVO_4$-coated slides following a published procedure[16]. Cobaltocene (Strem, >98%) was loaded into a canister in a glove box, and the canister was sealed using a gasket connection to a steel bellows valve. The canister was removed from the glove box and loaded onto the ALD instrument (Cambridge Nanotechnology) using another gasket fitting, and was heated by a heating sleeve. Ozone was created by a Del Ozone LG-7 Corona Discharge ozone generator. The cobaltocene was heated to 80 $^{\circ}$C and the substrate was maintained at 150 $^{\circ}$C. The cobaltocene precursor was pulsed for 5 s, with the following purge with N_2(g) at 20 cm^3 min^{-1} for 15 s before an ozone pulse for 2 s and another purge for 15 s, to complete a full ALD cycle.

The finished CoO_x/n-$BiVO_4$/FTO slides were made into electrodes ~1 cm wide by 1 cm in length. Electrical contact between the electrode and a wire was made using Ag paint, and the entire contact and any exposed FTO glass was covered with non-conductive epoxy. The epoxy was used to mask the exposed area of electrode to 1 cm^2. The wire was encased in a glass tube and the end of the tube epoxied to the contacting assembly to allow for O_2-production experiments.

Characterization of Electrodes

Spectral response characterization measurements were performed using a 300 W Xe lamp and monochromator (Newport Oriel Instruments) and lock-in amplifiers (Stanford

Research Instruments). XPS measurements were performed with an M-probe spectrometer (VG-Surface Science Instruments, Pleasanton, CA) at a nominal base pressure of ca. 1×10^{-8} Torr. The excitation for XPS was provided by monochromatic Al Kα X-rays (1486.6 eV) incident at 35° with respect to the surface plane and with an elliptical focused-beam size of 250 × 1000 μm. The emitted photoelectrons were collected into a hemispherical energy analyzer at a takeoff angle identical to the angle of incidence, with a retarding (pass) energy of 154.97 eV. XPS data were fitted using Hawk 7 software (V7.03.04; Service Physics, Bend, OR) and were referenced to the adventitious carbon peak at 284.6 eV. Photoelectrochemical and impedance experiments were performed using a Bio-Logic SP-200 potentiostat.

J-E measurements were performed using a 3- or 4-neck 50-mL round-bottom flask that had been modified with a planar quartz window. The wattage of the Xe lamp (Newport) used for illumination could be varied to produce the desired incident illumination power. The light intensity was adjusted to produce the same short-circuit current density as produced by 100 mW cm^{-2} of AM1.5G sunlight on a secondary standard Si photodiode. A three-electrode configuration was used with a SCE or a Ag/AgCl reference electrode (BAS Inc.) and a Pt gauze counter electrode located in a fritted compartment that contained the same pH 13 electrolyte as contained in the main cell compartment.

For $O_2(g)$ evolution experiments, a Neofox fluorescence probe was used in an airtight cell, along with a Ag/AgCl reference electrode. The Pt gauze counter electrode was positioned in a separate, fritted compartment. The cell volume was 51 mL, and the cell

was purged with a stream of Ar(g) for ~1 h prior to data collection. The experiment was run for 30 min after a 10-min waiting period at open circuit.

UV-Vis spectroscopy was performed using a Shimadzu Solidspec-3700 spectrometer with an integrating sphere for diffuse/specular reflectance measurements. Atomic force microscopy (AFM) measurements were performed using a Bruker Dimension Icon.

Further Results

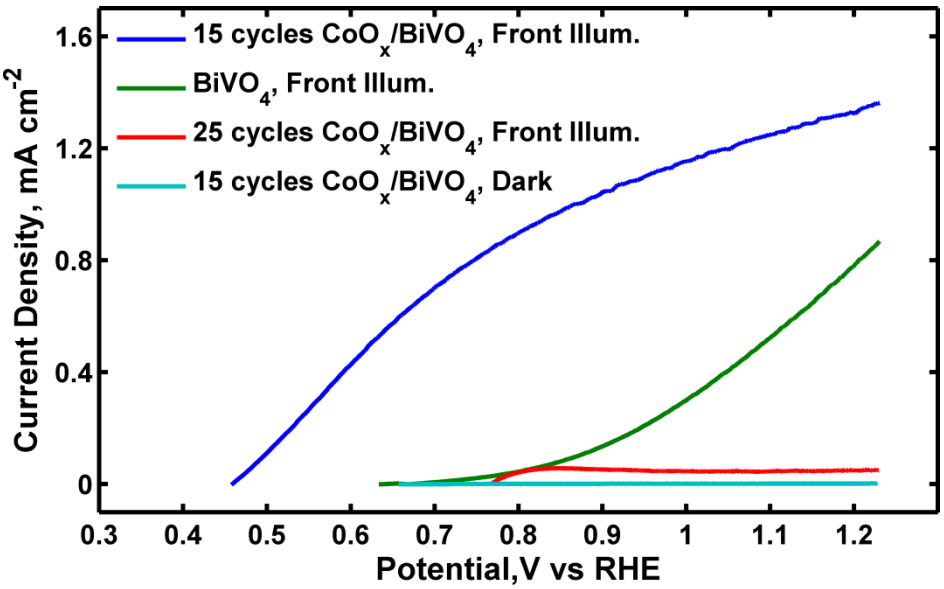

Figure S2: Linear Sweep Voltammograms of plain $BiVO_4$, $BiVO_4$ with 15 ALD cycles of cobalt oxide, and $BiVO_4$ with 25 ALD cycles of cobalt oxide.

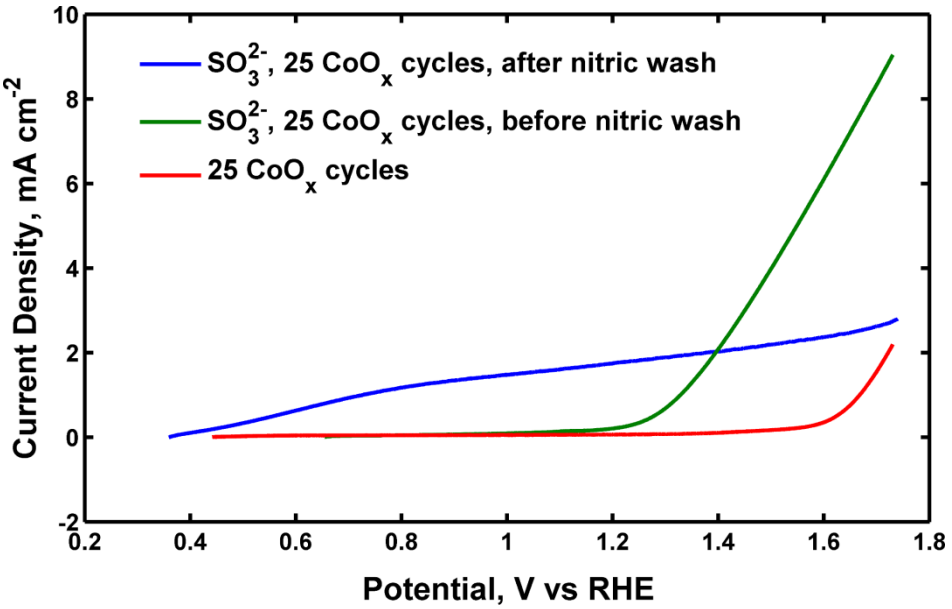

Figure S3: Linear Sweep Voltammograms under 1 sun illumination at pH 13 of 25 ALD cycles of CoO_x on $BiVO_4$, 25 ALD cycles of CoO_x on $BiVO_4$ with sodium sulfite present as a sacrificial hole acceptor, and 25 ALD cycles of CoO_x on $BiVO_4$ with sulfite present after the electrode has been briefly washed with 1.0 M nitric acid. The 1.0 M nitric acid wash produced an electrode that displayed effectively identical photoelectrochemical behavior to an electrode that had no CoO_x present, or one with fewer cycles of CoO_x.

Spectral Response

Figure S4 shows a the spectral response data for the CoO_x/n-$BiVO_4$ and for the unmodified n-$BiVO_4$ electrodes, as a function of the electrode potential vs RHE. As would be expected from the *J-E* data, more positive potentials produced larger anodic photocurrents, corresponding to a higher quantum efficiency as the electrode potential increased.

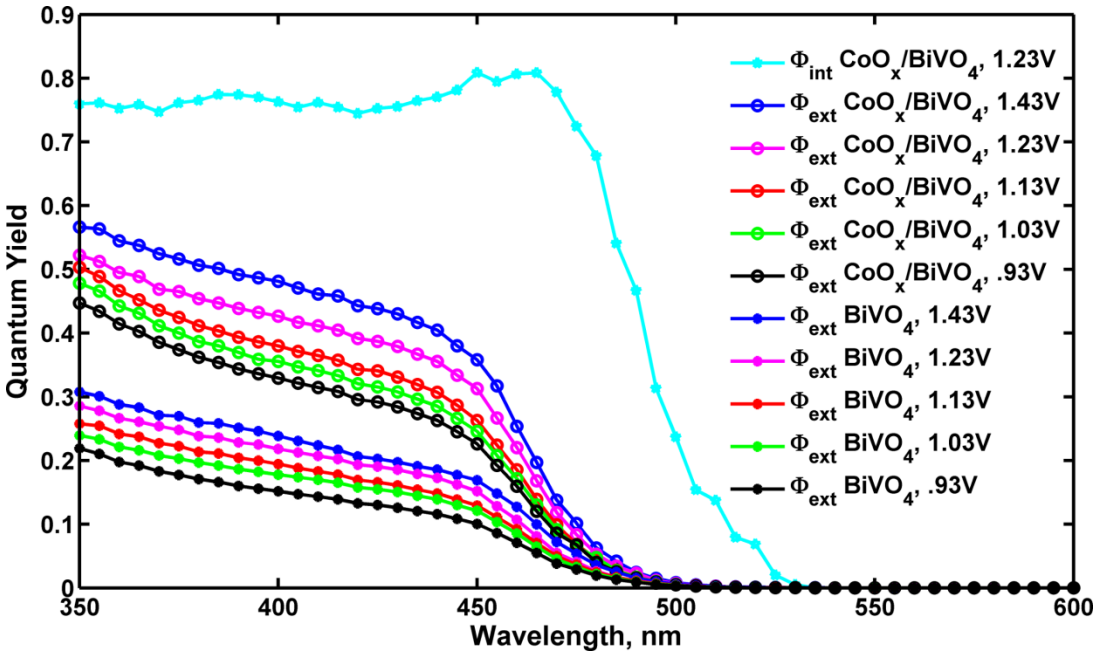

Figure S4: Quantum Yield measurements at multiple potentials vs. RHE

Calculations for Spectral Response

A calibrated silicon photodiode with known spectral responsivity from Thor Labs was used to calibrate the apparatus. The electrode of interest (calibrated Si or $(CoO_x)/BiVO_4$ electrode) was attached to a potentiostat, which relayed chopped current data to a lock-in-amplifier, from which data was collected as current and normalized by an internal photodiode. The collected photoresponse was divided by the maximum photoresponse expected at each wavelength as determined from the calibrated diode in order to determine the Incident Photon to Current Efficiency (External Quantum Yield). Absorbed Photon to Current Efficiency (Internal Quantum Yield) was found by simply dividing this number by the absorbtance as described in the text.

Integrating the results for External Quantum Yield from the data at 1.23 V vs. RHE against the tabulated AM 1.5G spectral intensity from gave a predicted current density of 2.03mA cm^{-2}, which indicates that the performance of this system may be slightly undereestimated by analysis of the *J-E* data described herein. The ASTM G-173, Global tilt data were used as the source spectrum.

XPS Spectra

Figure S5 shows the XPS spectra for Bi, V, O and Co for an electrode (a) after deposition of the cobalt oxide (and exposure to standard atmosphere), (b) after 10 cyclic voltammetric cycles and (c) after 30 min at 0.97 V vs. RHE under photoanodic operation at pH 13. The cobalt oxide signals indicated the presence of Co_3O_4 in all scans, although the initial signals also demonstrated the formation of $Co(OH)_2$ or CoO, as indicated by presence of a strong satellite peak at 786 eV. Only the Co $2p^{3/2}$ peak is shown, because the Co $2p^{1/2}$ peak was very close in energy to the Bi $4p^{1/2}$ peak. On peaks where multiple constituent peaks are summed, the individual peaks are displayed in blue and the summed model is displayed in purple. For peak models made of only one constituent peak, the single constituent is shown in purple.

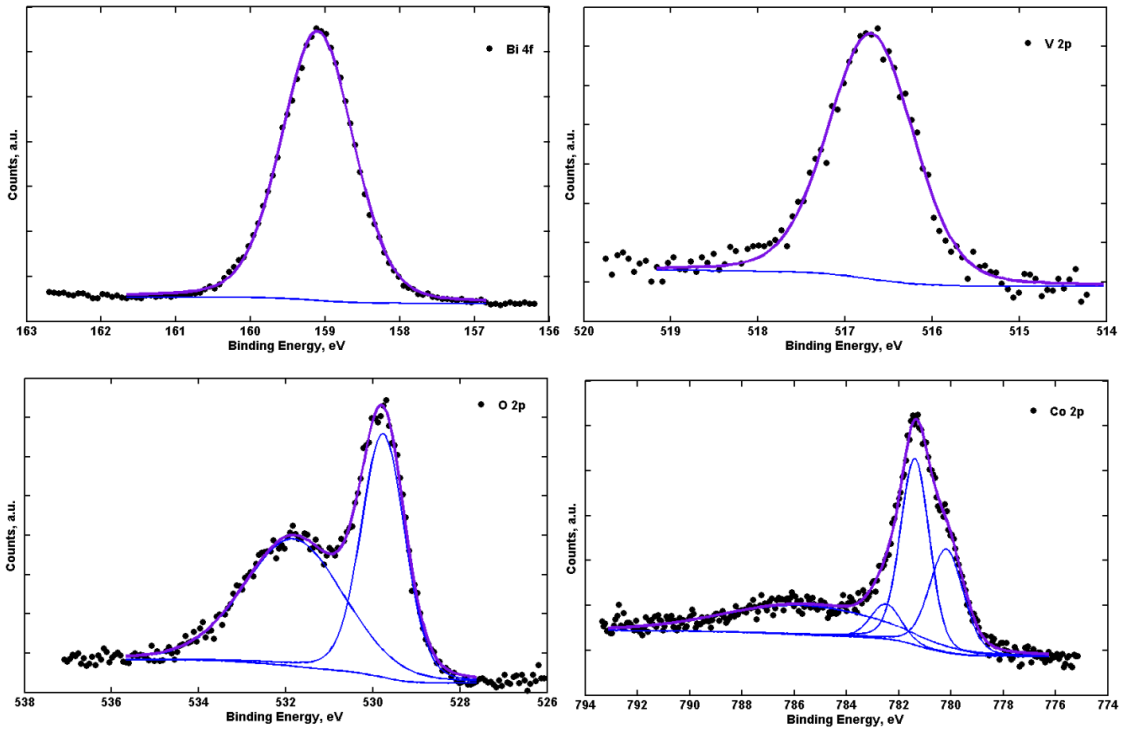

Figure S5a: XPS spectra taken after cobalt oxide deposition.

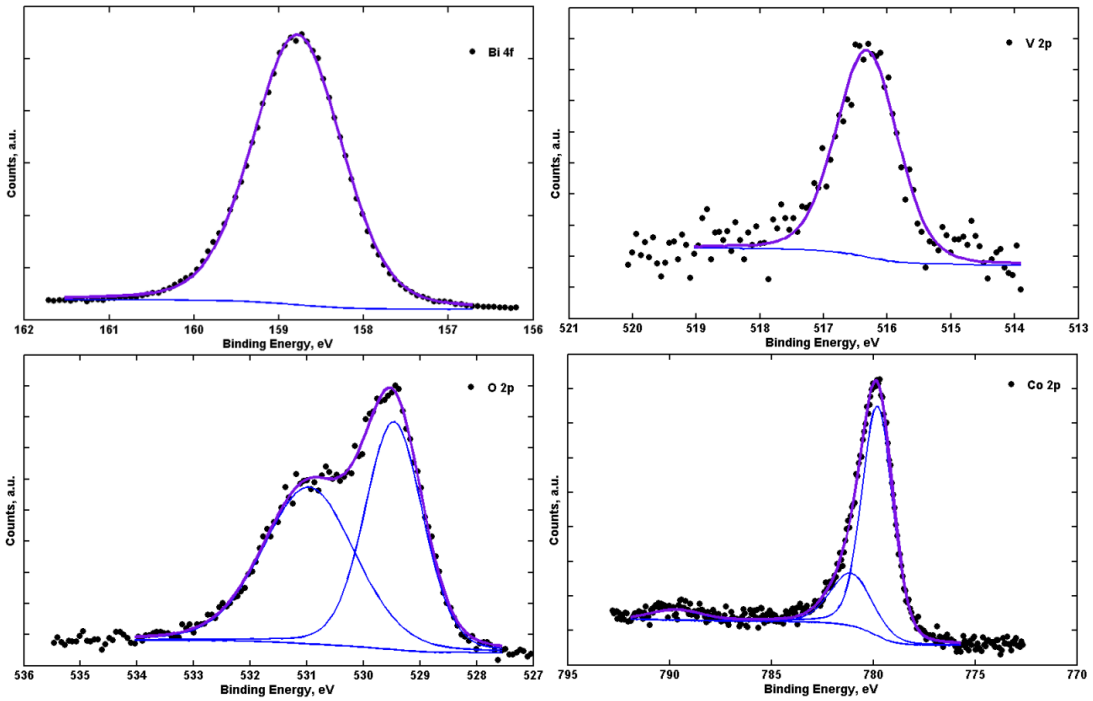

Figure S5b: XPS data after 10 cyclic voltammetric sweeps.

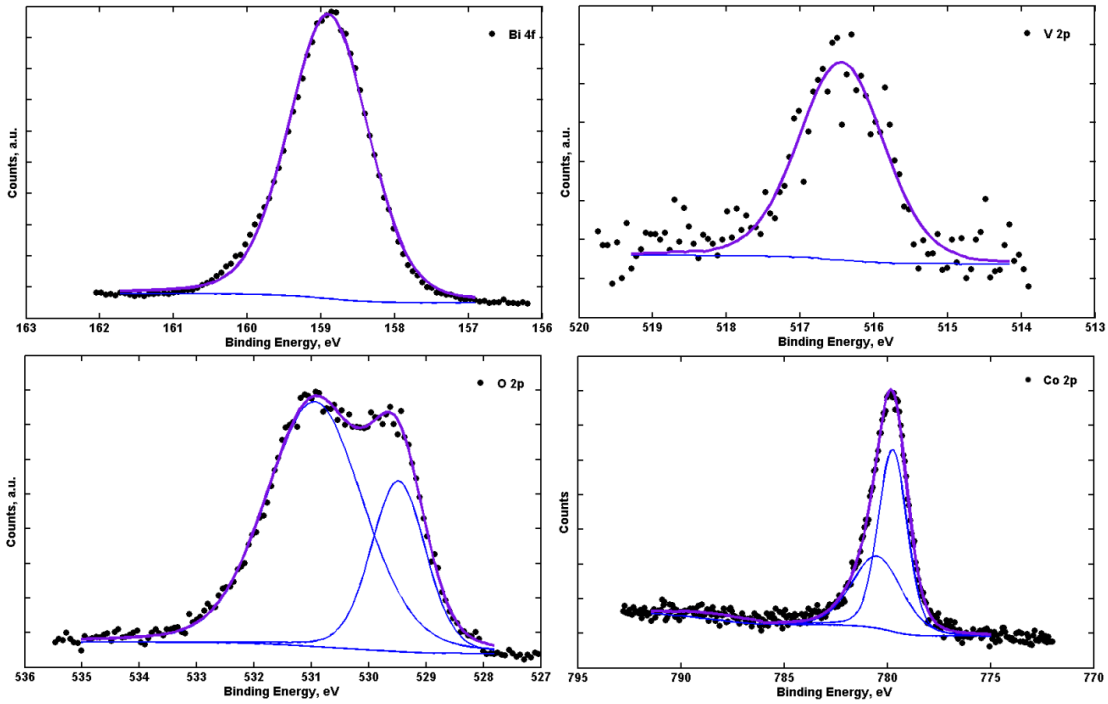

Figure S5c: XPS data after 30 min of photoanodic operation under illumination at 0.97 V vs. RHE in pH 13 KOH(aq).

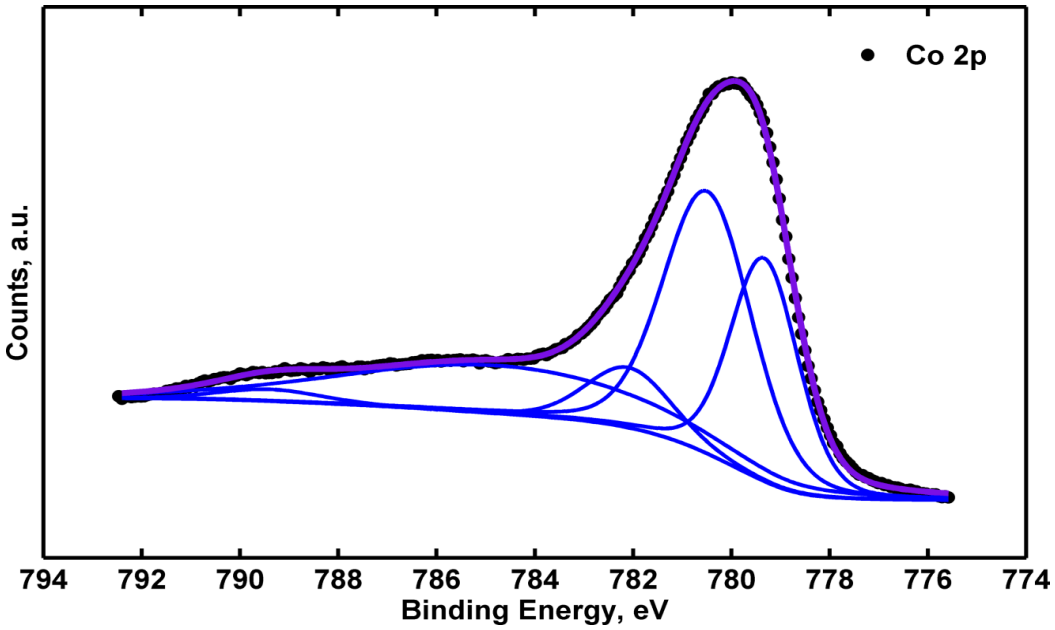

Figure S6a: XPS data for cobalt for 200 cycles of CoO_x deposited on FTO, directly after deposition.

Figure S6 contains data for 200 ALD cycles of CoO_x on FTO under a similar set of conditions: (a) after deposition, (b) after 10 cyclic voltammogram (CV) sweeps to 1.5mA cm^{-2}, and (c) after 30 minutes of galvanostatic current flow at 1.5 mA cm^{-2}.

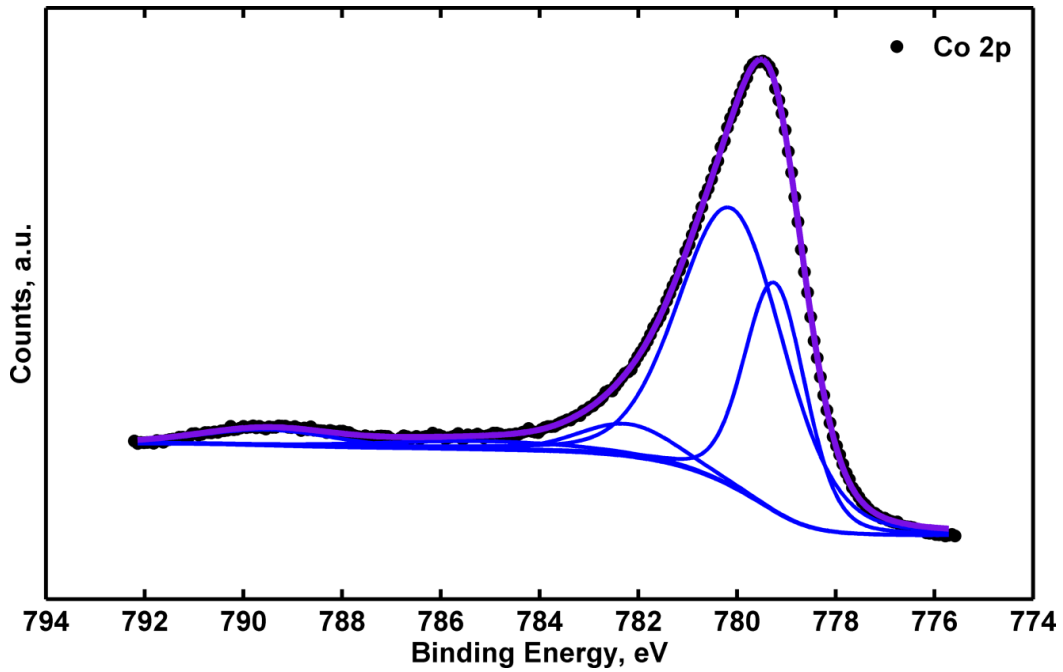

Figure S6b: XPS data for cobalt for 200 cycles of CoO_x after 10 CV sweeps.

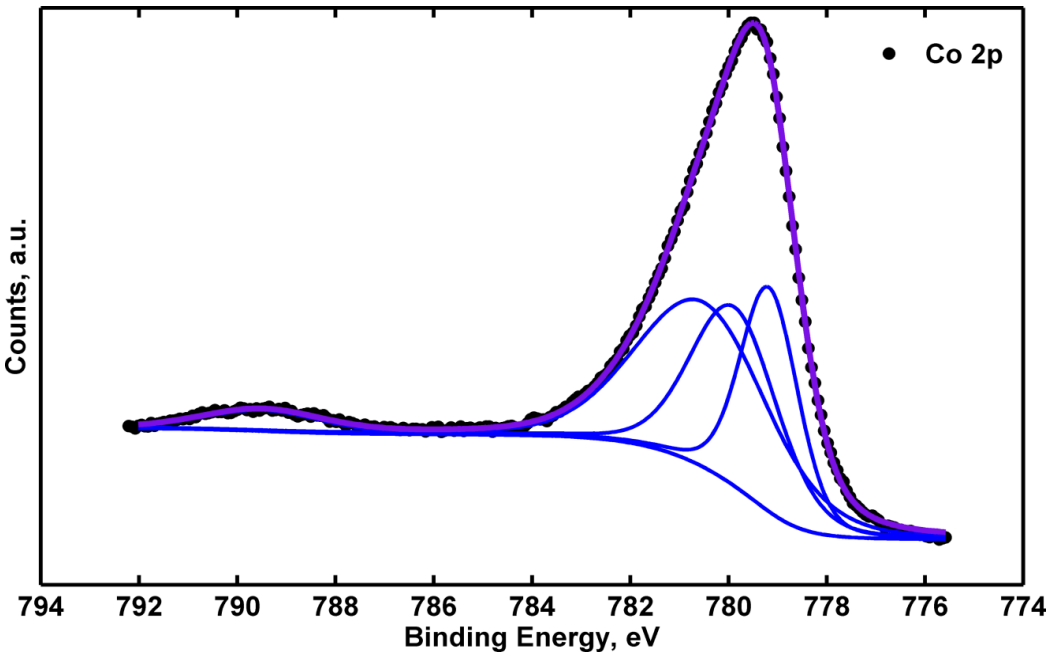

Figure S6c: XPS data for cobalt for 200 cycles of CoO_x after 30 minutes of OER catalysis.

While the small amount of CoOx on the active $CoO_x/BiVO_4$ samples does not allow for a definitive assignment of the oxidation state of the cobalt, the thicker films formed from 200 ALD cycles allow for a concise determination of the form of cobalt oxide present. The large shoulder near 786 eV in the as-deposited sample clearly present in both the $CoO_x/BiVO_4$ samples as well as the thick CoO_x samples indicates that the cobalt oxide as-deposited contains a significant fraction of Co(II), likely as $Co(OH)_2$ or CoO, in addition to Co_3O_4 or CoOOH which is indicated by the satellite near 790 eV.[20] However, even a brief amount of current flow leads to a quick change in the spectra for the cobalt, in which the satellite near 786 eV disappears almost entirely (Fig. S7b) and then entirely (Fig. S7c), leaving only the main peak at 780 eV and the satellite at 790 eV with no satellite at 786 eV. This strongly suggests the active form for water oxidation in pH 13 is CoOOH.[20]

Thickness Determination

Overlayer thicknesses were modelled using the equation[18]

$$\left(\frac{I_{Co}}{I_{Bi}}\right)\left(\frac{SF_{Bi}}{SF_{Co}}\right)\left(\frac{\rho_{Bi}}{\rho_{Co}}\right) = \exp\left(\frac{d_{ov}}{\lambda_{Bi}\sin\theta}\right) - \exp\left[-\left(\frac{d_{ov}}{\lambda_{Co}\sin\theta}\right) + \left(\frac{d_{ov}}{\lambda_{Bi}\sin\theta}\right)\right]$$

where I_{Co} and I_{Bi} are the respective normalized intensities, given by the peak area divided by number of scans, of the Co $2p^{3/2}$ and Bi $4f^{7/2}$ peaks in the XPS spectra. SF_{Bi} and SF_{Co} are the sensitivity factors for Co $2p^{3/2}$ and Bi $4f^{7/2}$ peaks, respectively; ρ_{Bi} and ρ_{Co} the corresponding atomic densities. $\lambda_{Bi\ and}$ λ_{Co} are the attenuation depths for photoelectrons at either 160 eV (for λ_{Bi}) or 780 eV (for λ_{Co}), and were given by an online database based on published work.[21] d_{ov} is the thickness of the cobalt oxide overlayer, and θ is 35°. The database provided values of 25.8 nm for λ_{Bi} and 69.2 nm for λ_{Co}. With the above data, d_{ov} was calculated as 0.9 nm for 20 ALD cycles, which is a reasonable result, since the ALD procedure followed here has been previously determined to produce a growth rate of 0.05 nm per cycle. [16]

Atomic Force Microscopy

Atomic Force Microscopy (AFM) was used to investigate the surface before and after deposition of the catalyst layer.

Figure S7 (a-f) displays representative 2-D and 3-D images of (a,b) the unmodified n-$BiVO_4$ electrode, (c,d) n-$BiVO_4$ with 12 ALD cycles of CoO_x, and (e,f) n-$BiVO_4$ with 24 ALD cycles of CoO_x.

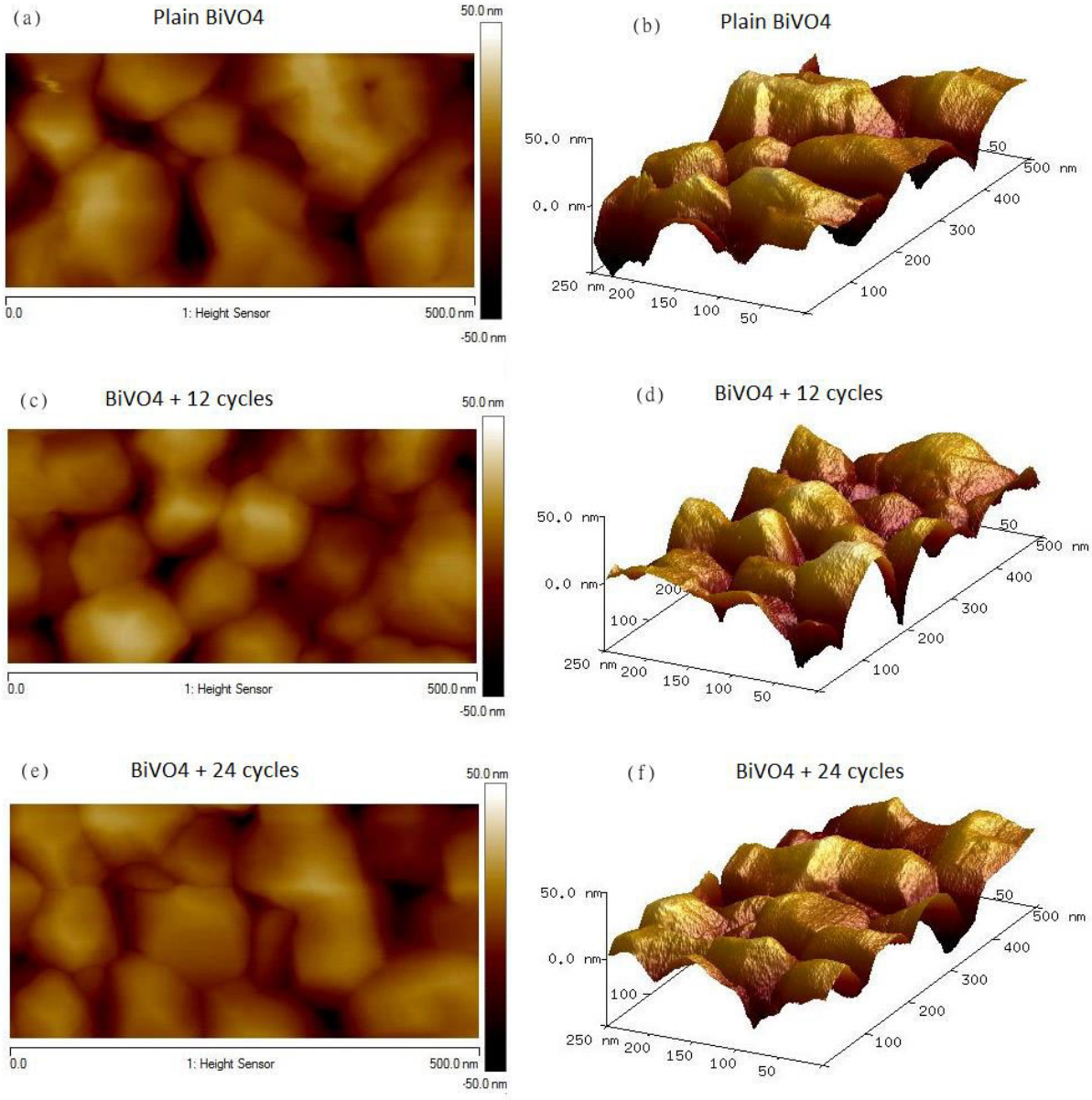

Further *J-E* Characterization

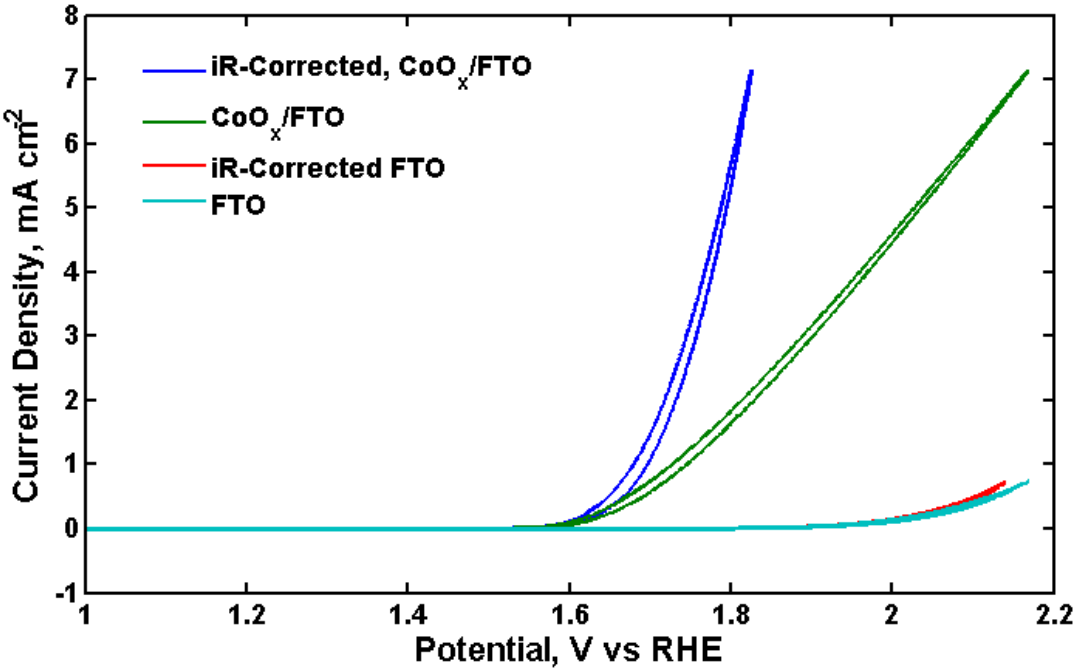

Figure S8: CoO_x/FTO and plain FTO activity for OER, un-corrected and iR-corrected, at pH 13.

Calculations for Oxygen Measurement and Faradaic Efficiency

The data were collected and modeled using a Matlab script. The data from the flourescence probe were converted into micrograms of O_2 by first correcting for any O_2 leaks during the first 10 min of the experiment, followed by multiplying the reported percentage of oxygen by the number of micrograms of O_2 dissolved in water under these conditions (7700 µg/L) as well as by the cell volume (51.5 mL), and dividing by the density of O_2 in standard air, which was in the form reported by the probe(20.9). This process produced the mass of O2 in micrograms at each time point. To calculate the charge vs time data from the potentiostat, the amount of charge passed (in mAh) was multiplied by 3.6 to convert the data into coulombs. This value was then multiplied by 83 to convert the value into micrograms of O_2, since this constant equals the conversion factor of 1 coulomb of electrons into 1 microgram of O_2.

REFERENCES

1. Lichterman, M. F.; Shaner, M. R.; Handler, S. G.; Brunschwig, B. S.; Gray, H. B.; Lewis, N. S.; Spurgeon, J. M., Enhanced Stability and Activity for Water Oxidation in Alkaline Media with Bismuth Vanadate Photoelectrodes Modified with a Cobalt Oxide Catalytic Layer Produced by Atomic Layer Deposition. *J. Phys. Chem. Lett.* **2013,** *4* (23), 4188-4191.
2. Walter, M. G.; Warren, E. L.; McKone, J. R.; Boettcher, S. W.; Mi, Q.; Santori, E. A.; Lewis, N. S., Solar Water Splitting Cells. *Chem. Rev.* **2010,** *110* (11), 6446-6473.
3. Luo, W.; Yang, Z.; Li, Z.; Zhang, J.; Liu, J.; Zhao, Z.; Wang, Z.; Yan, S.; Yu, T.; Zou, Z., Solar hydrogen generation from seawater with a modified BiVO4 photoanode. *Energy Environ. Sci.* **2011,** *4* (10), 4046-4051.
4. (a) Ding, C.; Shi, J.; Wang, D.; Wang, Z.; Wang, N.; Liu, G.; Xiong, F.; Li, C., Visible light driven overall water splitting using cocatalyst/BiVO4 photoanode with minimized bias. *Phys. Chem. Chem. Phys.* **2013,** *15* (13), 4589-4595; (b) Gawande, S.; Thakare, S., Graphene wrapped BiVO4 photocatalyst and its enhanced performance under visible light irradiation. *Int Nano Lett* **2012,** *2* (1), 1-7.
5. Wan, Y.; Wang, S.; Luo, W.; Zhao, L., Impact of Preparative pH on the Morphology and Photocatalytic Activity of BiVO4. *International Journal of Photoenergy* **2012,** *2012*, 7.
6. Seabold, J. A.; Choi, K.-S., Efficient and Stable Photo-Oxidation of Water by a Bismuth Vanadate Photoanode Coupled with an Iron Oxyhydroxide Oxygen Evolution Catalyst. *J. Am. Chem. Soc.* **2012,** *134* (4), 2186-2192.
7. Abdi, F. F.; Han, L.; Smets, A. H. M.; Zeman, M.; Dam, B.; van de Krol, R., Efficient solar water splitting by enhanced charge separation in a bismuth vanadate-silicon tandem photoelectrode. *Nat. Commun.* **2013,** *4*.
8. (a) Abdi, F. F.; Firet, N.; van de Krol, R., Efficient BiVO4 Thin Film Photoanodes Modified with Cobalt Phosphate Catalyst and W-doping. *ChemCatChem* **2013,** *5* (2), 490-496; (b) Su, J.; Guo, L.; Bao, N.; Grimes, C. A., Nanostructured WO3/BiVO4 Heterojunction Films for Efficient Photoelectrochemical Water Splitting. *Nano Lett.* **2011,** *11* (5), 1928-1933.
9. (a) Pilli, S. K.; Deutsch, T. G.; Furtak, T. E.; Brown, L. D.; Turner, J. A.; Herring, A. M., BiVO4/CuWO4 heterojunction photoanodes for efficient solar driven water oxidation. *Phys. Chem. Chem. Phys.* **2013,** *15* (9), 3273-3278; (b) Ye, H.; Park, H. S.; Bard, A. J., Screening of Electrocatalysts for Photoelectrochemical Water Oxidation on W-Doped $BiVO_4$ Photocatalysts by Scanning Electrochemical Microscopy. *J. Phys. Chem. C* **2011,** *115* (25), 12464-12470; (c) Pilli, S. K.; Furtak, T. E.; Brown, L. D.; Deutsch, T. G.; Turner, J. A.; Herring, A. M., Cobalt-Phosphate (Co-Pi) Catalyst Modified Mo-doped $BiVO_4$ Photoelectrodes for Solar Water Oxidation. *Energy Environ. Sci.* **2011,** *4* (12), 5028-5034; (d) Zhong, D. K.; Choi, S.; Gamelin, D. R., Near-Complete Suppression of Surface Recombination in Solar Photoelectrolysis by "Co-Pi" Catalyst-Modified W:$BiVO_4$. *J. Am. Chem. Soc.* **2011,** *133* (45), 18370-18377.
10. Park, Y.; McDonald, K. J.; Choi, K.-S., Progress in bismuth vanadate photoanodes for use in solar water oxidation. *Chem. Soc. Rev.* **2013,** *42* (6), 2321-2337.
11. (a) Haussener, S.; Xiang, C.; Spurgeon, J. M.; Ardo, S.; Lewis, N. S.; Weber, A. Z., Modeling, simulation, and design criteria for photoelectrochemical water-splitting

systems. *Energy Environ. Sci.* **2012,** *5* (12), 9922-9935; (b) Merle, G.; Wessling, M.; Nijmeijer, K., Anion exchange membranes for alkaline fuel cells: A review. *J. Membrane Sci.* **2011,** *377* (1–2), 1-35.
12. (a) Hernandez-Pagan, E. A.; Vargas-Barbosa, N. M.; Wang, T.; Zhao, Y.; Smotkin, E. S.; Mallouk, T. E., Resistance and polarization losses in aqueous buffer-membrane electrolytes for water-splitting photoelectrochemical cells. *Energy Environ. Sci.* **2012,** *5* (6), 7582-7589; (b) McKone, J. R.; Lewis, N. S.; Gray, H. B., Will Solar-Driven Water-Splitting Devices See the Light of Day? *Chemistry of Materials* **2013**.
13. Corrigan, D. A., The Catalysis of the Oxygen Evolution Reaction by Iron Impurities in Thin Film Nickel Oxide Electrodes. *J. Electrochem. Soc.* **1987,** *134* (2), 377-384.
14. Tüysüz, H.; Hwang, Y.; Khan, S.; Asiri, A.; Yang, P., Mesoporous Co3O4 as an electrocatalyst for water oxidation. *Nano Res.* **2013,** *6* (1), 47-54.
15. Jeon, T. H.; Choi, W.; Park, H., Cobalt-phosphate complexes catalyze the photoelectrochemical water oxidation of BiVO4 electrodes. *Phys. Chem. Chem. Phys.* **2011,** *13* (48), 21392-21401.
16. Donders, M. E.; Knoops, H.; Van de Sanden, M. C.; Kessels, W. M.; Notten, P., Remote Plasma Atomic Layer Deposition of Co3O4 Thin Films. *ECS Transactions* **2009,** *25* (4), 39-47.
17. Trotochaud, L.; Mills, T. J.; Boettcher, S. W., An Optocatalytic Model for Semiconductor–Catalyst Water-Splitting Photoelectrodes Based on In Situ Optical Measurements on Operational Catalysts. *J. Phys. Chem. Lett.* **2013,** *4* (6), 931-935.
18. Haber, J. A.; Lewis, N. S., Infrared and X-ray Photoelectron Spectroscopic Studies of the Reactions of Hydrogen-Terminated Crystalline Si(111) and Si(100) Surfaces with Br2, I2, and Ferrocenium in Alcohol Solvents. *J. Phys. Chem. B* **2002,** *106* (14), 3639-3656.
19. Strandwitz, N. C.; Comstock, D. J.; Grimm, R. L.; Nichols-Nielander, A. C.; Elam, J.; Lewis, N. S., Photoelectrochemical Behavior of n-type Si(100) Electrodes Coated with Thin Films of Manganese Oxide Grown by Atomic Layer Deposition. *J. Phys. Chem. C* **2013,** *117* (10), 4931-4936.
20. Biesinger, M. C.; Payne, B. P.; Grosvenor, A. P.; Lau, L. W. M.; Gerson, A. R.; Smart, R. S. C., Resolving surface chemical states in XPS analysis of first row transition metals, oxides and hydroxides: Cr, Mn, Fe, Co and Ni. *Appl. Surf. Sci.* **2011,** *257* (7), 2717-2730.
21. Henke, B. L.; Gullikson, E. M.; Davis, J. C., X-Ray Interactions: Photoabsorption, Scattering, Transmission, and Reflection at E = 50-30,000 eV, Z = 1-92. *Atomic Data and Nuclear Data Tables* **1993,** *54* (2), 181-342.

I.3. XPS and EIS analysis of the $BiVO_4$ – CoO_x interface

X-ray photoelectron spectroscopy is a valuable technique that allows not only for the analysis of chemical states within a thin layer at the surface of a material but can also reveal information about the band structure of a material, provided sufficient time and information are provided to analyze and model the data. One interesting aspect regarding the data presented above in Section I.2. is Figure S3; namely, that after deposition of more than ~1.5nm of cobalt oxide by ALD, the photoperformance of the system was destroyed resulting in an effectively ohmic connection between the FTO and the cobalt oxide catalyst on the surface. XPS[1] was used to probe varying thicknesses of cobalt oxide[2] deposited by ALD[3] in an attempt to uncover the underlying reasons for which this decrease in performance was observed. An introduction to such experiments is provided below before the results are presented. Impedance spectroscopy is then applied and discussed.

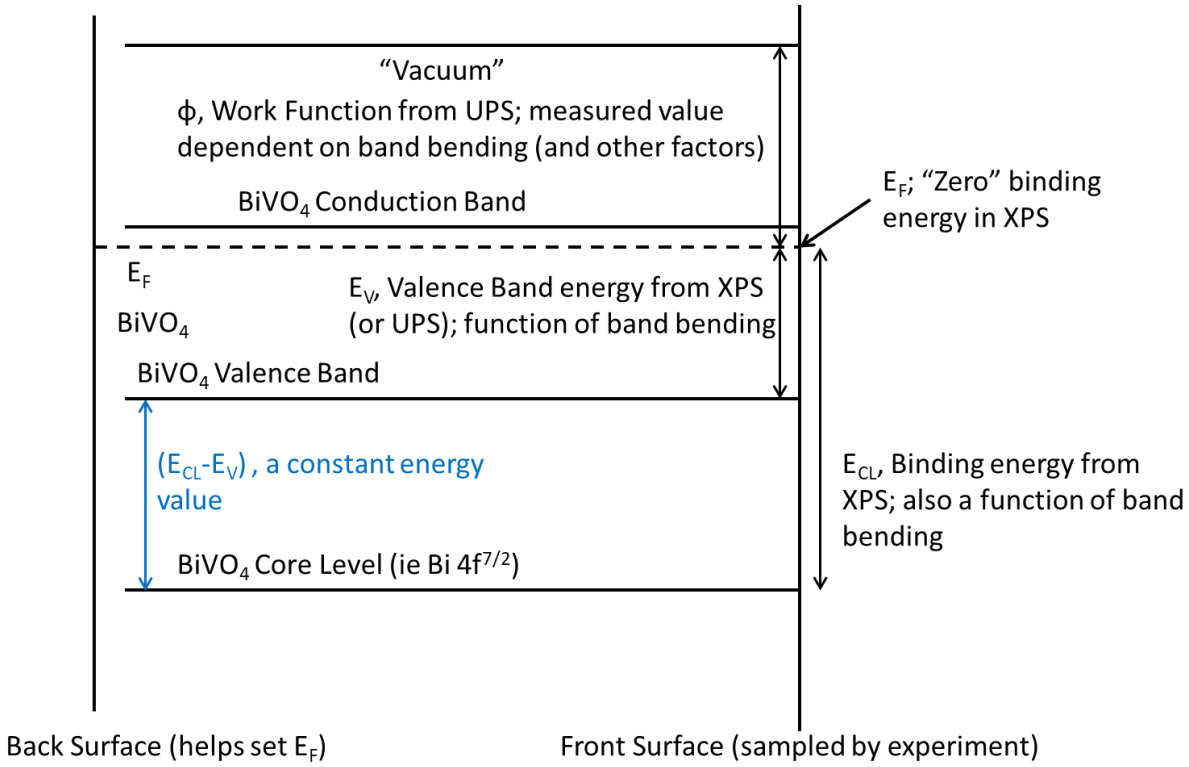

Figure 1. The XPS puck or stage is at the back on the left; the sampling surface on the right; the arrows indicate the data that can be collected between UPS and XPS. The blue arrow is constant regardless of band bending, while the others are dependent on band bending.

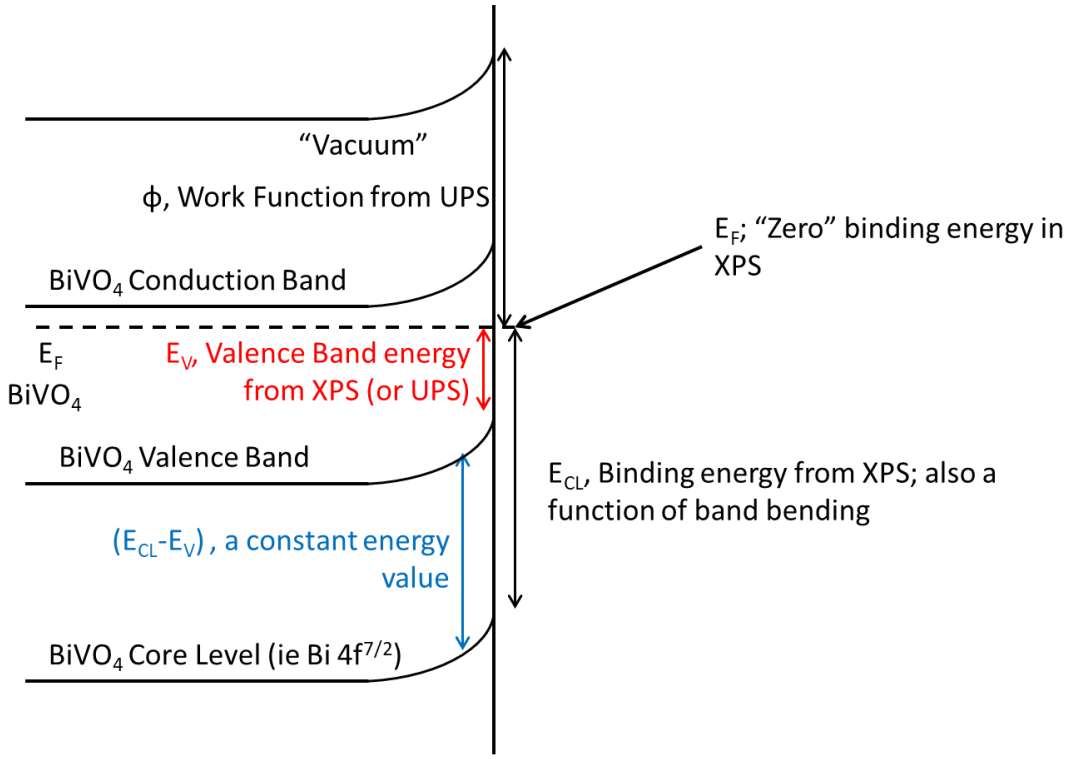

Figure 2. A possible structure to be analyzed by XPS. The relevant data which can be collected (or modeled) is shown. The positions of the core levels can be analyzed and from that data the valence band data extrapolated. In some cases the valence band offsets can be determined directly.

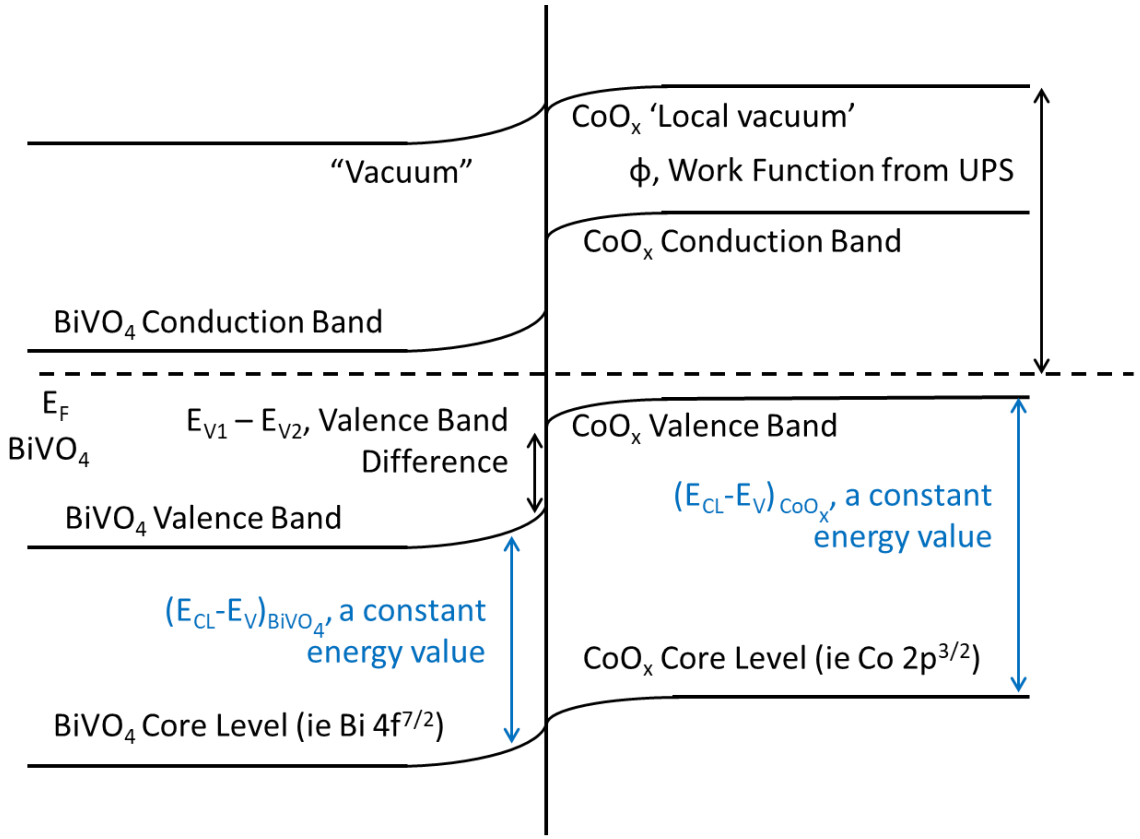

Figure 3. Another possible structure for XPS analysis.

Data was collected on $BiVO_4$ samples with varying thicknesses of cobalt oxide deposited on top by ALD. The thicknesses used are described in terms of the number of cycles. Approximately 17 cycles correspond to a cobalt oxide film nominally 1 nm thick.

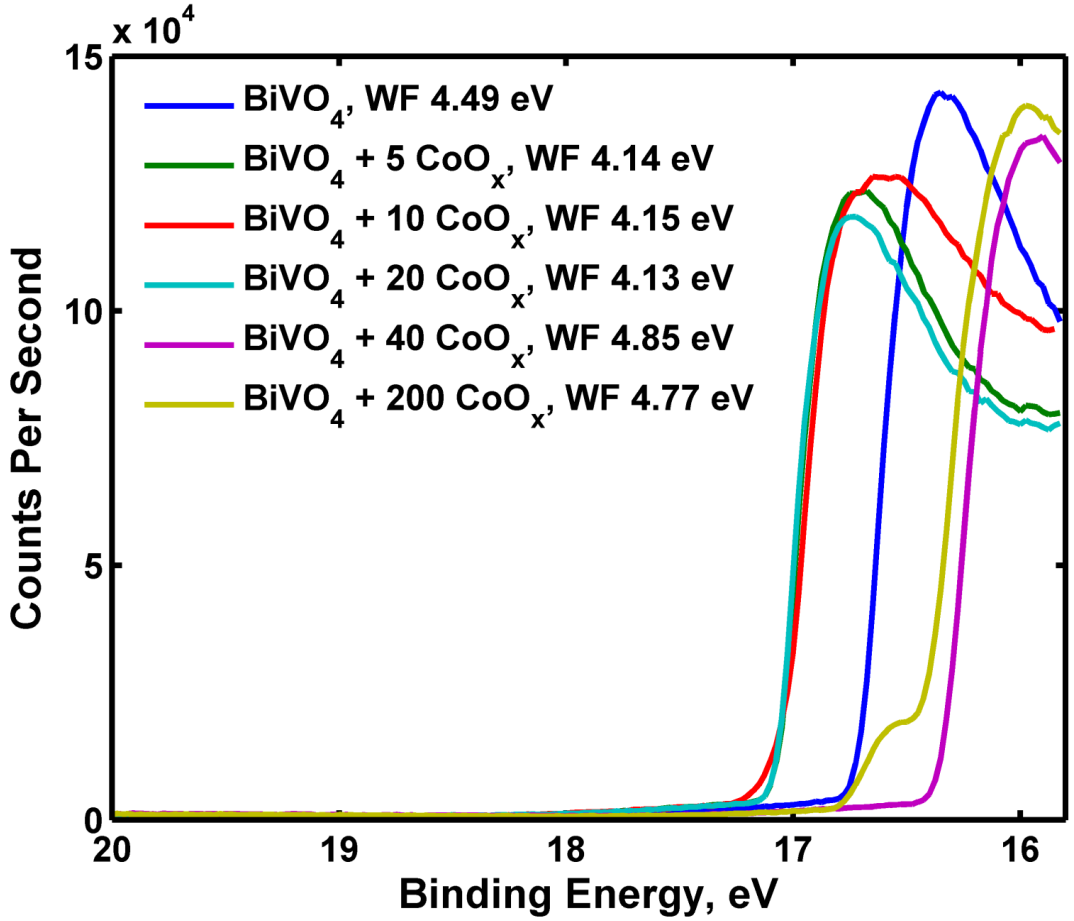

Figure 4. Work functions derived from UPS on $CoO_x/BiVO_4$ films. The work function was calculated by subtracting the extrapolated x-intercept of the secondary electron cutoff from the value 21.22 eV.

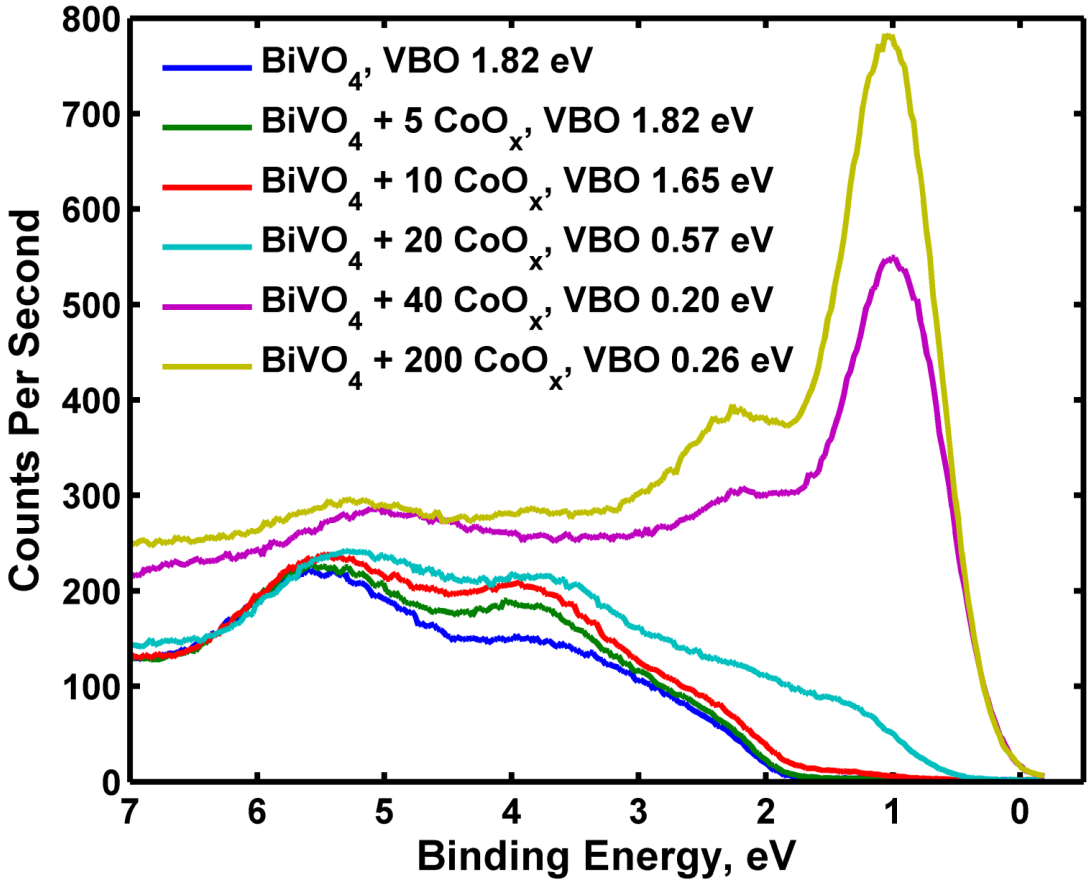

Figure 5. Valence band offset data collected from various $CoO_x/BiVO_4$ structures. The VBO was calculated by extrapolating the largest 'feature' at low binding energy toward zero. 0 binding energy was used as the Fermi energy.

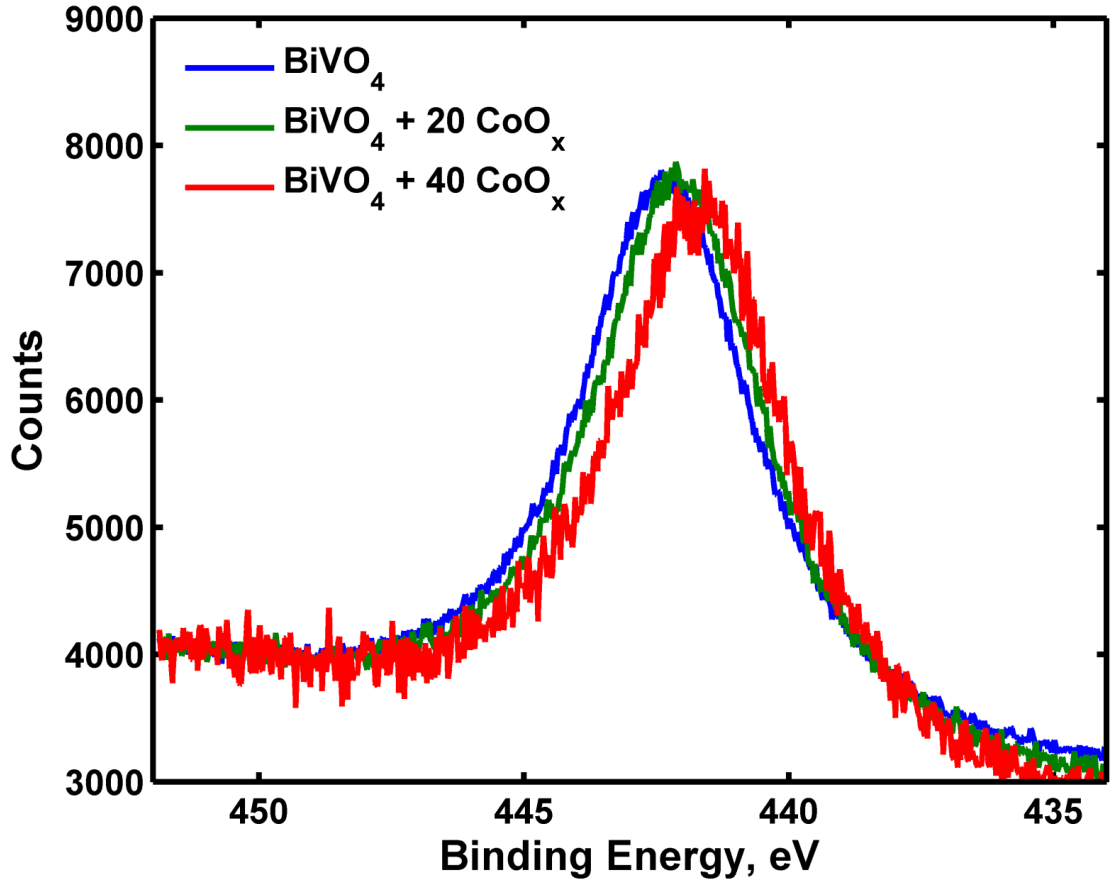

Figure 6. Bi 4d XPS peak. The decreasing binding energy suggests increasing band bending.

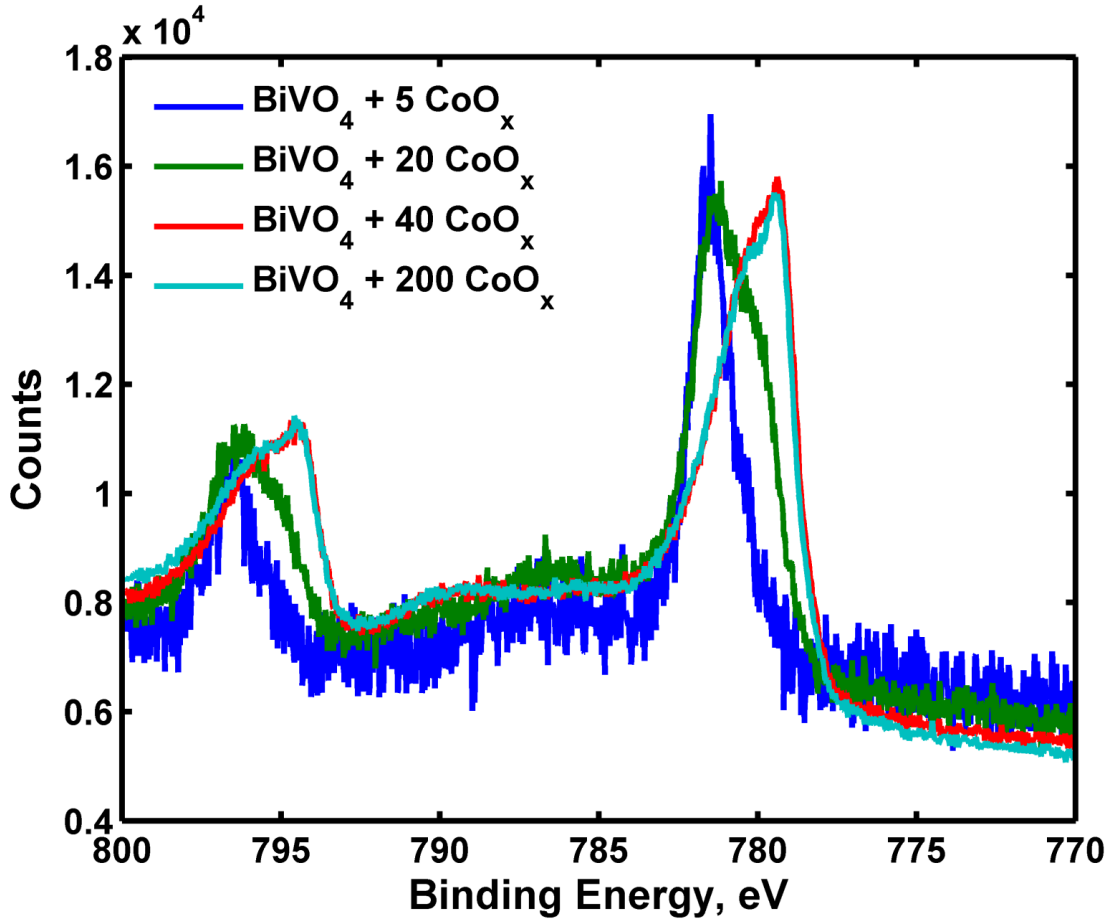

Figure 7. Cobalt 2p XPS data. XPS data from the 40 cycle sample and the 200 cycle sample are qualitatively identical.

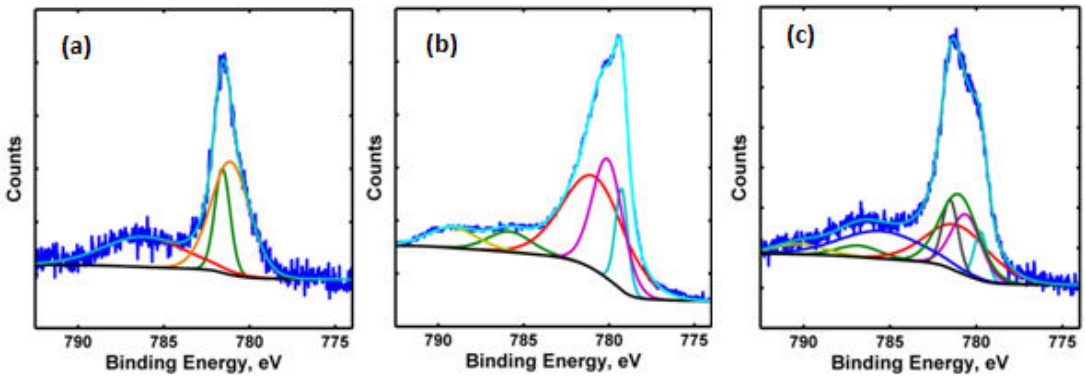

Figure 8 (a-c). XPS of Cobalt $2p^{3/2}$ core level for (a) 10 ALD CoO^x cycles (resulting in $Co(OH)_2$ or CoO), (b) 200 ALD CoOx cycles (giving Co_3O_4), and (c) 20 cycles, where both are visible, as is an electronic effect from band bending giving a displacement.

The above data was collected, modeled, and fitted to give the resulting band diagrams shown below.

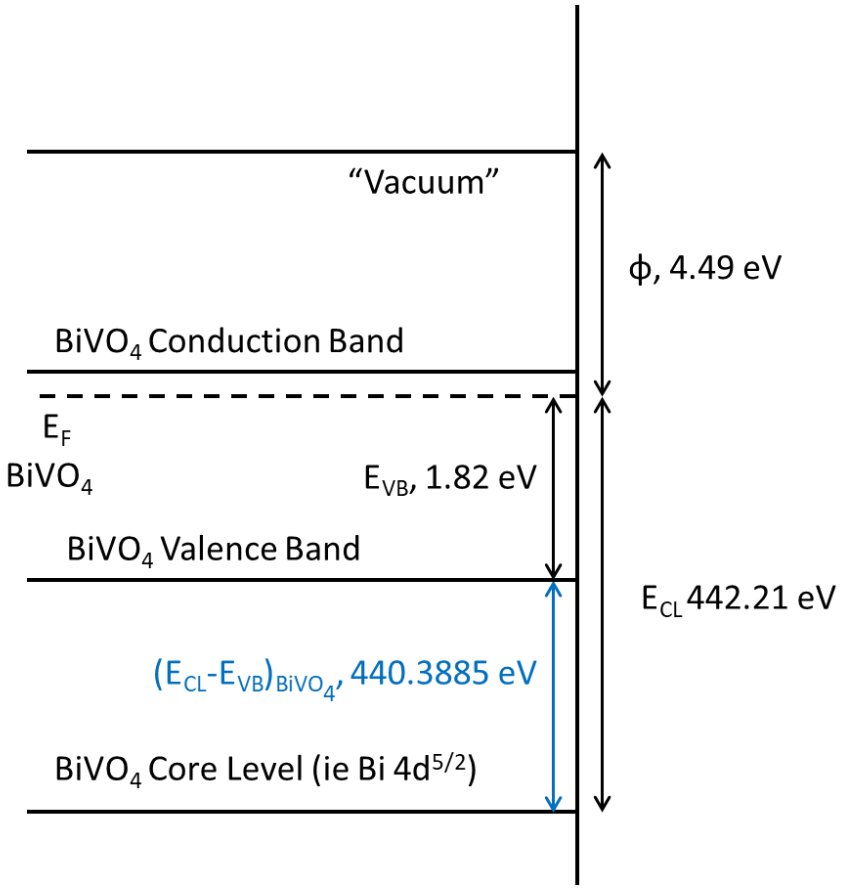

Figure 9. Band diagram of pure $BiVO_4$, assuming the initial VBO is at flat band. All future data is referenced to this point.

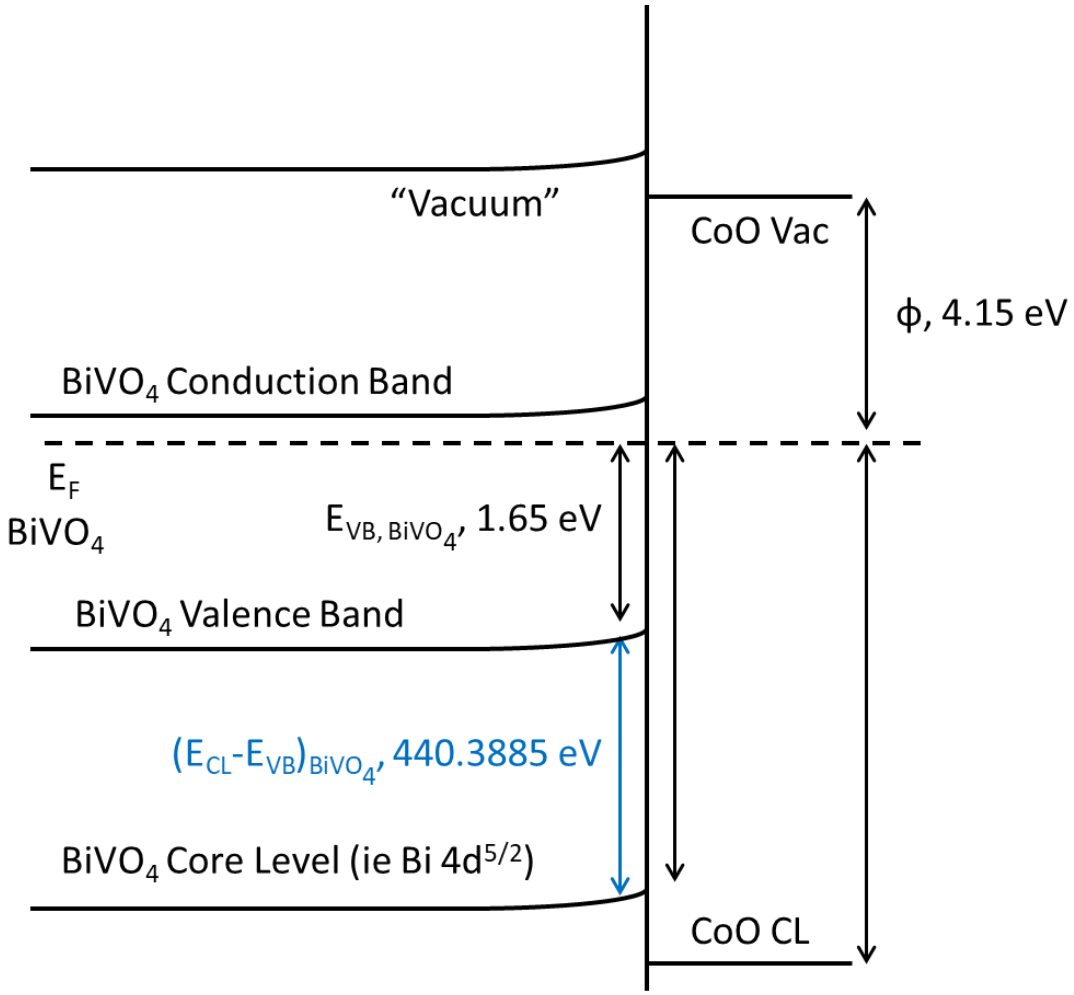

Figure 10. $BiVO_4$ with 10 CoO_x cycles. No exact value is given for the CoO core level as it is a broad peak and can be used here primarily for relative shifts. Approximately .09 eV of band bending is seen in the $BiVO_4$.

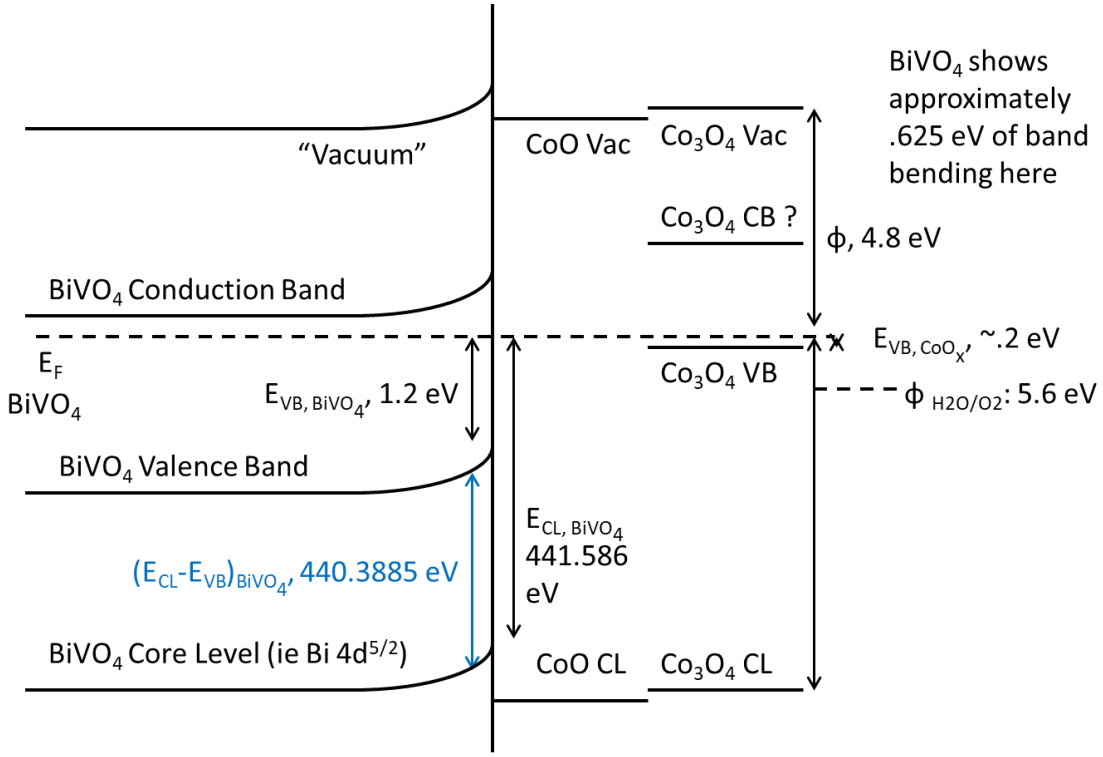

Figure 11. Data for $BiVO_4$ and 40 ALD CoO_x cycles. Despite the increased amount of band bending in the BiVO4 observed (which should lead to more photoactivity), the Co_3O_4 valence band is seen to be above the water oxidation energy. However, these energetic are only calibrated to pH 0.

These results, while interesting, are not necessarily a complete story. These electrodes were removed from the XPS instrument and ran under photolytic conditions with 10 CV sweeps, then returned to the XPS for further investigation. The pH 13 solution and applied potentials were seen to clearly affect the binding energies observed.

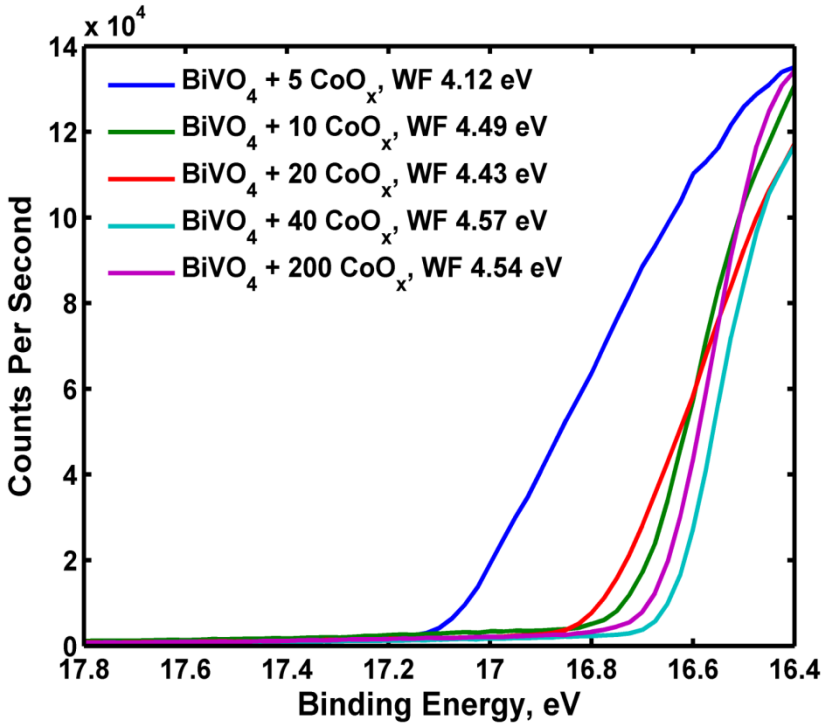

Figure 12. Work function data after photolytic conditions.

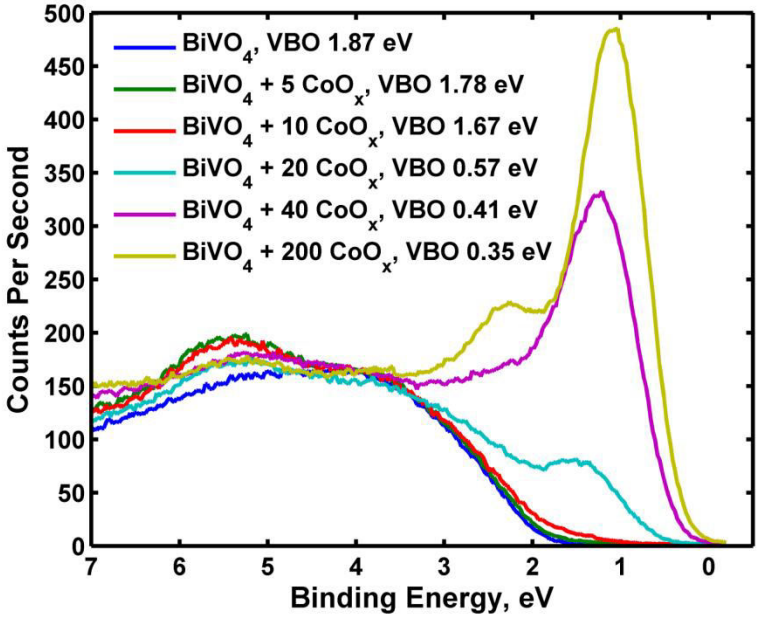

Figure 13. Valence Band Offset data after photolytic conditions.

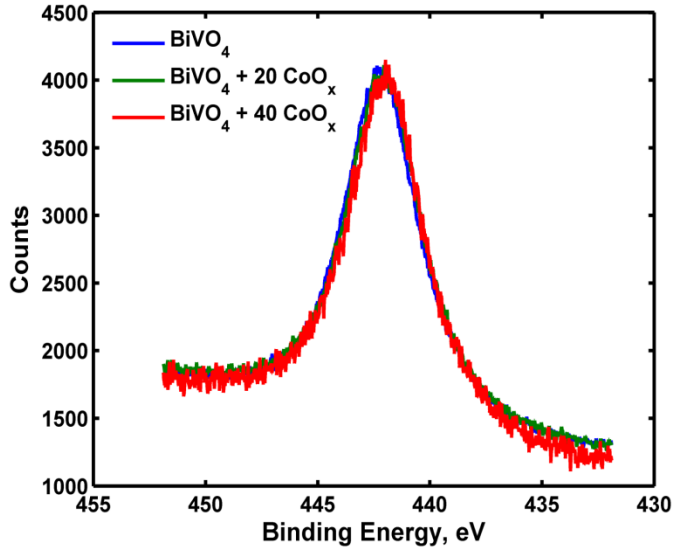

Figure 14. Bismuth $4d^{5/2}$ peak data after photolytic conditions.

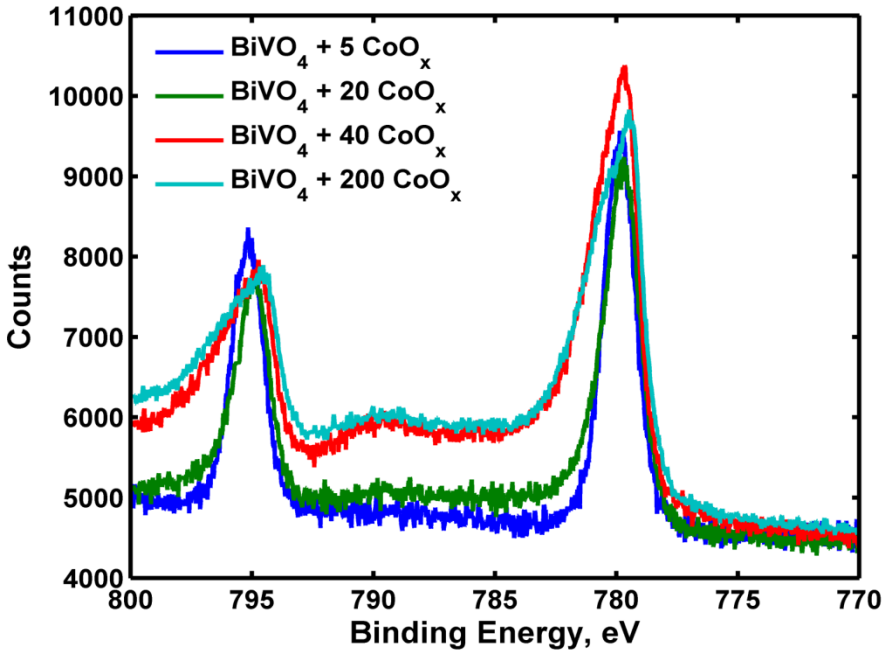

Figure 15. Co 2p peak data after photolytic conditions.

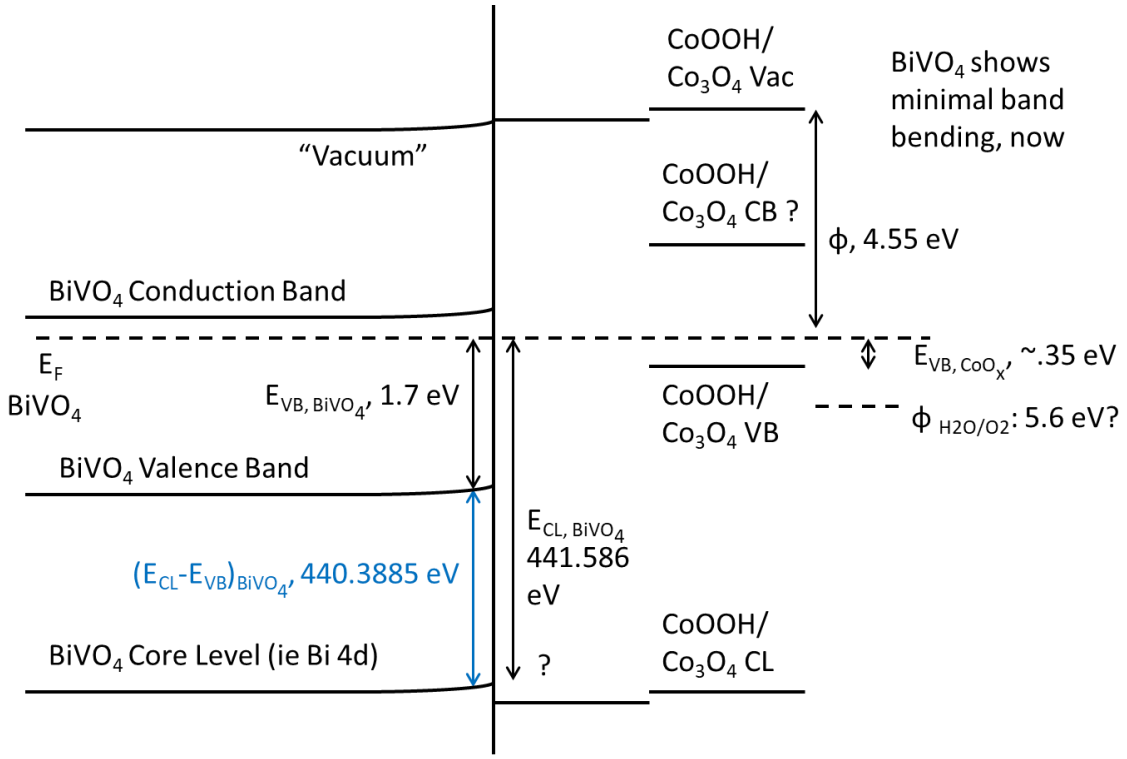

Figure 16. After PEC conditions, the band structure shows a minimal amount of band bending in the $BiVO_4$. This suggests a quick conversion of the surface as a result of exposure to solution results in a "dead" photoelectrode.

The gap between $BiVO_4$ and CoO_x valence bands may allow thermalization of charge carriers and loss of photovoltage. Also, these results suggest XPS conditions more similar to the photoelectrochemistry experiment would be helpful in order to allow band alignment to the solution instead of the vacuum. A somewhat unexplored area of work that could be considered here is the formation of a buried heterojunction between $BiVO_4$ and a different metal oxide with a higher work function.

Electrical Impedance Spectroscopy(EIS) uses an alternating voltage at various frequencies applied to an electrode at various potentials to extract data involving band

bending, the flat band potential, dopant type, and carrier concentrations.[4] As EIS may be performed on an electrode in solution, it may be run as an *in situ* experiment, whereas XPS is generally (although not always) *ex situ*. As a result, the data may be more directly relatable to the working (or not working) system at hand. The primary problem with such experiments is that unlike XPS, where binding energies are observed directly, the data from an EIS experiment must be fitted using a model circuit in order for data to be extracted from it, and the details of the design of the model circuit are crucial to the validity of the fit. As is generally the case with any modeling type experiment, a more complicated model (involving, for example, a higher number of capacitors, resistors, and various parallel or serial circuits) will generally allow a better fit to a large set of data than a simpler model; however, the more complicated model might be completely meaningless or otherwise unintelligible if it has more components than can be directly related to the system at hand.

One common model used for the analysis of a semiconductor-liquid junction is the Randles circuit, below, which consists of a resistor in series with a parallel RC circuit. In this model, the series resistance is the general resistance through the electrolyte (R_e), the parallel capacitor the capacitance within the semiconductor (C_{SC}), and the parallel resistance the charge transfer resistance (R_{CT}).

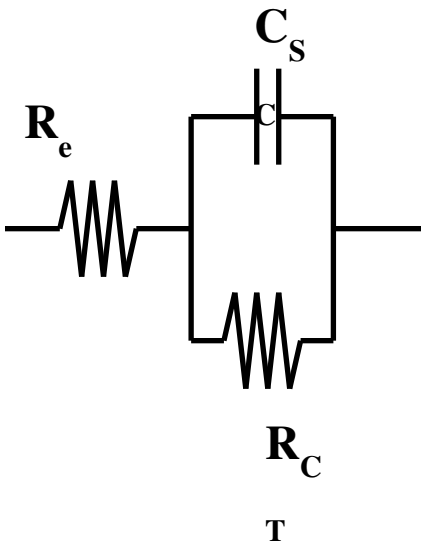

Figure 17. Randles Circuit.

Data was collected on electrodes in pH 13 electrolyte under dark conditions. Electrodes tested included bare FTO electrodes, BiVO4 on FTO electrodes, and 300 cycle CoOx on $BiVO_4$/FTO electrodes. The data was subsequently fitted with a Randles circuit and analyzed with the Mott Schottky equation, shown below:

$$\frac{1}{C^2} = \frac{2}{\varepsilon\varepsilon_0 A^2 e N_D}\left(V - V_{FB} - \frac{k_B T}{e}\right)$$

where *C* is the capacitance, ε the permittivity of vacuum, ε_0 the relative permittivity, A the area of the electrode, *e* the elementary charge, N_D the number of dopants (or carrier concentration assuming full ionization), V the potential, V_{FB} the flat band potential, k_B Boltzmann's constant, and *T* the temperature. From the x-intercept of a Mott-Schottky plot ($1/C^2$ vs V), the flat band potential may be determined; from the slope of the line, the dopant density may be found.

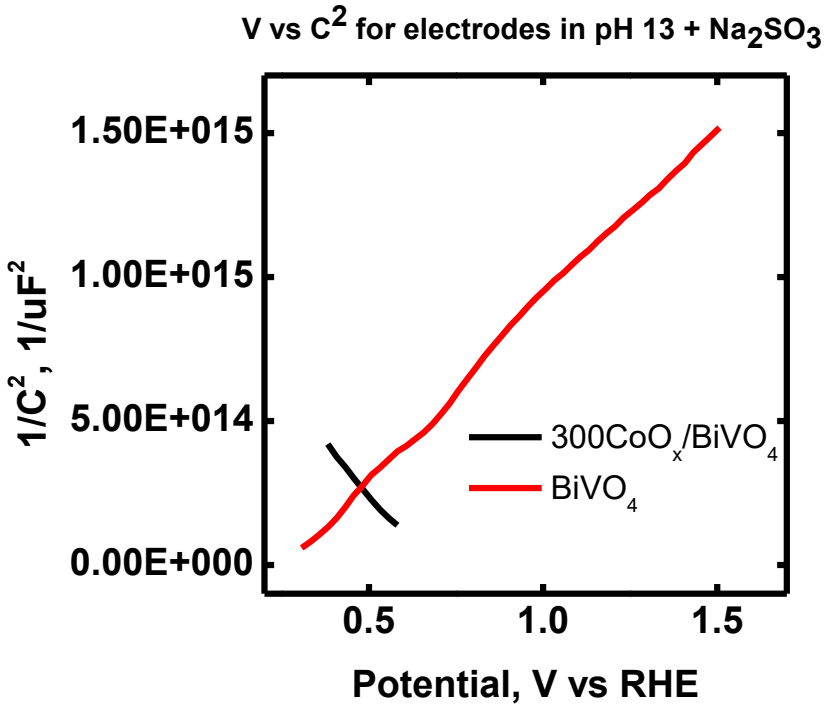

Figure 18: Mott Schottky results for bare $BiVO_4$ and an electrode comprised of 300 cycles of CoO_x on $BiVO_4$, in contact with a mixed solution of pH 13 KOH and Na_2SO_3.

As can be seen from figure 18, the bare $BiVO_4$ electrode displays expected n-type behavior and a flat-band potential near .25V vs RHE; the electrode with a substantial amount of CoOx, however, instead displays p-type behavior (and a flat-band potential near .7V vs RHE). The flat-band potential is interesting insofar as it suggests this material, if the electronic properties were sufficiently improved, may actually work as a capable photocathode. That aside, the clear change from n to p type capacitance data indicates that the $BiVO_4$/solution or $BiVO_4/CoO_x$ interfaces are no longer operating as the active material in this junction; instead, the CoO_x/solution interface is now the dominant

interface in the junction and the other interfaces are effectively ohmic. This is also supported and indicated by the (photo)electrochemical data.

References

1. Mierwaldt, D.; Mildner, S.; Arrigo, R.; Knop-Gericke, A.; Franke, E.; Blumenstein, A.; Hoffmann, J.; Jooss, C., In Situ XANES/XPS Investigation of Doped Manganese Perovskite Catalysts. *Catalysts* **2014,** *4* (2), 129-145.

2. (a) Lichterman, M. F.; Shaner, M. R.; Handler, S. G.; Brunschwig, B. S.; Gray, H. B.; Lewis, N. S.; Spurgeon, J. M., Enhanced Stability and Activity for Water Oxidation in Alkaline Media with Bismuth Vanadate Photoelectrodes Modified with a Cobalt Oxide Catalytic Layer Produced by Atomic Layer Deposition. *J. Phys. Chem. Lett.* **2013,** *4* (23), 4188-4191; (b) Donders, M. E.; Knoops, H.; Van de Sanden, M. C.; Kessels, W. M.; Notten, P., Remote Plasma Atomic Layer Deposition of Co3O4 Thin Films. *ECS Transactions* **2009,** *25* (4), 39-47.

3. Kalanyan, B.; Parsons, G., Atomic Layer Deposited Oxides for Passivation of Silicon Photoelectrodes for Solar Photoelectrochemical Cells. *ECS Transactions* **2011,** *41* (2), 285-292.

4. (a) Wang, H.; Pilon, L., Intrinsic limitations of impedance measurements in determining electric double layer capacitances. *Electrochimica Acta* **2012,** *63* (0), 55-63; (b) Góes, M. S.; Joanni, E.; Muniz, E. C.; Savu, R.; Habeck, T. R.; Bueno, P. R.; Fabregat-Santiago, F., Impedance Spectroscopy Analysis of the Effect of TiO2 Blocking Layers on the Efficiency of Dye Sensitized Solar Cells. *J. Phys. Chem. C* **2012,** *116* (23), 12415-12421.

II. ALD-TiO_2 as a protecting layer for unstable or quasistable photoanode systems

Introduction.

While metal-oxide semiconductors may be advantageous in that they are often easily (and cheaply) prepared from abundant materials, few such systems are capable of delivering the high photocurrents necessary to drive a highly efficient water splitting device. For this reason, the use of a smaller bandgap material which is capable of delivering a larger photocurrent may be preferable. However, small bandgap materials, such as relevant III-V and II-VI semiconductors in addition to silicon and germanium, while often reductively stable, are generally unstable to oxidative conditions. As a result, the modification of these semiconductors with a protective film to allow them to function under OER conditions may allow for a highly efficient device to be constructed from materials once thought unusable in a water splitting device, particularly in conditions where HER and OER kinetics for efficient catalysis are favorable (i.e., highly alkaline or highly acidic media).

II.1. Protection of Gallium Phosphide in acid and base, and XPS analysis

The protection of moderate and small-bandgap semiconductors is of crucial important to the development of an artificial photosynthesis device that hopes to operate in highly reactive media such as KOH or H_2SO_4, as these electrolytes are generally rather destructive (at best) toward such semiconductors. Gallium phosphide has a larger than ideal bandgap[1] for water splitting but the alloys thereof in the III-V[2] family are incredibly well-suited for use in such endeavors. The structure semiconductor/TiO_2/catalyst allows, in theory, for stable or quasistable systems in a variety of conditions, depending on the identity of the catalyst.

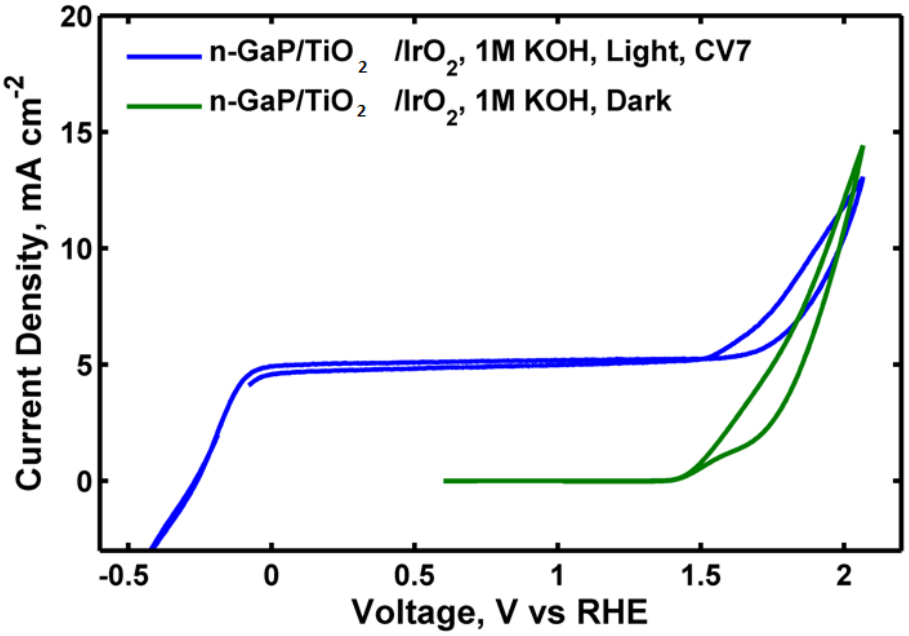

Figure 1. J-V curves for n-GaP/ TiO_2/IrO_x, in which the TiO2 was deposited through atomic layer deposition (ALD) and the IrOx was deposited from a reactive sputter in an oxygenated atmosphere. Illumination was approximately 1 sun.

As shown in Figure 1, above, GaP is not stable when coated with TiO_2/IrO_x and placed in KOH. The incredibly high Voc under illumination is indicative of direct photocorrosion of the semiconductor (and removal of the overlayer of TiO_2). However, the fault in this system lies in the nature of the IrO_x deposition; as a reactive sputter, the substrate is heated to ~350^{o}C during deposition of IrO_x, during which various structural changes may take place in the TiO_2 which cause pinholes to develop, leading to the quick death of the device. An alternate route is shown below, in Figure 2.

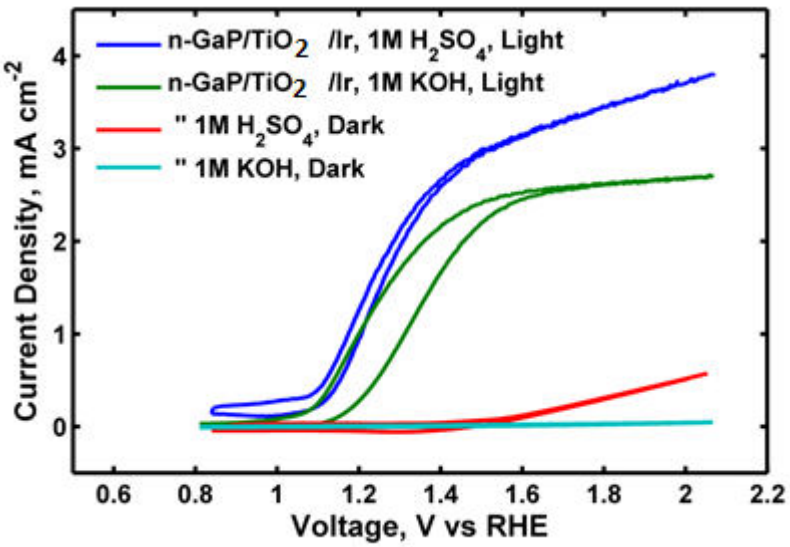

Figure 2. J-V curves for electrodes of the type n-GaP/TiO_2/Ir. Illumination was approximately 1 sun.

As shown in Figure 2, the n-GaP/TiO2 system can in fact work in both acidic and basic media for OER, provided a sufficiently active (and stable) catalyst[3] is placed on the surface and the TiO_2 layer is not destroyed or altered with a heat treatment after deposition. The Ir layer herein was approximately 4 nm thick. However, the Ir catalyst layer showed marked instability and the photoelectrochemical performance of these electrodes decreated quickly within 1 hr of constant applied potential.

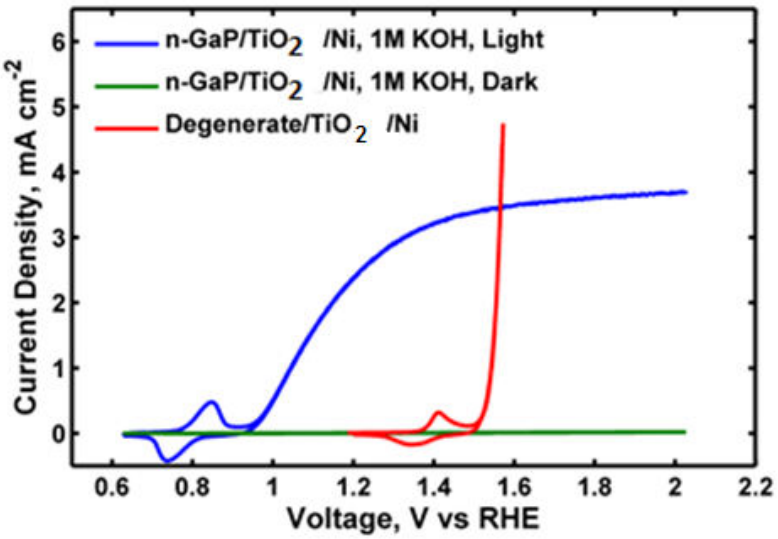

Figure 3. J-V curves for electrodes of the type n-GaP/TiO_2/Ni. The degenerate electrode is one in which the semiconductor base is degenerately doped so as to act metallic.

As shown in Figure 3, the n-GaP/TiO_2/Ni structure provided the best photoperformance for the n-GaP set of electrodes (compare to Figs 1 and 2)[4]. Stability was approximately 5 hours, beyond which presumed pinhole formation lead to KOH contact to the underlying n-GaP which eventually resulted in curves analogous to those shown in Figure 1. However, the Ni catalyst was found to be stable in KOH and provided electrodes that gave photovoltages of ~500 mV. One attempt to change the surface

energetics on the GaP was the deposition of Ir directly onto the semiconductor to give a high-work function contact which might provide a better (schottky) contact with a higher photovoltage; however, as shown in Figure 4, this was not to be the case. Initial oxygen flourescene measurements (Figure 5) indicate faradaic conversion of photocurrent to oxygen production in initial conditions, i.e., before pinhole formation and stability loss.

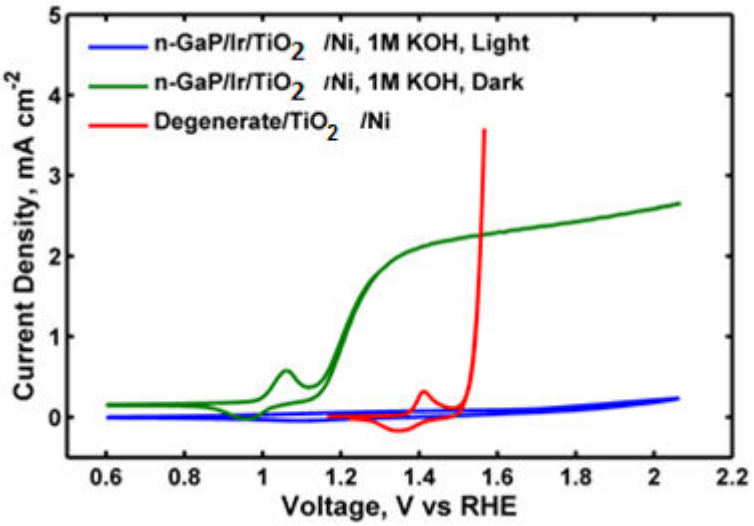

Figure 4. J-V curves for n-GaP/Ir/TiO_2/Ni photoelectrodes.

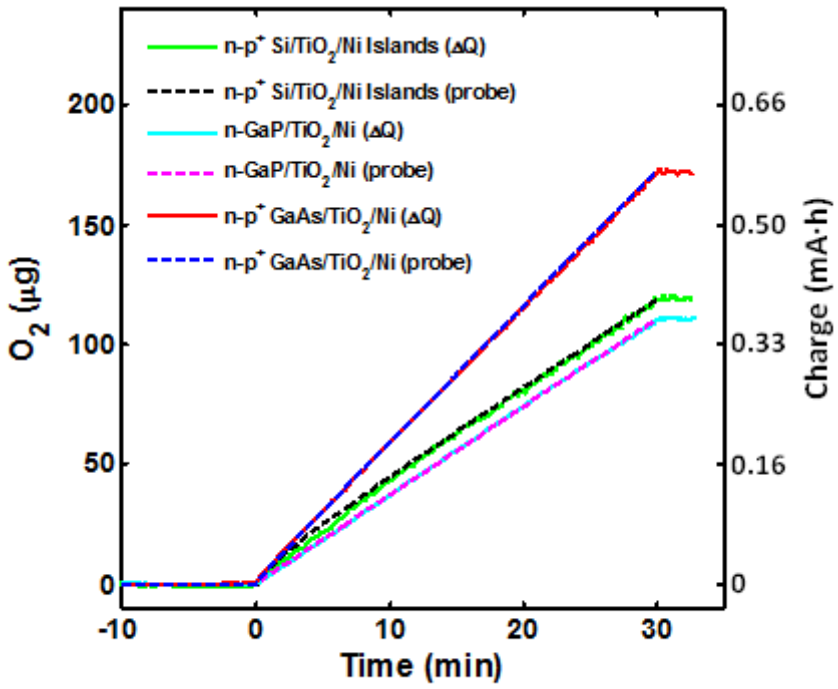

Figure 5. O_2 flourescene probe measurements for n-GaP/TiO_2/Ni photoelectrodes and other systems.

It is worth noting here that a number of attempts were undertaken to address the failure aspect of these devices in KOH and none of them showed any promise. These include altering the pulse rates of the ALD deposition; altering the nature of catalyst deposition (vacuum or otherwise); and making changes to electrode fabrication. On a fundamental level, it currently seems that the TiO_2-GaP interface is simply not sufficiently passivating as to allow long lifetimes in KOH. Varying the materials set is likely the most promising path toward stability, as will be discussed below.

Using a similar approach as to that taken in the first section to analyze the $BiVO_4$/CoOx junction, XPS[5] and UPS[6] were used to obtain the nature of the n-GaP/TiO_2 heterojunction. As the n-GaP used here has $N_D = 2 * 10^{17}$ cm^{-3}, we expect the fermi level to be present approximately 100 meV-150 meV below the conduction band.

Equivalently, the valence band should be approximately 2.11-2.16 eV below the Fermi level by XPS measurements when at flatband.

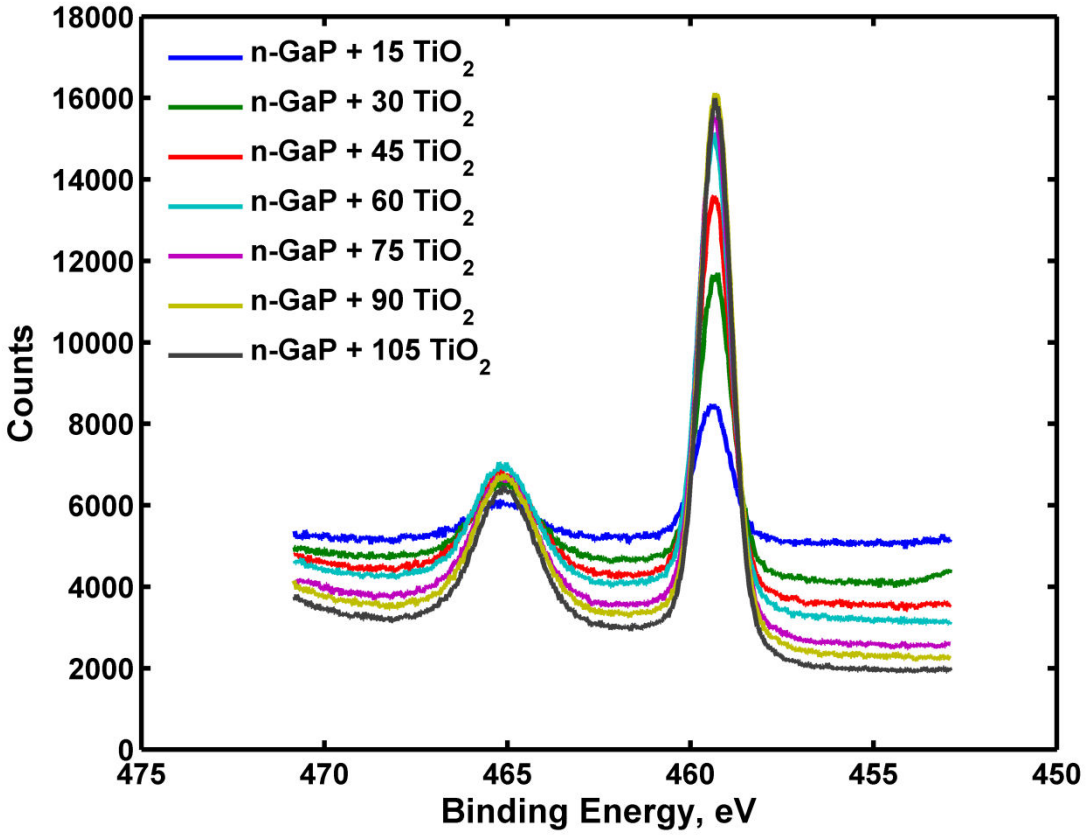

Figure 6. Ti 2p XPS region for varying thicknesses of TiO_2 on n-GaP.

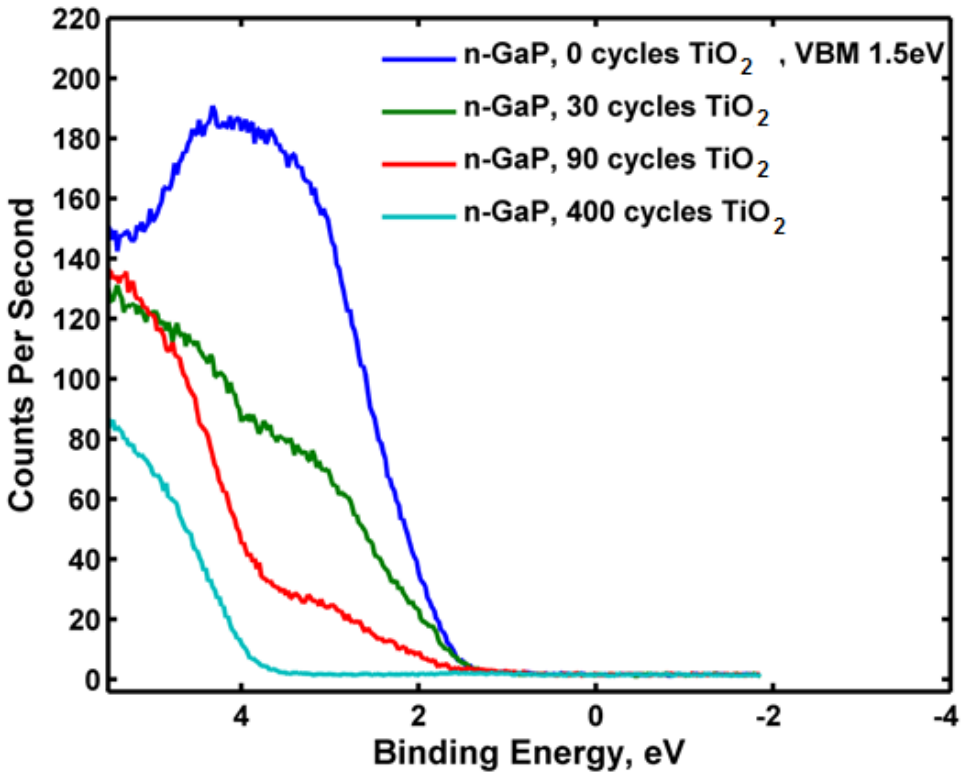

Figure 7. Valence band XPS region for varying thicknesses of TiO_2 on n-GaP (wide view).

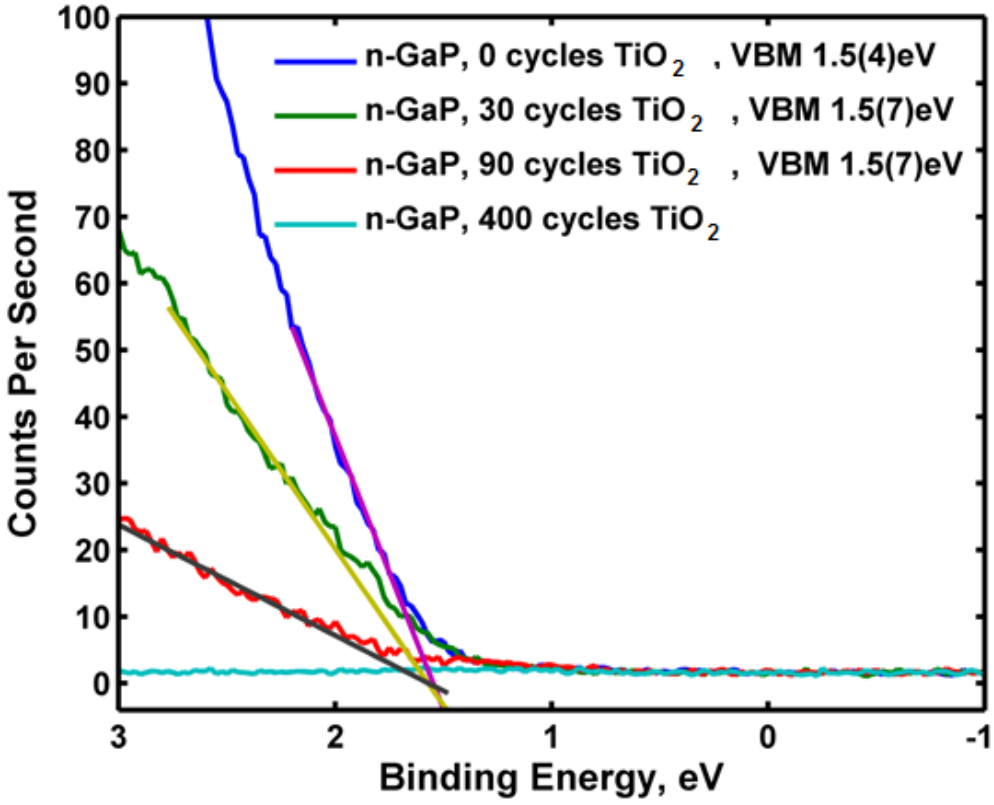

Figure 8. Valence band XPS region for varying thicknesses of TiO_2 on n-GaP (zoomed in). The observed valence band offsets (from the Fermi energy) are listed.

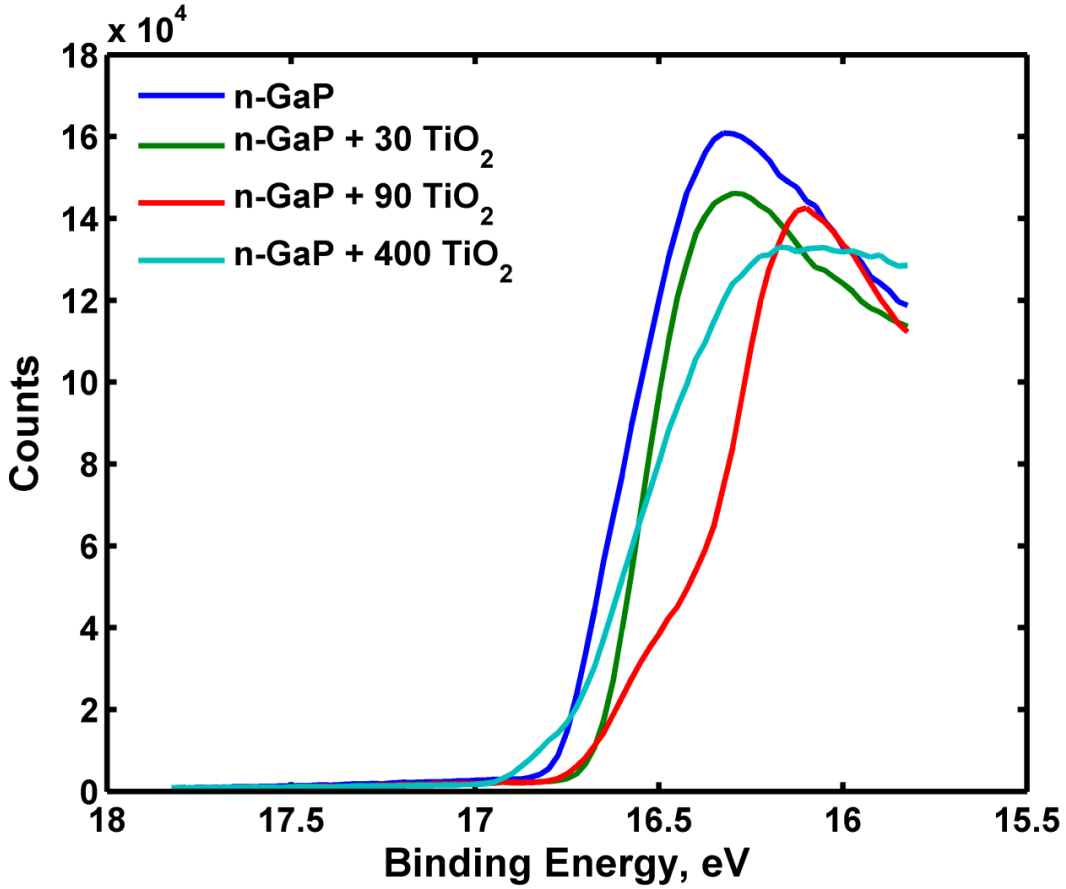

Figure 9. Observed UPS secondary electron cutoff to indicate the work function of these samples.

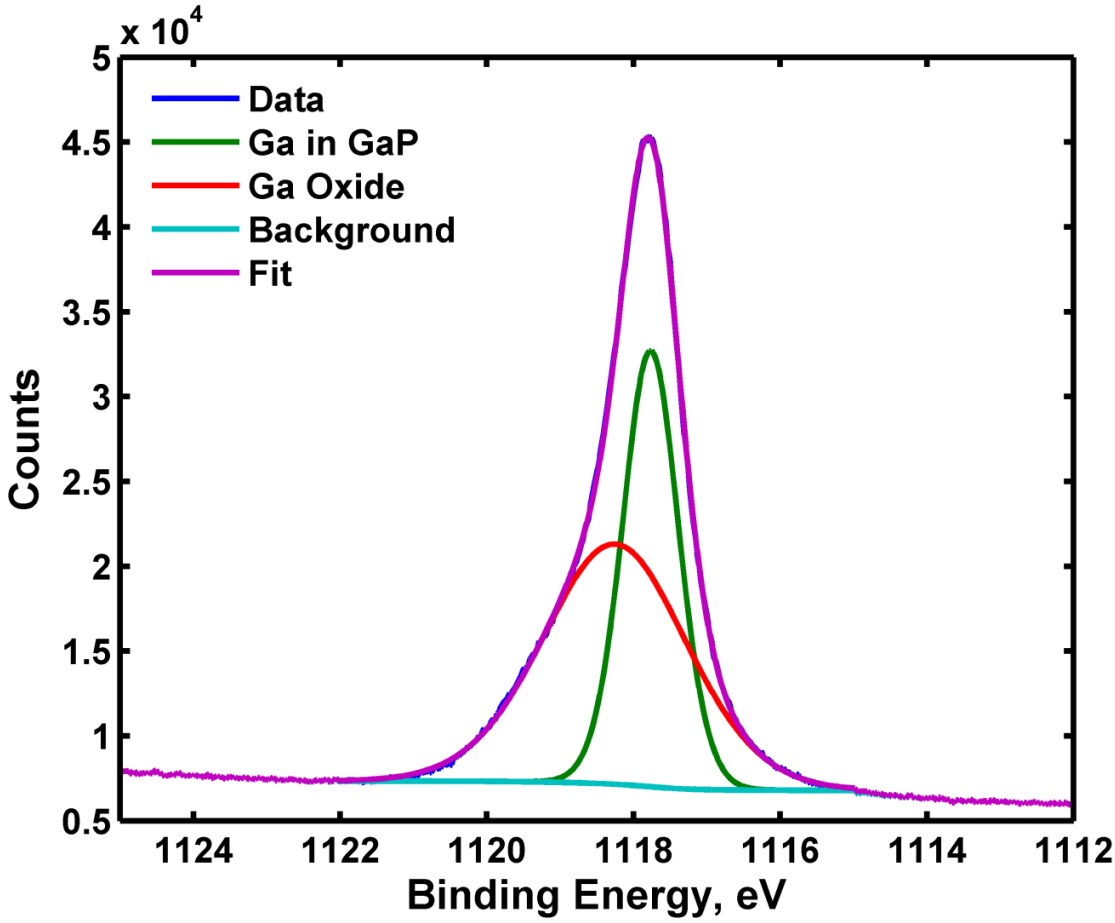

Figure 10. Gallium in GaP and Gallium oxide, shown combined. The oxide peak is very substantial and is responsible for the photovoltage observed.

The observed photovoltage of ~500mV is consistent with the valence band offsets of 1.55 eV observed. This valence band offset indicates that after etching, the exposure of the semiconductor to oxygen prior to loading into the ALD system is responsible for a surface oxidation which pins the energetics and provides a poor buried junction which is responsible for the observed photovoltage. Surface modification to protect and set a better surface dipole could lead to substantially improved photovoltages with GaP.

References

1. Walter, M. G.; Warren, E. L.; McKone, J. R.; Boettcher, S. W.; Mi, Q.; Santori, E. A.; Lewis, N. S., Solar Water Splitting Cells. *Chem. Rev.* **2010,** *110* (11), 6446-6473.
2. Tanabe, K., A review of ultrahigh efficiency III-V semiconductor compound solar cells: multijunction tandem, lower dimensional, photonic up/down conversion and plasmonic nanometallic structures. *Energies* **2009,** *2* (3), 504-530.
3. McCrory, C. C. L.; Jung, S.; Peters, J. C.; Jaramillo, T. F., Benchmarking Heterogeneous Electrocatalysts for the Oxygen Evolution Reaction. *J. Am. Chem. Soc.* **2013,** *135* (45), 16977-16987.
4. Hu, S.; Shaner, M. R.; Beardslee, J. A.; Lichterman, M. F.; Brunschwig, B. S.; Lewis, N. S., Amorphous TiO2 coatings stabilize Si, GaAs, and GaP photoanodes for efficient water oxidation. *Science* **2014,** *344* (6187), 1005-1009.
5. (a) Mierwaldt, D.; Mildner, S.; Arrigo, R.; Knop-Gericke, A.; Franke, E.; Blumenstein, A.; Hoffmann, J.; Jooss, C., In Situ XANES/XPS Investigation of Doped Manganese Perovskite Catalysts. *Catalysts* **2014,** *4* (2), 129-145; (b) Kaichev, V. V.; Prosvirin, I. P.; Bukhtiyarov, V. I., XPS for in situ study of the mechanisms of heterogeneous catalytic reactions. *J Struct Chem* **2011,** *52* (1), 90-101.
6. Lewerenz, H. J., Surface scientific aspects in semiconductor electrochemistry. *Chem. Soc. Rev.* **1997,** *26* (4), 239-246.

II.2. Protection of Cadmium Telluride by ALD-TiO_2

Originally published as "Stabilization of n-cadmium telluride photoanodes for water oxidation to O_2(g) in aqueous alkaline electrolytes using amorphous TiO2 films formed by atomic-layer deposition" in *Energy and Environmental Science*[1].

Although II-VI semiconductors such as CdS, CdTe, CdSe, ZnTe, and alloys thereof, can have nearly ideal band gaps and band-edge positions for the production of solar fuels, II-VI photoanodes are well-known to be unstable towards photocorrosion or photopassivation when in contact with aqueous electrolytes. Atomic-layer deposition (ALD) of amorphous, "leaky" TiO_2 films coated with thin films or islands of Ni oxide has been shown to robustly protect Si, GaAs, and other III-V materials from photocorrosion and therefore to facilitate the robust, solar-driven photoelectrochemical oxidation of H_2O to O_2(g). We demonstrate herein that ALD-deposited 140-nm thick amorphous TiO_2 films also effectively protect single crystalline n-CdTe photoanodes from corrosion or passivation. An n-CdTe/TiO_2 electrode with a thin overlayer of a Ni-oxide based oxygen-evolution electrocatalyst produced 435 ± 15 mV of photovoltage with a light-limited current density of 21 ± 1 mA cm^{-2} under 100 mW cm^{-2} of simulated Air Mass 1.5 illumination. The ALD-deposited TiO_2 films are highly optically transparent and electrically conductive. We show that an n-CdTe/TiO_2/Ni oxide electrode enables the stable solar-driven oxidation of H_2O to O_2(g) in strongly alkaline aqueous solutions, where passive, intrinsically safe, efficient systems for solar-driven water-splitting can be operated.

BROADER CONTEXT. High-efficiency photoelectrochemical (PEC) solar-driven water splitting and/or carbon dioxide reduction will require the use of semiconductors capable of delivering a substantial amount of current as well as the photovoltage required to drive the fuel-forming anodic and cathodic half-reactions, respectively. Although metal oxides have received much attention as photoanodes due to their stability against oxidation, such systems generally suffer from low maximum photocurrent densities in sunlight due to the large band gaps of the materials explored to date. Semiconductors with smaller band gaps, such as CdTe, are better matched to the solar spectrum and have more suitable valence-band positions; however, such materials are generally unstable in aqueous electrolytes under photoanodic conditions. We demonstrate herein that atomic-layer deposition of amorphous TiO_2 films forms a protection layer on n-CdTe photoanodes that, with a Ni-oxide based electrocatalyst layer, allows for photocatalytic water oxidation at the electrolyte interface. Such n-CdTe/TiO_2/Ni oxide photoanodes yielded quantitative oxidation of water to O_2(g) with internal quantum yields approaching unity for extended periods of operation under 100 mW cm^{-2} of simulated solar illumination.

CdTe, with a 1.44 eV band gap, has been widely studied since the 1980s[2], and is currently used primarily in thin-film solar cells in which p-CdTe is deposited upon n-CdS to form a buried heterojunction device.[3] CdTe has furthermore been investigated for use in photoelectrochemical (PEC) applications but is known to undergo a number of facile photooxidation or photocorrosion processes in various aqueous, as well as organic, media.[2a, b] Strongly alkaline or strongly acidic media have numerous benefits for the electrolysis of water due to their high conductivity without the need for added electrolyte or buffering species and minimal pH gradients under operating conditions. Further, at high and low pH, viable permselective ionophoric membranes are available to separate the products of electrolysis, and the kinetics of water oxidation with suitable electrocatalysts is rapid, thus making construction of a passive, intrinsically safe and efficient solar-driven water-splitting device possible.[4] However, efficient photoanodes typically are unstable and rapidly corrode or passivate when operated in contact with electrolytes in these pH ranges.[5] Recently, a number of reports have been published in which the protection of otherwise unstable materials is carried out using a protecting layer such as TiO_2, MnO or metal-modified ITO.[6] Facile electron conduction is expected through the conduction band of TiO_2, and hence TiO_2 has been developed as a protection layer for photocathodes. In contrast, stoichiometric TiO_2 should present a tunnel barrier to photogenerated holes at energies near that required for water oxidation. We report herein that 140 nm thick amorphous TiO_2 films deposited by atomic-layer deposition (ALD) and modified by the addition of a Ni oxide catalytic layer effectively protect n-CdTe photoanodes from corrosion or passivation and effect the quantitative oxidation of H_2O to $O_2(g)$. Protected n-CdTe photoanodes produced 435 ± 15 mV of photovoltage and

light-limited current densities of 21 ± 1 mA cm^{-2} under 100 mW cm^{-2} of simulated Air Mass (AM) 1.5 illumination.

Atomic-layer deposition (ALD) was employed to deposit films of TiO_2 up to 150 nm in thickness on (111)-oriented n-CdTe samples with a carrier concentration of 1 x 10^{17} cm^{-3}. The electrical characteristics of such films have been described previously.[5a] A thin film of Ni was then deposited by sputtering. The Ni layer upon oxidation produces an earth-abundant, highly active, low overpotential Ni oxide electrocatalyst for the oxygen-evolution reaction (OER).[5a] Figure 1 shows a cross-sectional scanning-electron micrograph of a resulting photoelectrode.

Figure 2 shows typical current density vs potential (*J-E*) data for (a) an n-CdTe/TiO_2/Ni photoanode in pH = 14 KOH(aq) plotted against the reversible hydrogen electrode potential, RHE[a], and (b) an n-CdTe/TiO_2/Ni photoanode in contact with an aqueous ferro/ferricyanide solution (KCl, $Fe(CN)_6^{3-}$, and $Fe(CN)_6^{4-}$, of 1, 0.05, and 0.35 M concentrations, respectively), both under 100 mW cm^{-2} of simulated AM1.5 illumination (Xenon lamp with an AM1.5 filter set). Unetched samples exhibited lower photovoltages and low fill factors (Fig. S1), whereas samples etched for 30 s in Br_2/CH_3OH produced superior fill factors, high photocurrents and improved photovoltages. Etching concentrations in the range of 0.1% to 1% Br_2/CH_3OH produced the most optimized photoelectrodes from the n-CdTe wafer used in this study. Open-circuit photovoltages of approximately 435 mV and light-limited photocurrent densities of 21 mA cm^{-2} were observed for n-CdTe/TiO_2/Ni photoanodes in pH = 14 KOH (aq) as well as in contact with the aqueous ferri/ferrocyanide solutions (Fig. 2). For comparison,

[a] $E_{RHE} = E_{NHE} + 0.059$ x pH = $E_{Ag/AgCl} + 0.197 + 0.059$ x pH. Water oxidation at any pH and STP occurs at 1.23V vs RHE.

a similarly protected n-Si photoanode has been shown to provide 28 mA cm^{-2} of light-limited photocurrent density and 410 mV of photovoltage, a similarly protected n-GaP photoanode has been shown to provide a light-limited photocurrent of 3.4 mA cm^{-2} and 590 mV of photovoltage, and a similarly protected gallium arsenide photoanode containing a buried junction, np^{+}-GaAs, has been shown to provide photocurrent densities of 14.3 mA cm^{-2} and photovoltages of 810 mV.[5a] To provide perspective on the performance produced provided by the protection scheme, load-line analysis indicated that obtaining the observed *J-E* performance of the n-CdTe/TiO_2/Ni photoanode using a Si photovoltaic (PV) cell electrically in series with an electrocatalytic anode that exhibited identical *J-E* behavior to that of a 2 nm Ni film on a titanium electrode[7] would require the use of a 7.5% efficient Si PV cell with a V_{oc} of 0.48 V, a J_{sc} of 22 mA cm^{-2}, and a *ff* of 0.71.

Scanning-electron microscopy (SEM) and energy-dispersive X-ray spectroscopy (EDS) were used to further analyze the n-CdTe/TiO_2/Ni interface. As shown in the cross-sectional view (Fig. 1), the thickness of the TiO_2 layer was 140 nm, which implies a growth rate of 0.056 nm $cycle^{-1}$ for the 2500 cycle TiO_2 sample. Figures S2 and Table S1 show the EDS data obtained at various locations in the n-CdTe/TiO_2/Ni structure. Notably, the EDS data indicated that a slightly Cd-poor region was present at the interface, as would be expected for an oxidizing etch that produced a Cd-poor, acceptor-rich interface. This behavior suggests that the interfacial layer is key to producing the photovoltage exhibited by these samples, and agrees well with prior suggestions that such etches form an acceptor-rich, Cd-poor surface at the CdTe interface,[8] which pins the photovoltage to ~ 0.5 V under similar illumination conditions.[9]

XPS experiments were performed to characterize the surface properties of the etched n-CdTe wafers prior to the ALD of the TiO_2 overlayer. An unetched wafer showed nearly equal amounts of tellurium and cadmium at the surface, in addition to a substantial amount of tellurium oxide (Fig. S3 and Table S2), whereas the Br_2/CH_3OH-etched samples had a 0.75:1 ratio of cadmium to tellurium at the surface and exhibited a much smaller tellurium oxide peak. This ratio suggests the formation of a p-type layer at the surface of the n-CdTe wafer, which influences the magnitude of the observed photovoltages. Brief (15 s) argon-ion sputter-etching between XPS scans quickly returned the Te:Cd ratio to unity before leading to a Cd-rich surface, due to the different sputter-etching rates of tellurium and cadmium. While the different sputter-etching rates made rigorous depth profiling difficult using this experimental technique, these results show that the Br_2/CH_3OH etch only created this p-type layer within a very narrow layer at the surface, with a depth on the order of nanometers.

The spectral response data for n-CdTe/TiO_2/Ni electrodes indicated a high quantum yield for water oxidation (Fig. 3), with minimal absorption of light by the TiO_2/Ni overlayers. Spectral response measurements were undertaken at 2.07 V vs RHE; this potential was chosen as it allows for data to be collected in high photocurrent regions (at the light-limited current density). Based on integration of the spectral response data with the wavelength-dependent irradiance of the AM 1.5G solar spectrum, the sample etched with 1% Br_2 in CH_3OH resulted in photoelectrodes that exhibited excellent quantum yields in lower-wavelength regions, as well as high quantum yields at long wavelengths. Integration of the wavelength-dependent quantum yield of such electrodes with respect to the spectral irradiance distribution of the AM 1.5G solar spectrum

produced a light-limited photocurrent density of 20.5 mA cm^{-2}, which compared well with the observed value of 21.5 mA cm^{-2} (Fig. 2) at 2.07 V vs RHE.

Similar to the behavior of n-Si/TiO_2/Ni photoelectrodes[8], n-CdTe/TiO_2/Ni photoelectrodes were stable for > 100 hours of continuous operation during photoanodic current flow (Fig. 4a). An n-CdTe sample etched in the same manner but with only Ni deposited by sputtering, in the absence of ALD TiO_2, exhibited a decay in performance of ~40% over this same period of operation (Fig. S4). Figure S5 shows a comparison of the *J-E* behavior before and after 4 h of potentiostatic electrolysis at 2.07 V vs RHE. The n-CdTe/TiO_2/Ni electrode remained effectively unchanged whereas both the photocurrent density and fill factor of an n-CdTe/Ni electrode decayed substantially over the same time period. Approximately 20 times more holes were passed through the circuit over 100 hours than atoms present in the entire CdTe electrode, which strongly suggests that the photocurrent shown in Figure 4a was predominantly associated with the faradaic oxidation of water to O_2. Direct verification of this hypothesis was obtained using an oxygen detector,[10] which revealed that n-CdTe/TiO_2/Ni samples operated in pH = 14 KOH(aq) (see ESI for details) produced an amount of O_2 detected by the probe that was within experimental error of the amount of oxygen calculated based on the coulometry assuming 100% faradaic efficiency for O_2 production (Fig. 4b). The flat regions in the data before, in between, and after the measurement of photocurrent, and the time evolution of the detected O_2, correlated completely with the photoanodic current flow for two thirty minute periods, strongly indicating that the detected O_2 was the result of water oxidation by the photoanode.

The amorphous TiO_2 coatings prepared by ALD yield buried junctions in which the semiconductor surface is protected from corrosion or passivation by the contacting electrolyte. The photovoltage of systems that do not contain a n-p^+ type base-emitter buried junction, such as n-CdTe/TiO_2/Ni electrodes, could be improved further through chemical control over the interfacial energetics at the semiconductor/oxide interface, including the introduction of surface dipoles, band-edge engineering, and other approaches to reduce the majority-carrier currents in the device. Nevertheless, this work shows that CdTe, generally believed to be unstable and not suited for investigation as a photoanode for the oxidation of water to O_2(g), can be beneficially used at least on the laboratory time scale for such purposes. Experiments are currently underway to quantify the methods by which the photovoltage and electrode stability can be further optimized in such systems.

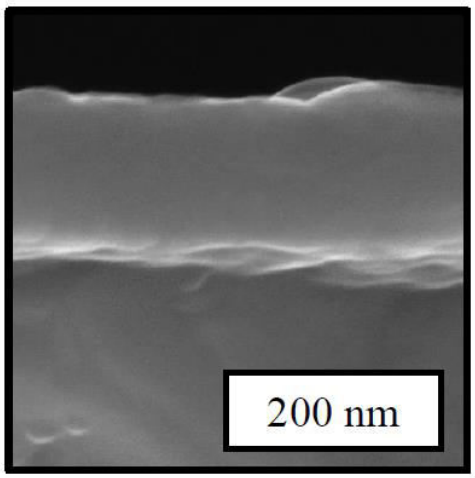

Figure 1. Representative cross-sectional scanning electron micrograph of a n-CdTe/TiO_2/Ni electrode depicting the ALD-grown TiO_2 film above the n-CdTe wafer section. The Ni deposited onto the TiO_2 is not visible in this micrograph but was detected by EDS (see ESI Figure S3).

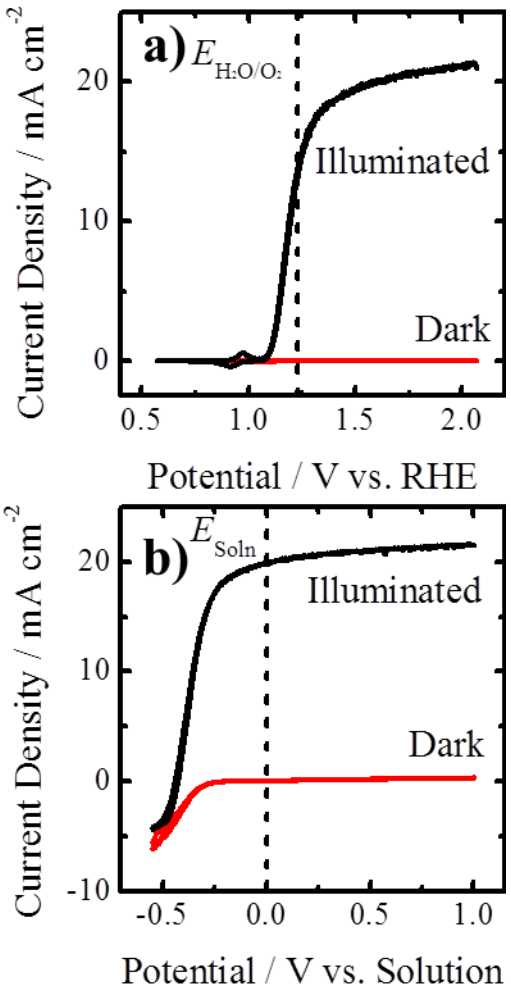

Figure 2. *J-E* data obtained with a n-CdTe/TiO_2/Ni electrode in the dark and under illumination in (a) pH = 14 KOH(aq) and (b) a $Fe(CN)_6^{3-/4-}$ solution. Illumination was provided by a Xenon arc lamp with an AM 1.5 filter set and the light intensity was calibrated to 100 mW cm^{-2} of AM 1.5G illumination using a secondary standard calibrated Si solar cell.

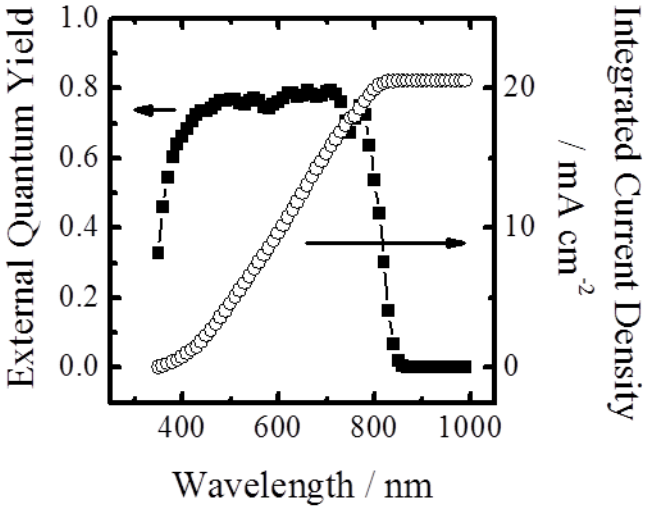

Figure 3. External quantum yield for a n-CdTe/TiO_2/Ni electrode biased at 2.07 V vs. RHE in pH = 14 KOH(aq) solution and derived current density from integration against the AM 1.5G spectrum.

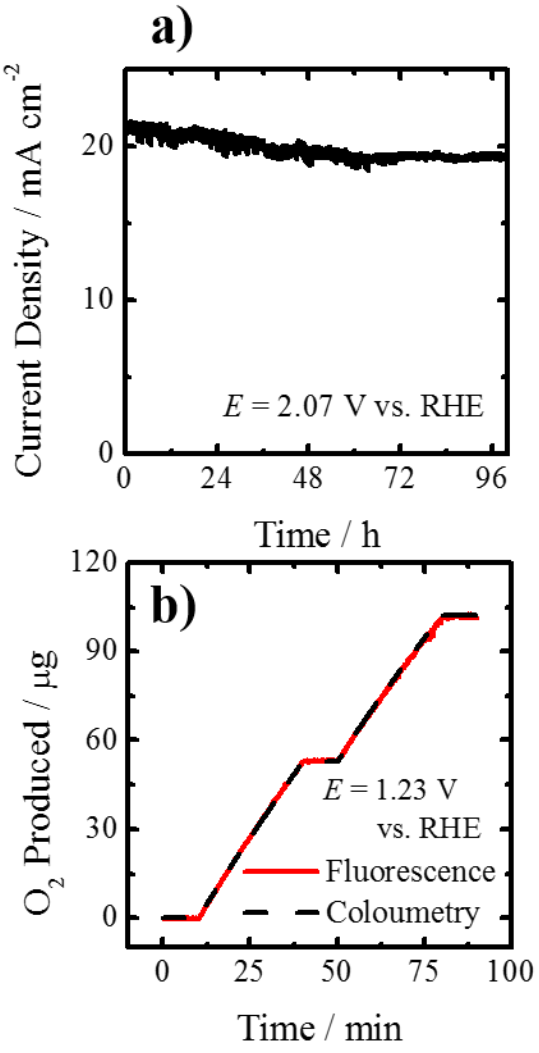

Figure 4. (a) Current density as a function of time during potentiostatic electrolysis at 2.07 V vs. RHE in pH = 14 KOH(aq). (b) Oxygen production detected by a fluorescent probe and derived from coulometry during constant potential electrolysis at 1.23 V vs. RHE in pH = 14 KOH(aq). In (a), the n-CdTe/TiO_2/Ni electrode was illuminated by a Xenon arc lamp that had been calibrated to provide 100 mW cm^{-2} of simulated AM 1.5G illumination; in (b), 20mW cm^{-2} was used to prevent bubble formation.

SUPPLEMENTARY INFORMATION AVAILABLE. Detailed experimental methods, SEM/EDS data, XPS data, and other photoelectrochemical information are available in the Supporting Information.

ACKNOWLEDGMENTS. This material is based upon work performed by the Joint Center for Artificial Photosynthesis, a DOE Energy Innovation Hub, supported through the Office of Science of the U. S. Department of Energy under Award Number DE-SC0004993. The authors gratefully acknowledge Dr. Ke Sun for insightful discussions and Dr. Slobodan Mitrovic for assistance collecting XPS data. AIC is grateful to the National Science Foundation for support from an NSF Graduate Research Fellowship. BSB acknowledges the Beckman Institute of the California Institute of Technology for support.

Supporting Information

S1. Contents

This document contains detailed descriptions of the experimental procedures used in this work (Section S2), photoelectrochemical data detailing the effect of Br_2/CH_3OH etching on photoelectrode performance (Section S3), energy dispersive X-ray spectroscopy of the interface of an n-CdTe/TiO_2/Ni electrode (Section S4), X-ray photoelectron spectroscopic analysis of the Br_2/CH_3OH etched n-CdTe surface (S5), and photoelectrochemical data describing the stability of n-CdTe/Ni electrodes in comparison to n-CdTe/TiO_2/Ni electrodes (Section S6)

S1. Contents

This document contains detailed descriptions of the experimental procedures used in this work (Section S2), photoelectrochemical data detailing the effect of Br_2/CH_3OH etching on photoelectrode performance (Section S3), energy dispersive X-ray spectroscopy of the interface of an n-CdTe/TiO_2/Ni electrode (Section S4), X-ray photoelectron spectroscopic analysis of the Br_2/CH_3OH etched n-CdTe surface (S5), and photoelectrochemical data describing the stability of n-CdTe/Ni electrodes in comparison to n-CdTe/TiO_2/Ni electrodes (Section S6)

S2. Experimental Methods

Preparation of Electrodes

CdTe pieces were cut from an n-CdTe(111) (carrier concentration 5.5 x 10^{17} cm^{-3}) wafer that had previously been polished and contacted at the back with evaporated In. Pieces were etched for 30 s in a freshly prepared solution of Br_2 (Sigma Aldrich, 99.999%)/CH_3OH (EMD Millipore, >99.9%) dissolved in CH_3OH, rinsed vigorously with CH_3OH, and immersed in CH_3OH until being dried with a stream of N_2(g) before being placed in the atomic-layer deposition (ALD) chamber (Cambridge Nanotechnology). TiO_2 was deposited by ALD using H_2O and tetrakis(dimethylamido)titanium(IV) (TDMAT) (Sigma, 99.999%). A 0.1 s pulse of TDMAT was followed by a 15 s purge with N_2(g) at 20 sccm, followed by a 0.015 s pulse of H_2O and another 15 s purge. The coating cycle was repeated 2500 times, and the deposition was performed out at 150 ^{0}C. Substantial experimentation was performed to optimize this system, and varying the ALD temperatures generally resulted in poorer or completely nonconductive films. The results presented herein are currently the most optimized results from these experiments thus far. Ni deposition was performed in a sputterer (AJA International) under an Ar atmosphere at 8.5 mtorr. RF power was used with the Ni target (Kurt Lesker, 99.995%) to deposit ~ 2 nm of material.

Final assembly of the electrodes began with application of Ga-In eutectic (Sigma Aldrich, 99.99%) onto the back of the n-CdTe, followed by use of Ag paint (SPI Supplies) to contact the sample to a Cu wire. The area around the wire and n-CdTe was then coated with non-conductive epoxy (Hysol 9460). Electrode areas were derived from computer captured optical images analyzed with ImageJ software.

Electrode Characterization

Spectral response data were collected using a 300 W Xe lamp in conjunction with a monochromator (Newport Oriel Instruments) and lock-in amplifiers (Stanford Research Instruments). The voltammetry, chronoamperometry, and electrochemical impedance experiments were performed using a Bio-Logic SP-200 potentiostat.

Voltammetric measurements in pH 14 KOH (aq) were performed using a 3- or 4-necked 50-mL round-bottom flask that had been modified with a planar quartz window. The power of the Xenon lamp (Newport) used for illumination was adjusted to produce the desired incident illumination power. A ground glass diffuser ensured a uniform illumination intensity. The light intensity was adjusted to produce the same short-circuit current density as produced by 100 mW cm^{-2} of Air Mass (AM) 1.5G sunlight on a secondary standard Si photodiode. A three-electrode configuration was used with a saturated calomel electrode (SCE) or a Ag/AgCl(sat) reference electrode (BAS Inc.) and a Pt gauze counter electrode located in a fritted compartment that contained the same pH 14 or $Fe(CN)_6^{3-/4-}$ electrolyte as in the main cell compartment.

For experiments with $Fe(CN)_6^{3-/4-}$, a solution containing 0.050 M $K_3Fe(CN)_6$, 0.350 M $K_4Fe(CN)_6$, and 0.500 M K_2SO_4(aq) was prepared prior to use. This solution was contained in an electrochemical cell that had a small separation between the cell edge and the working electrode surface, to minimize the absorbing effects of the $Fe(CN)_6^{3-/4-}$ solution. A Pt wire and Pt gauze were the reference and counter electrodes, respectively, for these measurements.

For O_2(g) evolution experiments, a Neofox fluorescence probe was used in an airtight cell, along with a Ag/AgCl(sat) reference electrode. The Pt gauze counter

electrode was positioned in a separate, fritted compartment. The cell volume was 51 mL, and the cell was purged with a stream of Ar(g) for ~1 h prior to data collection. The experiment was run for 30 min after a 10 min waiting period at open circuit, then held at open circuit for ten minutes, then run for another 30 minutes to show that oxygen had been produced electrochemically and did not simply leak into the cell. The electrode area was 0.25 cm^2.

Scanning-electron micrographs (SEM) were obtained using a FEI Nova NanoSEM 450 at an accelerating voltage of 15 kV with a working distance of 5 mm and an in-lens secondary electron detector. Energy-dispersive X-ray spectroscopy was performed in the SEM at a working distance of 12 mm, using an accelerating voltage of 15 kV and an Oxford Instruments Si drift detector.

X-ray photoelectron spectroscopy (XPS) was performed using a Kratos Axis Nova system with a base pressure of $< 2\times10^{-9}$ torr. A monochromatic Al Kα source was used to irradiate the sample with X-rays with an energy of 1486.7 eV at a power of 450 W. A hemispherical analyzer oriented for detection along the sample surface normal was used for maximum depth sensitivity. High-resolution spectra were acquired at a resolution of 50 meV with a pass energy of 10 eV. An octopole ion gun was used to sputter-etch the sample surface with 500 eV Ar^+ ions in increments of 15 s.

S1. Photoelectrochemical Behavior of n-CdTe/TiO_2/Ni Electrodes with or without Etching

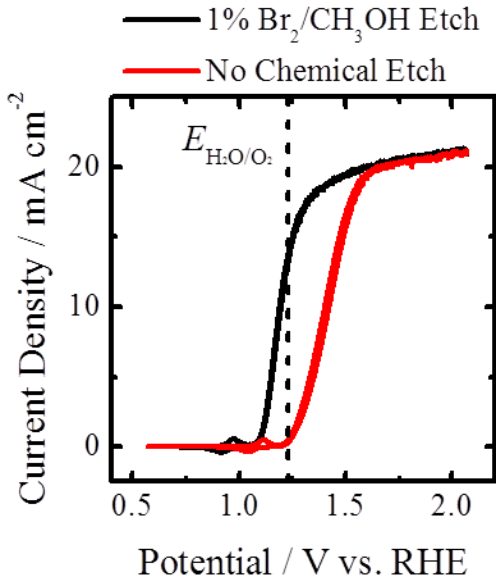

Figure S1. *J-E* data of n-CdTe/TiO_2/Ni photoelectrodes in pH = 14 KOH(aq) under illumination with a Xe arc lamp calibrated to 100 mW cm^{-2} of AM 1.5G illumintion. The n-CdTe was either etched with 1% Br_2/CH_3OH, or not chemically etched at all (beyond cleaning with CH_3OH) prior to deposition of the TiO_2.

S2. Energy Dispersive X-Ray Spectroscopy of an n-CdTe/TiO_2/Ni Interface

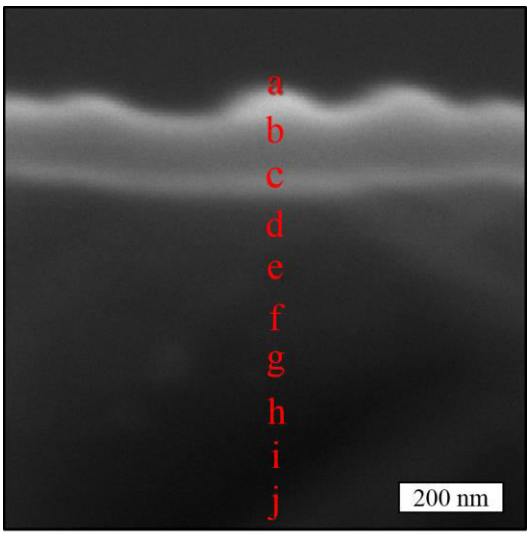

Figure S2. Cross-sectional scanning-electron micrograph of an n-CdTe/TiO_2/Ni electrode showing the ALD-grown TiO_2 film above the n-CdTe wafer section. The labels denote the positions where the EDS data in Table S1 were acquired.

Position	Cd	Te	Ti	Ni
a	1.16	1.00	3.70	2.04
b	1.06	1.00	4.83	0.39
c	1.09	1.00	2.64	
d	0.93	1.00	0.69	
e	0.93	1.00	0.30	
f	0.92	1.00	0.17	
g	0.99	1.00	0.12	
h	0.97	1.00	0.05	
i	0.94	1.00		
j	1.00	1.00		

Table S1. Atomic ratios derived from EDS acquired from an n-CdTe/TiO_2/Ni electrode at the positions indicated in Figure S1. All of the values were normalized to those of Te.

S3. X-Ray Photoelectron Spectroscopic Analysis of the Br_2/CH_3OH Etched n-CdTe Surface

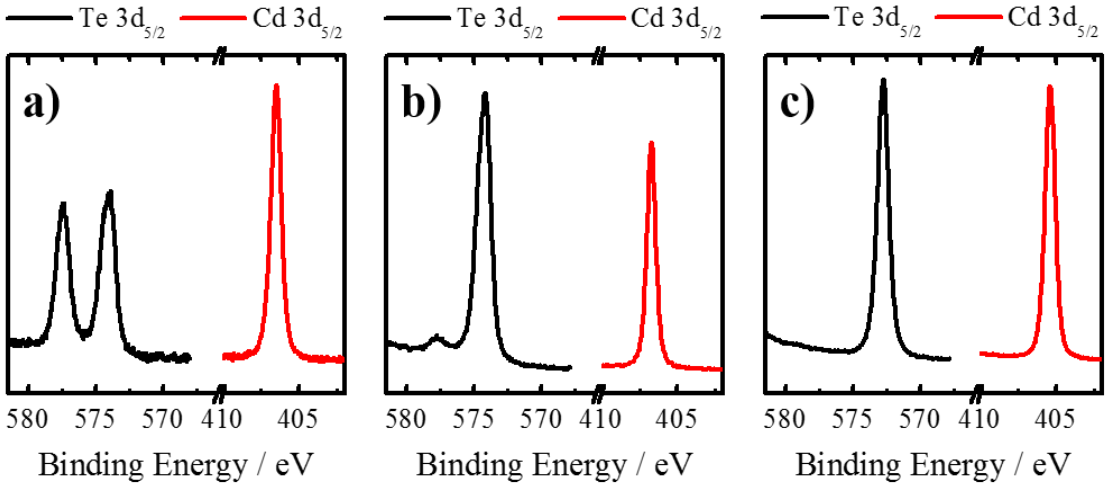

Figure S3. High-resolution X-ray photoelectron spectra in the regions of the Te $3d_{5/2}$ and Cd $3d_{5/2}$ core levels of (a) as-delivered n-CdTe. (b) 1% Br_2/CH_3OH etched n-CdTe and (c) the same as (b) after 15 s of Ar^+ sputter-etching.

Preparation	Ratio Cd:Te
As-Delivered	.93
Etched	.75
Etched / 15 s Ar^+ Sputtered	1.07
Etched / 30 s Ar^+ Sputtered	1.16
Etched / 45 s Ar^+ Sputtered	1.16

Table S2. Te:Cd atomic ratio as determined by X-Ray photoelectron spectroscopy for an as-delivered n-CdTe, n-CdTe etched with 1 % Br_2/CH_3OH and n-CdTe etched with 1 % Br_2/CH_3OH and then sputter-etched with Ar^+ ions for 15 s, 30 s, or 45 s.

S4. Photoelectrochemical Stability of n-CdTe/Ni and n-CdTe/TiO_2/Ni Electrodes

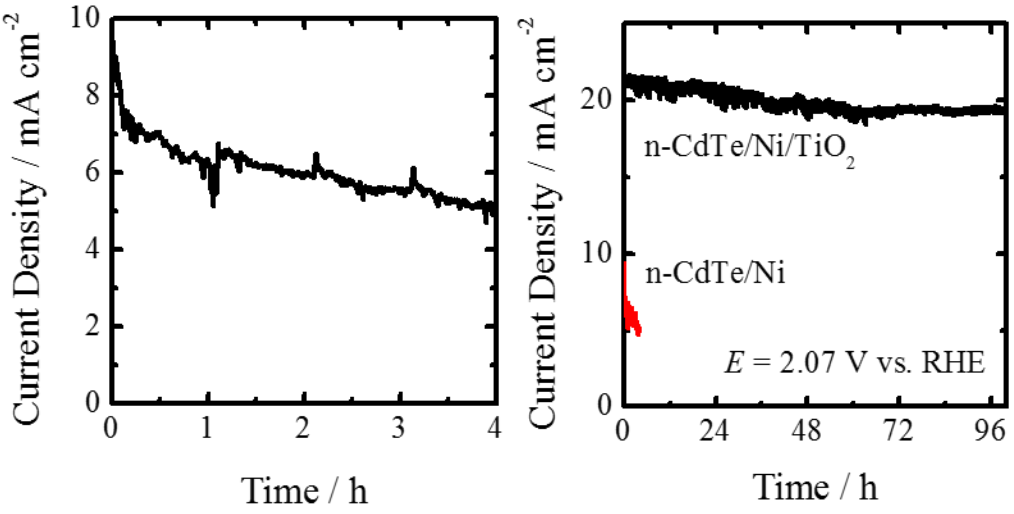

Figure S4. Current density as a function of time during potentiostatic electrolysis with an n-CdTe/Ni electrode (left) and plotted against data from an n-CdTe/TiO_2/Ni electrode under the same conditions at 2.07 V vs. RHE in pH = 14 KOH(aq) under illumination with a Xe arc lamp calibrated to 100 mW cm^{-2} of AM 1.5G illumination.

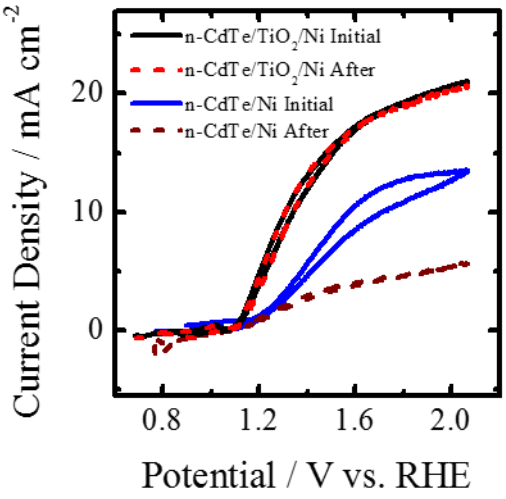

Figure S5. *J-E* data obtained with n-CdTe/Ni and n-CdTe/TiO_2/Ni electrodes, respectively, in pH = 14 KOH(aq) under illumination by a Xe arc lamp calibrated to 100

mW cm^{-2} of AM 1.5G illumination. *J-E* data were obtained before and after 4 h of potentiostatic electrolysis under illumination at 2.07 V vs. RHE.

REFERENCES.

1. Lichterman, M. F.; Carim, A. I.; McDowell, M. T.; Hu, S.; Gray, H. B.; Brunschwig, B. S.; Lewis, N. S., Stabilization of n-cadmium telluride photoanodes for water oxidation to O2(g) in aqueous alkaline electrolytes using amorphous TiO2 films formed by atomic-layer deposition. *Energy Environ. Sci.* **2014,** *7* (10), 3334-3337.
2. (a) Lincot, D.; Vedel, J., Surface modifications and recombination processes at the n-CdTe/electrolyte interface. *J. Cryst. Growth* **1985,** *72* (1–2), 426-431; (b) Curran, J. S., The Photocorrosion of N-Cadmium Telluride and Its Suppression. *J. Electrochem. Soc.* **1980,** *127* (9), 2063-2067; (c) Mathew, X.; Enriquez, J. P.; Romeo, A.; Tiwari, A. N., CdTe/CdS solar cells on flexible substrates. *Sol. Energy* **2004,** *77* (6), 831-838; (d) Mandal, K. C.; Basu, S.; Bose, D. N., CdTe photoelectrochemical solar cells—chemical modification of surfaces. *Bull. Mater. Sci.* **1988,** *10* (4), 349-351; (e) Liu, D.; Zheng, Z.; Wang, C.; Yin, Y.; Liu, S.; Yang, B.; Jiang, Z., CdTe Quantum Dots Encapsulated ZnO Nanorods for Highly Efficient Photoelectrochemical Degradation of Phenols. *J. Phys. Chem. C* **2013,** *117* (50), 26529-26537; (f) Li, Q.; Yang, Y.; Sun, M.; Mu, Y.; Fu, W.; Yang, H.; Tian, L., Electrodeposition of a novel CdTe array on Ni foils and photoelectrochemical performance. *Cryst. Eng. Comm.* **2013,** *15* (35), 6911-6917.
3. (a) Kumar, S. G.; Rao, K. S. R. K., Physics and chemistry of CdTe/CdS thin film heterojunction photovoltaic devices: fundamental and critical aspects. *Energy Environ. Sci.* **2014,** *7* (1), 45-102; (b) Romeo, A.; Terheggen, M.; Abou-Ras, D.; Bätzner, D. L.; Haug, F. J.; Kälin, M.; Rudmann, D.; Tiwari, A. N., Development of thin-film Cu(In,Ga)Se2 and CdTe solar cells. *Prog. Photovoltaics Res. App.* **2004,** *12* (2-3), 93-111.
4. (a) Haussener, S.; Xiang, C.; Spurgeon, J. M.; Ardo, S.; Lewis, N. S.; Weber, A. Z., Modeling, simulation, and design criteria for photoelectrochemical water-splitting systems. *Energy Environ. Sci.* **2012,** *5* (12), 9922-9935; (b) Merle, G.; Wessling, M.; Nijmeijer, K., Anion exchange membranes for alkaline fuel cells: A review. *J. Membrane Sci.* **2011,** *377* (1–2), 1-35; (c) Hernandez-Pagan, E. A.; Vargas-Barbosa, N. M.; Wang, T.; Zhao, Y.; Smotkin, E. S.; Mallouk, T. E., Resistance and polarization losses in aqueous buffer-membrane electrolytes for water-splitting photoelectrochemical cells. *Energy Environ. Sci.* **2012,** *5* (6), 7582-7589.
5. (a) Hu, S.; Shaner, M. R.; Beardslee, J. A.; Lichterman, M. F.; Brunschwig, B. S.; Lewis, N. S., Amorphous TiO2 coatings stabilize Si, GaAs, and GaP photoanodes for efficient water oxidation. *Science* **2014,** *344* (6187), 1005-1009; (b) Walter, M. G.; Warren, E. L.; McKone, J. R.; Boettcher, S. W.; Mi, Q.; Santori, E. A.; Lewis, N. S., Solar Water Splitting Cells. *Chem. Rev.* **2010,** *110* (11), 6446-6473.
6. (a) Seger, B.; Tilley, D. S.; Pedersen, T.; Vesborg, P. C. K.; Hansen, O.; Gratzel, M.; Chorkendorff, I., Silicon protected with atomic layer deposited TiO2: durability studies of photocathodic H2 evolution. *RSC Adv.* **2013,** *3* (48), 25902-25907; (b) Strandwitz, N. C.; Comstock, D. J.; Grimm, R. L.; Nichols-Nielander, A. C.; Elam, J.; Lewis, N. S., Photoelectrochemical Behavior of n-type Si(100) Electrodes Coated with Thin Films of Manganese Oxide Grown by Atomic Layer Deposition. *J. Phys. Chem. C* **2013,** *117* (10), 4931-4936; (c) Sun, K.; Shen, S.; Cheung, J. S.; Pang, X.; Park, N.; Zhou, J.; Hu, Y.; Sun, Z.; Noh, S. Y.; Riley, C. T.; Yu, P. K. L.; Jin, S.; Wang, D., Si

photoanode protected by a metal modified ITO layer with ultrathin NiOx for solar water oxidation. *Phys. Chem. Chem. Phys.* **2014,** *16* (10), 4612-4625.
7. Shaner, M. R.; Fountaine, K. T.; Lewerenz, H.-J., Current-voltage characteristics of coupled photodiode-electrocatalyst devices. *Appl. Phys. Lett.* **2013,** *103* (14), 143905.
8. White, H. S.; Ricco, A. J.; Wrighton, M. S., Characterization of p-type cadmium telluride electrodes in acetonitrile/electrolyte solutions. Nearly ideal behavior from reductive surface pretreatments. *J. Phys. Chem.* **1983,** *87* (25), 5140-5150.
9. Tanaka, S.; Bruce, J. A.; Wrighton, M. S., Deliberate modification of the behavior of n-type cadmium telluride/electrolyte interfaces by surface etching. Removal of Fermi level pinning. *J. Phys. Chem.* **1981,** *85* (25), 3778-3787.
10. Lichterman, M. F.; Shaner, M. R.; Handler, S. G.; Brunschwig, B. S.; Gray, H. B.; Lewis, N. S.; Spurgeon, J. M., Enhanced Stability and Activity for Water Oxidation in Alkaline Media with Bismuth Vanadate Photoelectrodes Modified with a Cobalt Oxide Catalytic Layer Produced by Atomic Layer Deposition. *J. Phys. Chem. Lett.* **2013,** *4* (23), 4188-4191.

III. AP-XPS Investigation of Semiconductor-liquid junctions

III.1. Mechanism by which ALD-TiO_2 functions *via* metallization of the semiconductor/liquid interface: *operando* XPS studies

Originally published as "Direct observation of the energetics at a semiconductor/liquid junction by *operando* X-ray photoelectron spectroscopy" in Energy and Environmental Science.

Photoelectrochemical (PEC) cells based on semiconductor/liquid interfaces provide a method of converting solar energy to electricity or fuels. Currently, the understanding of semiconductor/liquid interfaces is inferred from experiments and models. *Operando* ambient-pressure X-ray photoelectron spectroscopy (AP-XPS) has been used herein to directly characterize the semiconductor/liquid junction at room temperature under real-time electrochemical control. X-ray synchrotron radiation in conjunction with AP-XPS has enabled simultaneous monitoring of the solid surface, the solid/electrolyte interface, and the bulk electrolyte of a PEC cell as a function of the applied potential, U. The observed shifts in binding energy with respect to the applied potential have directly revealed ohmic and rectifying junction behavior on metallized and semiconducting samples, respectively. Additionally, the non-linear response of the core-level binding energies to changes in the applied electrode potential has revealed the influence of defect-derived electronic states on the Galvani potential across the complete cell.

Broader Context

While much work has been devoted to the study of semiconductor/liquid junctions, the direct observation by XPS methods of the semiconductor/liquid junction under applied biases has not heretofore been explored. We demonstrate that the *operando* XPS technique applied to a semiconductor/liquid junction can directly measure the positions of the electronic states of the electrode and the electrolyte. The use of tender X-rays allows for the direct evaluation of the energetics for the electrode surface, the electrochemical double layer, and the adjacent bulk water. The data provide direct insight into the nature of the rectifying or ohmic junction in addition to allowing for the calculation of defect state densities and band bending in such photoelectrochemical half cells. All of these directly observed parameters are crucial variables for the design and operation of semiconductor/liquid junction devices.

Introduction

Electrochemical-solar energy conversion is based on the rectifying properties of semiconductor-electrolyte junctions. The fundamental concept of semiconductor/ electrolyte contacts was introduced by Gerischer in 1975 [1]. The theory was based on the relation of the Fermi energy E_F of a solid to the electrochemical potential of an electrolyte [2]. Gerischer drew an analogy between semiconductor/liquid contacts and a Schottky contact at semiconductor/metal interfaces [3-5]. At equilibrium the Fermi energy E_F of the semiconductor must equal $-e\bar{\mu}_e^S$ where $\bar{\mu}_e^S$ the electrochemical potential of the electron in solution and e is the absolute charge of an electron. This causes charge to flow between the semiconductor and the solution and produces a space-charge region in the semiconductor with an accompanying electric field. The electric field causes the energy of the electron levels to "bend" as they move through the field and shifts the relative

positions of the Fermi energy and the solution electrochemical potential. At the semiconductor/liquid junction, only a small fraction of the overall contact potential difference drops across the electrochemical double layer in solution [1,6,7]. The electrochemical potential of a phase given by $\bar{\mu} = \mu - e\varphi$, where μ is the chemical potential of the phase and φ is the electrostatic potential of the phase.

The band bending present in the semiconductor space-charge region drives the separation of electron/holes pairs and thus facilitates applications of these systems for photelectrochemical energy conversion. Accordingly, efficient and moderately stable photoelectrochemical energy-conversion systems were developed a few years after the introduction of the concepts outlined above [8,9]. Despite many investigations using surface science methods [10-13], however, direct measurements of the energetic relations at a semiconductor/electrolyte junction have not previously been obtained.

In this work, we present a method that allows, in an unprecedented manner, a direct analysis of the electronic properties of a semiconductor/electrolyte junction by applying photoelectron spectroscopy (PES) to semiconductor/electrolyte junctions under near-ambient-pressure conditions. Investigations using *ex situ* X-ray photoelectron spectroscopy (XPS) [14], photocurrent [15] and capacitance-voltage spectroscopy [16], spectral response [17], open-circuit photovoltage [18], Fermi-level pinning [19], system design [20], flat-band potential [21], physicochemical principles [22], and various surface-modification strategies [23-25] have been performed to characterize the behavior of various semiconductor/liquid junctions. These methods, however, do not allow the direct observation of the band energetics and surface chemistry that are of fundamental importance to the performance of such systems. Conventional XPS experiments typically are performed under ultra-high vacuum (UHV), and so cannot probe the behavior of the

semiconductor/liquid interface under the electrochemical potential control associated with an operating PEC cell. For example, frozen electrolytes in UHV [12] have been used to investigate a semiconductor/electrolyte junction and the chemistry therein, but potential control is not possible in such a configuration. The *operando* experiment allows the measurement of the kinetic energy of photoelectrons that are emitted from semiconductors in contact with thin water/electrolyte films. The tender X-ray range of 1.5 to 8 keV allows for a range of sampling depths. The use of 4 keV X-rays allows for monitoring each section of thin-layer structures because the inelastic mean free path, which depends on the photoelectron kinetic energy, is substantially larger than in soft X-ray PES.

X-ray photoelectron spectroscopy can determine the chemical composition and positions of the electronic states (energy-band relations) of a material. X-ray radiation incident on the sample creates photoelectrons with a kinetic energy E_K that depends on the binding energy E_B of the core level, the photon energy $h\nu$, and the work function ϕ of the material/analyzer. Due to the low inelastic mean-free path (IMFP) of photoelectrons in solids, XPS is surface-sensitive and typically has an information depth in the nanometer range [26]. Photoelectrons that are ejected by tender X-rays (1.5 keV to 8 keV) have IMFPs in the range of 4 to 10 nm (see Table S1). The core-level emission binding energy reflects a base binding energy E_B^0 [27] and a band-bending term ΔE_{BB}. The binding energy of the electrode is given by (see Figure 1):

$$E_{B,electrode} = h\nu - E_K = E^0_{B,electrode} + \Delta E_{BB}\,, \qquad (1)$$

where E_K is the kinetic energy of the emitted photoelectron with respect to the Fermi energy of the analyzer. All binding energies are measured with respect to the shared

Fermi energy of the analyzer and working electrode, as both share a common ground (E_F). In the experiment the electrolyte is at the applied potential *U*. Thus the binding energy of the photoelectrons originating from the electrolyte depends on the applied potential (Figure 1):

$$\mathrm{E_{B,electrolyte}}(U_{\mathrm{eff}}(U)) = \mathrm{h\nu} - \mathrm{E_K} - \mathrm{e}U_{\mathrm{eff}}(U) = \mathrm{E^0_{B,electrolyte}} + \Delta\mathrm{E_{BB}} - \mathrm{e}U_{\mathrm{eff}}(U)\ , \tag{2}$$

where *U* is measured relative to the reference electrode (in these experiments, Ag/AgCl). Under an applied potential, the binding energy of bulk water levels, $E_{B,electrolyte,}$ will shift with the applied potential *U*, i.e. positive bias will yield a lower binding energy and negative bias will yield a higher binding energy. With respect to the Fermi energy of the analyzer, the effective (observed) core-level shift under applied potential *U* depends on the difference between the energy of the reference electrode E^0_{REF} (4.64 eV vs. E_{VAC} [28]) and the electrochemical potential of the electron in solution, $\bar{\mu}_e^S$:

$$\mathrm{e}U_{\mathrm{eff}}(U) = \mathrm{e}U + \mathrm{E^0_{REF}} - \mathrm{e}\bar{\mu}_e^S. \tag{3}$$

Ambient-pressure X-ray photoelectron spectroscopy (AP-XPS) [29-31] has been used to investigate gas/solid and gas/liquid interface such as metal oxide formation [32], mechanisms of heterogeneous catalysis [33], oxygen reduction on fuel cell cathodes [34], and other systems [35,36]. Recent developments in AP-XPS allow for the use of liquid electrolytes at the surface of interest during operation, therefore closely approximating a conventional PEC cell [37]. We demonstrate herein the use of AP-XPS with *real-time control* of the electrochemical potential through a conductive liquid electrolyte on a PEC

system to investigate the chemical and electrochemical nature of a semiconductor/liquid junction.

A three-electrode photoelectrochemical cell using a ~ 13 nm thick meniscus thin-film electrolyte on the working electrode permitted electrochemical control (Fig. S2) of the solid/liquid interface. XPS analysis was performed at 20-27 mbar by using a differential pumping system in conjunction with a photoelectron analyzer as described elsewhere [37]. The resulting *operando* AP-XPS data were used to directly characterize the behavior of TiO_2/electrolyte and TiO_2/Ni/electrolyte interfaces that have recently been shown to enhance the stability of small band-gap photoanodes during solar-driven water oxidation to produce $O_2(g)$ [38]. The AP-XPS data have allowed experimental confirmation of key theoretical aspects of the behavior of semiconductor/liquid junctions, directly revealing the band energetics and interfacial electronic structures of such systems.

Experimental

Films of amorphous TiO_2 produced by atomic-layer deposition (ALD) [38] were prepared on degenerately boron-doped p-type silicon ("p^+-Si") substrates (see SI for details). The silicon provided a topologically flat, ohmic back contact and did not otherwise contribute to the results described herein. An ALD cycle consisted of a 0.1s pulse of tetrakis(dimethylamido)titanium (TDMAT) followed by a 15 s purge of N_2 at 20 sccm, followed by a 0.015 s pulse of water before another 15 s N_2 purge. For Ni-containing electrodes, Ni was deposited by RF sputtering for 20 s to 60 s with a sputtering power of 150 W.

Operando AP-XPS data were collected using a differential-pumping Scienta R4000 HiPP-2 system that allowed a pressure of 20-27 mbar inside the experimental chamber on beamline 9.3.1 at the Advanced Light Source, which was used to provide

Tender X-rays at 4 keV [37]. The pressure range used herein was bounded by an upper limit of photoelectron collection efficiency and detector/analyzer protection and by a lower limit given by the boiling point of water. The p^+-Si/TiO_2/(Ni) working electrode was grounded to the detector to equalize the Fermi energy of the detector with the back contact of the working electrode. Along with the working electrode, the Ag/AgCl reference and platinum foil counter electrodes were mounted and contacted to a three-axis manipulator (Fig. S2). The electrodes were 'dipped and pulled' into an electrolyte-filled beaker (1.0 M KOH) and were positioned in front of the XPS sampling cone while maintaining contact with the electrolyte. The XPS collection position was optimized to maximize signal detection for both the electrode and electrolyte, as previously reported in investigations of the solution/metal interface [37] and as described further in the Supporting Information. Although the data were obtained in a hanging meniscus "emersion" configuration, negligible steady-state faradaic current was passed at any potential in the experiments described herein. Hence, the working electrode was under potential control and comprised an isopotential surface, so the experimental method is appropriately designated as *operando*. The data were analyzed with CasaXPS and IgorPro. 1.0 M KOH(aq) provided a conductive and adhering thin-film electrolyte that enabled AP-XPS data to be collected while maintaining potential control of the electrode. In conjunction with AP-XPS data, current density vs. potential (*J*-*U*) data (Fig. S3) were collected on p^+-Si/TiO_2 and p^+-Si/TiO_2/Ni working electrodes in a conventional three-electrode potentiostatic configuration. Electrochemical *J*-*U* and impedance vs. potential data were recorded on SP-200 and SP-300 Bio-Logic potentiostats. The impedance data were fitted with a Randles equivalent circuit using EC-LAB software to extract the differential capacitance (C_d) vs. potential data of the interface.

Results

Figure 2 depicts the O 1s core-level spectra for a p^+-Si/TiO_2 electrode, in 0.2 V steps, for potentials between -1.4 V and +0.4 V vs. Ag/AgCl. The data show the shift in O 1s binding energies as a function of the electrode potential, *U,* for the oxygen in H_2O(g), H_2O(l), OH^- and TiO_2, respectively. Ti 2p core-level spectra are also shown at these same electrode potentials. Analogous data were also obtained for TiO_2-coated electrodes that additionally contained a film of Ni/NiO_x on the surface (Fig. S4). Figure 3 shows the change in peak position vs. potential for the O 1s and Ti 2p data for (a) a bare p^+-Si/TiO_2 electrode and (b) a p^+-Si/TiO_2/Ni electrode. Figures 4 and S5 summarize the band-edge positions and band-bending information on the semiconductor/liquid interface obtained from the data of Figure 3(a).

In addition to Mott-Schottky (C_d^{-2}-U) data, Figure 5 depicts the full width at half maximum (FWHM), as well as the higher and lower binding-energy half widths at half maximum ($HWHM^+$, $HWHM^-$), for the Ti $2p_{3/2}$ peak of a p^+-Si/TiO_2 electrode. The potential at which minimum peak width was observed (i.e., the expected flat-band potential) in the AP-XPS data, U_{fb} = -0.9 V vs. Ag/AgCl, was in excellent agreement with the flat-band potential extracted from the conventional, electrochemically based, Mott-Schottky analysis (Fig. 5b).

Discussion

Semiconductor/liquid junctions resemble semiconductor/metal (Schottky) junctions [39]. It is well accepted, but has not been directly shown, that an ideal semiconductor/liquid junction has band edges that are essentially fixed with respect to the electrochemical potential of contacting electrolytes when a Galvanic potential is applied between the semiconductor working electrode and a reference electrode in a

three-electrode cell. Ideally, the band edges are fixed at semiconductor/liquid interfaces, and the Galvani potential drops mostly across the space-charge region in the semiconductor, giving rise to "band bending". Hence, the rectifying behavior of semiconductor/liquid junctions share the same "band bending" origin as those in Schottky junctions, and semiconductor/liquid junctions have accordingly been exploited for photoelectrochemical solar-energy conversion and storage [40]. In the presence of surface or bulk electronic states that have energies in the band gap of the semiconductor, the Galvani potential should drop partially (or completely, depending on the density of the surface states) across the surface, partially (or completely) at bulk in-gap states, and/or across the semiconductor space-charge region. The partial (or complete) filling of defect states results in Fermi level pinning [19] at the occupation limit of the surface defects, and thus pinning of semiconductor band edges should in principle be observable using AP-XPS. Upon application of a potential to a semiconductor/liquid junction, several "band bending" conditions can thus be established: flat-band, accumulation, depletion with or without defect-state pinning, and strong inversion at increased positive potentials (for an n-type semiconductor). Except for the latter, all of these "band bending" conditions have been directly observed, characterized, and analyzed by *operando* AP-XPS in this work.

For a metal/liquid contact, the metal core level binding energies remain constant with respect to various applied potentials, i.e., flat-band conditions are maintained because metals cannot support electric fields in their bulk, and thus have a constant potential within the metal. Therefore, for metal/liquid interfaces, the Galvani potential drops across the electrolyte double layer (the Helmholtz layer). In contrast, the potential drop across the double layer is negligible for an ideal semiconductor/liquid junction. Such flat-band conditions may also be observed with a metallized semiconductor surface that

acts as a metal, wherein an ohmic electrical connection is established between the semiconductor and metal.

Although the aforementioned theory is generally accepted and used to design PEC devices [25,41], the PEC-AP-XPS experiments described herein have allowed a direct verification of the theoretically expected behavior for the semiconductor/liquid junctions under evaluation. The semiconductor core-level peaks in an ideal semiconductor/liquid junction should exhibit the same decrease in measured binding energies (notated E_B, with units of electron volts) with applied potential ($U_{Applied}$) as the liquid water O 1s peaks, with a slope of $\Delta = -1\ eV \cdot V^{-1}$. This behavior is expected because the band bending occurs exclusively in the semiconductor electrode; the electron analyzer and working electrode are grounded at the same Fermi level; and the binding energies of the core levels are always referenced to this equalized Fermi level (Fig. S2). In contrast, for a metal/liquid junction, the metal core levels are expected to maintain a constant binding energy with varying applied potentials, where the potential difference drops across the electrochemical double layer (ECDL). In both cases, the bulk liquid water (i.e., water outside the double layer) core levels should shift consistently with the applied potential because the electrochemical potential of bulk liquid water is constant with respect to the reference electrode.

As shown in Figure 3, on the p^+-Si/TiO_2 electrode, the liquid water O 1s peak shifted linearly with the applied potential, with a slope of $\Delta = -1\ eV \cdot V^{-1}$. This slope is expected when the contribution to the binding-energy shift is negligible from water within the electrochemical double layer. This condition is applicable to the conditions investigated herein, because the width of the double layer is ~ 1 nm in 1.0 M KOH(aq). The inelastic mean-free path (IMFP) for the O 1s electrons in water is ~ 10 nm at

E_K = 3466 eV (the average kinetic energy of the water O 1s photoelectron from a X-ray photon energy of 4 keV) [42]. Therefore, for a ~ 13 nm thick electrolyte film, the double layer is expected to make only a small contribution to the overall peak position. Extra-atomic relaxation or surface charging can be neglected as well (see SI for details).

In contrast to the behavior of the O 1s H_2O signal, the observed TiO_2 O 1s and Ti 2p core-level binding energies were not a monotonic function of the applied potential, *U*. For the TiO_2 electrode, the Ti 2p and TiO_2 O 1s peak binding energies did not shift linearly with potential over the entire potential range (Fig. 3(a)). At potentials, *U*, between -1.4 V and -1.0 V vs. Ag/AgCl (notated as U_1) and -0.6 V and -0.2 V vs. Ag/AgCl (notated as U_3), the binding energies of the Ti 2p and O 1s (TiO_2) core levels stayed nearly constant. Figure S6 shows a second set of data for a different set of samples, demonstrating the reproducibility of the relative peak shifts with respect to the applied potential *U*.

As illustrated in Figure 4a, in region U_1 the Fermi level potential is shifted negative of the conduction band edge position. This behavior results in the formation of an accumulation layer in which semiconductor surface conduction-band states are being filled with electrons, resulting in a high surface concentration of electrons. Therefore, further band bending downwards is inhibited, and the Fermi level is "pinned" at the position of the TiO_2 conduction band minimum. For $U < -1$ V vs. Ag/AgCl, the accumulation layer causes a shift of the band edges with the applied potential in the same fashion as that expected for a metal/liquid junction. Instead of a potential drop due to band bending in TiO_2, under such conditions, the potential drops across the double layer. Given that the conduction-band edge is located close to -1 V vs. Ag/AgCl, the constant binding energies observed for $U < -1.0$ V vs. Ag/AgCl are in excellent agreement with the

Mott-Schottky analysis as well as with prior electrochemical data for n-TiO_2 photoelectrodes [43].

The core-level binding energy was also not sensitive to the applied potential in the range -0.6 to -0.2 V (U_3) (see Fig. 4). This potential range is located energetically between the conduction band and the middle of the band gap. This insensitivity to applied potential is attributed to charging and discharging of TiO_2 defect states and is explained by Fermi level pinning [19]. As illustrated in Figure 4c, when the applied voltage places the Fermi energy across the defect state region, the charging and discharging of the defect states lead to the voltage dropping at the defect states instead of producing additional band bending in the semiconductor. As shown in *ex situ* UHV-XPS data depicted in Figure S7, these defect states exist at energies 1.8-2.8 eV above the top of the TiO_2 valence band. This energetic location corresponds to a potential range of -0.7 to +0.3 V vs. Ag/AgCl, which spans the energy range within which the binding energy insensitivity was observed by *operando* AP-XPS. The observed behavior is thus in excellent agreement with separate, prior photoelectrochemical and photoelectron spectroscopy measurements [10,44]. Beyond a sufficiently positive applied voltage, 0 V vs. Ag/AgCl, the defect states are sufficiently discharged to allow for a return to nearly ideal semiconductor/liquid junction behavior, as shown in Figure 4c.

Sputter deposition of Ni makes the TiO_2 films anodically conductive, such that the TiO_2/Ni combination may be used for photoanode protection [38]. As shown in Figures 4 and S4, the addition of Ni substantially altered the potential response observed in the AP-XPS data. Specifically, the binding energies of the TiO_2 core levels became almost independent with respect to the electrolyte, i.e., the Fermi level of the TiO_2 was pinned by the Ni layer. Ni will quickly react under oxidizing conditions to form a nickel oxide but,

once formed, NiO_x is stable under our operating conditions, per the Pourbaix diagram for Ni. As indicated by Figure 3b, the addition of Ni allows for the ALD-TiO_2 to maintain a band structure much closer to flat-band across the entire potential range examined herein, thus removing a large voltage barrier to conduction. Effectively, the electrical connection between the surface of the Ni-deposited TiO_2 and the solution converts the electrical behavior of the solid/liquid junction from rectifying to ohmic. This behavior appeared to be generally true across the TiO_2/Ni electrode, as evidenced by the uniform coverage of Ni on the electrode (Fig. S8), as opposed to a mechanism involving localized islands or pinholes leading to charge conduction. These observations are relevant to elucidating the anodic conduction mechanism observed previously in amorphous TiO_2/Ni films and the importance of the Ni contact. The addition of Ni removes a rectifying barrier from the TiO_2/solution interface which would otherwise block charge conduction. [38] As was shown for the p^+-Si/TiO_2 electrodes, these results were similarly reproduced, as shown in Figure S6.

One measure with which to prove the validity of the AP-XPS approach is to derive electrochemical parameters directly from the XPS data and then to compare these values to independent measurements of the same quantities. When substantial band bending is present, the XPS sampling depth will collect photoelectrons across a range of binding energies. Hence, for a semiconductor capable of supporting a space-charge region, a broader XPS peak is expected for potentials at which band bending is maximized, and a narrower XPS peak should be observed for potentials close to flat-band conditions (see SI for details). Therefore, the flat-band potential (U_{fb}) of the semiconductor can be obtained solely from *operando* AP-XPS measurements, without the use of Mott-Schottky[45] analysis. Based on this approach, the flat-band potential observed by AP-XPS coincides

with the minimum of the FWHM and HWHM data. The Mott-Schottky data yielded U_{fb} = -0.9 V vs. Ag/AgCl, agreeing well with other investigations for n-type TiO_2 [43]. The FWHM and HWHM data from the AP-XPS analysis exhibited a minimum near -0.9 V vs. Ag/AgCl (Fig. 5), demonstrating that *semiconductor electrochemistry data can be derived directly from operando AP-XPS data*, without the need for an equivalent-circuit based model, which is required to analyze the interfacial impedance data. The HWHM and FWHM data accurately describe this system as defined by Mott-Schottky analysis, and demonstrate the internal consistency between the different parts of the data reported herein. As shown in Figure S9, for a metallized system that effectively appears ohmic, no clear dependence was observed between the Ti $2p_{3/2}$ FWHM and the applied voltage. A further description of the analysis of these data is contained in the Supporting Information.

In conjunction with a model based on metal-oxide-semiconductor (MOS) solar cells [46,47], we show that the AP-XPS data allow us to derive an equation that quantifies the density of electrochemically active defect states in a semiconductor/liquid junction. In the mid-gap potential region where a deviation from the ideal core-level binding-energy shift for TiO_2 of Δ = -1 eV·V^{-1} was observed, defect states are associated with the voltage drop that is not observed across the semiconductor. Hence, the lack of change in the binding energies of the core levels of the semiconductor, relative to the expected 1:1 shift in binding energy with the applied voltage, can be used to measure the defect-state density by equation (4):

$$N_{DS}(U) = -\frac{C_A}{e} \cdot \frac{\partial(|E_{B,SC}(U) - E_{B,Ref}(U)|e^{-1})}{\partial(eU)}, \qquad (4)$$

where $N_{DS}(U)$ is the density of electrochemically active in-gap defect states (units: states $eV^{-1} \cdot cm^{-2}$), $E_{B,SC}(U)$ is the semiconductor core-level binding energy at the applied potential U, $E_{B,Ref}(U)$ is a reference binding energy (bulk water) that scales with the applied voltage, C_A is the average differential capacitance per square centimeter at the potential of interest, U is the potential of interest, and e is the unsigned charge on an electron. The term $|E_{B,SC}(U) - E_{B,Ref}(U)| \cdot e^{-1}$ is the derivation of voltage drop in the electrochemical double layer from the core-level data. The surface-state density for the bare TiO_2 electrode, calculated from equation (4) from *operando* AP-XPS and from the capacitance data, are presented in Figure S10. Integrating over the in-gap defect states yields a density of 2.3×10^{13} cm^{-2} (which is equal to 1.1×10^{20} cm^{-3}). The data show excellent agreement with the *ex situ* XPS data displayed in Figure S7, in which the defect states were observed at 1.8-2.8 eV above the valence band. These results demonstrate that the AP-XPS approach is capable of providing an accurate measure of the electrochemically active defect states in charging or discharging to modify the band alignment at the semiconductor/liquid interface.

Conclusions

The *operando* photoelectron spectroscopic investigation of a photoelectrochemical cell has been demonstrated and applied to describe the operational characteristics of important semiconductor/liquid junctions. Tender X-ray analysis enables the investigation of the semiconductor surface, the electrolyte double layer and the bulk water layer, while maintaining electrochemical control over the entire system. Moreover, the potential range over which data could be collected extended beyond the thermodynamic limits for the oxidation or reduction of water. Semiconductor accumulation, depletion and Fermi level pinning by defect states were directly quantified by Tender X-ray AP-XPS, in addition to ohmic and/or rectifying behavior depending on the behavior of metallized semiconductor/film contacts. Further use of the tender AP-XPS method will enable a detailed, direct understanding of the behavior of other important semiconductors, metals, and composite semiconductor-electrocatalyst systems for water photolysis and (light-induced) carbon dioxide reduction.

Acknowledgements

This work was supported through the Office of Science of the U.S. Department of Energy (DOE) under award no. DE-SC0004993 to the Joint Center for Artificial Photosynthesis, a DOE Energy Innovation Hub. The Advanced Light Source is supported by the Director, Office of Science, Office of Basic Energy Sciences, of the U.S. Department of Energy under Contract No. DE-AC02-05CH11231.We acknowledge Dr. Philip Ross for his contributions to the conceptual development of the AP-XPS endstation and experimental design, and Junko Yano for fruitful discussions. We acknowledge Fadl Saadi, Beomgyun Jeong, and Sana Rani for assistance during data collection at the beamline.

Author Contributions

MFL, SH, and MHR contributed to the design, execution, and analysis of the experiment; EJC was critical in the design, building and testing of the end station that allows atmospheric pressure XPS data collection on a solution under potentiostatic control. SA contributed to design of the end station; MF and WD contributed to data collection; ZH provided direction and funding for the end station; TM, BSB, NSL, ZL, and H-JL advised on the undertaking and analysis of the experiment.

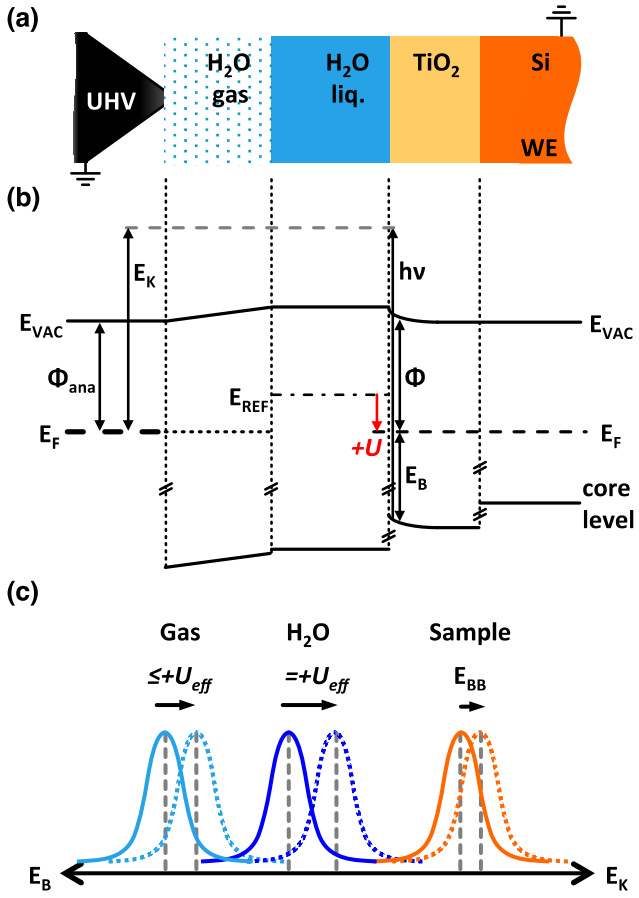

Figure 1: (a) Scheme of the principal arrangement of p^+-Si/TiO_2/H_2O(liq.)/H_2O(gas) to the analyzer front cone. (b) The energy band relations of the p^+-Si/TiO_2/H_2O(liq.)/H_2O(gas) system under applied potential U. The working electrode (Si) and analyzer are grounded and all the kinetic energies of the emitted photoelectrons are referenced to the Fermi energy of the analyzer. In the three-electrode configuration the Fermi energy is shifted by U with respect to the reference electrode. (c) The core level emission under applied potential (dashed curves) with respect to the core level emission under open circuit (solid line). The effective potential U_{eff} is given by $\mathrm{e}U_{\mathrm{eff}}(U) = \mathrm{e}U + \mathrm{E}^0_{\mathrm{REF}} - \mathrm{e}\bar{\mu}^S_e$.

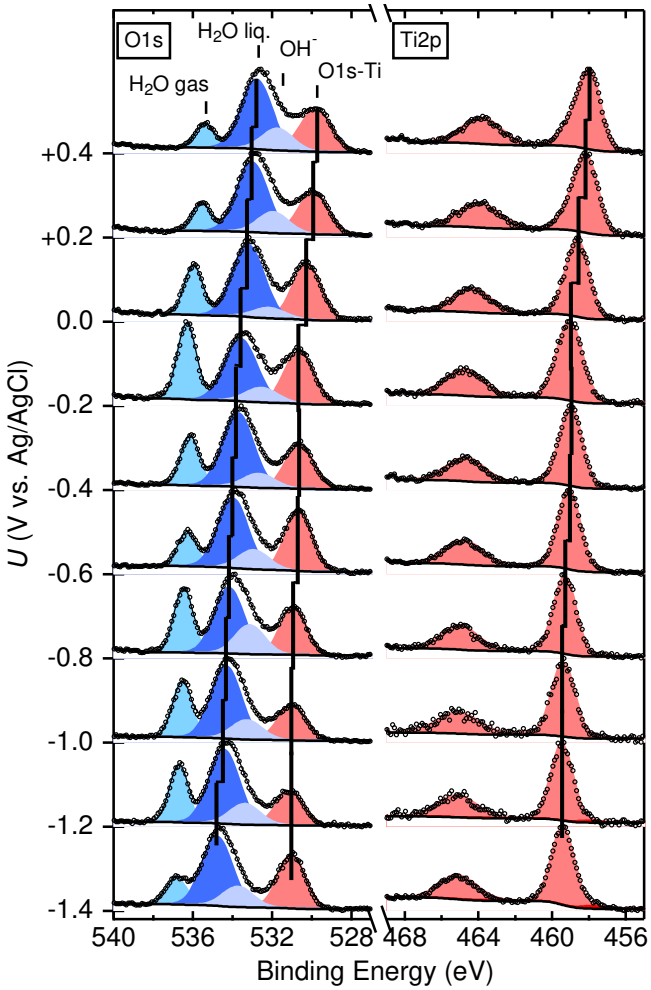

Figure 2: Raw AP-XPS data and fitted peaks for the O 1s and Ti 2p peaks at potentials between +0.4 V and -1.4 V vs. Ag/AgCl for a bare p^+-Si/TiO_2 electrode. Peaks for H_2O gas, H_2O liquid, OH^-, and TiO_2 – O 1s are shown; the center of each peak position for the liquid water, TiO_2 O 1s, and Ti 2p peaks at each potential has been marked with a black line.

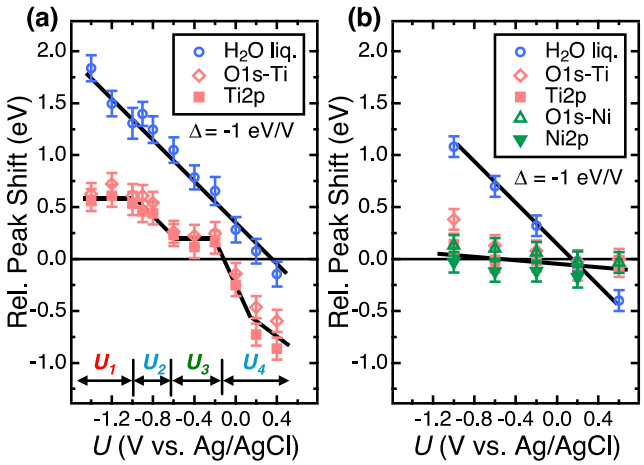

Figure 3: (a) AP-XPS peak positions of O 1s and Ti $2p_{3/2}$ signals for liquid water and TiO_2 as a function of the potential, U, of a bare p^+-Si/TiO_2 electrode in 1.0 M KOH(aq). Different potential regions U_1 to U_4 are shown. A solid line corresponding to a slope of $\Delta = -1$ eV·V^{-1} has been drawn through the water O 1s data; a solid line drawn as a visual guide is shown for the titania data. (b) Analogous AP-XPS peak positions vs. electrode potential for a p^+-Si/TiO_2/Ni (deposited by 60 s of Ni sputtering) interface.

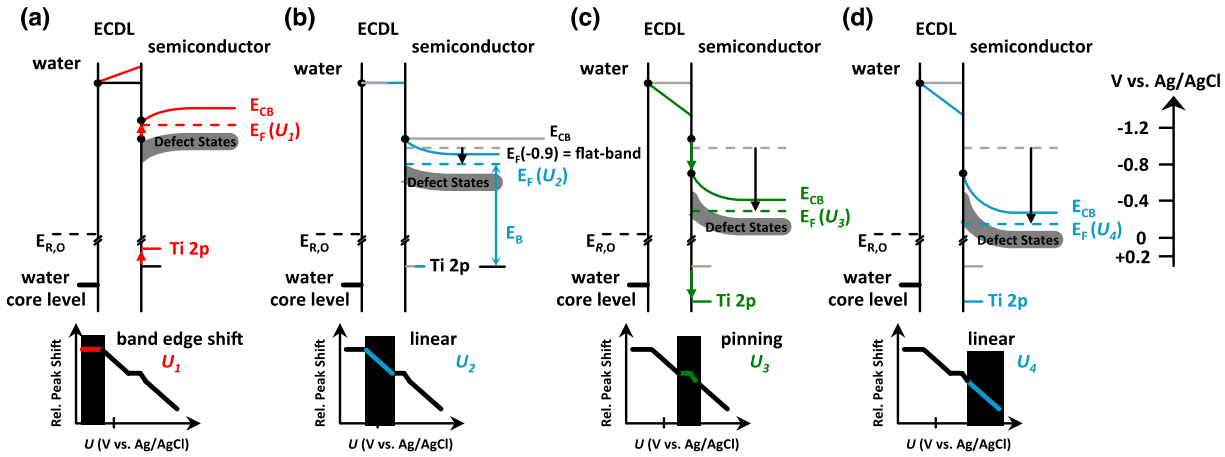

Figure 4: Schematic energy diagram of the TiO_2/liquid junction. (a): For highly negative bias (U_1 region, red lines), band shifting in the TiO_2 is observed (<-1.2 V). (b): In the ideal semiconductor region U_2, from -0.9 V to -0.6 V (blue lines), band bending in the TiO_2 is observed (compare to Fig. 3) with no further potential drop in the electrochemical double layer. (c): For increased positive biased (U_3 region, green lines), the Fermi level is pinned to the defect states, and the TiO_2 bands shift with the complete potential drop that occurs in the electrochemical double layer. (d): At potentials positive of -0.2 V (region U_4), ideal behavior is once again observed. In all cases, the shift in water O 1s binding energy is linear with the applied voltage. The Ti 2p binding energy shifts linearly for band bending regimes (U_2 and U_4) and remains constant for the band shifting regimes (U_1 and U_3).

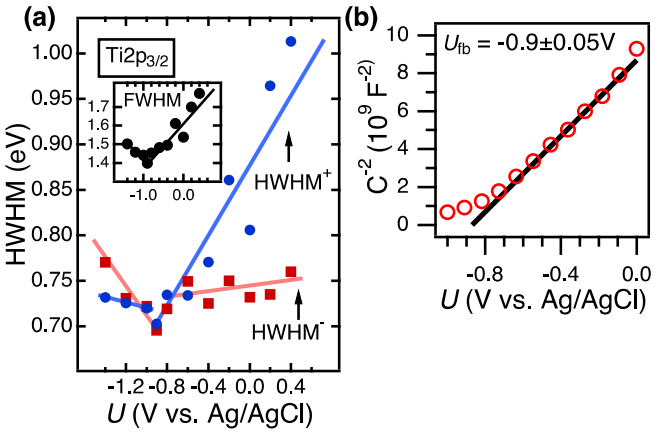

Figure 5: (a) High and low energy half widths at half maximum ($HWHM^+$, $HWHM^-$) for the Ti $2p_{3/2}$ peak of a p^+-Si/TiO_2 electrode as a function of applied potential. The higher binding-energy half width, $HWHM^+$, is shown in blue and the lower binding-energy half width, $HWHM^-$, in red. The inset depicts the overall full width at half maximum (FWHM = $HWHM^+$ + $HWHM^-$) as a function of applied potential. The blue, red, and black lines are guide-lines for the eye. Error bars are ~ ±0.1 eV for the half widths; while the error bars are considerably larger than the trends at negative potentials, the data confirms that the width of the peak increases with an absolute value of U as expected from theoretical simulation. (b) Mott-Schottky data for a p^+-Si/TiO_2 electrode, with U_{fb} calculated as -0.9 V vs. Ag/AgCl from a linear fit; a Randles circuit was used as the equivalent circuit.

Supporting Information:

Electrolyte Choice

At room temperature and pressure, water requires 1.23 V, plus catalytic overpotentials to produce 1 atm of hydrogen and oxygen gas. The overpotential at ~ 10 $mA \cdot cm^{-2}$ for the OER is ~ 200–300 mV and is for the HER ~ 5–200 mV with a good catalyst. Thus the electrochemical window for water splitting is ~ 1.4 V to 1.7 V. The potential window is still further increased for a poor catalyst and/or a substantial resistive element in the cell. For example, as TiO_2 is a poor OER catalyst, the usable potential range is substantially increased. While a lower pressure of oxygen and/or hydrogen will slightly lower (by ~ 100 mV) the potential required, the potential window is substantially larger than 1.23 V.

Although aqueous KOH is highly corrosive, the Pourbaix diagram for titanium has a large region in which TiO_2 thermodynamically (and also kinetically) is the stable phase over a pH region from 0 to 14 and a potential range that spans the limits of water splitting (and beyond). Thus, a TiO_2 electrode is stable in contact with 1 M KOH at the potentials used here. Under an oxidizing potential the nickel will convert to a nickel oxide, NiO_x, which is also Pourbaix stable in 1 M KOH.

Experimental

Electrodes of TiO_2, deposited by ALD as has been described recently [1], were prepared on degenerately boron-doped p-type silicon ("p^+-Si") substrates. Silicon wafers were cleaned with RCA SC-1 by soaking in a 3:1 (by volume) solution of concentrated H_2SO_4 to 30% H_2O_2 for 2 min before etching for 10 s in a 10% (by volume) solution of hydrofluoric acid. The wafers were then etched with RCA SC-2 procedure of soaking in a

5:1:1 (by volume) solution of H_2O, 36% hydrochloric acid, and 30% hydrogen peroxide for 10 min at 75°C. Directly after the cleaning procedure, TiO_2 was deposited by ALD from a tetrakis(dimethylamido)titanium (TDMAT) precursor. A 0.1 s pulse of TDMAT was followed by 15 s purge of N_2 at 20 sccm, following by a 0.015 s pulse of H_2O before another 15 s purge with N_2. This process was repeated for 1500 cycles. Samples requiring Ni were loaded into a RF sputtering system. Ni was deposited at a RF sputtering power of 150 W for 20 s to 60 s. Atomic-force microscopy (AFM) images (Fig. S8) attested to the smoothness of these films.

To prepare electrodes for *operando* XPS investigation, strips of the p^+-Si/TiO_2/(Ni) wafers were cut to 1 cm x 3.5 cm. An In/Ga eutectic was scribed into the back of the Si wafer, followed by Ag paint. The electrode was then was contacted by a strip of Cu tape supported on a 0.8 cm x 3 cm glass slide. The entire assembly was enclosed with non-conductive epoxy (Hysol 9460) to ensure that there no contact of the In/Ga, silver paint, copper tape, or Si electrode back and edges by the electrolyte during the AP-XPS measurements.

To perform the *operando* AP-XPS measurements, the p^+-Si/TiO_2/(Ni) electrode was mounted and contacted by a three-axis manipulator onto which the Ag/AgCl reference electrode (eDAQ) and a platinum foil counter electrode were also mounted and separately contacted (Fig. S2). The manipulator movements were computer controlled, allowing for manipulation of the sample position and the optimization of data collection, with a spatial resolution of ±10 μm. A PEC-beaker positioned below the three-electrode setup was filled with the electrolyte (1.0 M KOH) and raised or lowered as necessary, and was generally held as close to the XPS sampling cone as possible. To maintain the water-

vapor pressure and to prevent the rapid evaporation of water from the PEC-beaker, a second, larger beaker, filled with sacrificial 18.2 MΩ cm resistivity water, was positioned next to the PEC-beaker (see Fig. S2). The working, reference, and counter electrode clips from a Biologic SP-300 potentiostat were connected to their respective external connection clips on the stage. The working electrode was also grounded to the detector of the UHV surface analysis system, to equalize the Fermi energy of the detector with the back contact of the working electrode.

To collect data, the sample was "dipped" into the electrolyte before a potential was set. The electrode was then raised to such a height that a thin film of the electrolyte (~ 13 nm) was present at the XPS sampling location. The signal at the detector was maximized by manipulation of the sample position, and locations were chosen at which both the H_2O and TiO_2 signals were clearly resolved in the O 1s core level during snapshot mode operation of the detector. This process ensured sufficient electrolyte coverage, necessary for the control of electric potential, while allowing for the collection of data from the underlying electrode.

AP-XPS data were collected on a Scienta R4000 HiPP-2 system in which the photoelectron collection cone was aligned to the beamline X-ray spot at a distance of ~ 300 μm^2. The system used differential pumping supplied by four turbo pumps, backed by liquid-nitrogen trap protected rough pumps, to maintain a pressure of ~ 5 x 10^{-7} mbar at the detector while allowing a stable pressure of 20-27 mbar at the sampling position. The pressure range used herein was bounded by an upper limit due to photoelectron collection efficiency and the pumping speed of the differential pumping system and by a lower limit given by the boiling point of water. Higher vapor pressures led to significantly

longer data collection times and a decrease in the signal to noise ratio. Beamline 9.3.1 at the Advanced Light Source was used to provide Tender X-rays at 4 keV of energy out of a possible photon energy range of 2.3-5.2 keV with a resolving power of $E/\Delta E$ = 3000-7200. Photoelectrons for Ti 2p, O 1s, and Ni 2p levels were therefore collected in kinetic energy ranges of 3538±8 eV, 3466±8 eV, and 3142±8 eV, respectively.

Table S1 lists the inelastic mean-free paths (IMFPs) through titania and water for photoelectrons at the above kinetic energies [3]. One critical aspect of this experiment is the significantly higher IMFP of photoelectrons through the water than through the titania, which effectively determines that the titania, and not the thickness of the water overlayer above it, will be the primary determinant affecting the sampling depth of the XPS experiment within the electrode. As the inelastic mean free path of a photoelectron that originates in the TiO_2 or Nickel /Nickel Oxide is substantially higher in water than in the solid, the effect of small variations in electrolyte layer thickness is small. The numbers provided for IMFP through water are likely somewhat underestimated due to the model used by the TPP2M calculation, as a recent publication suggests [4].

Consecutive iterative scans of the O 1s, Ti 2p, and Ni 2p core levels were performed individually at potentials between -1.4 V and +0.6 V vs. the Ag/AgCl reference. Potentials outside of this range (under HER or OER conditions) resulted in a dried out electrolyte layer, resulting in a loss of potential control; a thicker electrolyte layer, resulting in a loss of observation of data from the underlying electrode; or caused bubbles, which disrupted or destroyed the conductive electrolyte film and risked damaging the detector. After collection, the consecutive scans were averaged. The data presented herein were obtained from the summed data. Generally, relatively few scans

(~ 7) were needed for the O 1s spectra, whereas more scans were needed for robust detection and analysis of the Ti 2p (~ 21) signal. The Ni data required hours (>50 sweeps) to produce spectra with an acceptable signal-to-noise ratio. All of the AP-XPS data were fitted with CasaXPS and IgorPro.

Differential capacitance vs. potential data was recorded on SP-200 and SP-300 Bio-Logic potentiostats equipped with impedance spectroscopy. The impedance vs. potential data was fitted with Zfit to obtain the desired differential capacitance vs. potential data. A Randles circuit, which contains a resistor in series with a parallel resistor and capacitor as shown below, was used as the equivalent circuit model for the impedance data.

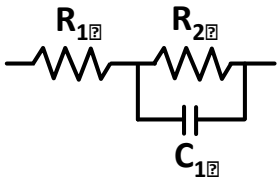

Charging and Extra Atomic Relaxation

In addition to the applied potential, a screening and surface charging effect could also affect the position of core levels, through extra atomic relaxation and surface charging of a compact oxide layer. For a structure in contact with solution, the latter can be neglected as photogenerated surface charges are neutralized. The former can be considered constant for a single compound and electrode geometry, as described in [5]. We can therefore discuss the findings in terms of energy-band relations.

Band Bending analysis and calculation

A narrow AP-XPS peak is expected near the flat-band potential (the Fermi level is 0.2 eV below the CB, see Fig. S7; the band gap for TiO_2 is 3.34 eV [1]) whereas a wider peak is expected at other applied potentials. This effect is due to integral nature of the summation of the core signals, and is observed provided that the space-charge region is of a size comparable to the escape depth, λ, of the created photoelectrons, i.e., $0.1<d_{SCR}/3\lambda<10$. Considering a doping concentration of ~ 2 x 10^{19} cm^{-3}, as obtained from Mott-Schottky analysis for $\varepsilon_r = 85$ (Fig. 5b), and a potential of U=1.0 V the width of the space charge region is in the order of the escape depth for Ti 2p with λ=56.86 Å, i.e., d_{SCR} = 30 nm and $d_{SCR}/3\lambda = 1.8$.

For such systems, equation (S1) describes the numerical evaluation of the core level emission line profile as a function of applied potential U, with the relative contribution of each subsequent band-bending depth layer to the overall XPS peak intensity. PF is the peak function of the corresponding core level (e.g., a Voigt profile), d is the sample thickness and $\xi(x, U)$ is the electrostatic potential as obtained by solving the Poisson equation using Fermi-Dirac statistics instead of the more simple Boltzmann statistics. The potential behavior of the core level emission line profile is then described by:

$$\mathrm{I}(U) = \int_0^{\mathrm{d}} \mathrm{e}^{\left(-\mathrm{x}/\lambda\right)} \cdot \mathrm{PF}\left(\xi(\mathrm{x}, U)\right) \partial \mathrm{x} \,. \qquad \text{(S1)}$$

Figure S11 depicts the numerical simulation of a core level under an increasingly positive potential. In conjunction with an expected core level shift to lower binding energies, a peak broadening on the higher binding-energy part of the core level is predicted for positive potentials, resulting in an asymmetric peak shape. From such

results, extraction of the flat-band potential (U_{fb}) of the semiconductor can be performed without the use of Mott-Schottky [6] analysis. Specifically, the flat-band potential should coincide with the minimum of the FWHM, e.g. $U_{BB}(x)=0$.

Additionally, an asymmetry in the Ti signal is expected, due to limited sampling of the dropping (for $U > U_{fb}$) or rising ($U < U_{fb}$) region of band bending associated with the integral exponential dependence of the core level intensity from the information depth (see Fig. S11). As can be seen from the relative contributions of the left (higher binding energy) and right (lower binding energy) sides of the peak, this asymmetry was observed experimentally, and agrees well with the Mott-Schottky data.

Table S1: Inelastic Mean-Free Path for elements under investigation for relevant photoelectron energies, as calculated by IMFP-TPP2M [3]. The following material parameters were used for water: 1 g·cm^{-3} bulk density; 6.9 eV band gap; 4 HBE (H 1s + O 2s); 4 LBE (O 2p).

Material	Photoelectron energy (eV)	Inelastic mean free path (Å)
TiO_2	3540	56.86
	3470	55.94
NiO	3540	47.25
	3470	46.49
	3145	42.92
Ni	3540	41.69
	3470	41.02
	3145	37.88
H_2O	3540	96.94
	3470	95.32
	3145	87.77

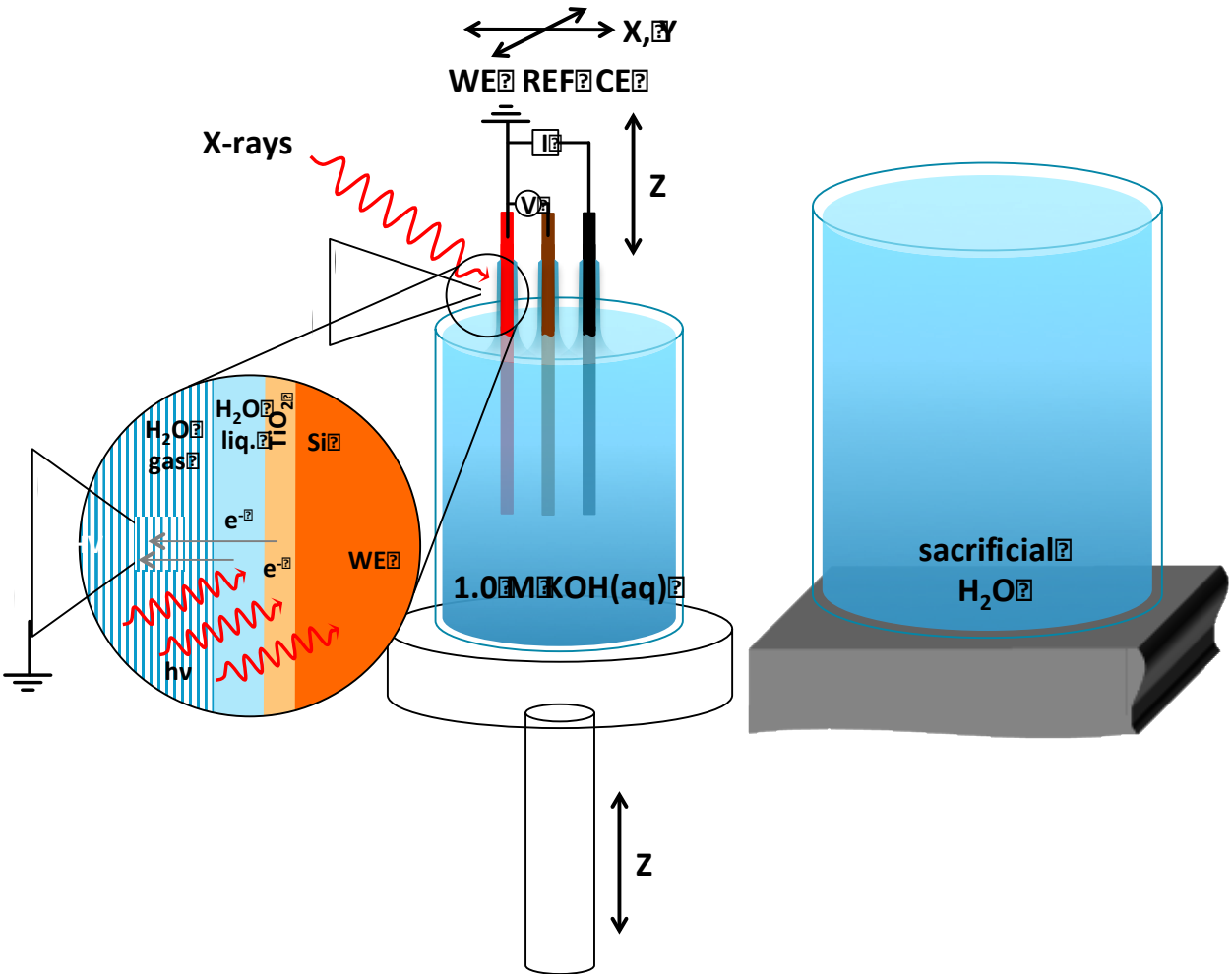

Figure S2: Scheme of the *operando* PES-PEC setup. The working electrode and analyzer were grounded to each other. The potential of the working electrode was changed with respect to the reference electrode. A second beaker filled with sacrificial millipore water was positioned in the analysis chamber next to the PEC-beaker to keep the water pressure constant and to counteract against increased water evaporation from the PEC-beaker. The PEC-beaker could be moved in the z-direction whereas the three-electrode mount could be moved in the x-, y-, and z-directions.

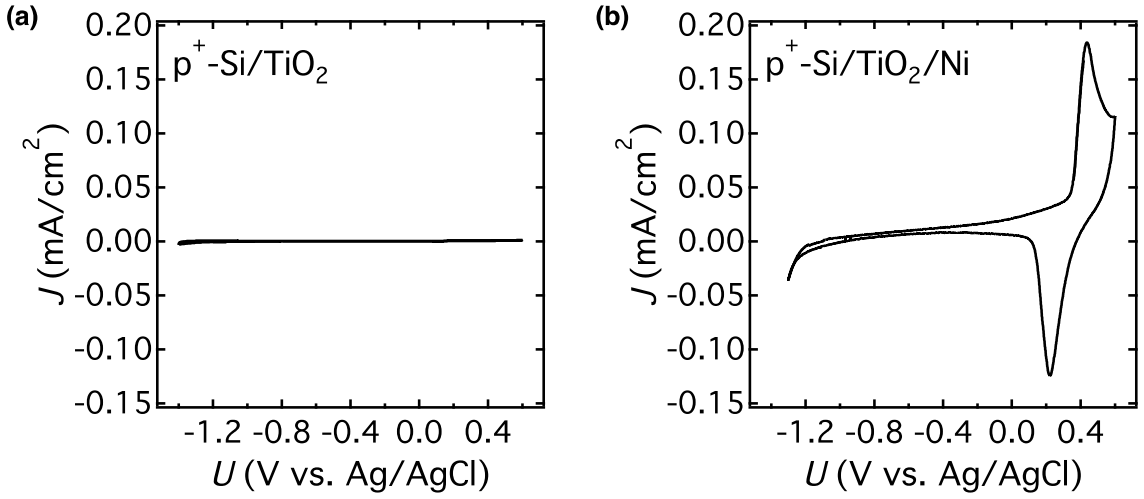

Figure S3: (a) Cyclic voltammetry (25 $mV \cdot s^{-1}$) of p^+-Si/TiO_2 and (b) p^+-Si/TiO_2/Ni electrodes in 1.0 M KOH(aq).

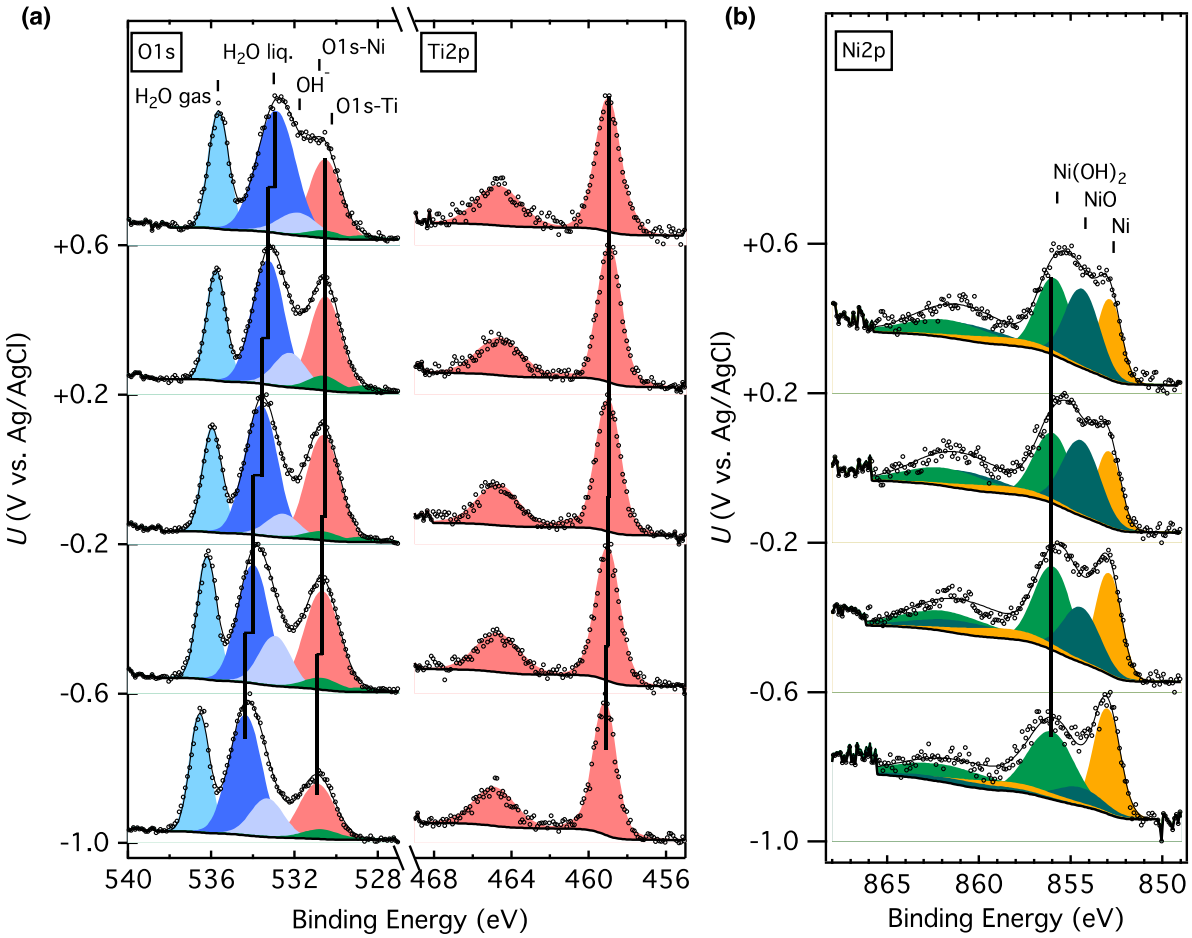

Figure S4: (a) Raw data and fitted peaks for the O 1s and Ti 2p peak from potentials ranging from +0.6V to −1.0V vs. Ag/AgCl for the bare TiO_2/Ni(sputter deposited for 60 s) electrode. Peaks for H_2O gas, H_2O liquid, OH^-, O 1s (TiO_2), O 1s (NiO/NiOH), and Ti 2p are shown; the center of each peak position for the liquid water, O 1s (TiO_2), and Ti 2p peaks at each potential has been marked with a black line. (b) The Ni 2p peaks for the same electrode and potentials, with a line marking the center of the $Ni(OH)_2$ Ni $2p_{3/2}$ peak at each potential.

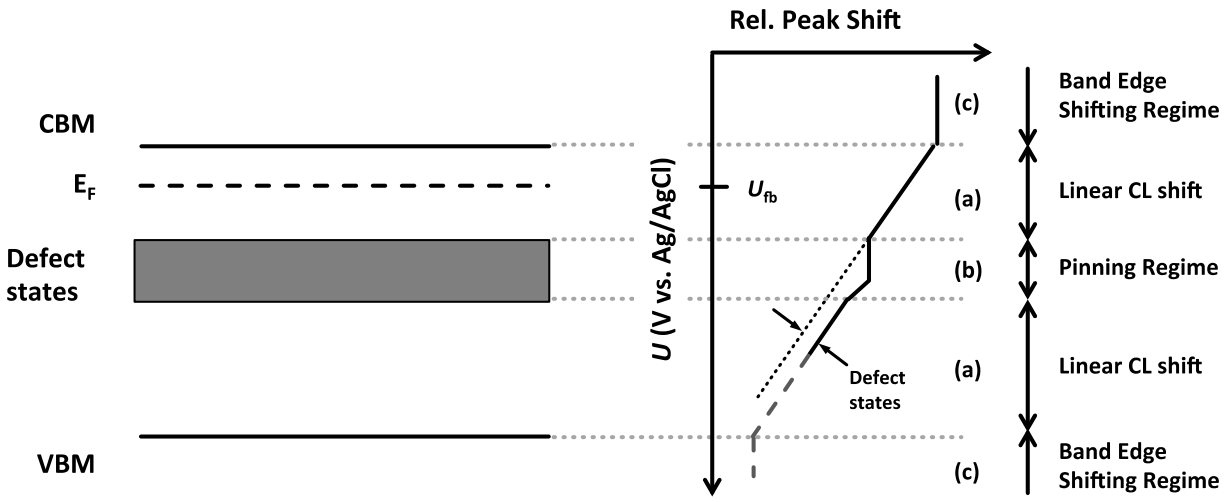

Figure S5: Ti 2p core-level (CL) binding-energy shift behavior as a function of the applied potential (not to scale). Three regimes are evident in the relative core-level shift as indicated by the arrows (compare to Fig. 3 and 4): linear CL shift (a); Fermi level pinning (b); and band edge shifting (c). The defects states induce a parallel shift between the linear core-level shift regimes (a).

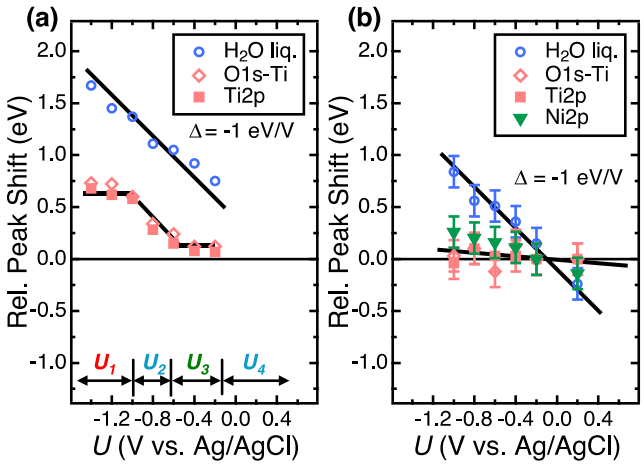

Figure S6: Reproduction of relative peak shifts depending on applied potential *U* for a second set of samples. (a) AP-XPS peak positions of O 1s and Ti $2p_{3/2}$ signals for liquid water and TiO_2 as a function of the potential, *U*, of a bare p^+-Si/TiO_2 electrode in 1.0 M KOH(aq). Different potential regions U_1 to U_4 are shown. A solid line corresponding to a slope of $\Delta = -1$ eV·V^{-1} has been drawn through the water O 1s data; a solid line drawn as a visual guide is shown for the titania data. (b) Analogous AP-XPS peak positions vs. electrode potential for a p^+-Si TiO_2/Ni (deposited by 20 s of Ni sputtering) interface.

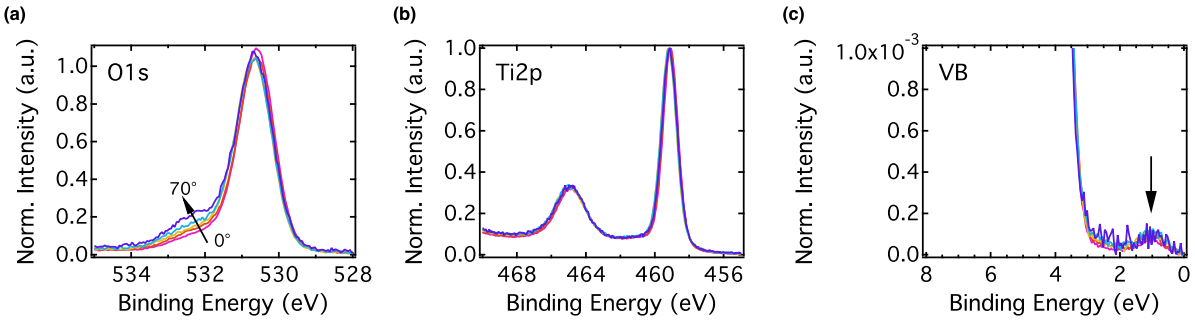

Figure S7: XPS spectra of the O 1s, Ti 2p core levels and of the valence band for different emission angles from θ=0° to θ=70° relative to the surface normal. With increased surface sensitivity (increased θ), an increase in the oxygen shoulder at 532.5 eV was observed, which is typical for the surface of several metal oxides [7] and can be attributed to dumbbell di-oxygen species, OH- groups, and/or to reconstruction of the TiO_2.

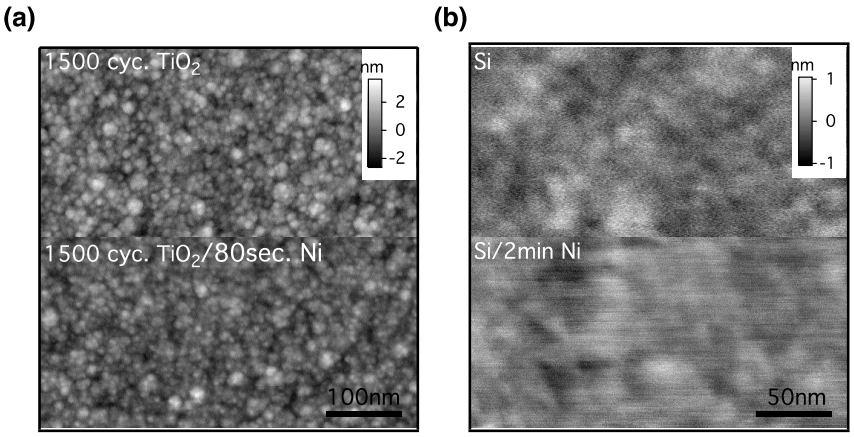

Figure S8: (a) Surface of bare ALD TiO_2 (top) and ALD TiO_2 covered by Ni deposited by 80 sec of RF sputtering (bottom). (b) Surface of bare Si (top) and Si covered by Ni deposited by 2 min of RF sputtering (bottom). Both AFM images indicate homogenous coverage by Ni. Statistical analysis of roughness, skewness, and kurtosis returned approximately equal values before and after nickel deposition.

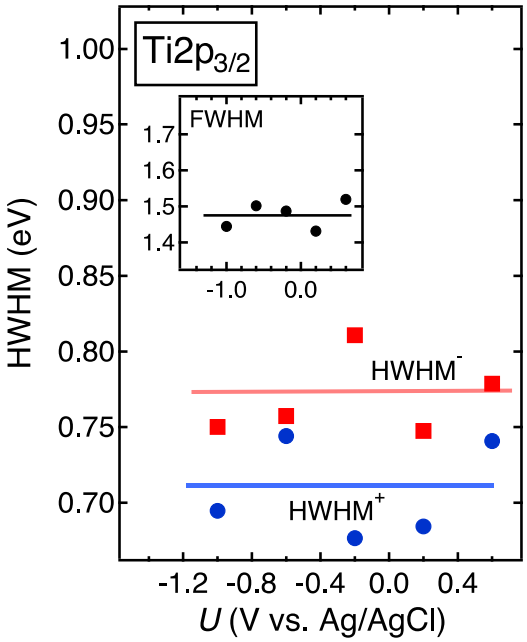

Figure S9: From the TiO_2/Ni(60 s of sputter deposition) data, the HWHM for the Ti $2p_{3/2}$ peak at each potential is plotted for the higher binding-energy side ($HWHM^+$, red symbols and line) and lower binding-energy side ($HWHM^-$, blue symbols and line) of the peak. The inset indicates the overall FWHM at each potential (FWHM = $HWHM^+$ + $HWHM^-$). Error bars are ~ ±0.1 eV for the half widths.

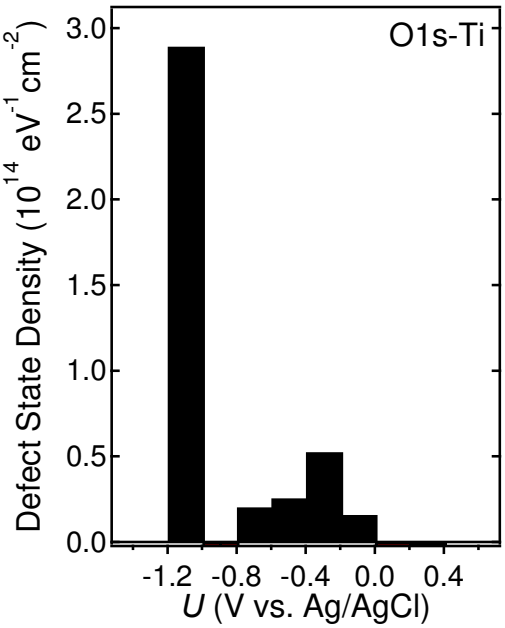

Figure S10: Surface-state density calculated by equation (4). Ti in-gap defect states are observed between –0.8 V and 0.0 V vs. Ag/AgCl.

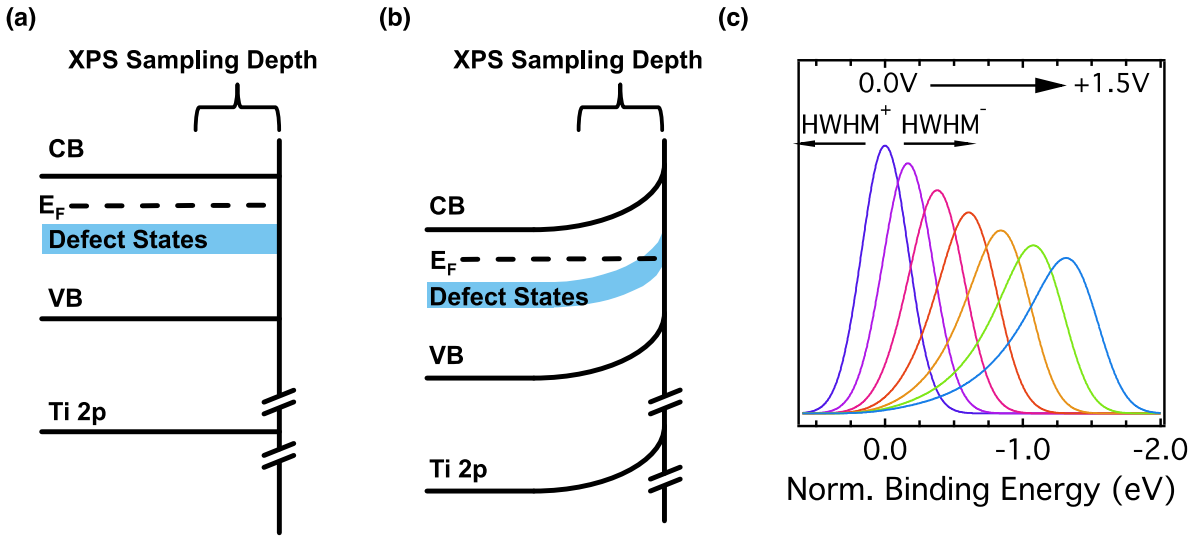

Figure S11: (a) A semiconductor at U_{fb}; (b) A semiconductor with the bands bent. In the case with band bending, a wider core-level peak is expected due to the contribution of photoelectrons across the range of energies samples by the photoelectron escape depth. A model of the peak width increasing with increasing band bending resulting from an applied potential from 0 to +1.5 V vs. U_{fb} is depicted in (c).

References

1. H. Gerischer, *Journal of Electroanalytical Chemistry and Interfacial Electrochemistry*, 1975, **58**, 263–274.
2. S. R. Morrison, *Electrochemistry at Semiconductor and Oxidized Metal Electrodes*, New York, 1st edn. 1980.
3. W. Schottky, *Z Phys*, 1939, **113**, 367–414.
4. W. Schottky, *Physikalische Zeitschrift*, 1940, **41**, 570–573.
5. W. Schottky, *Z Phys*, 1942, **118**, 539–592.
6. H. Gerischer, *Zeitschrift für Physikalische Chemie*, 1960, **26**, 223–247.
7. H. Gerischer, *Zeitschrift für Physikalische Chemie*, 1961, **27**, 48–79.
8. A. Heller, *Accounts Chem. Res.*, 1981, **14**, 154–162.
9. A. Heller, *Catalysis Reviews*, 1984, **26**, 655–681.
10. K. Schwanitz, E. Mankel, R. Hunger, T. Mayer, and W. Jaegermann, *CHIMIA*, 2007, **61**, 796–800.
11. M. Sander, W. Jaegermann, and H. J. Lewerenz, *J. Phys. Chem.*, 1992, **96**, 782–790.
12. T. Mayer, M. V. Lebedev, R. Hunger, and W. Jaegermann, *J. Phys. Chem. B*, 2006, **110**, 2293–2301.
13. T. Mayer, M. Lebedev, R. Hunger, and W. Jaegermann, *Appl. Surf. Sci.*, 2005, **252**, 31–42.
14. J. C. Bernède, S. Houari, D. Nguyen, P. Y. Jouan, A. Khelil, A. Mokrani, L. Cattin, and P. Predeep, *physica status solidi (a)*, 2012, **209**, 1291–1297.
15. A. Heller, K. C. Chang, and B. Miller, *J. Am. Chem. Soc.*, 1978, **100**, 684–688.
16. K. Kobayashi, Y. Aikawa, and M. Sukigara, *J. Appl. Phys.*, 1983, **54**, 2526–2532.
17. A. Heller, K. C. Chang, and B. Miller, *J. Electrochem. Soc.*, 1977, **124**, 697–700.
18. N. S. Lewis, *J. Electrochem. Soc.*, 1984, **131**, 2496–2503.
19. A. J. Bard, A. B. Bocarsly, F. R. F. Fan, E. G. Walton, and M. S. Wrighton, *J. Am. Chem. Soc.*, 1980, **102**, 3671–3677.
20. A. J. Bard, *J. Phys. Chem.*, 1982, **86**, 172–177.
21. P. Allongue and H. Cachet, *Solid State Commun*, 1985, **55**, 49–53.
22. A. J. Nozik and R. Memming, *J. Phys. Chem.*, 1996, **100**, 13061–13078.
23. B. Miller, A. Heller, S. Menezes, and H. J. Lewerenz, *Faraday Discuss. Chem. Soc.*, 1980, **70**, 223–232.
24. J. R. C. Lattimer, B. S. Brunschwig, N. S. Lewis, and H. B. Gray, *J. Phys. Chem. C*, 2013, **117**, 27012–27022.
25. M. G. Walter, E. L. Warren, J. R. McKone, S. W. Boettcher, Q. Mi, E. A. Santori, and N. S. Lewis, *Chem. Rev.*, 2010, **110**, 6446–6473.
26. M. P. Seah and W. A. Dench, *Surf. Interface Anal.*, 1979, **1**, 2–11.
27. J. F. Moulder, W. F. Stickle, P. E. Sobol, and K. D. Bomben, *Handbook of x-ray photoelectron spectroscopy*, 1995.
28. S. Trasatti, *Pure and Applied Chemistry*, 1986, **58**, 955–966.
29. M. Salmeron and R. Schlögl, *Surf. Sci. Rep.*, 2008, **63**, 169–199.
30. D. E. Starr, Z. Liu, M. Hävecker, A. Knop-Gericke, and H. Bluhm, *Chem. Soc. Rev.*, 2013, **42**, 5833–5857.
31. E. J. Crumlin, H. Bluhm, and Z. Liu, *J. Electron Spectrosc.*, 2013, **190**, 84–92.
32. A. Y. Klyushin, T. C. R. Rocha, M. Hävecker, A. Knop-Gericke, and R. Schlögl,

Phys. Chem. Chem. Phys., 2014, **16**, 7881–7886.
33. V. V. Kaichev, I. P. Prosvirin, and V. I. Bukhtiyarov, *J Struct Chem*, 2012, **52**, 90–101.
34. H. S. Casalongue, S. Kaya, V. Viswanathan, D. J. Miller, D. Friebel, H. A. Hansen, J. K. Nørskov, A. Nilsson, and H. Ogasawara, *Nat. Commun.*, 2013, **4**.
35. D. Zemlyanov, B. Aszalos-Kiss, E. Kleimenov, D. Teschner, S. Zafeiratos, M. Hävecker, A. Knop-Gericke, R. Schlögl, H. Gabasch, W. Unterberger, K. Hayek, and B. Klötzer, *Surf. Sci.*, 2006, **600**, 983–994.
36. Y.-C. Lu, E. J. Crumlin, G. M. Veith, J. R. Harding, E. Mutoro, L. Baggetto, N. J. Dudney, Z. Liu, and Y. Shao-Horn, *Sci. Rep.*, 2012, **2**, 715.
37. S. Axnanda, E. J. Crumlin, B. Mao, S. Rani, R. Chang, P. G. Karlsson, M. O. M. Edwards, M. Lundqvist, R. Moberg, P. Ross, Z. Hussain, and Z. Liu, *Sci. Rep.*, 2015, **5**, 9788.
38. S. Hu, M. R. Shaner, J. A. Beardslee, M. F. Lichterman, B. S. Brunschwig, and N. S. Lewis, *Science*, 2014, **344**, 1005–1009.
39. J. Tersoff, *Phys. Rev. Lett.*, 1984, **52**, 465–468.
40. P. V. Kamat, K. Tvrdy, D. R. Baker, and J. G. Radich, *Chem. Rev.*, 2010, **110**, 6664–6688.
41. M. X. Tan, P. E. Laibinis, S. T. Nguyen, J. M. Kesselman, C. E. Stanton, and N. S. Lewis, *Principles and Applications of Semiconductor Photoelectrochemistry*, John Wiley & Sons, Inc., Hoboken, NJ, USA, 1994, vol. 41.
42. D. Emfietzoglou and H. Nikjoo, *Radiation Research*, 2007, **167**, 110–120.
43. M. Radecka, M. Rekas, A. Trenczek-Zajac, and K. Zakrzewska, *J Power Sources*, 2008, **181**, 46–55.
44. Konrad Schwanitz, Ulrich Weiler, Ralf Hunger, A. Thomas Mayer, and W. Jaegermann, *J. Phys. Chem. C*, 2006, **111**, 849–854.
45. F. Fabregat-Santiago, G. Garcia-Belmonte, J. Bisquert, P. Bogdanoff, and A. Zaban, *J. Electrochem. Soc.*, 2003, **150**, E293–E298.
46. H. Kobayashi, T. Mori, K. Namba, and Y. Nakato, *Solid State Commun*, 1994, **92**, 249–254.
47. H. Kobayashi, Y. Yamashita, T. Mori, Y. Nakato, T. Komeda, and Y. Nishioka, *Jpn. J. Appl. Phys.*, 1995, **34**, 959–964.

III.2. An Electrochemical, Microtopographical and Ambient Pressure-X-ray Photoelectron Spectroscopic Investigation of $Si/TiO_2/Ni$/Electrolyte Interfaces

Originally published as "An Electrochemical, Microtopographical and Ambient Pressure-X-ray Photoelectron Spectroscopic Investigation of Si/TiO2/Ni/Electrolyte Interfaces" in the Journal of the Electrochemical Society.

The electrical and spectroscopic properties of the TiO_2/Ni protection layer system, which enables stabilization of otherwise corroding photoanodes, have been investigated in contact with electrolyte solutions by scanning-probe microscopy, electrochemistry, and *in-situ* ambient pressure X-ray photoelectron spectroscopy (AP-XPS). Specifically, the energy-band relations of the p^+-Si/ALD-TiO_2/Ni interface have been determined for a selected range of Ni thicknesses. AP-XPS measurements using tender X-rays were performed in a three-electrode electrochemical arrangement under potentiostatic control to obtain information from the semiconductor near-surface region, the electrochemical double layer (ECDL) and the electrolyte beyond the ECDL. The degree of conductivity depended on the chemical state of the Ni on the TiO_2 surface. At low loadings of Ni, the Ni was present primarily as an oxide layer and the samples were not conductive, although the TiO_2 XPS core levels nonetheless displayed behavior indicative of a metal-electrolyte junction. In contrast, as the Ni thickness increased, the Ni phase was primarily metallic and the electrochemical behavior became highly conductive, with the AP-XPS data indicative of a metal-electrolyte junction. Electrochemical and microtopographical methods have been employed to better define the nature of the TiO_2/Ni electrodes and to contextualize the AP-XPS results.

Introduction

Photoelectron spectroscopy can be used to directly characterize the energy relations of semiconductor/liquid junctions that underlie the operation of photoelectrochemical cells [1], provided that the kinetic energy of the emitted photoelectrons can elastically penetrate the water film on the electrode surface. Conventional X-ray photoelectron spectroscopy (XPS) experiments are performed in ultra-high vacuum (UHV) in the absence of electrolyte, and thus do not allow for electrochemical control of an operating device during collection of XPS data. Recent theoretical work has shown that the inclusion of structured solvation layers on electrodes can alter the surface dipole by 0.5 – 0.7 eV (1.9 – 2.1 eV) for IrO_2 (WO_3) [2]. Established *in-system* techniques that allow analyses of (photo)electrodes after electrochemical operation enable assessment of aspects of the surface chemistry and of the associated energetic behavior [3-5]. However, such experiments are limited in scope and interpretation due to the rinsing, drying, and outgassing procedures required prior to insertion of the sample into the UHV analysis chamber. In contrast, the use of tender X-rays having photon energies in the 2.3 – 5.2 keV energy range allows generation of photoelectrons that have a substantially increased inelastic mean free path. This approach allows "operando" XPS studies in conjunction with a classical three-electrode potentiostatic arrangement and also facilitates investigation of the influence of the applied potential on the band-edge energies of metal, semiconductor, and hybrid electrodes at such interfaces [6,7]. Band bending and band-edge shifts can thus be determined directly by this spectroscopic technique [7].

We describe herein surface-sensitive analysis techniques for the characterization of TiO_2/Ni/electrolyte interfaces. The protection and stabilization of photoanodes for water oxidation to $O_2(g)$ is of interest because high performance and stability can be achieved simultaneously by protecting a variety of otherwise unstable semiconductor photoanodes [8-11]. Specifically, TiO_2 has been used as a protection layer for photoelectrodes in either alkaline or acidic media [7,12-17]. Some work indicates that annealing the TiO_2 allows for charge conduction with minimal band bending, with unannealed TiO_2 preferred for photocathodes. However, the role of the metallization layer in determining the charge-conduction properties of the films has not been well elucidated [18]. A thin layer of TiO_2 can protect Si and allows for water oxidation with an Ir oxygen-evolution catalyst, but in such systems increases beyond 2 nm in the thickness of the TiO_2 film led to a substantial increase in resistance, such that a 10 nm film was nearly nonconductive even when contacted with Ir [11]. In contrast, TiO_2 has been found to be a nearly ideal protection layer from the viewpoint of the band-edge alignment when used on p-InP or p-Si photocathodes [19,20]. Thus, while the band positions of the TiO_2 films appear to be inherently conducive to photocathode protection, the nature of the TiO_2/(metal)/electrolyte contact requires further investigation. Specifically, when contacted with Ni metal, TiO_2 films allow for the sustained use of highly efficient semiconductor materials (Si, III-V, II-VI) for water splitting and in other oxidizing environments, especially in alkaline media where efficient, intrinsically safe solar-driven water-splitting systems can be built [12,13].

We describe herein the use of a three-electrode photoelectrochemical cell that contains a meniscus-based ~ 13 nm thick electrolyte on the working electrodes formed from p^+-Si/TiO_2/Ni interfaces, which allows XPS measurements under electrochemical

control through the solution [6,7]. Combined electrochemistry-photoelectron spectroscopic data that extend the previous characterization of this system [7] have been collected in this work.

Degenerately doped Si was used as a back contact for the TiO_2 to ensure that the changes in the observed binding energies originated from electric fields (or their absence) in the TiO_2 and not in the underlying Si. (Photo)electrochemical and microtopographical characterization using scanning probe microscopy have additionally been performed to assess the nature of the electrode surfaces and their conductivity properties as a function of the amount of metal deposited onto the TiO_2-coated photoanode surface. Recent work [15] in addition to work from our labs [7,12,13,17] suggests that the presence or absence of band bending is a key factor for facilitating charge conduction through these films. The experiments reported herein demonstrate that the degree of band-bending in a semiconductor (photo)electrode is not the only parameter that allows for charge conduction. The data also indicate that metallization that decreases the band bending is necessary for conduction. Hence multiple parameters must be optimized to obtain a functional protected photoelectrode.

Experimental

Films of TiO_2 were produced by atomic-layer deposition (ALD) [12,13,21,22] on degenerately doped p-type silicon ("p^+-Si") substrates. (100)-oriented boron doped Si wafers with a resistivity $\rho < 0.005$ Ω·cm were first cleaned *via* an oxidizing etch, with the Si soaked for 2 min in a 3:1 (by volume) "piranha" solution of concentrated H_2SO_4 (98 %) to 30 % H_2O_2(aq), followed by an etch for 10 s in a 10 % (by volume) solution of

HF(aq). The wafers were then immediately etched in a 5:1:1 (by volume) solution of H_2O, 36 % hydrochloric acid, and 30 % hydrogen peroxide for 10 min at 75 °C before being moved into the ALD chamber. The TiO_2 was deposited from a tetrakis(dimethylamido)titanium (TDMAT) precursor in a Cambridge Nanotech Savannah ALD reactor. In an ALD cycle, a 0.1 s pulse of TDMAT was followed by a 15 s purge of N_2 at 20 sccm, followed by a 0.015 s pulse of H_2O before another 15 s purge with N_2. This process was repeated for 1500 cycles to provide films ~ 70 nm in thickness. Where desired, Ni was deposited at a rate of ~ 2 nm per min by use of a RF sputtering power of 150 W for 20 s – 300 s in an AJA-International sputtering system. The time used to sputter the Ni is denoted herein as t_{sp}.

Atomic-force microscopy (AFM) data were collected using a Bruker Dimension Icon AFM, using Peakforce Quantitative Nanomechanical parameters, to provide information on the height, adhesion and deformation of the sample surface. ScanAsyst mode was used to optimize the tapping frequency and other experimental parameters, e.g., the gain, set point, and cantilever tuning. ScanAsyst-Air tips (silicon nitride) were used, with a nominal tip radius of 2 nm and a rotated (symmetric) geometry.

Electrochemical characterization was performed at a scan rate of 50 mV s^{-1} in either 1.0 M KOH(aq) or 50/350 mM $Fe(CN)_6^{3-/4-}$(aq), using Biologic SP-200 and SP-300 potentiostats. In KOH, a leak-free Ag/AgCl reference electrode (eDAQ) and a platinum counter electrode were used. For measurements in $Fe(CN)_6^{3-/4-}$(aq), the reference and counter electrodes were each Pt mesh electrodes.

Operando AP-XPS experiments were performed at the Advanced Light Source, Berkeley at the tender X-ray beamline 9.3.1 [6,7]. Fig. 1 presents schematically the geometry of the end station. Potentials were applied between the reference electrode,

E_{REF}, and the Fermi energy, E_F, of the working electrode. X-rays at an energy of 4 keV were selected from a range of 2.3 keV – 5.2 keV with an energy resolution of $E/\Delta E$ = 3000-7200. The X-ray beam spot size at the beam line was 1 mm x 2 mm [6]. The photoelectron collection cone was aligned to the beam line X-ray spot at a distance of ~ 300 μm (Fig. 1). The experiments were performed using an electrochemical cell with a hanging meniscus "emersion" configuration. Negligible steady-state faradaic current was passed at the potentials used in the experiments described herein. We designate this condition as "*operando"* because the observed region of the working electrode was under potential control and the working electrode itself comprised an isopotential surface. The pressure in the sample chamber was between 20 and 27 mbar, which is considered ambient pressure in the context of X-ray spectroscopy. To prepare electrodes for *operando* AP-XPS, strips of the p^+-Si/TiO_2/(Ni) wafers were cut into 1 cm x 3.5 cm rectangles. Highly doped p^+-Si was used simultaneously as a support material as well as to provide an effective back contact to the ALD-TiO_2. The ohmic contact at the back of the semiconductor was connected to the photoelectron analyzer to provide a high conductivity ground for the sample. To make ohmic contact to the sample, an In/Ga eutectic was scribed into the back of the Si wafer, and Ag paint was used to contact the electrode to a strip of Cu tape that was supported on a 0.8 cm x 3 cm glass slide.

Results

TiO_2/Ni/electrolyte structures having varying thicknesses of Ni were analyzed in detail. The Ni thickness is referred to by the sputter deposition time, t_{sp}, as described in the experimental section. For short deposition times, the Ni films were incomplete and

non-uniform. Thus, the deposition time is more informative than a calculated thickness, and hence t_{sp} has been quoted herein as the independent variable that was varied experimentally to produce the different interfaces under study.

Electrochemical Characterization

Deposition of Ni onto relatively thick (44 nm to 150 nm) ALD-grown TiO_2 enables charge conduction through the TiO_2 [12,13]. In previous photoelectrochemical analyses [12,13], Ni deposits consisted either of large islands (3 x 7 micron grid) or of thin, t_{sp} ~ 120 s, sputtered Ni films. Herein we investigate the characteristics of interfaces formed by deposition of a variety of Ni layer thicknesses.

Fig. 2a shows the current density vs. potential (*J-U)* characteristics of TiO_2/Ni electrodes in 1.0 M KOH formed using Ni deposition times of 0 s, 20 s, 60 s, or 300 s. The *J-U* sweeps were initiated in the positive direction from the open-circuit potential, U_{OC}. The data were recorded after completion of the AP-XPS measurements, to establish the interrelation of the voltammograms with the photoelectron spectra. Five main features were observed in the voltammetric data for TiO_2/Ni (60 s) and TiO_2/Ni (300 s) interfaces. For t_{sp} = 60 s, the onset of hydrogen evolution (HER) occurred at -1.1 V vs. Ag/AgCl, and an anodic peak, wave A, was observed at U = -0.7 V vs. Ag/AgCl, attributable to the oxidation of metallic Ni(0) to Ni(II) [23]. The related cathodic peak associated with the reduction of Ni(II) to Ni(0) was not observed. At positive potentials, the *J-U* data exhibited an oxidative transformation at U = +0.39 V (wave B; anodic current) ascribable to Ni(II) to Ni(III), prior to the onset of the oxygen-evolution reaction (OER) at +0.52 V vs. Ag/AgCl. A reductive peak at U = +0.23 V vs. Ag/AgCl (wave C; cathodic current) was observed on the return sweep. For t_{sp} = 300 s, the anodic and cathodic waves at

+0.34 V and +0.28 V vs. Ag/AgCl, respectively, exhibited less separation, and the catalytic OER current was observed at 0.49 V vs. Ag/AgCl. The samples that had lower catalyst loadings, e.g. t_{sp} = 20 s, did not display the Ni(0)/Ni(II) and Ni(II)/Ni(III) redox peaks.

Fig. 2b shows the electrochemical data obtained when the electrodes were in contact with $Fe(CN)_6^{3-/4-}$(aq). An analogous trend was observed, and only electrodes with Ni thicknesses of > 2 nm (sputter times ≥ 60s) exhibited substantial current flow, even in the presence of an electrochemically reversible one-electron redox couple.

Surface Microtopography

Tapping mode AFM data were obtained to determine the coverage and structure of the Ni overlayer (Fig. 3). Only minor differences (~ 4 %) in roughness between bare TiO_2 and TiO_2 with t_{sp} = 20 s or 60 s of Ni deposition (Table 1) were observed in the sample height data obtained using peak force quantitative nanomechanical measurements (Fig. 3a). However, a local minimum in deformation was observed for the electrode that had been coated with Ni for 20 s. For increased sputter times, i.e., for the sample with t_s = 300 s, much higher roughness (~ 30 %) and deformations (~ 160 %) were observed. Electrodes having t_{sp} = 60 s generally were very similar to the behavior observed for bare TiO_2.

Junction Energy Relations: AP-XPS

TiO_2/(Ni) electrodes were examined by AP-XPS in a manner analogous to that described previously [7], with Ni deposited for t_{sp} = 0 s, 20 s, 60 s, or 300 s, respectively.

The binding energy, E_B, of a core level can be calculated as $E_B = h\nu - E_{K,VAC} - \phi_{sample}$ where $E_{K,VAC}$ is the kinetic energy of the photoelectron with respect to the vacuum energy level (E_{VAC}), ϕ_{sample} is the work function of the sample, and $h\nu$ is the X-ray energy. E_B is measured relative to the Fermi energy, E_F, of the analyzer (or of the sample, which are equal, because the two components are in electrical contact). However, ϕ_{sample} is unknown during the XPS measurements, and the kinetic energy is referenced to the Fermi energy, E_F, if not otherwise noted, i.e., $E_K = E_{K,VAC} + \phi_{sample}$ (where ϕ_{sample} is the energetic difference between the E_{VAC} and the Fermi level of the sample). This approach provides binding energies that are referenced to the analyzer. To provide a description from an electrochemical perspective, we define E_B' as the core-level binding energy referenced to the solution potential instead of referenced to E_F of the working electrode/analyzer. Because the potentials are set at the working electrode with respect to the reference electrode, E_B' can be defined by equation (1)

$$E_B' = E_B + qU_{eff}, \qquad (1)$$

where q is the absolute charge of an electron and U_{eff} tracks the difference in the electrochemical potentials between the solution and the working electrode. U_{eff} is given by $U_{eff} = U - U_{fb}$, where U is the applied potential and U_{fb} is the flat-band potential for the bare TiO_2 electrode (for details see Ref. [7]). Hence the solution-corrected core-level binding energy, E_B', measures the binding energy of a level relative to the solution potential. In this approach, the solution-corrected binding energies E_B' of core levels of materials in solution, such as the O 1s level of solution (bulk) water, should remain constant as the potential at the working electrode is varied (the effect of water in the double layer is negligible at the ionic strengths used). Semiconductors that have “fixed”

band edges in a semiconductor/liquid junction should show no change in E_B' at the interface with a change in U_{eff}, because in this picture, the band edges are fixed relative to the solution energetics. However, for cases in which the band edges of the semiconductor shift, such as in the case of accumulation or Fermi-level pinning due to defect states [7], the solution-corrected binding energy would be expected to shift with respect to the solution potential. Thus when the binding energy is referenced to the solution potential or to the potential of the reference electrode, the E_B' of the water O 1s level and of the semiconductor/liquid junction semiconductor core levels would be expected to be independent of the solution potential, and should exhibit a shift parameter $\Delta' \equiv \partial E_B'/\partial U_{eff} = 0$ eV V^{-1}. However, for cases where the band edges shift with respect to the solution, as may result from Fermi level pinning, a change in the solution-corrected binding energies with solution potential is expected. This situation can be contrasted with the results expected when the binding energies are determined with respect to the analyzer [7], because when referencing binding energies to the analyzer (E_B), the water O 1s and pure (without metallization) semiconductor/liquid junction semiconductor core levels are expected to show a shift $\Delta \equiv \partial E_B/\partial U_{eff} = \Delta = -1$ eV V^{-1} with respect to the applied voltage [7].

Fig. 4 plots solution-corrected XPS spectra for the O 1s and Ti 2p core levels for a bare TiO_2 electrode, in which the photoemission intensities are plotted against E_B', and Fig. 5 plots the solution-corrected XPS spectra for the Ni 2p, O 1s and Ti 2p core levels of the TiO_2/Ni (20 s) electrode vs E_B'. The bare TiO_2 XPS peaks showed less band-edge shifting whereas electrodes with Ni showed a larger shift. Fig. 6a displays the full width at half maximum (FWHM) of the liquid water O 1s core level, as well as of the TiO_2 O 1s peak, for the bare TiO_2 electrode. The FWHM data are expected to reach a minimum at

the flat-band potential [7]. Fig 6a shows that for the bare TiO_2 electrode, the FWHM for the TiO_2 O 1s peak reaches a minimum at -0.9 V vs. Ag/AgCl. Fig. 6b shows the solution-corrected core level shift for the Ti $2p_{3/2}$ core levels across a range of potentials for the three different TiO_2/(Ni) electrodes. The slopes, Δ'_{Ti}, of the fitted lines show that the solution-referenced binding energy E_B' of the Ti $2p_{3/2}$ core level shifted with a slope of 1.0 ± 0.08 eV V^{-1} for TiO_2/Ni (20 s), 0.9 ± 0.10 eV V^{-1} for TiO_2/Ni (60 s), and 1.0 ± 0.07 eV V^{-1} for TiO_2/Ni (300 s). Fig. 6c shows that the relative peak shift, Δ'_{Ni}, of E_B' for the Ni $2p_{3/2}$ core level for TiO_2/Ni (20 s) was 0.7 ± 0.07 eV V^{-1}; that for TiO_2/Ni (60 s) was 0.9 ± 0.08 eV V^{-1}; and the value for TiO_2/Ni (300 s) was 1.0 ± 0.08 eV V^{-1}. The errors associated with these slopes result primarily from the resolution of, and uncertainty inherent to, the measurement.

Fig. 7 displays XPS data showing the Ni $2p_{3/2}$ core level for samples prepared with $t_{sp} = 20$ s, 60 s and 300 s. The electrode was maintained at a potential of -1.0 V vs. Ag/AgCl, and the Ni(0), Ni(II), and Ni(III) peaks as well as the satellite peaks are labeled. A clear lack of a metallic Ni phase was observed for the $t_{sp} = 20$ s sample at potentials positive of flat-band, and only a very small amount of metallic Ni (6 %, Ni $2p_{3/2}$ peak area) was visible under reducing conditions at $U = -1.0$ V vs. Ag/AgCl. In contrast, the $t_{sp} = 60$ s sample had a significant peak area fraction (40%) of metallic Ni and the sample prepared using $t_{sp} = 60$ s showed a large fraction (51 %) of metallic Ni. The Ni(III) content was 94 % for t_{sp} = 20 s, 47 % for t_{sp} = 60 s, and 22 % for t_{sp} = 300 s, based on peak areas in the Ni $2p_{3/2}$ peak.

Discussion

Electrochemistry

For lower Ni coverage, the electrode exhibited resistive behavior with very low currents in both the KOH electrolyte and the $Fe(CN)_6^{3-/4-}$ redox solution (Fig. 2). However, currents become substantial for the electrode that had t_{sp} =60 s (~ 2 nm) of Ni. The typical electrochemical signatures of Ni oxidation and reduction as well as HER and OER were observed, with the Ni(II)/(III) redox reaction showing irreversible behavior with a peak separation of 0.16 V. Increasing t_{sp} to 300 s decreased this peak separation to 0.06 V, indicating that the conductivity of the sample improved. Starting at the open-circuit potential and scanning toward more positive potentials, the electrodes became covered with NiO, and then NiOOH, as evidenced by the observation of a partial reduction of Ni(III) to Ni(II) (peak C, Fig. 2) in the cathodic branch of the voltammetry. After several cycles in which the potential scan was stopped in the anodic waves, the initially existing Ni metal had been partially oxidized. The corresponding current for Ni oxidation was small because the successfully oxidized Ni overlayers inhibited further oxidation of Ni metal. Prior XPS data on these 2 nm thick Ni films [7] support this conclusion by showing a decrease in the Ni(0) signal with a concomitant increase in the Ni(II) signal. The increase in sample conductivity for thicker Ni coverages is evident in Fig. 2b, where current densities > 10 mA cm^{-2} are evident at +0.1 V vs. Ag/AgCl. Thus, the data show a distinct difference in the sample conductivity depending on the amount of Ni deposited and on the anodization procedure [12].

AFM Microtopography

Microtopography data indicated that for small t_{sp} values, the sample exhibited surface roughness and a deformation of the bare TiO_2/solution interface. The dip in the

deformation data for the t_{sp} = 20 s sample suggests the presence of a different surface material than that observed for either bare TiO_2 or for the thicker Ni-coated TiO_2 surfaces. This behavior is consistent with expectations for a NiO_x/TiO_2 surface that does not contain underlying metallic Ni. The increasing trend in deformation from t_{sp} = 20 s to t_{sp} = 300 s suggests that only after a 20 s deposition of Ni did a substantial metallic phase exist at the TiO_2/NiO_x interface. This conclusion is also supported by XPS data of the Ni 2p core level (Fig. 7).

Energy relations by AP-XPS measurements

The XPS technique integrates the signal over the spot examined in the experiment. Fig. 8 shows a schematic of the energy-band relations and the resulting description of the structures considered herein. In the physical representation, the kinetic energies plus the work function, E_K, of the photoelectrons are referred to the Fermi level E_F of the working electrode, which coincides with that of the analyzer, to deduce E_B. In the electrochemical frame of reference, kinetic energies are referred to the reference electrode potential to define E_B'. To be consistent, changes in E_B' were measured with respect to the potential at which the flat-band condition was observed for the bare TiO_2 electrode. This approach allows evaluation of the shift in the band edges with respect to the solution potential as the applied potential is varied. If the shift in E_B' with potential is greater than zero (see equation 1), band-edge movement occurs. Provided that the sampling depth of the technique is smaller than the width of the space-charge region, the shift of E_B, Δ, and of E_B', Δ', with potential should approximately be related by equation (2):

$$\Delta' = \Delta + 1 \text{ eV V}^{-1} . \qquad (2)$$

Hence, the semiconductor core levels in an ideal semiconductor/liquid junction will have corrected peak shifts Δ', relative to the reference electrode, of $\Delta' = 0.0$ eV V^{-1}; the electrolyte will also exhibit no shift; while the metal core levels in a pure metal/electrolyte junction will shift with the full applied potential *relative to the reference electrode*, i.e. $\Delta' = 1.0$ eV V^{-1}.

Analysis of the electrochemical data alone does not directly allow assessment of whether a rectifying or an ohmic contact was formed, because the high resistivity ($t_{sp} = 20$ s) could also be observed for an isolated system that contains a buried Schottky barrier. The AP-XPS data, however, enables this evaluation of the electrical properties of the materials in the device and at the interfaces of interest.

As shown in Fig. 6b, the average solution-corrected binding energies of the Ti $2p_{3/2}$ core level for the TiO_2/Ni (20 s) interface shifted by 1.0 eV V^{-1}; those for TiO_2/Ni (60 s) shifted by 0.9 eV V^{-1}; and those for TiO_2/Ni (300 s) shifted by 1.0 eV V^{-1}, all showing metal-like behavior. For comparison, the band edges for bare TiO_2 were observed to shift only in the potential range in which defect states occurred, and were otherwise stationary (at potentials more positive than the conduction-band edge))[7], suggesting that the bare TiO_2 acts like a semiconductor outside of the potential range where the defect states induce Fermi level pinning. Hence, the TiO_2/Ni (20 s), TiO_2/Ni (60 s) and the TiO_2/Ni (300 s) electrodes all exhibited only small amounts of rectification in the underlying TiO_2 layer. The improvements in observed conductivity (Fig. 2) of the TiO_2/Ni electrodes in the order t_{sp} =0 s < 20 s < 60 s < 300 s therefore likely result from more than simply the removal of rectification in the underlying TiO_2. Furthermore, as shown in Fig. 7, the amount of interfacial metallic Ni increased significantly, with almost no Ni(0) present for $t_{sp} = 20$ s and half of the layer consisting of

Ni(0) for t_{sp} = 300 s [24]. Hence, the data are consistent with the presence of Ni, as opposed to NiO_x, at the TiO_2/Ni interface playing a dominant role in determining the charge conduction through the device.

The importance of the Ni contact, as opposed to NiO_x, to the TiO_2, is evident based on the combination of the electrochemistry (Fig. 2), the solution corrected Ti 2p and Ni 2p core level shifts from AP-XPS data (Fig. 6), and the catalyst compositions (chemical states) from the Ni $2p_{3/2}$ core level AP-XPS (Fig. 7). The bare TiO_2 sample is both nonconductive and observed to be generally rectifying (Fig. 2 and 6), whereas the TiO_2 samples with substantial amounts of metallic Ni ($t_{sp} \geq 60$ s) are ohmic at the semiconductor/liquid junction (i.e., band-edge shifts of $\Delta' \sim 1.0$ eV V^{-1}), and are electrically conductive, as evidenced by the *J-U* behavior. The sample with the NiO_x layer (t_{sp} = 20 s) is, therefore, unique, in that it displays similar AP-XPS data in that the band edges of the TiO_2 appear to be similarly disconnected from the solution, such that they shift with respect to the solution potential, as is the case for the samples that have substantial metallic Ni. However, the TiO_2 in the NiO_x-containing samples is nonconductive, as observed in electrochemical analysis (Fig. 2). The junction between NiO_x and TiO_2 appears electronically distinct from that between Ni and TiO_2 in that charge conduction is not present for the NiO_x/TiO_2 structure even though rectification at the TiO_2/liquid junction has largely been removed [24]. If a purely conduction-band transport mechanism operates in the TiO_2, such that Ni metal is not required to contact the TiO_2, the loss of rectification for the t_{sp} = 20 s sample should have allowed for conduction to be observed for the device in contact with the $Fe(CN)_6^{3-/4-}$ redox solution. Therefore, the lack of conduction in the samples for t_{sp} = 20 s is consistent with the presence of NiO_x, as opposed to Ni, heavily influencing the electrical behavior of the TiO_2, leading to an

increase in resistivity and a consequent loss in film conductivity. The E_B for the Ti $2p_{3/2}$ core level in the TiO_2/Ni samples with thick Ni was observed to be equal to that observed for the bare TiO_2 films at a potential at the midpoint of the mid-gap states (459.0 eV to 459.1 eV), suggesting an interplay between the mid-gap "defect" states and the Ni overlayer. These results are summarized in Fig. 9 by the schematic energy diagrams of the solid/liquid interface. Fig. 9a-c shows the situation for negative potentials *U* with respect to the flat-band condition, and Fig. 9d-f depicts the situation for positive potentials *U* with respect to flat-band of the TiO_2/electrolyte (Fig. 9a and 9d), TiO_2/NiO_x/electrolyte (Fig. 9b and 9e) and TiO_2/Ni/NiO_x/electrolyte (Fig. 9c and 9f) systems. In the presence of NiO_x and Ni, Fermi level pinning at the mid-gap states occurs. In the absence of Ni or NiO_x, TiO_2 develops a space-charge region with fixed band-edge positions outside of regions involving Fermi-level pinning or accumulation [7].

Conclusions

The results presented herein demonstrate that *operando* AP-XPS can be used to observe and quantify the degree to which catalysts influence the band energetics of underlying protection layers and the ECDL. In addition to providing information regarding the band energetics, layer composition, and chemical state, AP-XPS also provides direct evidence regarding the nature of the rectification and contact at the interface. For various thicknesses of deposited Ni or NiO_x, the rectification in the underlying TiO_2 is mostly removed; however, the increase in conductivity for deposited Ni only occurs when the Ni phase contains a substantial amount of metallic Ni and not merely an oxide phase. As a result, the data indicate that the band lineups between the

semiconductor and the metal or metal oxide overlayer, as well as electronic effects that result from this equilibration, are the crucial factors that induce conduction in the TiO_2 films under evaluation. Sufficiently dense metallization allows for stable conduction through such films.

Acknowledgments

This work was supported through the Office of Science of the U.S. Department of Energy (DOE) under award no. DE SC0004993 to the Joint Center for Artificial Photosynthesis, a DOE Energy Innovation Hub. The Advanced Light Source is supported by the Director, Office of Science, Office of Basic Energy Sciences, of the U.S. Department of Energy under Contract No. DE AC02 05CH11231. We thank Dr. Philip Ross for contributions to the conceptual development of the AP-XPS end station and experimental design.

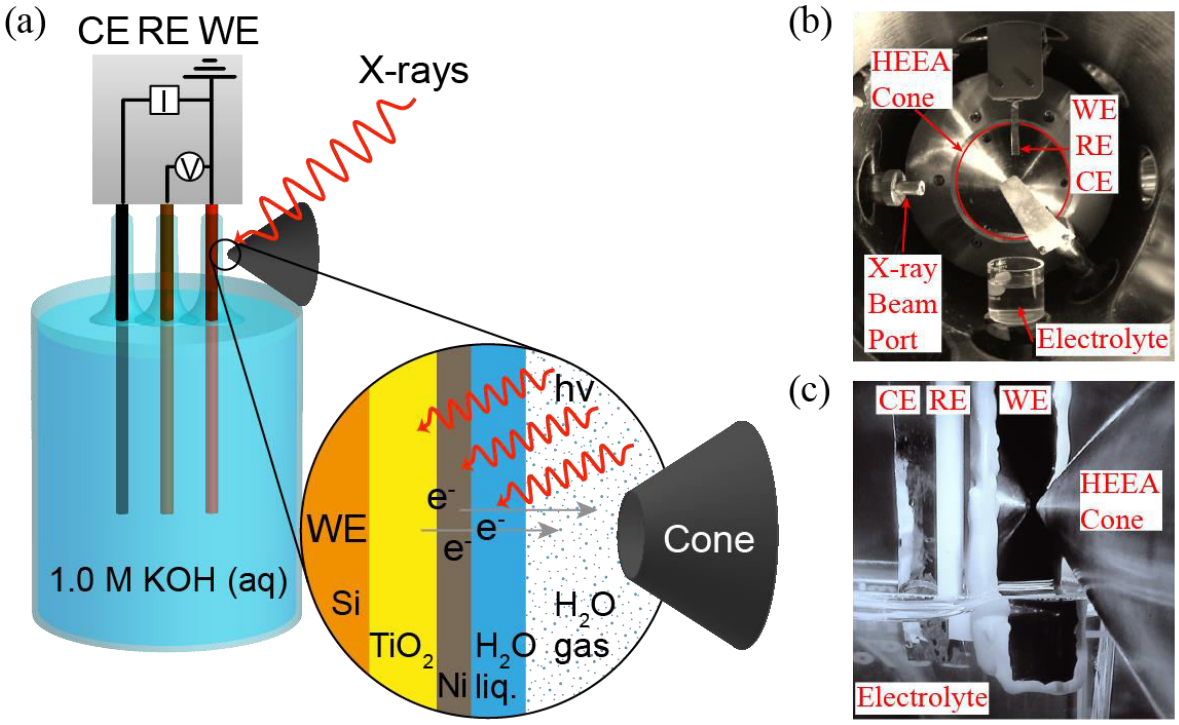

Figure 1: (a) Scheme of the *operando* XPS-PEC setup. The working electrode and the hemispherical electron energy analyzer (HEEA) were grounded to each other. The potential of the working electrode was changed with respect to the reference electrode. The PEC-beaker containing the electrolyte could be moved in the z direction whereas the three-electrode mount could be moved in the x-, y-, and z-directions. (b) View into the high-pressure analysis chamber. The X-ray beam enters through the window on the left, the three-electrode setup is on the top, the electrolyte beaker on the bottom, and the electron analyzer cone is in the center. (c) Three-electrode setup pulled up and in measurement position (compare to (a)).

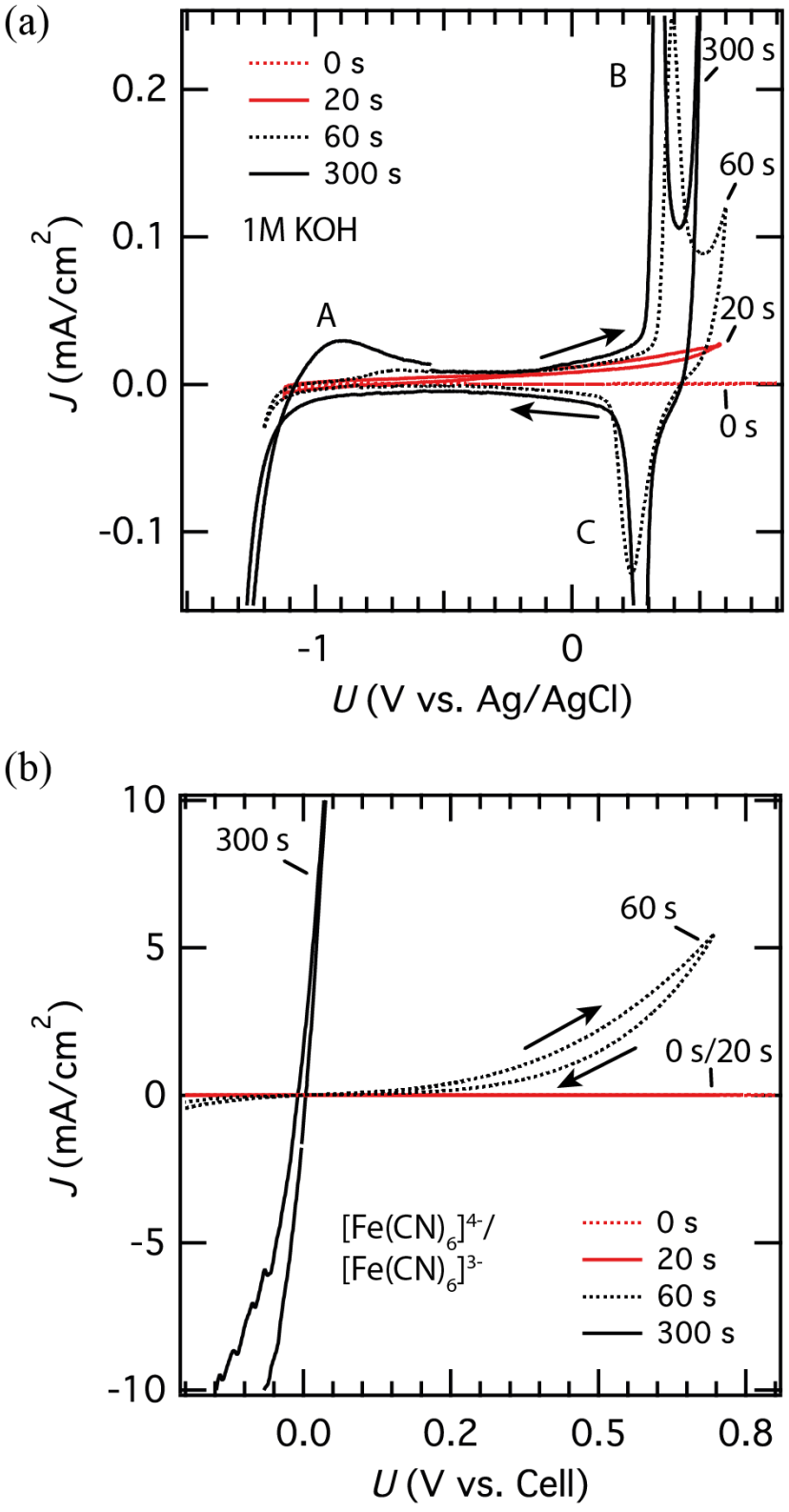
(a)
0 s
20 s
60 s
300 s
1M KOH
A
B
C
300 s
60 s
20 s
0 s
0.2
0.1
0.0
-0.1
-1
0
J (mA/cm2)
U (V vs. Ag/AgCl)
(b)
300 s
60 s
0 s/20 s
[Fe(CN)6]4-/
[Fe(CN)6]3-
0 s
20 s
60 s
300 s
10
5
0
-5
-10
0.0
0.2
0.5
0.8
J (mA/cm2)
U (V vs. Cell)

Figure 2: (a) *J-U* data collected for bare TiO_2, TiO_2/Ni (20 s), TiO_2/Ni (60 s), and TiO_2/Ni (300 s) electrodes, respectively, in 1.0 M KOH(aq). Three peaks are observed: for t_{sp} = 60 s, an anodic peak A at -0.7 V, an anodic peak B at +0.39 V, and a cathodic peak at +0.23 V vs. Ag/AgCl. For t_{sp} = 300 s, these peaks shifted to -0.85 V, +0.34 V and +0.28 V vs. Ag/AgCl. (b) *J-U* data measured in 50/350 mM $Fe(CN)_6^{3-/4-(}$aq) solution. Arrows show the scan direction.

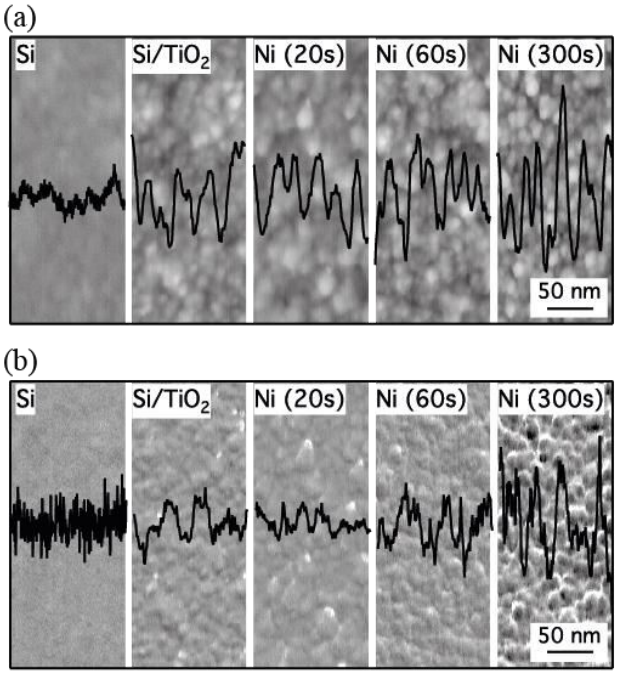

Figure 3: AFM microtopographs of bare silicon, ~ 70 nm thick TiO_2 on silicon, $Si/TiO_2/Ni$ (20 s), $Si/TiO_2/Ni$ (60 s), and $Si/TiO_2/Ni$ (300 s). (a) depicts the height information and (b) the surface deformation by the AFM tip. The sub-micrographs in (a) and (b) have the same height scaling. In each graph the insets show line scans from the middle of the microtopographs.

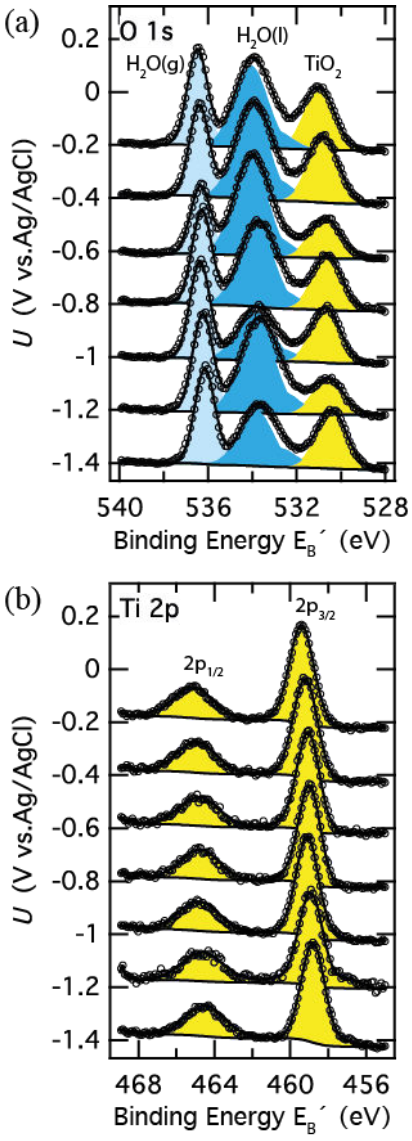

Figure 4: O 1s (a) and Ti 2p (b) X-ray photoemission spectra of the bare TiO_2 electrode in 1.0 M KOH(aq) for U = -1.4 V to -0.2 V vs. Ag/AgCl. The binding energies are referenced to the solution potential as explained in the text and corrected by the applied potential with respect to flat-band conditions at U_{fb} = -0.9 V vs. Ag/AgCl [7].

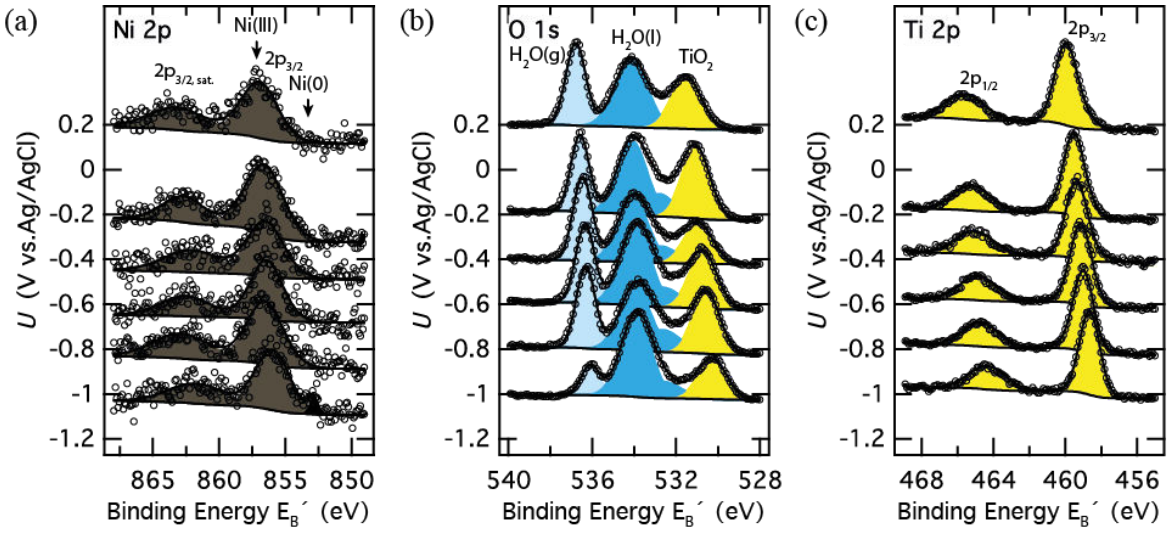

Figure 5: Ni 2p (a), O 1s (b), and Ti 2p (c) X-ray photoemission spectra of a TiO_2/Ni (20 s) electrode in 1.0 M KOH(aq) for U = -1.0 V to +0.2 V vs. Ag/AgCl. The binding energies are referenced to the solution potential as explained in the text and corrected by the applied potential with respect to flat-band conditions at U_{fb} = -0.9 V vs. Ag/AgCl [7] (see Equation 1 and 2). The positions of metallic (Ni(0)) and fully oxidized Ni (Ni(III)) are indicated in (a) by arrows.

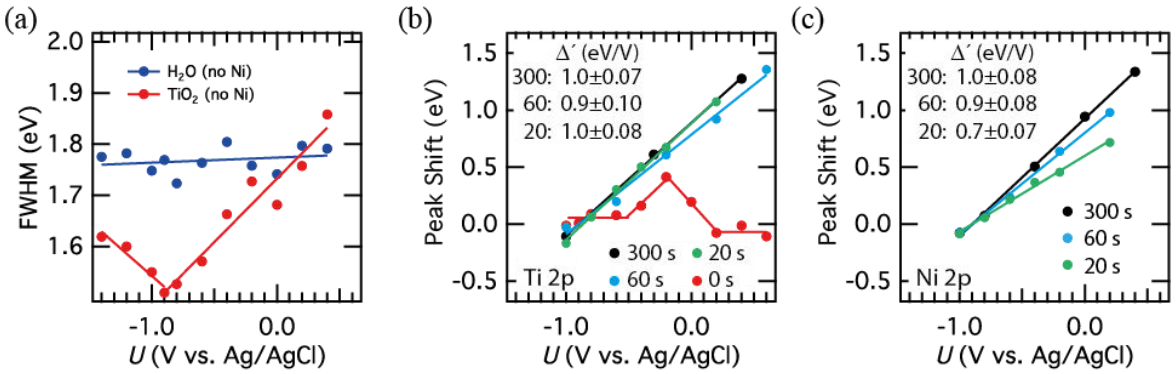

Figure 6: (a) Full width at half maximum (FWHM) peak data for the water O 1s and TiO_2 O 1s core levels for a bare TiO_2 electrode. (b) The core level peak shifts with respect to the binding energy at flat-band, which indicate the band-edge shift of the semiconductor with respect to the electrolyte, of the Ti $2p_{3/2}$ core level for TiO_2/electrolyte, TiO_2/Ni (20 s)/electrolyte, TiO_2/Ni (60 s)/electrolyte, and TiO_2/Ni (300 s)/electrolyte geometries. (c) Similar to (b) but plotting only the Ni $2p_{3/2}$ core level peak shift for the t_{sp} = 20 s, 60 s, and 300 s electrodes. The binding energies are referenced to the solution potential as explained in the text, and are corrected by the applied potential with respect to flat-band conditions at U_{fb} = -0.9 V vs. Ag/AgCl [7] (see Equation 1 and 2).

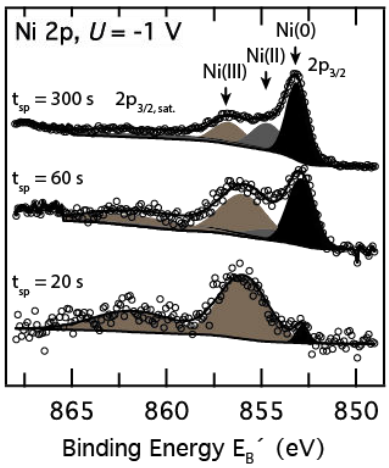

Figure 7: Ni $2p_{3/2}$ X-ray photoemission spectra for t_{sp} = 20 s, 60 s, and 300 s for U = -1 V vs. Ag/AgCl. The binding energies are referenced to the solution potential as explained in the text and corrected by the applied potential with respect to flat-band conditions at U_{fb} = -0.9 V vs. Ag/AgCl [7] (see Equation 1 and 2). The positions of metallic (Ni(0)), Ni(II), and fully oxidized Ni (Ni(III)) are indicated by arrows.

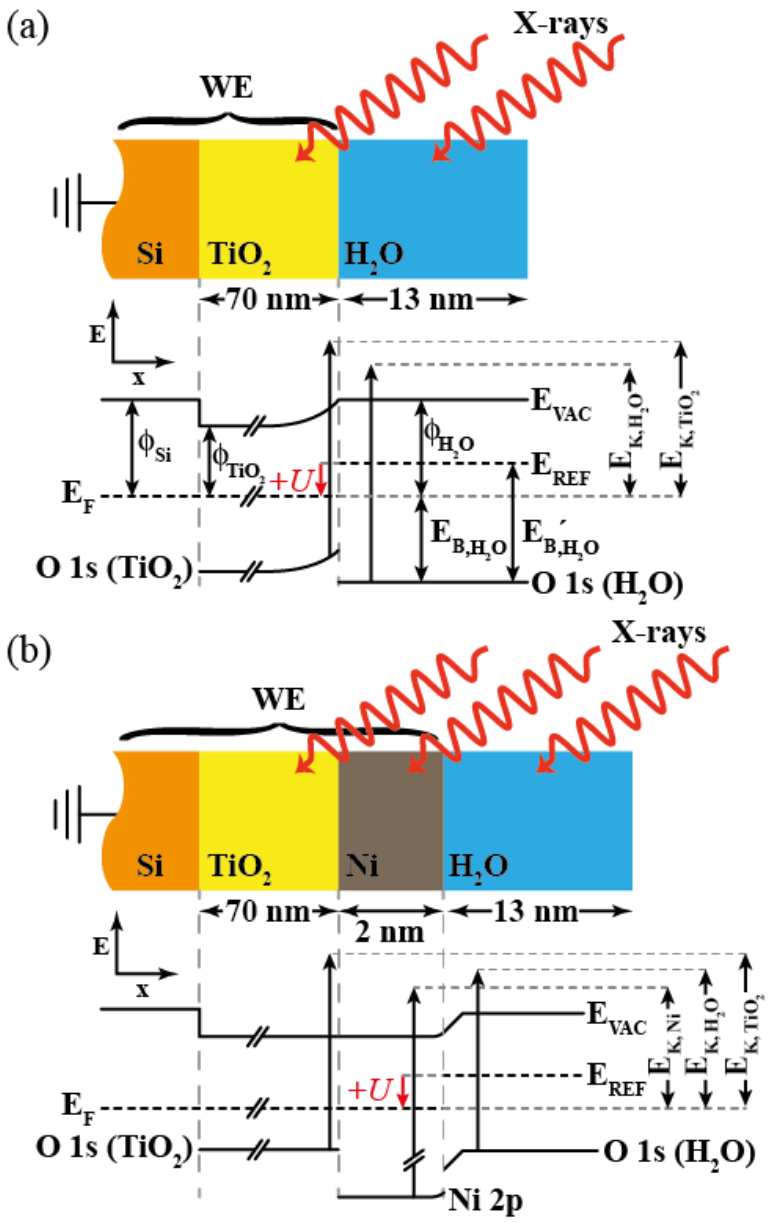

Figure 8: Scheme of the energy-band relations of *operando* photoelectron spectroscopy for (a) the Si/TiO_2/electrolyte geometry and (b) the Si/TiO_2/Ni/electrolyte geometry. The working electrode and analyzer are grounded. A potential is applied to the working electrode in the electrolyte with respect to the reference electrode in a three-electrode configuration. The work function of the material Φ is the difference between the Fermi energy, E_F, and the vacuum energy E_{VAC}. The kinetic energies, $E_K = E_{K,VAC} + \Phi$, of the photoelectrons are measured with respect to the Fermi energy of the analyzer. The

binding energy, E_B, is calculated based the photon energy with $E_B = h\nu - E_K = h\nu - E_{K,VAC} - \Phi$, whereas the binding energy with respect to the reference electrode is $E_B' = E_B + qU_{eff}$ (Equation 1), as illustrated for the binding energy of the water O 1s core level in (a).

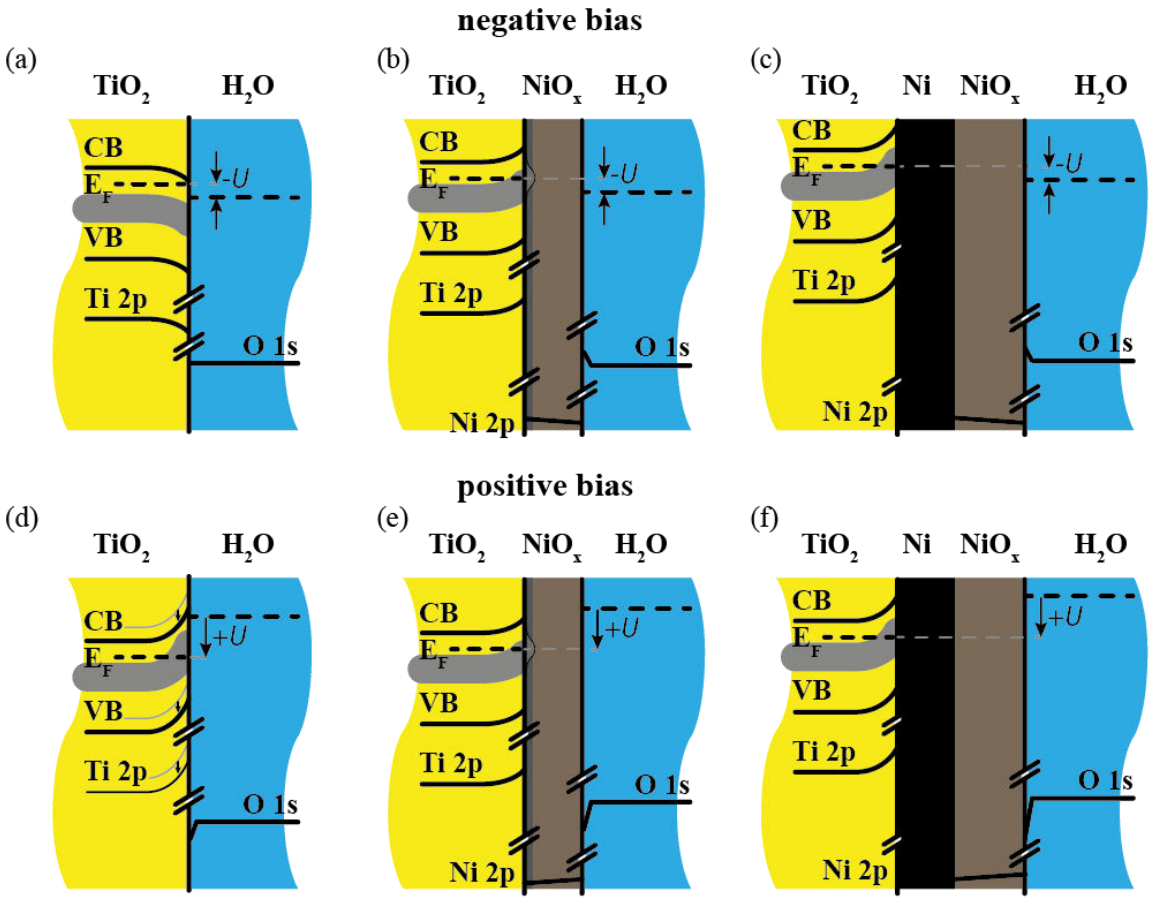

Figure 9: Band diagrams that summarize the experimental findings described herein. (a-c) for negative potential *U* with respect to flat-band and (d-f) for negative potential *U* with respect to flat-band. The thick grey line marks the position of the mid-gap state band in TiO_2. For (b, c and e, f), Fermi level pinning at the mid-gap states occurs. (a, d) In the absence of Ni or NiO_x, TiO_2 develops a space-charge region with fixed band-edge positions outside of regions involving Fermi-level pinning or accumulation [7]. For increasingly positive potentials, the Fermi level crosses the mid-gap states and band edge shifting in TiO_2 is observed (indicated by the arrows). The potential drop (the amount necessary to charge/discharge the surface states) occurs now in the electrochemical double layer. (b, e) The Fermi energy at the TiO_2/NiO_x interface is pinned near the mid-gap states due to NiO_x interface states [24]. With Fermi level pinning, the band edges shift

with the applied potential. (c, f) With a sufficiently dense and thick Ni film at the interface to TiO_2, the TiO_2 band edges are effectively disconnected from the solution, and the presence of metallic Ni allows for charge conduction.

Table 1: Surface roughness parameters obtained by AFM for the height distribution and the surface deformation. While the surface roughness and deformation parameters stay nearly constant up to 60 s (with a minimum for 20 s) the change (increase by up to 160 %) of the surface properties is more drastic after Ni deposition with a 300 s sputter time.

Roughness / Ni	Height		Deformation	
	RMS (nm)	Ra (nm)	RMS (nm)	Ra (nm)
0 sec	0.71	0.55	0.17	0.12
20 sec	0.68	0.53	0.14	0.10
60 sec	0.69	0.55	0.17	0.13
300 sec	0.91	0.72	0.44	0.33

References

1. H. Gerischer, *Journal of Electroanalytical Chemistry and Interfacial Electrochemistry*, **58**, 263–274 (1975).

2. Y. Ping, W. A. Goddard III, and G. A. Galli, *J. Am. Chem. Soc.*, **137**, 5264–5267 (2015).

3. H. J. Lewerenz, *J. Electrochem. Soc.*, **139**, L21–23 (1992).

4. H. J. Lewerenz, T. Bitzer, M. Gruyters, and K. Jacobi, *J. Electrochem. Soc.*, **140**, L44–L46 (1993).

5. K. Jacobi et al., *Phys. Rev. B*, **51**, 5437–5440 (1995).

6. S. Axnanda et al., *Sci. Rep.*, **5**, 9788–22 (2015).

7. M. F. Lichterman et al., *Energ. Environ. Sci.*, **8**, 2409–2416 (2015).

8. K. Sun et al., *Energy Environ. Sci.*, **5**, 7872–7877 (2012).

9. K. Sun et al., *P Natl Acad Sci Usa*, **112**, 3612–3617 (2015).

10. K. Sun et al., *Phys. Chem. Chem. Phys.*, **16**, 4612–4625 (2014).

11. Y. W. Chen et al., *Nat. Mater.*, **10**, 539–544 (2011).

12. S. Hu et al., *Science*, **344**, 1005–1009 (2014).

13. M. F. Lichterman et al., *Energy Environ. Sci.*, **7**, 3334–3337 (2014).

14. M. F. Lichterman et al., *Catal Today* (2015).

15. B. Mei et al., *J. Phys. Chem. C*, **119**, 15019–15027 (2015).

16. P. Reckers et al., *J. Phys. Chem. C*, **119**, 9890–9898 (2015).

17. M. T. McDowell et al., *ACS Appl. Mater. Interfaces*, **7**, 15189–15199 (2015).

18. B. Seger et al., *J. Mater. Chem. A*, **1**, 15089–15094 (2013).

19. Y. Lin et al., *J. Phys. Chem. C*, 150126152338001 (2015).

20. B. Seger et al., *Rsc Adv*, **3**, 25902–25907 (2013).

21. M. F. Lichterman et al., *ECS Transactions*, **66**, 97–103 (2015).

22. M. H. Richter et al., *ECS Transactions*, **66**, 105–113 (2015).

23. M. E. G. Lyons, R. L. Doyle, I. Godwin, M. O'Brien, and L. Russell, *J. Electrochem. Soc.*, **159**, H932–H944 (2012).

24. M. H. Richter et al. (in preparation).

IV. *Operando* AP-XPS Analysis of the Electrochemical Double Layer at the interface of Ir and KOH(aq)

Originally published as "Operando X-ray Photoelectron Spectroscopic Investigations of the Electrochemical Double Layer at Ir/KOH(aq) Interfaces" in the Journal of Electron Spectroscopy and Related Phenomena[1].

Tender x-ray *operando* photoemission spectroscopy has been used to directly analyze the energetics of the double layer at a metal-water interface in a dilute electrolyte having a Debye length of several nanometers. The data are compared to a theoretical evaluation of the potential of the solution near the electrode. Due to its noble nature, Ir was chosen as a working electrode material, and KOH(aq) at varied concentrations and thicknesses constituted the electrolyte. Shifts in peak width and binding energy of the water O 1s core level were analyzed by modeling based on Debye-Hückel approximations. The data verify electrochemical formulations of the double layer that provide a foundation to electrochemistry.

Introduction

The interface between an electrode and electrolyte is said to constitute "the heart of electrochemistry."[2] The electronic properties of the double layer are key to many capacitive,[3] electrocatalytic,[4] and biological[5] processes. An initial model of the double layer by Helmholtz described this interface as a parallel-plate microcapacitor containing a single plate of charges on the metal electrode and a single sheet of charges, of a similar magnitude, in the adjacent solution.[6] A separate model was independently proposed by

Gouy in 1910[7] and Chapman in 1913[8] to suggest a diffuse double layer in which ionic concentrations in solution, modeled by Maxwell-Boltzman statistics, result in a potential in the solution that decreases exponentially with distance from the electrode, termed a diffuse layer. In 1924, Sterm combined the Helmholtz and Gouy-Chapman models to formulate a model in which, near the electrode surface, a more ordered layer can form as a result of electrostatic ionic adhesion.[9] More recently, Müller and coworkers have refined this theory to include the orientation of solvent molecules at the interface.[10] In this model, the Inner Helmholtz Plane (IHP) is a plane that passes through the center of any specifically absorbed ions, and the Outer Helmholtz Plane (OHP) includes the first layer of solvated ionic charges adjacent to the electrode. Beyond the OHP, a diffuse layer accounts for the remaining charge and consequently for the remaining voltage drop across the double layer.[10]

Numerous experimental approaches have been used to investigate the properties of the double layer. For example, electrochemical impedance spectroscopy allows determination of the size of a modeled double layer capacitance. However, this approach has various limitations, generally arising from the fact that the RC models used to analyze the impedance data are often not sufficient to describe the double layer.[11] Liquid microjet experiments have been performed to investigate the influence of different protonation states of silicate nanoparticles on the energetics of the surroundings.[12] These experiments are confounded by the expectation that the double-layer structure and energetics depend on the electrode potential, which is uncontrolled in such experiments. Infrared spectroscopy has been performed by a rotating emersion technique, but the method does not yield direct access to the electronic characteristics of the double layer.[13]

X-ray photoelectron spectroscopic (XPS) studies of emersed electrodes examine primarily the retained salts of the electrolyte as opposed to delineating directly the energetics at the solid/liquid junction.[14] Initial *operando* ambient pressure XPS (AP-XPS) experiments on the double layer have recently been performed at one specific electrolyte thickness.[15]

We have recently shown[16] that the semiconductor band bending, band-edge shifts, and other properties such as the semiconductor flat-band potential can be analyzed using *operando* AP-XPS, in which a three-electrode electrochemical apparatus allows for potential control on a working electrode relative to a reference.[16] The working electrode is grounded to the detector and the electrochemical cell is held in a chamber maintained at ~ 15 torr while the photoelectron analyzer is kept at a pressure of 5×10^{-7} torr. The previous set of experiments examined the energetics of the semiconductor surface region, whereas herein we describe the corresponding behavior of the electrochemical double layer (ECDL) in dilute electrolytes. The Galvani potential profile occurs in the ECDL and can be considered as an analogue to the electrostatic field profile that occurs in the semiconductor space-charge region (albeit with fundamental differences between solid and liquid phases), and may similarly be examined by XPS. Two principle differences exist between these experiments: 1) the semiconductor, as a solid, has a constant sampled thickness, unlike the case in which a Galvani potential occurs in the ECDL; 2) in our experimental setup, the band bending in the semiconductor occurs at the top surface of the material closest to the detector, and therefore is highly sensitive to investigation by XPS because all of the collected photoelectrons are indicative of the band positions for a non-degenerate semiconductor. In contrast, the potential drop in a double layer is more

pronounced near the electrode surface, whereas the bulk of the solution (d >10 nm into the solution for the electrolytes examined herein) is closer to the detector and therefore obscures the shifts in binding energy due to the Galvani potential changes in the double layer. Hence, the core-level peak shifts that are expected due to the voltage drop in the double layer are much smaller than the peak shifts expected in an equivalently sized space-charge region of a semiconductor. Nonetheless, the changes in binding energy due to the double layer ought to be detectable using the *operando* AP-XPS approach. Figure 1 demonstrates these basic concepts and geometries. Herein we report that dilute electrolytes can be investigated with this AP-XPS approach, which allows for definition of the energetics of dilute electrolytes as well as facilitating investigation of various thickness values of the electrolyte.

Experimental

To form the working electrode, a degenerately boron-doped p-type Si wafer was used as a substrate for sequential deposition of Ti followed by Ir. The Si wafer was first cleaned in buffered oxide etch for 10 min before being loaded into a sputtering system (AJA International). 10 nm of Ti, as an adhesion layer, followed by 50 nm of Ir, were sputtered from an RF source in Ar(g) at a pressure of 8.5 mTorr and a power of 150 W. Following deposition, the sample was cut to dimensions of 1 cm x 4 cm, and the Ir was electrically contacted to Cu tape with low pressure Ag epoxy (Ted Pella). The back and edges of the electrode were then coated with epoxy (Hysol 9460) to ensure that only the Ir surface contacted the solution.

Operando AP-XPS data were collected between -0.7 V and +0.3 V vs Ag/AgCl at pH 14 as well as between -0.9 V and +0.1 V vs Ag/AgCl at pH 11.5, at beamline 9.3.1 at the Advanced Light Source (ALS). Tender X-ray photons at 4 keV were used from a range of 2.3 – 6.0 keV. Potentials were stepped in 200 mV increments. At each potential, the electrode was dipped, a potential was set, and the electrode was then retracted to allow for data collection. KOH pellets were added to water that had been purified through a Millipore filtration system to make electrolytes that ranged in concentration from 1.0 M to 3.16 mM (pH 14 to pH 11.5). The thickness of the electrolyte layer was critical for the measurements, and was varied throughout the data collection. This thickness was determined for each data point by analysis of the peak size of the Ir 4f and water O 1s core levels. The XPS end station used herein has been described in detail previously.[16c, 17]

Calculations were performed using MATLAB. XPS data were analyzed with CasaXPS, IgorPro and Fityk and were plotted with IgorPro.[18]

Results

Figure 1a presents a schematic describing the geometry of the experimental setup and the potential drops in the system. The *operando* AP-XPS experiments allowed determination of the binding energies, E_B, and of the peak widths as the applied potential and thickness of the electrolyte were varied, for different concentrations of KOH(aq). The thickness of the solution layer on the electrode was monitored by analyses of the core-level spectra. Reported binding energies were referenced to the working electrode, which was grounded to the analyzer.[16c, 19] The slope of the change in binding energy, E_B,

with respect to a change in applied potential, $\Delta E_B/\Delta U$, in $eV \cdot V^{-1}$, was measured over a range of potentials, electrolyte concentrations, and electrolyte thicknesses. The peak widths, as either full-width at half maximum [FWHM] or half-width at half maximum [HWHM], were also measured. The Debye length is a function of the ionic strength of the solution. Both the pH and ionic strength are defined by the KOH concentration, so for convenience Figure 2a presents the Debye length as a function of pH.

Figure 3 shows the details of the experiment and describes the variation in the XPS peak position and width as a function of the thickness of the electrolyte layer though which the XPS signal was observed. The binding energy of the XPS signal from a particular core level is a function of the Galvani potential at the position of the emitted electron. The Galvani potential in turn is a function of the ECDL thickness, and the applied potential. Figure 2b shows the expected relative shift of the XPS peak position with pH due to changes in the ECDL thickness as well as due to changes in the thickness of the electrolyte layer.

The photoelectron intensity will decay exponentially with distance from the exposed surface of the electrolyte, as a function of the inelastic mean-free path (IMFP) of the photoelectron (Figure 3b). The observed peak widths and binding energies result from the summation over the ensemble of states observed, each of which will exhibit a slightly different binding energy due to changes in the Galvani potential with position in the solution (Figures 3a, 3c). The observed peak position and width will therefore be a function of the applied potential, the ECDL width, and the thickness of the electrolyte layer on the electrode (Figures 3c, 3d).

Use of the Debye–Hückel approximation, i.e., applying the linearized version of the Poisson-Boltzmann equation to model the ECDL, allows calculation of the half width and peak position that ought to be observed in the XPS signal. In the linearized Poisson-Boltzmann equation for a z-z (for KOH(aq), 1:1) electrolyte, the potential in a liquid (no free charge) satisfies

$$(\nabla^2 - \kappa^2) \cdot \phi = 0 \qquad (1)$$

with

$$\kappa^2 = \frac{4\pi}{\epsilon_b} \sum_i N_i \cdot Z_i^2, \qquad (2)$$

where ϕ is the three-dimensional potential profile, ∇^2 is the Laplace operator, ϵ_b is the bulk dielectric constant, and the electrolyte contains a concentration N_i of species with charges Z_i. For KOH in water, N_1=N_2=10^{pH-14} M and Z_1=-Z_2=1, which results in $\kappa^{-1} \approx 10^{(14-pH)/2}$ x 0.304 nm at room temperature.

As described previously, the theoretical XPS core-level response produced by the potential distribution in the electrolyte can then be calculated for a given potential distribution in the material (obtained here through the linearized Poisson-Boltzmann equation):[16c, 20]

$$I_j(E_B) = \prod_{i>j}^{n} e^{\left(-d_i / \lambda_{i,j} \cdot cos(\theta)\right)} \cdot \int_0^{d_j} e^{\left(-x / \lambda_j \cdot cos(\theta)\right)} \cdot PF\left(\mathrm{E_{pot}}(x), E_B\right) dx \,. \qquad (3)$$

The core-level emission line profile I of the material layer j is simulated by the peak function PF (Voigt peak profile) of a single atomic layer and integrated over its layer depth d_j, where θ is the detection angle (takeoff angle) between the surface normal and

the electron analyzer ($\theta = 0°$ for this investigation). E_{pot} is the calculated potential for each atomic layer. The intensity of this signal is, however, attenuated by the *n-j* top layers, with IMFP λ (Figure 3).

Figure 4 shows calculations for changes in binding energies of the water O 1s core level vs potential, for pH 11.5 and pH 14 electrolytes. Figure 4 also displays the calculated peak widths, including the full-width at half maximum [FWHM] and the half-width at half maximum [HWHM].[16c] For a concentrated electrolyte (compact ECDL), the expected dependence of the binding energy on applied voltage is $\Delta E_B/\Delta U \sim -1$ eV·V^{-1}, whereas for more dilute electrolytes (spatially more extended ECDL) and a thin electrolyte layer, smaller magnitudes of $\Delta E_B/\Delta U$ should be obtained (measured) (Figure 4a). As a result, at pH 14, the binding energy peak, E_B, should shift with applied potential over most electrolyte thicknesses with a slope of ~ -1 eV·V^{-1} (Figure 4a). For lower ionic strength solutions at pH 11.5, the diffuse double layer extends much further from the electrode into the electrolyte, and the peak shift is a stronger function of the thickness of the electrolyte, varying from a small magnitude of about -0.1 to a large magnitude of -0.8 eV·V^{-1}. A maximum appears in the pH 11.5 FWHM and HWHM plots where the thickness approximately corresponds to the expected thickness of electrolyte needed to account for the entire double layer; while also present at pH 14, this thickness is very small. In Figures 4b through 4d, the change in broadening is normalized to the minimum calculated broadening at an applied potential of 0 V.

Figure 5 presents the electrochemical data for the Ir electrodes, which are generally in accord with the previously described electrochemistry of Ir metal in alkaline

solutions.[21] For pH 14, cathodic proton uptake peaks were observed at -0.67 V, -0.75 V, and -0.84 V, and corresponding desorption peaks were observed at -0.65 V -0.72 V, and -0.81 V vs Ag/AgCl. Catalytic current for the hydrogen-evolution reaction (HER) was present for U < -0.95 V vs Ag/AgCl and anodic current was observed for U > 0.45V vs Ag/AgCl. The potentials were restricted to U < 0.45 V to avoid the formation of a substantial surface oxide that would complicate the interpretation of the XPS signals. However, the oxide of Ir is known to be metallic,[22] and the large potential window in which Ir is stable according to its Pourbaix diagram allows for a wide potential range over which this material can be investigated.

Figure 6 shows *operando* AP-XPS spectra for the O 1s for thin and thick electrolyte layers, respectively, at pH 14 in the potential range of -0.7 V to +0.3 V vs Ag/AgCl as well as at pH 11.5 in the range from -0.9 V to +0.1 V vs Ag/AgCl. Figure 7 shows the observed change in binding energy with respect to the applied potential, $\Delta E_B/\Delta U$, for various pH values at a constant electrolyte layer thickness. The observed decrease in the magnitude of $\Delta E_B/\Delta U$ with decreasing pH (more dilute electrolyte) is in accord with the predicted trend. Figure 8 presents data for $\Delta E_B/\Delta U$ and the peak widths, for pH 11.5 and 14, across a range of electrolyte layer thicknesses, comparable to the measurements shown in Figure 4. For each set of Ir 4f and water O 1s core-level scans, the thickness of the electrolyte layer was calculated using the ratio of the peak intensities:

$$\frac{I_A}{I_B} = R = R^{\infty} \cdot \frac{[1-exp(-d/(\lambda_{A,A}\cdot\cos\theta))]}{exp(-d/(\lambda_{B,A}\cdot\cos\theta))} \quad , (4)$$

where I_A and I_B are the intensities for the top and bottom layer, respectively, R^{∞} is the ratio of the intensity factors of the core-level spectra (which is a function of the incident

photon energy), d is the thickness of the top layer, and $\lambda i,j$ is the IMFP of a photoelectron from layer i through layer j. For each set of Ir 4f and O 1s spectra, which were collected simultaneously, the intensity ratio $R=I_{H2O}/I_{Ir}$ was calculated. From these ratios, the thickness of electrolyte present for each data point was calculated, and the data were binned into subgroups of R that corresponded to the various electrolyte thicknesses shown in Figure 8. More information on these calculations, as well as Ir 4f spectra, are presented in the supplementary information.

The binding energies for these two electrolytes shifted with potentials and electrolyte thicknesses in a manner that matched the predictions. For example, the pH 14 electrolyte exhibited $\Delta E_B/\Delta U$ ~ -1 eV·V^{-1} at most ECDL thicknesses, while at pH 11.5, the slope changed substantially as the electrolyte thickness decreased. However, the peak widths in very thin electrolyte regimes were generally smaller for dilute electrolyte (pH 11.5) than for concentrated electrolytes (pH 14). Further details on the workup of data from the *operando* AP-XPS data, as well as calculation of the thickness of the electrolyte, is contained in the supplementary information.

Discussion

For a metallic electrode, no drop in potential occurs inside the electrode (apart from possible surface oxidation at positive potentials), and the change in applied potential occurs instead across the ECDL of the solution. Hence, a 1 V change in potential applied between the working electrode and the reference electrode should produce a -1 eV change in the core level binding energy of the bulk water signal. For concentrated electrolytes, even a substantial voltage drop in the double layer will be difficult to

observe with our XPS method, because the fraction of water within the ECDL is small, so the majority of signal will arise from bulk water. In contrast, for sufficiently thin layers of dilute electrolytes (<0.1 M), the Gouy Chapman diffuse part of the ECDL will extend sufficiently far into the solution that electrolyte in this region will affect the observed binding energy signal. In such electrolytes, the binding-energy shifts observed for the water layer, $\Delta E_B/\Delta U$, should have a smaller magnitude: $-\Delta E_B/\Delta U < 1$ eV·V^{-1}. Changes in the FWHM and HWHM of the water core level AP-XPS signals should also be evident, as described in detail below.

Figure 7 presents the relative slope of binding energies with respect to applied potential, in units of eV·V^{-1}, across a range of pH values at a substantial thickness of electrolyte. The observed relationship between the binding energy and applied potential is in good accord with expectations assuming a Gouy-Chapman type double layer, approaching a value of $\Delta E_B/\Delta U$ = -1 eV·V^{-1} for the highly concentrated electrolytes investigated experimentally.

For pH 14, no dependence of the O 1s water binding energies upon the electrochemical double layer is expected for electrolyte thicknesses greater than a few nm (Figure 4a). Hence, a value of $\Delta E_B/\Delta U$ =-1 eV·V^{-1} is expected between the O 1s water-level binding energies and the applied potential, because the photoelectrons should not sample a large region, as a fraction of the total number collected, of the water molecules subject to the double layer.

Using thickness binning, the expected trend of $\Delta E_B/\Delta U$ = -1 eV·V^{-1} was observed at pH 14. Furthermore, across a broad range of water thicknesses encompassing values

for which no Ir core levels were visible by XPS to those in which the Ir core levels were very intense, $\Delta E_B/\Delta U \sim$ -1 $eV \cdot V^{-1}$ (Figure 8a). In contrast, at pH 11.5, the magnitude of -$\Delta E_B/\Delta U$ decreased with decreasing electrolyte thickness. Hence, the dilute electrolyte concentrations yielded a substantially higher fraction of photoelectrons with binding energies influenced by the diffuse double layer.

Although at most electrolyte thicknesses (outside an extremely narrow thickness range) the core-level water O 1s signal at pH 14 is expected to be narrower than at pH 11.5, for the dilute electrolyte we instead observed lower FWHM peak widths by 0.2 – 0.4 eV. For sufficiently thin electrolyte layers, the peak width of dilute electrolytes is expected to decrease and the peak width of concentrated electrolytes to increase as the electrolyte thickness is reduced. Errors in the calculation of electrolyte thickness, combined with various sources of noise in the experiment, could potentially result in a peak width and electrolyte thickness that falls outside of predicted trends, pending further refinement of the model. Furthermore, most of the width difference in the FWHM originates in the $HWHM^-$ side of the core level peak, whereas the pH 14 core levels are narrower on the higher binding energy half of the peak, $HWHM^+$, suggesting that the data for the $HWHM^+$ side of the core level are better described by the model than the data on the $HWHM^-$ side of the core level peak. The increased width on the HWHM- side may therefore be ascribed to other components within the XPS spectra such as hydroxide ions, adsorbed water, and other lower binding energy components. Further investigations might include biological systems and other interfaces where the behavior of the double layer has yet to be defined in full experimentally.

Conclusion

In conclusion, *operando* AP-XPS has yielded direct information on the potential distribution of the electrolyte double layer as well as information on the energetics of the electrode/electrolyte interface. An isopotential at a working electrode surface can be maintained even in dilute electrolytes, allowing for full three-electrode electrochemistry to be performed under such conditions. The behavior of various electrolyte thicknesses has been probed directly to better define the nature of the electrochemical double layer.

Acknowledgments

This work was supported through the Office of Science of the U.S. Department of Energy (DOE) under award no. DE SC0004993 to the Joint Center for Artificial Photosynthesis, a DOE Energy Innovation Hub. The Advanced Light Source is supported by the Director, Office of Science, Office of Basic Energy Sciences, of the U.S. Department of Energy under Contract No. DE AC02 05CH11231. The authors thank Dr. Philip Ross for contributions to the conceptual development of the *operando* AP-XPS end station and experimental design. The authors thank Ethan Crumlin, Jonathan Thompson, Jonathan C. Crompton, and Paul Nunez for assistance with data collection.

Data availability

The data that support the findings of this study are available from the corresponding author upon request.

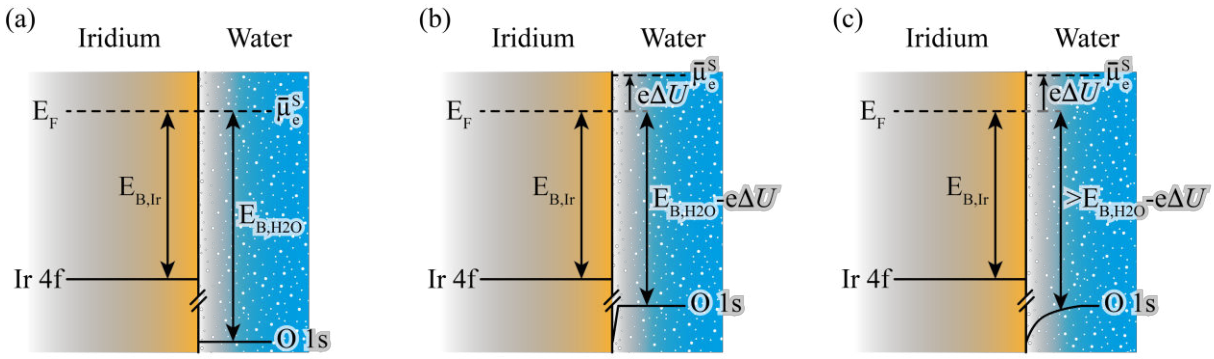

Figure 1. Schematic description of the band alignment for a metal electrode in contact with an electrolyte solution. (a) A system having a minimal contact potential difference between the Fermi level of the metal and the electrochemical potential of the solution; (b) a system in contact with a concentrated electrolyte with an applied potential, *U*; (c) the same system in contact instead with a dilute electrolyte. The binding energy changes as a function of distance from the interface are shown for the O 1s core level. The experiment collects photoelectrons from the electrolyte side of the interface. The shaded overlays show the relative count rate of the collected photoelectron data, in which the darker regions contribute more to the XP signal intensity whereas the signals from the lighter regions are more attenuated.

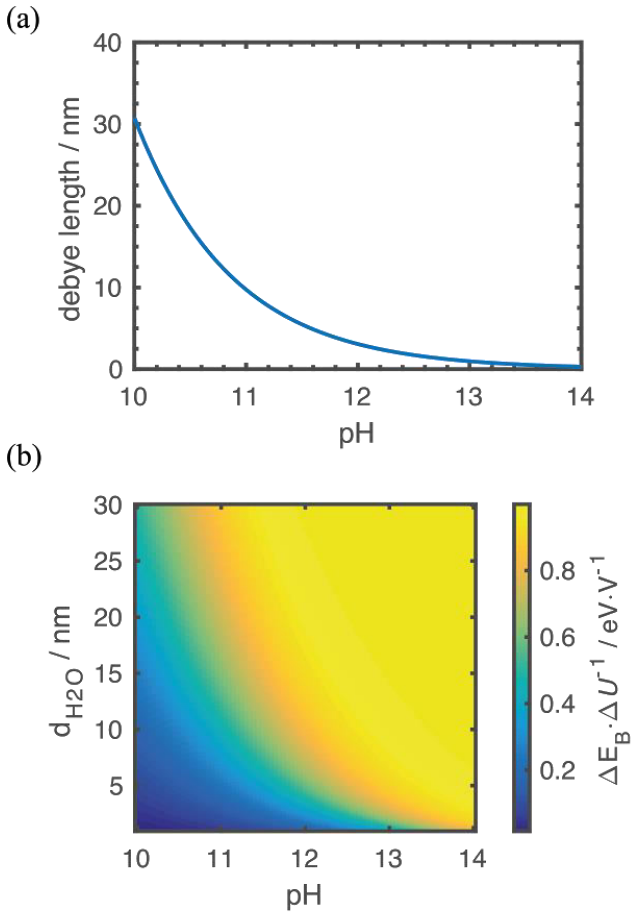

Figure 2. (a) Debye length as a function of pH in various concentations of KOH(aq) as the electrolyte. (b) The expected slope of the binding energy with respect to applied potential, $\Delta E_B/\Delta U$, plotted as a function of pH and electrolyte layer thickness. Even at pH 11, a substantial decrease in the binding energy vs. applied potential slope can be observed only for very thin electrolyte/solution layers.

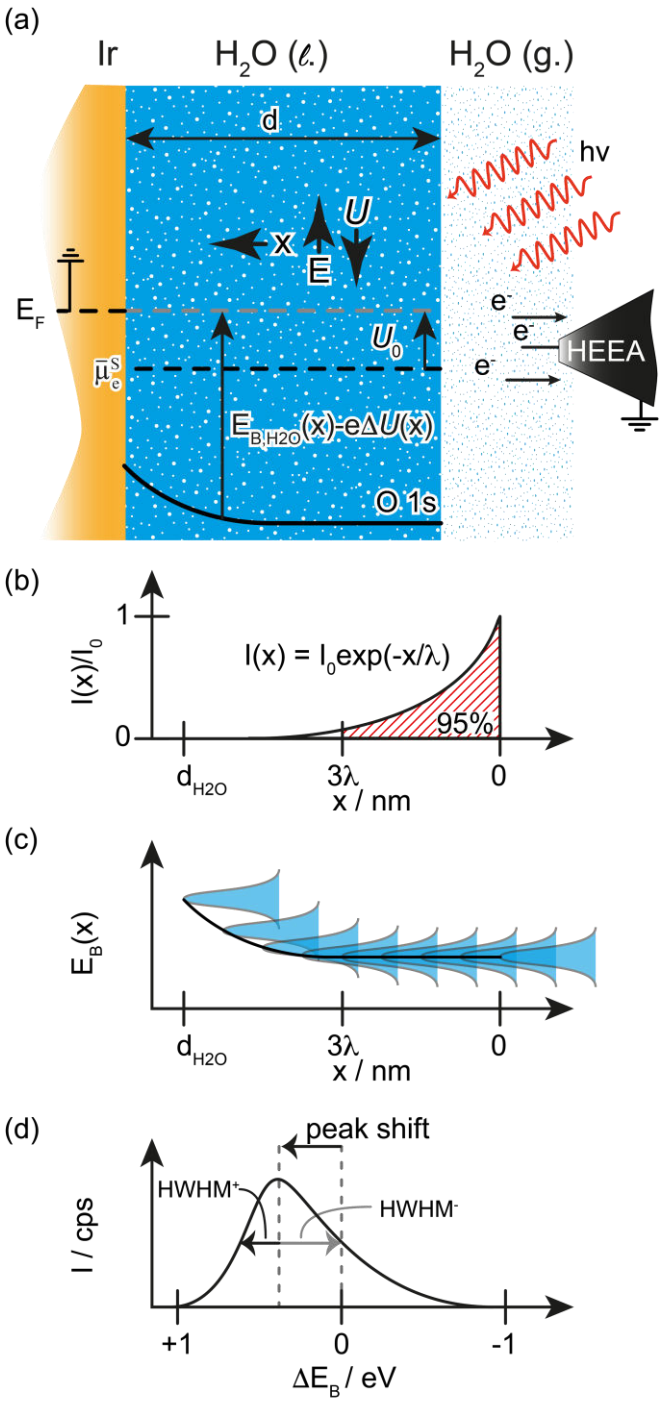

Figure 3*:* Schematic of the *operando* XPS energy relations of a liquid/metal junction under applied bias (a). The X-ray excited photoelectrons are collected by the hemispherical electron energy analyzer (HEEA). The thickness of the electrolyte is *d*. (b) Exponential decay of the intensity of the XP signal with distance from the exposed

surface of the electrolyte, *x*. Approximately 95% of the overall intensity arises from a depth of 3 x IMFP from the exposed electrolyte surface. (c) The core-level binding energy as a function of *x*. The binding energy peak follows the Galvani potential. (d) The asymmetric core-level peak profile resulting from the summation over the ensemble of XP signals from a given core level. The diagram shows the half width at half maxima on both the high energy, $HWHM^{+}$, and low energy, $HWHM^{-}$, sides, as well as the peak shift.

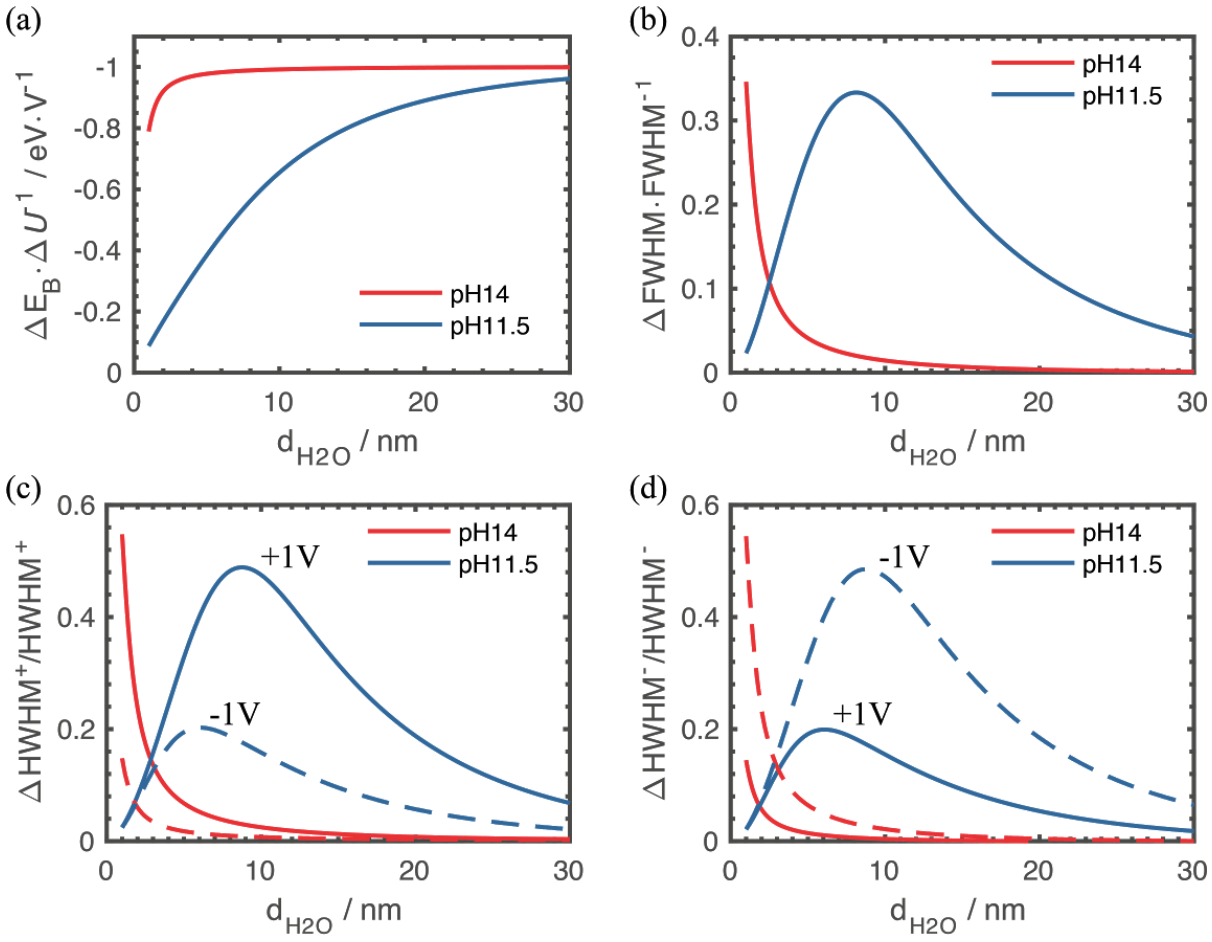

Figure 4. (a) Slope of change in binding energy with potential, $\Delta E_B/\Delta U$, vs thickness of electrolyte, for the water O 1s peak at pH 11.5 and 14, respectively. (b) Calculation of the normalized change in FWHM of the water O 1 peak with respect to electrolyte thickness. The change is normalized by the minimum calculated FWHM. (c,d) Same calculation as (b) for the change in $HWHM^+$ (higher binding energy half width half maxima, see Fig. 3c) and $HWHM^-$ (lower binding energy half width half maxima, see Fig. 3c), and with two applied potentials, U = 1.0 V (solid line) and U = -1.0 V (dashed line). The ionic strengths at pH 14 and pH 11.5 KOH(aq) were 1.0 M and 3.16 mM, respectively.

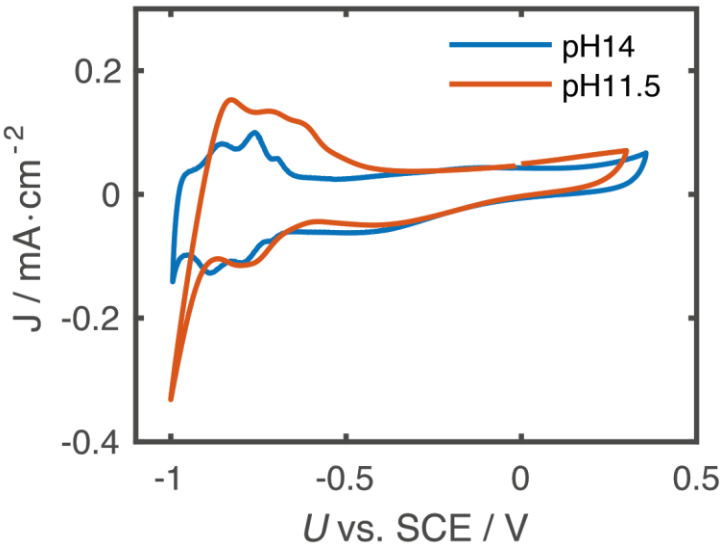

Figure 5. Cyclic voltammogram of Ir metal in pH 14 and 11.5 KOH(aq), respectively, in the AP-XPS chamber. For pH 14, proton uptake peaks were observed at U = -0.67 V, -0.75 V, and -0.84 V vs Ag/AgCl, whereas desorption peaks were observed at U = -0.65 V, -0.72 V, and -0.81 V vs Ag/AgCl. Catalytic current for the HER was observed for U > -0.95 V vs Ag/AgCl and OER current was observed for U > 0.45 V vs Ag/AgCl.

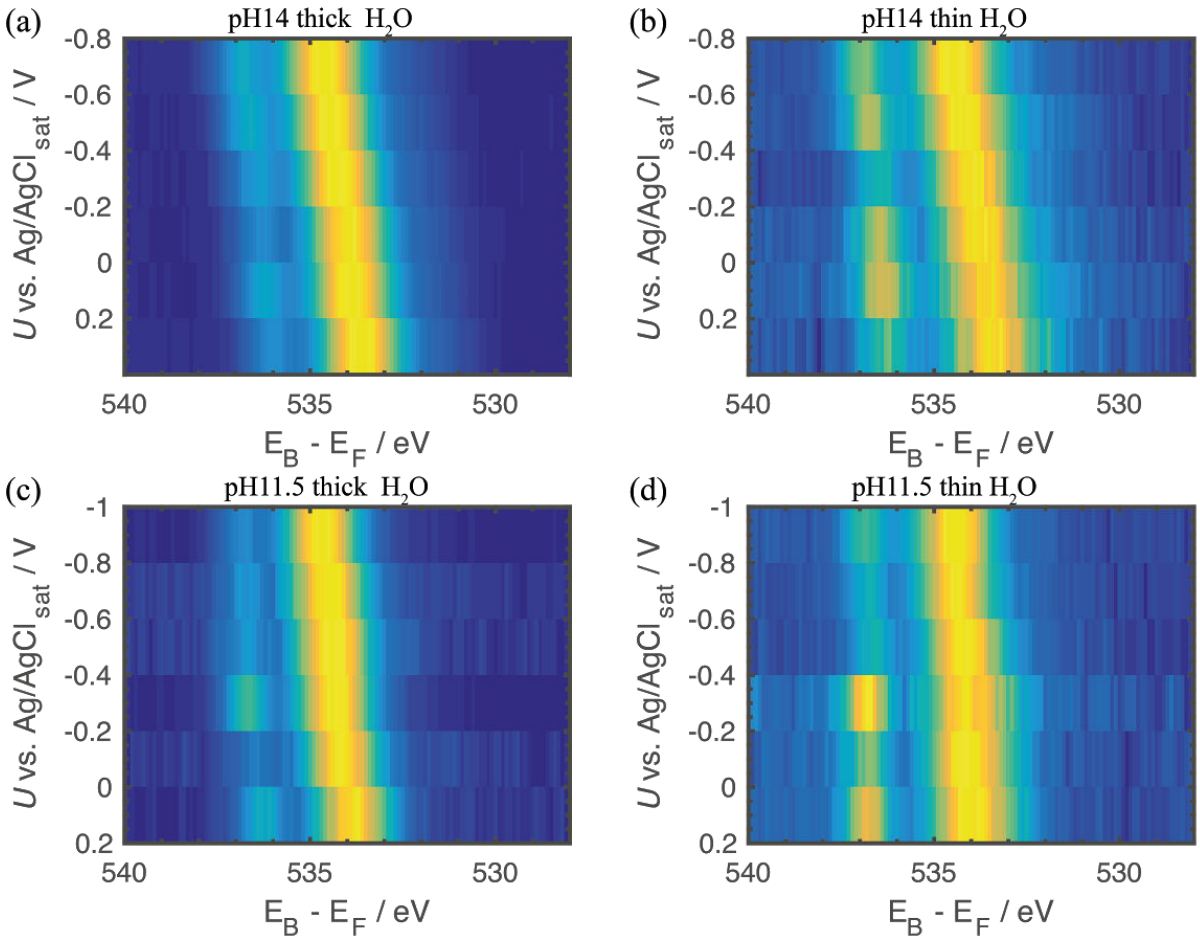

Figure 6. Two dimensional color plots of *operando* AP-XPS count-rate data for potentials of -0.7 V to +0.3 V vs Ag/AgCl for (a) the O 1s core level with a thick layer of electrolyte at pH 14 and (b) the O 1s core level with a thin electrolyte layer at pH 14. Corresponding data for potentials from -0.9 V to +0.1 V vs Ag/AgCl in (c) a thick electrolyte at pH 11.5; (d) O 1s core level with a thin electrolyte at pH 11.5. For a thick electrolyte, minimal Ir 4f intensity was observed, whereas the Ir 4f intensity was maximized for a thin electrolyte.

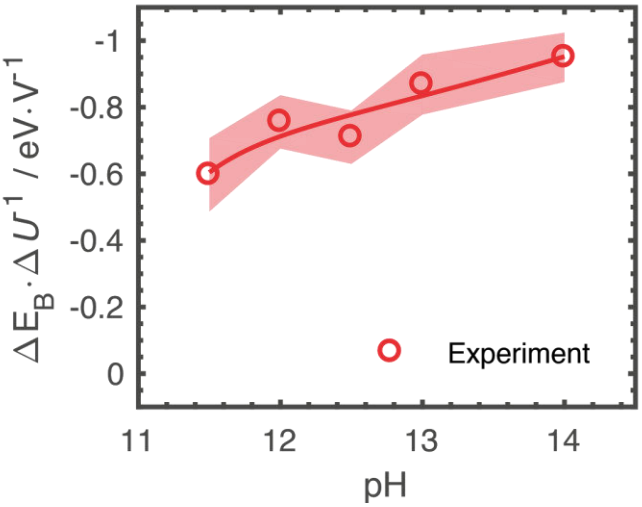

Figure 7. Plot of $\Delta E_B/\Delta U$ for a range of pH values at an electrolyte thickness of >30 nm, from the water O 1s peak.

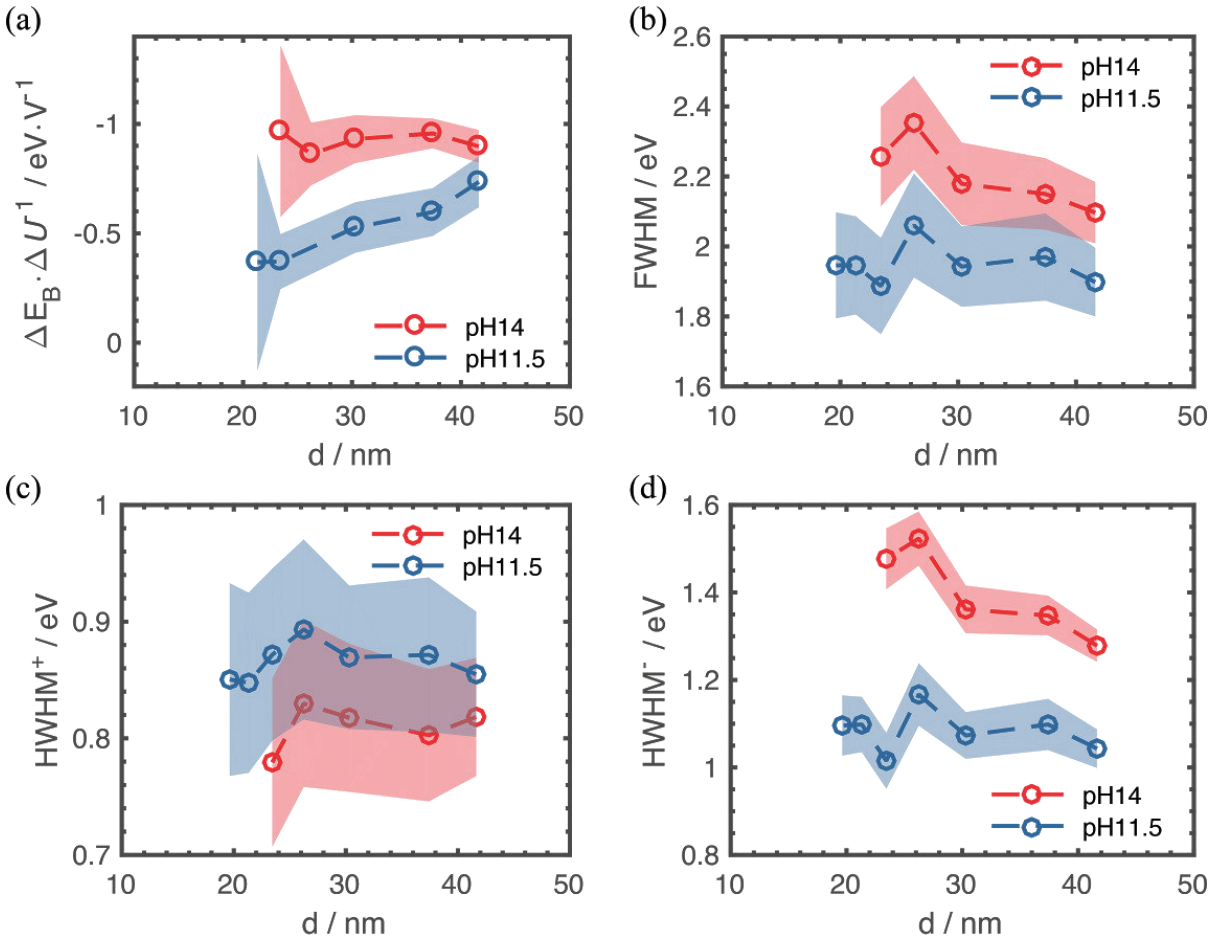

Figure 8. (a) Plot of $\Delta E_B/\Delta U$ for pH 11.5 and pH 14 across a range of low and intermediate electrolyte layer thicknesses. (b) Plot of FWHM, (c) $HWHM^+$, and (d) $HWHM^-$ for various low and intermediate electrolyte layer thicknesses for pH 11.5 and pH 14.

Supporting Information:

Table of Contents

I. Water layer Thickness determination from XPS core levels

For a two-layer structure (layer A on layer B, see Figure S1) the thickness, *d*, of layer A can be experimentally determined by XPS using the knowledge of the inelastic mean-free path (IMFP, λ) of the photoelectrons in conjunction with the XPS core-level intensity ratio of an infinitely thick single layer, $R^{\infty} = {I_A^{\infty}}/{I_B^{\infty}}$. The overall XPS Intensity from a core-level layer A with a mean free path of $\lambda_{A,A}$ is given by:

$$I_A = I_A^{\infty}\left[1 - exp\left(-d/(\lambda_{A,A} \cdot \cos\theta)\right)\right], \qquad \text{(S1)}$$

where θ is the photoelectron take-off angle with respect to the surface normal. For this investigation, θ was 0° and cos(0°) = 1. Analogously, the overall intensity of photoelectrons originating from a core level in layer B with mean free path of $\lambda_{B,A}$ through layer A is given by:

$$I_B = I_B^{\infty} \cdot exp\left(-d/(\lambda_{B,A} \cdot \cos\theta)\right), \qquad \text{(S2)}$$

The thickness d of layer A can already be calculated by use of either equation S1 or S2, is experimental conditions are stable. However, if fluctuation in the photon flux or clogging of the differentially pumped HEEA nozzle is expected, calculating the thickness *d* based on the ratio $R = {I_A}/{I_B}$ is better practice, as instabilities that appear on a longer time scale than the actual measurement will not affect the thickness determination (equation S3):

$$\frac{I_A}{I_B} = R = R^{\infty} \cdot \frac{[1-exp(-d/(\lambda_{A,A}\cdot\cos\theta))]}{exp(-d/(\lambda_{B,A}\cdot\cos\theta))} \quad . \qquad \text{(S3)}$$

The process is illustrated in Figure S1.

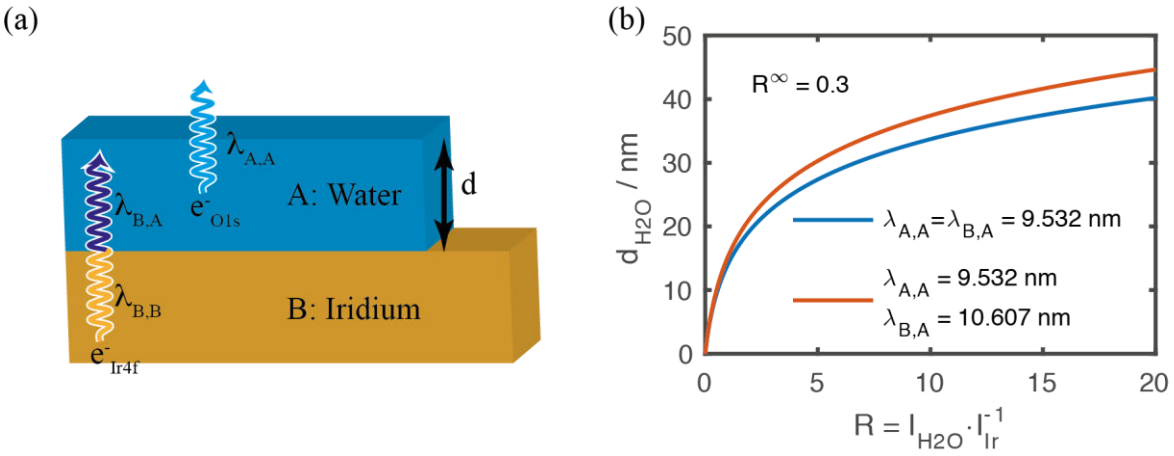

Figure S1: (a) illustration for the determination of the thickness d_{H2O} of the water layer on top of a metal iridium surface. $\lambda_{A,A}$, $\lambda_{B,B}$, $\lambda_{B,A}$ depict the inelastic mean free path of for photoelectron from O 1s core level through water ($\lambda_{A,A}$) and the Ir 4f core level though Ir ($\lambda_{B,B}$,) and water ($\lambda_{B,A}$). (b) Calculated water thickness d_{H2O} for various ratios of $R=I_{H2O}/I_{Ir}$ for two different conditions: $\lambda_{A,A} = \lambda_{B,A}$ (blue curve) and $\lambda_{A,A} \neq \lambda_{B,A}$. The obtained thickness is independent of the value of $\lambda_{B,B}$.

Values of the IMFP for photoelectrons from Ir 4f ($\lambda_{B,A}$ for E_{kin} = 3939 eV) and O 1s ($\lambda_{A,A}$ for E_{kin} = 3466 eV) core levels through water were calculated using IMFP-TPP2M[23]

using the following material parameters for water: 1 g·cm^{-3} bulk density; 6.9 eV band gap; 4 HBE (H 1s + O 2s); 4 LBE (O 2p).

During recording of both spectra, the reference intensities for an infinitely thick layer of Iridium I_B^{∞} and water I_A^{∞} under a constant pressure of 18 mTorr H_2O (g.) were measured to minimize photon flux instabilities of the X-ray beam and other disturbances that could influence the overall signal intensity. Both reference spectra for the Ir 4f core level of hydrated Ir and water are given in Figure S2. An experimental value of R^{∞}=0.3±0.1 was determined for this experiment.

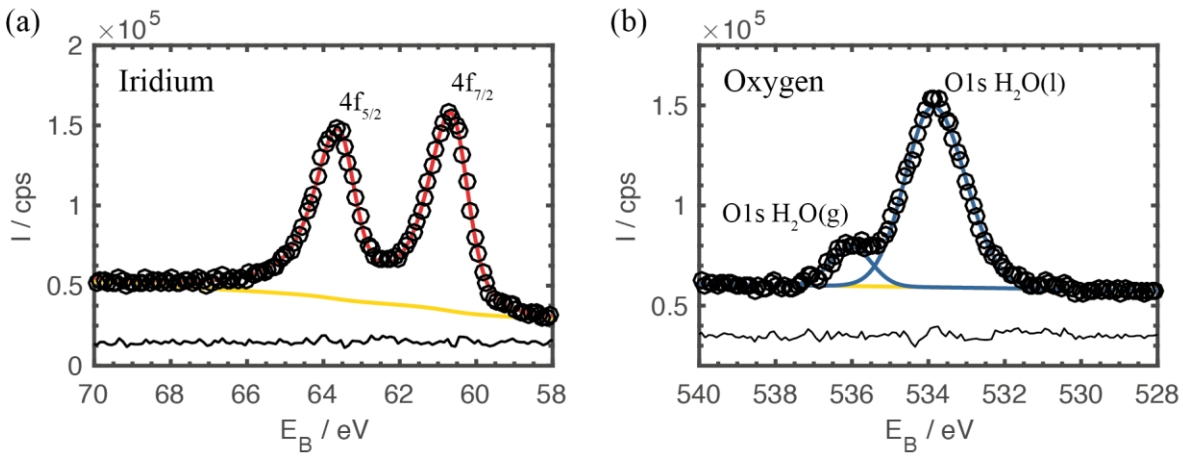

Figure S2: XPS spectra used for calculating of R^{∞}. The reference spectra of a hydrated (18 mTorr H_2O (g)) Ir surface is shown in (a) whereas the spectra for a thick water layer is given in (b). The residual signal after fitting is shown at the bottom of each spectrum.

II. XPS data analysis:

Each single pair of Ir 4f and O 1s core-level spectra (899 pairs in total) for different combinations of pH (11.5,12, 12.5 ,13, 14), water-layer thickness, and applied potentials between -0.9 V and +0.3 V vs Ag/AgCl was fitted with an automated algorithm in Fityk[18]. For Ir 4f the spin-orbit splitting was fixed to 2.98 eV[24] with an area ratio of the $f_{5/2}$ to $f_{7/2}$ core level of 3:4. Asymmetric Voigt peak profiles were used to account for the core-level tail.

For the O 1s core level, symmetric Voigt profiles were used for the O 1s (H_2O (g)) core level and asymmetric Voigt profiles were used for the O 1s (H_2O (l)) core level, to account for potential dependent peak broadening.

For each set (pair) of O 1s and Ir 4f core level signals, which were measured at the same time under nominally the same conditions, the intensity ratio $R = {I_{H2O}}/{I_{Ir}}$ was

calculated. Results for a fixed subrange of R were binned ($\frac{i}{10} \leq R^{-1} < \frac{i+1}{10}\Big|_{i=0..9}$) and assigned/grouped to a single average intensity ratio (water thickness as calculated by equation S3). Results for pairs of O 1s and Ir 4f spectra that displayed binding energy errors > 0.08 eV for the O 1s core level were discarded. For each thickness group, the potential-dependent slope (Δ) of the core-level shift, the FWHM, the $HWHM^+$ and the $HWHM^-$ for the O 1s (H_2O (l)) core level was determined for a constant pH value (11.5, 12, 12.5, 13, and 14).

Values for $\Delta(d_{H2O}, pH)$, $FWHM(d_{H2O}, pH)$, $HWHM^+(d_{H2O}, pH)$, and $HWHM^-(d_{H2O}, pH)$ were thus obtained (see Figure 8 of main text). Statistical errors were calculated for each data point.

III. Ir 4f XPS data:

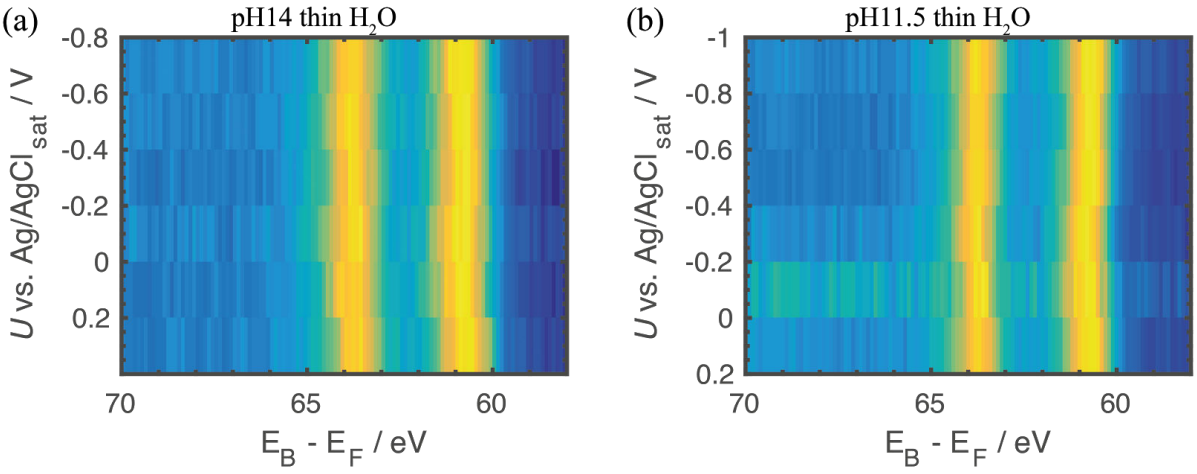

Figure S3: Ir 4f plots across a range of potentials for thin electrolyte layers at (a) pH 14 and (b) pH 11.5.

References

1. Lichterman, M. F.; Richter, M. H.; Brunschwig, B. S.; Lewis, N. S.; Lewerenz, H.-J., Operando X-ray photoelectron spectroscopic investigations of the electrochemical double layer at Ir/KOH(aq) interfaces. *Journal of Electron Spectroscopy and Related Phenomena* **2017,** *221* (Supplement C), 99-105.
2. Kolb, D. M., An atomistic view of electrochemistry. *Surface Science* **2002,** *500* (1–3), 722-740.
3. Sharma, P.; Bhatti, T. S., A review on electrochemical double-layer capacitors. *Energy Conversion and Management* **2010,** *51* (12), 2901-2912.
4. Waegele, M. M.; Chen, X.; Herlihy, D. M.; Cuk, T., How Surface Potential Determines the Kinetics of the First Hole Transfer of Photocatalytic Water Oxidation. *J. Am. Chem. Soc.* **2014,** *136* (30), 10632-10639.
5. Blank, M., *Electrical double layers in biology*. Plenum Press: 1986.
6. Helmholtz, H., Ueber einige Gesetze der Vertheilung elektrischer Ströme in körperlichen Leitern mit Anwendung auf die thierisch-elektrischen Versuche. *Annalen der Physik* **1853,** *165* (6), 211-233.
7. Gouy, M., Sur la constitution de la charge électrique à la surface d'un électrolyte. *J. Phys. Theor. Appl.* **1910,** *9* (1), 457-468.
8. Chapman, D. L., LI. A contribution to the theory of electrocapillarity. *Philosophical Magazine Series 6* **1913,** *25* (148), 475-481.
9. Stern, O., The theory of the electrolytic double shift. . *Z. Elektrochem. Angew. Phys. Chem* **1924,** *30*, 508-516.
10. Bockris, J. O. M.; Devanathan, M. A. V.; Muller, K., On the Structure of Charged Interfaces. *The Royal Society Proceedings A* **1963,** *274* (1356).
11. Wang, H.; Pilon, L., Intrinsic limitations of impedance measurements in determining electric double layer capacitances. *Electrochimica Acta* **2012,** *63* (0), 55-63.
12. Brown, M. A.; Beloqui Redondo, A.; Sterrer, M.; Winter, B.; Pacchioni, G.; Abbas, Z.; van Bokhoven, J. A., Measure of Surface Potential at the Aqueous–Oxide Nanoparticle Interface by XPS from a Liquid Microjet. *Nano Lett.* **2013,** *13* (11), 5403-5407.
13. Hansen, G. J.; Hansen, W. N., Infrared spectroscopy of the electrochemical double layer via electrode emersion. *Berichte der Bunsengesellschaft für physikalische Chemie* **1987,** *91* (4), 317-320.
14. Kolb, P. M.; Rath, D. L.; Wille, R.; Hansen, W. N., An ESCA Study on the Electrochemical Double Layer of Emersed Electrodes. *Berichte der Bunsengesellschaft für physikalische Chemie* **1983,** *87* (12), 1108-1113.
15. Favaro, M.; Jeong, B.; Ross, P. N.; Yano, J.; Hussain, Z.; Liu, Z.; Crumlin, E. J., Unravelling the electrochemical double layer by direct probing of the solid/liquid interface. *Nature Communications* **2016,** *7*, 12695.
16. (a) Stephanus Axnanda, E. J. C., Baohua Mao, Sana Rani, Rui Chang, Zhi Liu, Philip N Ross, Zahid Hussain, Ambient-Pressure "Tender" X-Ray Photoelectron Spectroscopy (APXPS) for in Situ study of Liquid-Solid Interface of Pt Foil in 6 M KF. *J. Electrochem. Soc.* **2013**, 921; (b) Axnanda, S.; Crumlin, E. J.; Mao, B.; Rani, S.;

Chang, R.; Karlsson, P. G.; Edwards, M. O. M.; Lundqvist, M.; Moberg, R.; Ross, P.; Hussain, Z.; Liu, Z., Using "Tender" X-ray Ambient Pressure X-Ray Photoelectron Spectroscopy as A Direct Probe of Solid-Liquid Interface. *Sci. Rep.* **2015,** *5*; (c) Lichterman, M. F.; Richter, M. H.; Hu, S.; Crumlin, E. J.; Axnanda, S.; Favaro, M.; Drisdell, W.; Hussain, Z.; Mayer, T.; Brunschwig, B.; Lewis, N. S.; Lewerenz, H. J.; Liu, Z., (Invited) Investigation of the Si/TiO2/Electrolyte Interface Using Operando Tender X-ray Photoelectron Spectroscopy. *ECS Transactions* **2015,** *66* (6), 97-103.

17. Lichterman, M. F.; Richter, M. H.; Hu, S.; Crumlin, E. J.; Axnanda, S.; Favaro, M.; Drisdell, W.; Hussain, Z.; Brunschwig, B. S.; Lewis, N. S.; Liu, Z.; Lewerenz, H.-J., An Electrochemical, Microtopographical and Ambient Pressure X-Ray Photoelectron Spectroscopic Investigation of Si/TiO2/Ni/Electrolyte Interfaces. *J. Electrochem. Soc.* **2016,** *163* (2), H139-H146.

18. Wojdyr, M., Fityk: a general-purpose peak fitting program. *Journal of Applied Crystallography* **2010,** *43* (5 Part 1), 1126-1128.

19. Lichterman, M. F.; Sun, K.; Hu, S.; Zhou, X.; McDowell, M. T.; Shaner, M. R.; Richter, M. H.; Crumlin, E. J.; Carim, A. I.; Saadi, F. H.; Brunschwig, B. S.; Lewis, N. S., Protection of inorganic semiconductors for sustained, efficient photoelectrochemical water oxidation. *Catalysis Today* **2016,** *262*, 11-23.

20. Richter, M. H.; Lichterman, M. F.; Hu, S.; Crumlin, E. J.; Mayer, T.; Axnanda, S.; Favaro, M.; Drisdell, W.; Hussain, Z.; Brunschwig, B.; Lewis, N. S.; Liu, Z.; Lewerenz, H. J., (Invited) Measurement of the Energy-Band Relations of Stabilized Si Photoanodes Using Operando Ambient Pressure X-ray Photoelectron Spectroscopy. *ECS Transactions* **2015,** *66* (6), 105-113.

21. Jaksic, M. M.; Johansen, B.; Tunold, R., Electrochemical behaviour of iridium in alkaline and acidic solutions of heavy and regular water. *International Journal of Hydrogen Energy* **1994,** *19* (4), 321-335.

22. Fengyan, Z.; Robert, B.; Greg, S.; Wei, P.; Deli, W.; Sheng-Teng, H., Synthesis of Metallic Iridium Oxide Nanowires via Metal Organic Chemical Vapor Deposition. *Japanese Journal of Applied Physics* **2005,** *44* (3L), L398.

23. Tanuma, S.; Powell, C. J.; Penn, D. R., Calculations of electron inelastic mean free paths. V. Data for 14 organic compounds over the 50–2000 eV range. *Surface and Interface Analysis* **1994,** *21* (3), 165-176.

24. Briggs, D., Handbook of X-ray Photoelectron Spectroscopy C. D. Wanger, W. M. Riggs, L. E. Davis, J. F. Moulder and G. E.Muilenberg Perkin-Elmer Corp., Physical Electronics Division, Eden Prairie, Minnesota, USA, 1979. 190 pp. $195. *Surface and Interface Analysis* **1981,** *3* (4), v-v.

V. Probing Buried III-V Interfaces by Raman Spectroscopy

This manuscript is being pushed toward publication at the date that this thesis was submitted, and will likely be in review prior to graduation.

Abstract

We demonstrate the use of Raman spectroscopy to analyze the band-bending present at buried III-V semiconductor junctions. While XPS may be used to analyze the near-surface energetics of semiconductor systems under applied bias, Raman spectroscopy allows for the delineation of semiconductor band energetics even in the case of deeply buried junctions. Herein we examine the bend energetics present in GaAs junctions formed with Au and TiO_2, and from these results demonstrate that in addition to band energetics, the influence of high injection carrier generation at different junctions may be analyzed through this method.

Introduction

The III-V semiconductor family forms the basis of many high efficiency photovoltaics currently produced.[1] This family contains zincblende and wurtzite materials composed of elements from groups III and V of the periodic table such as InP and GaAs, their tertiary allows such as AlGaAs or InGaAs, and quaternary alloys. The ability to produce many alloys of varied compositions provides a range of materials with which multi-junction devices that are well-matched to the solar spectrum as well as internally lattice-matched may be constructed. Decades of research into the production of high-quality III-V binary, tertiary, and quaternary films, tunnel junctions, and related aspects of such photovoltaics have allowed such cells to reach efficiency records as high as 46% for multi-junction cells with concentrated sunlight, 38.8% for multi-junction cells under one sun, and 28.8% for single junction cells under one sun.[1-2] Furthermore, recent work has demonstrated promise for the utilization of III-V structures in photoelectrochemical devices which directly convert sunlight into chemical fuels due to the ability of the III-V materials to deliver the necessary voltage to drive the relevant electrochemical reactions[3]. Much of this work has been enabled by the use of conformal coatings of transparent and conductive protective layers of metal-oxides, such as TiO_2, which inhibits chemical corrosion of the semiconductor material in the relevant electrolyte[4].

Raman spectroscopy can be utilized to ascertain the nature of the band bending at III-V semiconductor interfaces, which is of crucial importance to the design of more efficient photovoltaic or photoelectrochemical systems as the band bending present in these junctions provides the driving force for the separation of charges in photoactive materials. The band bending modulates the spectrum observed from the inelastic

scattering of the first order zone-center optical phonon modes. The longitudinal optical (LO) phonon mode is polarized parallel to the surface normal and thus should not effectively couple to incident excitation. However, coupling to a LO phonon mode is observed in the depletion region due to lattice deformation, this mechanism is known as deformation-potential (DP) scattering. Additionally, the bulk, there is coupling between the LO phonon mode and plasmon modes due to the presence of free carriers, and the LO phonon mode is split, and two coupled plasmon-LO phonon (PLP) modes, L+ and L-, are observable. Thus, intensities of the LO phonon and PLP modes are both a function of the depletion width. Additionally, the frequencies of the PLP modes depend on the concentration of free carriers and the thus the doping of the sample. The transverse optical (TO) phonon mode is polarized perpendicular to the surface normal and displays invariant, nonzero intensity. Thus, the ratios of the LO phonon and of the PLP modes to the TO phonon mode can provide a quantitative description of the size of the space charge region and, as a result, the voltage that it represents.[5]

In many cases, *in-situ* experiments have been done in UHV chambers, allowing for dosing of a gas to a clean semiconductor surface[6]; in others, near-surface interfaces of GaAs/Ge and other materials have been investigated[7]. Herein, we demonstrate that this approach can be expanded and that such results, when modeled appropriately, communicate important information of recombination rates at the semiconductor interface. The use of an applied potential as well as comparison of the Raman data to the observed quantum yields provides a more complete view of the nature of the semiconductor interface than that provided by simply the Raman data or the electrical

data alone. We demonstrate these results through a comparison of a Au/GaAs schottky diode and a "protected" TiO_2/GaAs semiconductor interface system.

Result and Discussion

A general schematic for the analysis of the GaAs LO and TO phonon intensities is demonstrated in Figure 1. Laser excitation was delivered normal to the sample surface and collected in a 180° backscatter geometry. An external bias is applied using pair of conductive ohmic contacts and the applied potential was varied systematically. A representative Raman spectrum at $U_{applied}$ = 2.5 V is shown in Figure 2a. The L^+ PLP mode was observed at ca. 300 cm^{-1} and displayed increased intensity at potentials approaching the flatband potential (U_{FB}). For n-GaAs(111)/Au/ITO, U_{FB} was found to be -.95V from Mott-Schottky measurements; identical measurements on n-GaAs(111)/TiO_2/Ni/Au/ITO returned U_{FB} = -.65. The coupled L^- mode would be expected near 150 cm^{-1} at this dopant density but was difficult to identify definitively due to spectral interference from a second-order acoustic phonon mode.[8] The TO and LO phonon modes were observed at 269 and 292 cm^{-1}, respectively. Figure 2c shows the progression of such peaks as applied potential is varied. Figure 3a shows representative current-voltage plots obtained using n-GaAs(111)/Au/ITO and n-GaAs(111)/TiO_2/Ni/Au/ITO devices. Figure 3b shows the corresponding internal quantum efficiency (IQE) values from the Raman experiments for various laser powers. Mott-Schottky plots for these systems are shown in the supplementary information.

Figure 4 shows contour plots for the LO/TO ratio for representative n-GaAs(111)/Au/ITO and n-GaAs(111)/TiO_2/Ni/Au/ITO devices with applied biases from 0.45 V to 3.00 V vs. U_{FB} for and 0.40 V to 3.00 V vs. U_{FB}, respectively. Notably, the

ratio at a given potential is effectively constant across all illumination powers used herein for the n-GaAs(111)/Au/ITO samples. In contrast, the n-GaAs(111)/TiO_2/Ni/Au/ITO samples show a substantial decrease of the LO/TO ratio at each potential as illumination power is increased. For the higher illumination powers, the LO/TO ratios observed herein are nearly constant across the entire voltage range. At lower illumination intensities, the LO/TO ratios increase with potential, albeit slower than is the case across the n-GaAs(111)/Au/ITO samples.

For a semiconductor with static dielectric constant ε, carrier density N and space charge voltage V, the space charge region has a width defined by

$$W = \sqrt{\frac{2\varepsilon V}{qN}}, \qquad (1)$$

where q is the magnitude of charge on an electron. For a semiconductor and wavelength combination with absorption coefficient α, the intensities of the LO and TO phonons can be related to the voltage in the space charge region with the following equation (assuming all LO intensity is due to DP scattering):

$$\frac{I_{LO}}{I_{TO}}(V) = \frac{I_{LO}}{I_{TO}}(V_\infty)[1\text{-}\exp(-2\alpha\sqrt{\frac{2\varepsilon V}{eN}})], \qquad (2)$$

where the intensity ratio for voltage V_∞ is that for a reference sample in which the space charge region may be considered to extend throughout the entirety of the sampling region. In practice, a semi-insulating sample of otherwise identical face and material is suitable for this purpose. Equation 2 may be rearranged to provide the voltage as

$$V = (eN/2\varepsilon)(\ln[(\frac{I_{LO}}{I_{TO}}(V) - \frac{I_{LO}}{I_{TO}}(V_\infty))/\frac{I_{LO}}{I_{TO}}(V_\infty)]/-2\alpha)^2 \ . \qquad (3)$$

The voltage related by Equation 3 in a semiconductor system wherein a voltage across the space charge region is defined by applying an external bias potential will be

equal to the sum of the applied bias and the built-in voltage of the junction (assuming surface photovoltage effects are negligible). Using Equation 3, and a value of 0.40 V for V_∞ as observed from a calibrating sample, the observed voltage in the space charge region (U_{SCR}) has been calculated for the different samples, as shown in Figure 5a. The observed voltage tracks well with the potential positive of the flat-band potential for n-GaAs(111)/Au/ITO. For n-GaAs(111)/TiO_2/Ni/Au/ITO, the observed decrease in the LO/TO ratios correlate directly as flattening of the bands, to a degree such that at high illumination power, there is only minimal (< 0.1 V) band bending for any potential applied. At lower intensities, the voltage observed in the space charge region remains substantially smaller than that which was the case for the n-GaAs(111)/Au/ITO samples. The difference between the observed voltage in the space charge region and that which would be predicted from the sum of the applied voltage and the flat-band voltage, termed V_{lost}, is shown in Figure 5b. The magnitude of V_{lost} measured for the n-GaAs(111)/Au/ITO device is substantially smaller than that measured for the n-GaAs(111)/TiO_2/Ni/Au/ITO, indicating the relative inferiority of the n-GaAs/TiO_2 junction to that of the n-GaAs/Au Schottky barrier.

While it may initially seem reasonable, if one assumes that any surface photovoltage observed originates from recombination in the closed circuit, to conclude that the size of U_{SCR} would track proportionally with the quantum yield at each potential and laser power – such that the observed U_{SCR} would be larger for sample in which recombination of photoinduced carriers is minimized – this alone is not the case. As shown in Figure 3, while at high power n-GaAs(111)/TiO_2/Ni/Au/ITO does indeed suffer relative to n-GaAs(111)/Au/ITO in terms of internal quantum efficiency, indicating

substantial recombination of the photogenerated carriers which leads to band flattening in the GaAs side of the junction, at low powers and moderate to higher potentials the TiO_2 containing sample is in fact superior in terms of internal quantum efficiency (UV-Vis data is contained in Figure SX in the supplementary information). Thus, changes in the photocurrent or quantum efficiency alone do not fully explain the difference in observed U_{SCR}. We investigate this by plotting the fractional lost voltage, $U_{SCR}/U_{expected}$, against the percent of charges recombined, calculated as 1-IQE in Figure 6. Whereas the n-GaAs(111)/Au/ITO sample has a small cluster of points all located near 10% recombination as a result of the relatively uniform response of the diode to varying intensities of light, the increased recombination of the n-GaAs(111)/TiO_2/Ni/Au/ITO sample may be clearly observed in that the percentage of voltage lost increases as light intensity is increased as opposed to simply holding constant or decreasing, as would be expected for a fixed, nominal amount of voltage lost due to Fermi level pinning. The high minimal value of U_{loss}, even in the case of very low recombination/high IQE (IQE > 0.95), indicates that Fermi level pinning is present here; however, the added losses that are observed by the Raman experiment furthermore indicate that recombination at the junction becomes crucial, as recombination that occurs here will be observed in the U_{loss} and U_{loss} fractions, which is the case here.

In order to validate the conclusions derived from the empirical data, computer modeling of the experimental devices was performed. Using a depletion approximation as well as parameterizing the light absorption to model a steady state concentration of photocarriers, it was observed that the experimental results for U_{SCR} are justified through theoretical calculations (Figure 7(a,b)). The band diagrams that result at short-circuit

current density, with $U_{applied}$ = 0 V, as calculated from drift/diffusion dynamics, are shown in Figure 7(c,d), and indicate that the recombination noted in Figure 6 is likely to occur at the n-GaAs/TiO2 interface in these samples, such that the voltage applied instead drops across the TiO_2 and the n-GaAs approaches flatband.

In conclusion, we have demonstrated that Raman analysis of the LO and TO peaks in III-V semiconductors provides a mathematical window by which carrier concentration and collection over various light intensities may be analyzed and understood in terms of the resulting amount of voltage dropped in the space-charge region of the semiconductor. In the future, we will demonstrate that this approach may be applied to photoelectrochemical systems, particularly those with mixed-phase contacts in which the size of the contacting phases is instrumental in determining the quality of the junction.

Experimental

All Raman samples used herein were formulated on n-GaAs (111) wafers with a doping density of ~2 x 10^{17} cm^{-3}. Ohmic contact was made to the back of the sample following an establish procedure[9]. Briefly, thin Au Schottky barrier samples were produced by etching the wafer in neat tracemetal grade H_2SO_4 (Fisher) for 30 s, rinsing in H_2O (18.2 MΩ cm resistivity, Barnstead Nanopure System), and loading into an e-beam evaporator, in which 7 nm of Au was deposited at a rate of 0.1 Å s^{-1}. To ensure sufficient conductivity across the Au contact, ~100 nm of indium-doped tin-oxide (ITO) was deposited atop the Au using a AJA International sputtering system from a Kurt Lesker ITO target at an RC power of 100 W, gas pressure of 5 mTorr, and a gas makeup of 95% Ar and 5% O_2. n-GaAs/TiO_2/Ni/Au/ITO samples, were produced on n-GaAs (111) wafers which had been etched and rinsed as above, then placed into an ALD system for TiO_2 growth, followed by Ni sputter in the AJA sputterer, as described previously[4c, 10]. Au and ITO were directly grown on these samples as described above. Contact to the ITO was made through application of silver paint (SPI) which was contacted to a copper plate.

Current-voltage and capacitance-voltage experiments were performed using a Biologic SP-200 potentiostat in a 2-electrode configuration. Raman spectra were collected with a Renishaw inVia Raman microprobe equipped with a Leica DM 2500 M microscope, a Leica N Plan L 50x objective (numerical aperture = 0.50), a 1800 lines mm^{-1} grating, and a CCD detector configured in a 180° backscatter geometry. A 532 nm diode-pumped solid-state (DPSS) laser (Renishaw RL532C50) was used as the excitation source and the radiant flux incident on the surface of the sample was varied between XX μW and XX mW. A quartz-wedge achromatic depolarizer (DPU-25-A, ThorLabs) was

used to depolarize the incident excitation and no polarization optics were utilized to filter the collected signal. For LO/TO ratio calibration, an undoped, semi-insulating GaAs (111) wafer was tested under identical but electronically unconnected conditions. Spectra for each experimental condition were each collected > 6 times.

Figures.

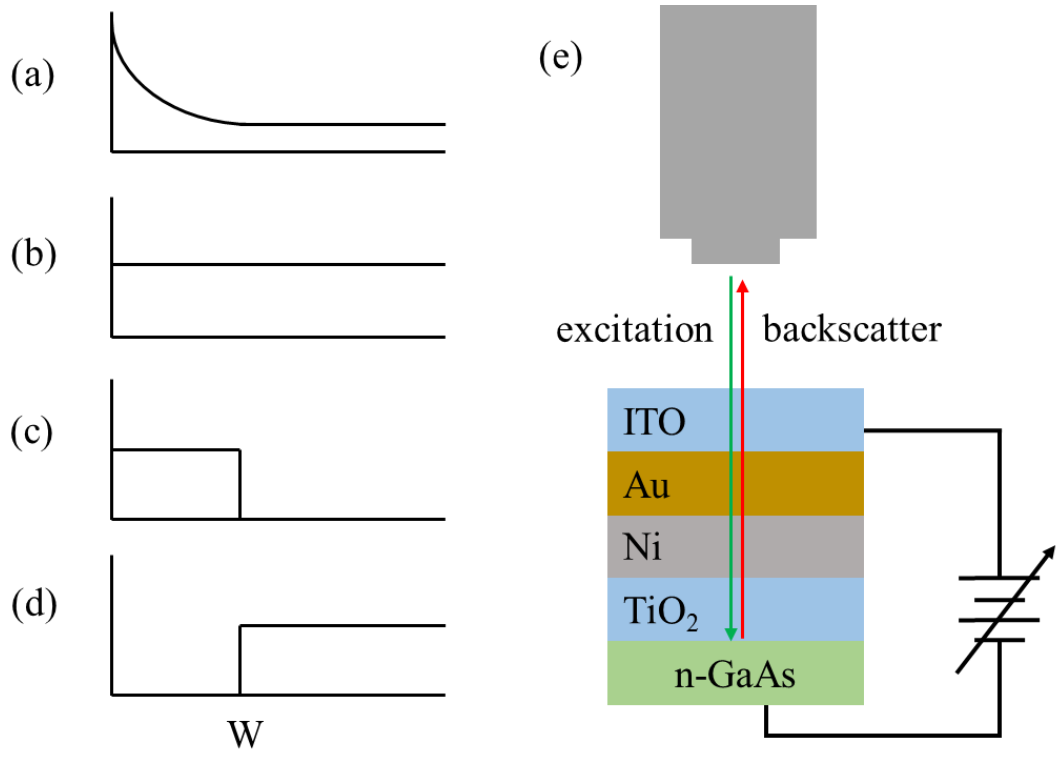

Figure 1. Plots of (a) the potential (U) and the intensity of the (b) TO phonon, (c) LO phonon and (d) and L^+ PLP modes as function of distance from the semiconductor top surface. (e) Schematic for Raman analysis of an electrically biased n-GaAs/TiO2/Ni/Au/ITO device. The incident and backscattered light are colored green and red for representative purposes only; in the experiment, incident light is at $\lambda = 532$ nm, and backscattered light generally has $532 < \lambda < 545$.

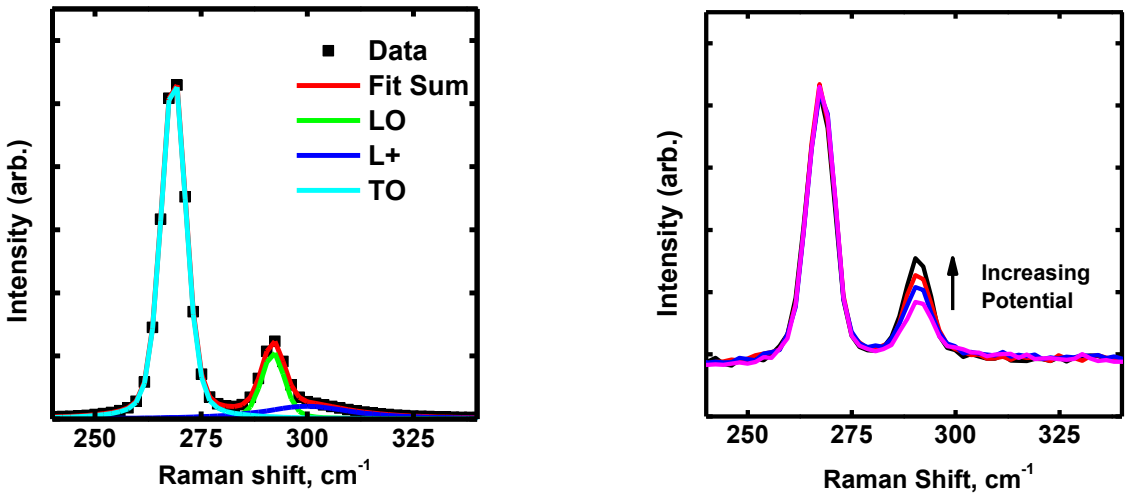

Figure 2. (a) Raman spectra collected from a n-GaAs/Au/ITO device biased at a potential near the flat-band potential (U_{app} = -1 V). Individual fits for the TO and LO phonon and L^+ PLP mode are indicated. (b) Series of Raman spectra analogous to that in (a) but at U_{app} potentials of 0V, .5V, 1V, and 2V.

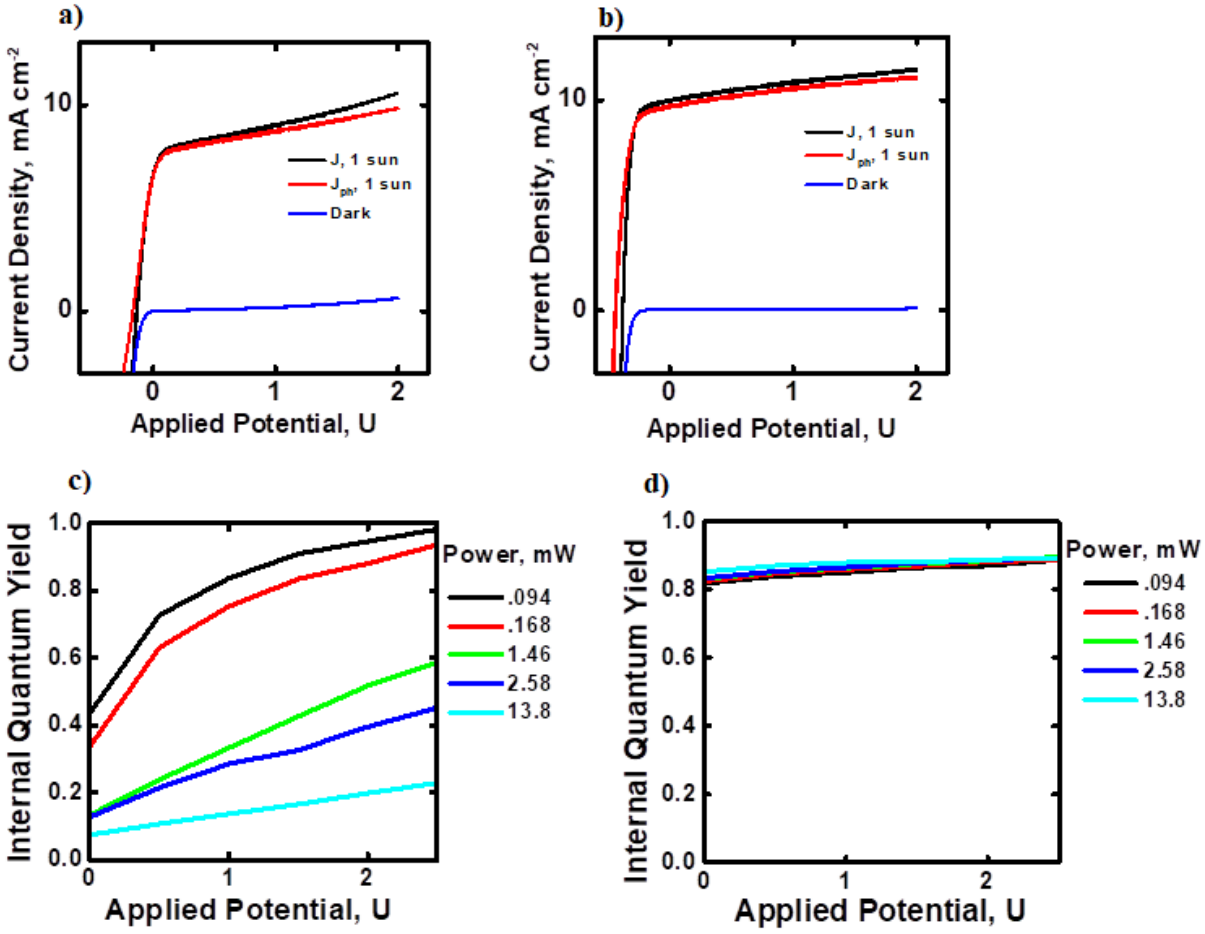

Figure 3. Cyclic voltammograms under dark conditions and at 1 sun illumination for (a) a n-GaAs/Au/ITO device and (b) a n-GaAs/TiO_2/Ni/Au/ITO device. J_{ph} is photocurrent density. Internal Quantum Yield (IQE) measurements with the samples in reverse bias, at varying excitation intensity, for (c) GaAs/TiO_2/Ni/Au/ITO and (d) n-GaAs/Au/ITO.

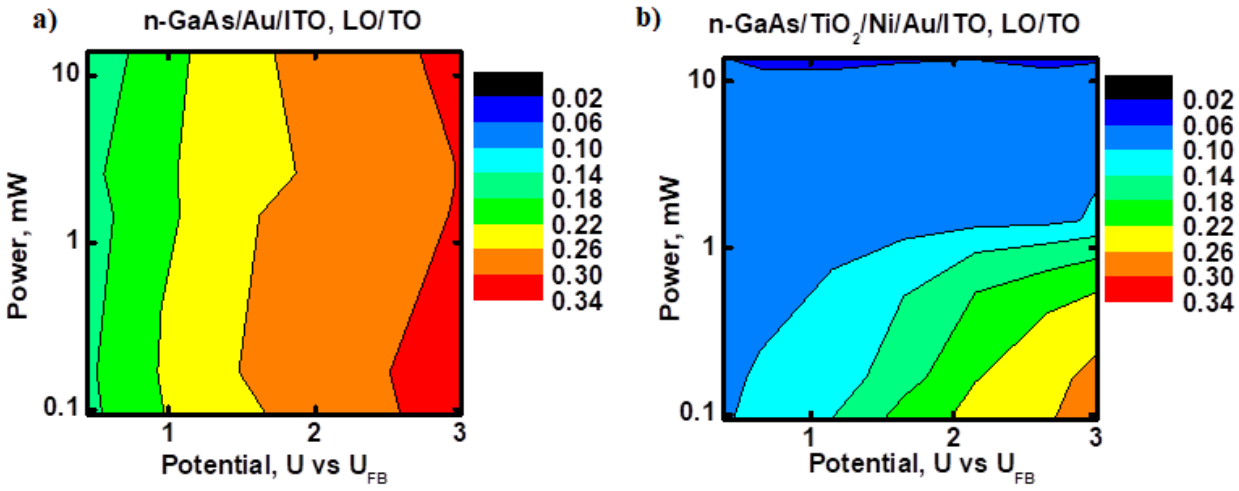

Figure 4. Contour plots showing the LO/TO ratios collected across a range of potentials for (a) n-GaAs/Au/ITO and (b) n-GaAs/TiO_2/Ni/Au/ITO. The LO/TO ratios are plotted with respect to voltage from the flat band potential. The color contour values are identical between the plots.

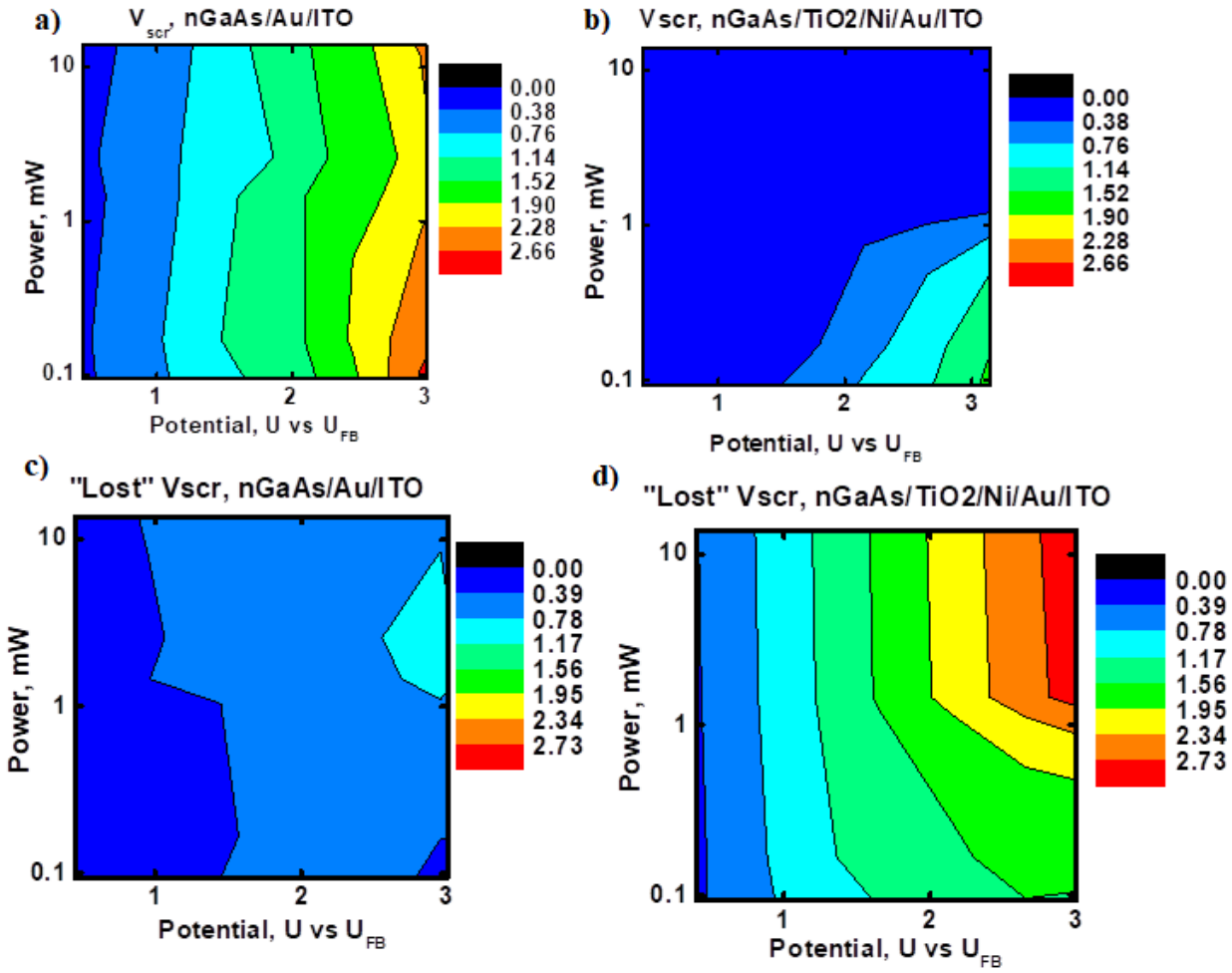

Figure 5. Contour plots for the calculated voltage in the space charge region (U_{SCR}) from equation 3 based on the LO/TO ratios in figure 4, for (a) n-GaAs/Au/ITO and (b) n-GaAs/TiO_2/Ni/Au/ITO. The contour coloring scheme is identical between the plots for ease of comparison. The difference between the amount of potential expected to be observed in the space charge region based on the potential with respect to flat band, and that actually observed in (a,b), is shown in (c,d) for (c) n-GaAs/Au/ITO and (d) n-GaAs/TiO2/Ni/Au/ITO. Again, the voltage is plotted against the flat band potential, the illumination is plotted logarithmically, and the contour coloring scheme is identical between (c) and (d) for ease of comparison.

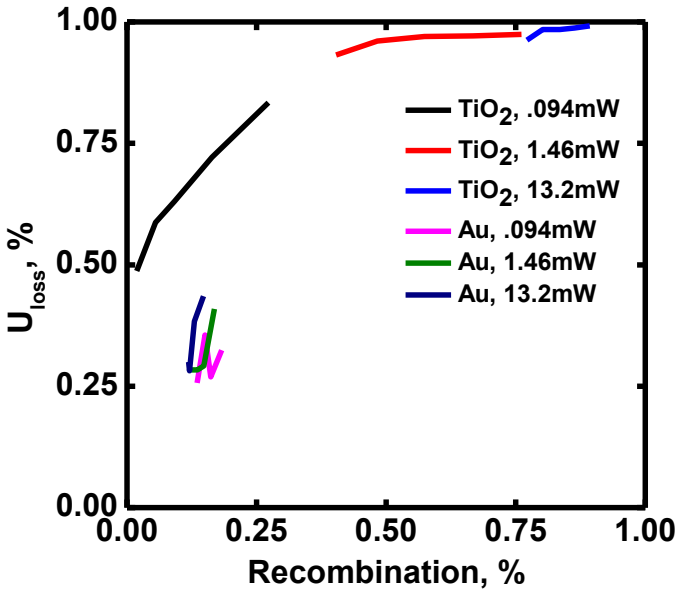

Figure 6. Percent loss of U_{SCR}, as determined by Raman measurements, plotted against percent of photocarriers which recombined, as determined from electronic measurements.

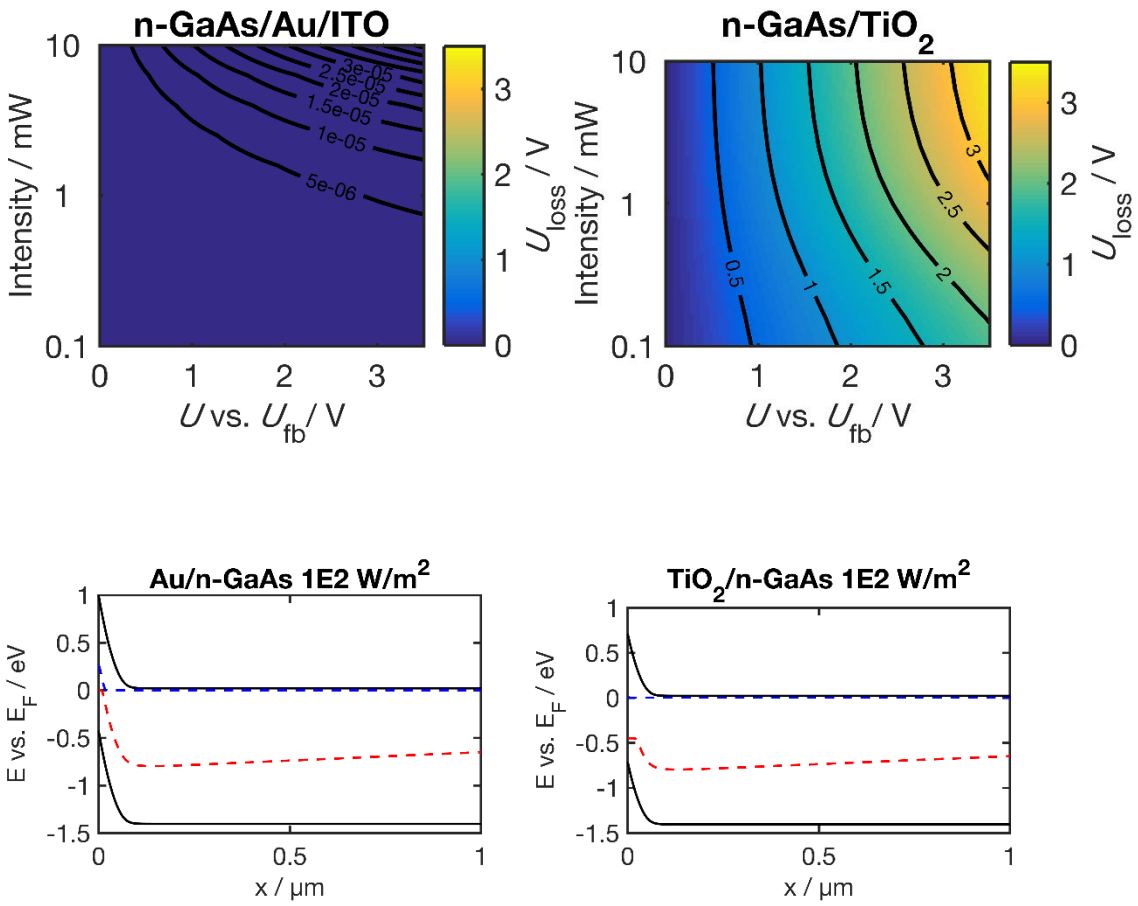

Figure 7. (a,b) Theory (Depilation Approximation) with additional parameter to account for charge carrier increase during illumination at steady state. (c,d) Band diagrams as calculated from drift/diffusion dynamics for each sample at short-circuit ($U_{applied}$ = 0 V) and at a light intensity of 532 nm light of 100 W m^{-2}.

Supplementary Information:

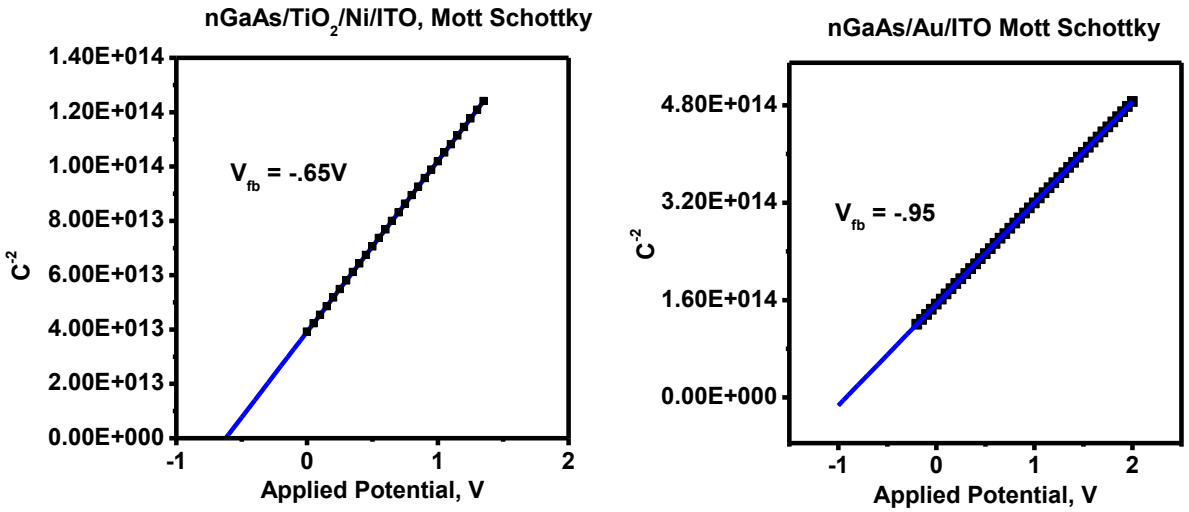

Figure S1. Mott-Schottky analysis of the two electrode types; the flat band potential is indicated on each.

References.

1. Tanabe, K., A review of ultrahigh efficiency III-V semiconductor compound solar cells: multijunction tandem, lower dimensional, photonic up/down conversion and plasmonic nanometallic structures. *Energies* **2009,** *2* (3), 504-530.
2. Laboratory, N. R. E., Best Research-Cell Efficiencies. **2017**.
3. (a) Verlage, E.; Hu, S.; Liu, R.; Jones, R. J. R.; Sun, K.; Xiang, C.; Lewis, N. S.; Atwater, H. A., A monolithically integrated, intrinsically safe, 10% efficient, solar-driven water-splitting system based on active, stable earth-abundant electrocatalysts in conjunction with tandem III?V light absorbers protected by amorphous TiO2 films. *Energy Environ. Sci.* **2015,** *8* (11), 3166-3172; (b) Sun, K.; Kuang, Y.; Verlage, E.; Brunschwig, B. S.; Tu, C. W.; Lewis, N. S., Sputtered NiOx Films for Stabilization of p+n-InP Photoanodes for Solar-Driven Water Oxidation. *Advanced Energy Materials* **2015,** *5* (11), 1402276-n/a; (c) Lee, M. H.; Takei, K.; Zhang, J.; Kapadia, R.; Zheng, M.; Chen, Y.-Z.; Nah, J.; Matthews, T. S.; Chueh, Y.-L.; Ager, J. W.; Javey, A., p-Type InP Nanopillar Photocathodes for Efficient Solar-Driven Hydrogen Production. *Angewandte Chemie International Edition* **2012,** *51* (43), 10760-10764.
4. (a) Lichterman, M. F.; Sun, K.; Hu, S.; Zhou, X.; McDowell, M. T.; Shaner, M. R.; Richter, M. H.; Crumlin, E. J.; Carim, A. I.; Saadi, F. H.; Brunschwig, B. S.; Lewis, N. S., Protection of inorganic semiconductors for sustained, efficient photoelectrochemical water oxidation. *Catalysis Today* **2016,** *262*, 11-23; (b) Sun, K.; Saadi, F. H.; Lichterman, M. F.; Hale, W. G.; Wang, H.-P.; Zhou, X.; Plymale, N. T.; Omelchenko, S. T.; He, J.-H.; Papadantonakis, K. M.; Brunschwig, B. S.; Lewis, N. S., Stable solar-driven oxidation of water by semiconducting photoanodes protected by transparent catalytic nickel oxide films. *P. N. A. S.* **2015,** *112* (12), 3612-3617; (c) Hu, S.; Shaner, M. R.; Beardslee, J. A.; Lichterman, M. F.; Brunschwig, B. S.; Lewis, N. S., Amorphous TiO2 coatings stabilize Si, GaAs, and GaP photoanodes for efficient water oxidation. *Science* **2014,** *344* (6187), 1005-1009.
5. Geurts, J., Analysis of band bending at III–V semiconductor interfaces by Raman spectroscopy. *Surf. Sci. Rep.* **1993,** *18* (1), 1-89.
6. Stolz, H.; Abstreiter, G., Raman spectroscopy as a surface sensitive technique on semiconductors. *Journal of Vacuum Science and Technology* **1981,** *19* (3), 380-382.
7. (a) Brugger, H.; Schäffler, F.; Abstreiter, G., In Situ Investigation of Band Bending during Formation of GaAs-Ge Heterostructures. *Physical Review Letters* **1984,** *52* (2), 141-144; (b) Fischer, R.; Masselink, W.; Klem, J.; Henderson, T.; McGlinn, T.; Klein, M.; Morkoc, H.; Mazur, J.; Washburn, J., Growth and properties of GaAs/AlGaAs on nonpolar substrates using molecular beam epitaxy. *Journal of Applied Physics* **1985,** *58* (1), 374-381; (c) Abstreiter, G.; Bauser, E.; Fischer, A.; Ploog, K., Raman spectroscopy—A versatile tool for characterization of thin films and heterostructures of GaAs and Al x Ga 1− x As. *Applied Physics A: Materials Science & Processing* **1978,** *16* (4), 345-352.
8. Parayanthal, P.; Pollak, F. H.; Woodall, J. M., Raman scattering characterization of Ga1−xAlxAs/GaAs heterojunctions: Epilayer and interface. *Appl. Phys. Lett.* **1982,** *41* (10), 961-963.

9. Peczonczyk, S. L.; Mukherjee, J.; Carim, A. I.; Maldonado, S., Wet Chemical Functionalization of III–V Semiconductor Surfaces: Alkylation of Gallium Arsenide and Gallium Nitride by a Grignard Reaction Sequence. *Langmuir* **2012,** *28* (10), 4672-4682.
10. Lichterman, M. F.; Hu, S.; Richter, M. H.; Crumlin, E. J.; Axnanda, S.; Favaro, M.; Drisdell, W.; Hussain, Z.; Mayer, T.; Brunschwig, B. S.; Lewis, N. S.; Liu, Z.; Lewerenz, H.-J., Direct observation of the energetics at a semiconductor/liquid junction by operando X-ray photoelectron spectroscopy. *Energy Environ. Sci.* **2015,** *8* (8), 2409-2416.